# OPTICS AND ULTRASOUND IN BIOMEDICINE: SENSING, IMAGING AND THERAPY

EDITED BY: Chao Tian, Jie Tian, Jun Xia, Xueding Wang, Zhihua Ding
and Zhaoyu Li
PUBLISHED IN: Frontiers in Physics

frontiers Research Topics

ISSN 1664-8714
ISBN 978-2-88971-075-1
DOI 10.3389/978-2-88971-075-1

## About Frontiers

Frontiers is more than just an open-access publisher of scholarly articles: it is a pioneering approach to the world of academia, radically improving the way scholarly research is managed. The grand vision of Frontiers is a world where all people have an equal opportunity to seek, share and generate knowledge. Frontiers provides immediate and permanent online open access to all its publications, but this alone is not enough to realize our grand goals.

## Frontiers Journal Series

The Frontiers Journal Series is a multi-tier and interdisciplinary set of open-access, online journals, promising a paradigm shift from the current review, selection and dissemination processes in academic publishing. All Frontiers journals are driven by researchers for researchers; therefore, they constitute a service to the scholarly community. At the same time, the Frontiers Journal Series operates on a revolutionary invention, the tiered publishing system, initially addressing specific communities of scholars, and gradually climbing up to broader public understanding, thus serving the interests of the lay society, too.

## Dedication to Quality

Each Frontiers article is a landmark of the highest quality, thanks to genuinely collaborative interactions between authors and review editors, who include some of the world's best academicians. Research must be certified by peers before entering a stream of knowledge that may eventually reach the public - and shape society; therefore, Frontiers only applies the most rigorous and unbiased reviews.
Frontiers revolutionizes research publishing by freely delivering the most outstanding research, evaluated with no bias from both the academic and social point of view. By applying the most advanced information technologies, Frontiers is catapulting scholarly publishing into a new generation.

## What are Frontiers Research Topics?

Frontiers Research Topics are very popular trademarks of the Frontiers Journals Series: they are collections of at least ten articles, all centered on a particular subject. With their unique mix of varied contributions from Original Research to Review Articles, Frontiers Research Topics unify the most influential researchers, the latest key findings and historical advances in a hot research area! Find out more on how to host your own Frontiers Research Topic or contribute to one as an author by contacting the Frontiers Editorial Office: frontiersin.org/about/contact

# OPTICS AND ULTRASOUND IN BIOMEDICINE: SENSING, IMAGING AND THERAPY

Topic Editors:
**Chao Tian,** University of Science, China
**Jie Tian,** Institute of Automation, China
**Jun Xia,** University at Buffalo, United States
**Xueding Wang,** University of Michigan, United States
**Zhihua Ding,** Zhejiang University, China
**Zhaoyu Li,** University of Queensland, Australia

**Citation:** Tian, C., Tian, J., Xia, J., Wang, X., Ding, Z., Li, Z., eds. (2021). Optics and Ultrasound in Biomedicine: Sensing, Imaging and Therapy. Lausanne: Frontiers Media SA. doi: 10.3389/978-2-88971-075-1

# Table of Contents

EDITORIAL
published: 17 June 2021
doi: 10.3389/fphy.2021.712405

# Editorial: Optics and Ultrasound in Biomedicine: Sensing, Imaging, and Therapy

*Chao Tian*[1]*, *Jun Xia*[2] *and Xueding Wang*[3]

[1]*College of Engineering Science, University of Science and Technology of China, Hefei, China,* [2]*Department of Biomedical Engineering, University at Buffalo, State University of New York, Buffalo, NY, United States,* [3]*Department of Biomedical Engineering, University of Michigan, Ann Arbor, MI, United States*

**Keywords: biomedical optics, ultrasound, medical imaging, photoacoustic imaging, optical coherence tomography, super-resolution imaging**

**Editorial on the Research Topic**

**Optics and Ultrasound in Biomedicine: Sensing, Imaging, and Therapy**

Biomedical optics is a branch of optics that studies the interaction of photon and biological tissues for the purpose of sensing, imaging, and treatment. Since light is fundamentally an electromagnetic wave with an ultra-short wavelength, optical-based sensing, imaging, and treatment technologies have advantages in resolution, contrast, sensitivity, and precision, and, therefore, have found unique applications in a range of biomedical fields. However, these applications are limited to superficial tissues due to the strong scattering of photons. Ultrasound, a mechanical wave with a longer wavelength, has a much greater penetration capability in soft tissues and can reach deep-seated biological targets. As a result, ultrasound-based technologies are widely used and intensively researched in many biomedical applications, ranging from diagnosis, intervention, to therapy. Essentially, biomedical optics and ultrasound both leverage the nature of waves and studies their interactions with biological tissues. Their synergy, such as emerging photoacoustics and photon-medicated ultrasound therapy, opens new possibilities for revolutionary applications in biology and medicine.

This Research Topic gathers and reviews the research community's accomplishments to date on optical- and ultrasound-based sensing, imaging, and therapeutic technologies and novel applications in medicine and biology through 15 contributions by 90 authors across the world. There are seven original contributions on optics-based biomedical research, reporting most recent progress in aberration and image reconstruction in structured illumination microscopy (SIM) (Liu et al.; Luo et al.), multi-wavelength diffuse optical tomography (DOT) (Zhang et al.), hyperspectral and video endoscopy (Cai et al.), femtosecond laser skin interaction (Wang et al.), fiber diffuse speckle based pulse wave measurement (Teng et al.), and backscattering based foodborne pathogens detection and classification (Wang et al.). There are two original contributions on ultrasound-based biomedical research, covering most recent progress in high-intensity focused ultrasound (HIFU) based vulvar lichen sclerosus treatment (Qu et al.) and portable ultrasound based food sweetness detection (Zhan et al.). There are four original contributions on the synergy of optics and ultrasound, discussing photoacoustic whole breast imaging (Zhang et al.), photoacoustic sensing of bone chemical composition (Feng et al.), Monte Carlo photon transport simulation in photoacoustic imaging (Lu et al.), and light- and ultrasound-activatable microcapsules for drug delivery (Zhu et al.). In addition, there are two review articles summarizing most recent advances in dual-modal photoacoustic imaging and optical coherence tomography (Hosseinaee et al.) and therapeutic ultrasound-enhanced immune checkpoint inhibitor therapy (Yuan et al.). These contributions encompass fundamental theory, technology developments, biomedical studies and clinical translations of optics and ultrasound in biomedicine and provides a useful snapshot of the fast evolving field that is representative of the international and interdisciplinary scope of interest.

OPEN ACCESS

***Edited and reviewed by:***
*Thomas Beyer,*
*Medical University of Vienna, Austria*

****Correspondence:***
*Chao Tian*
*ctian@ustc.edu.cn*

***Specialty section:***
*This article was submitted to Medical Physics and Imaging, a section of the journal Frontiers in Physics*

***Received:*** *20 May 2021*
***Accepted:*** *04 June 2021*
***Published:*** *17 June 2021*

***Citation:***
*Tian C, Xia J and Wang X (2021) Editorial: Optics and Ultrasound in Biomedicine: Sensing, Imaging, and Therapy. Front. Phys. 9:712405. doi: 10.3389/fphy.2021.712405*

The topic editors are grateful to the Frontiers in Physics support staff, as well as to the contributors and the reviewers for their invaluable dedication and support.

## AUTHOR CONTRIBUTIONS

All authors listed have made a substantial, direct, and intellectual contribution to the work and approved it for publication.

**Conflict of Interest:** The authors declare that the research was conducted in the absence of any commercial or financial relationships that could be construed as a potential conflict of interest.

frontiers in Physics

METHODS
published: 22 January 2020
doi: 10.3389/fphy.2019.00254

# Aberrations in Structured Illumination Microscopy: A Theoretical Analysis

*Xin Liu*[1], *Shijie Tu*[1], *Yan Xu*[1], *Hongya Song*[1], *Wenjie Liu*[1], *Qiulan Liu*[1], *Cuifang Kuang*[1,2,3], *Xu Liu*[1,2,3] *and Xiang Hao*[1]*

*[1] State Key Laboratory of Modern Optical Instrumentation, College of Optical Science and Engineering, Zhejiang University, Hangzhou, China, [2] Ningbo Research Institute, Zhejiang University, Ningbo, China, [3] Collaborative Innovation Center of Extreme Optics, Shanxi University, Taiyuan, China*

In super-resolution optical microscopes, aberrations often compromise the image performances by reducing its resolution and contrast. In previous works, the aberrations in stimulated emission depletion (STED) microscopy and single-molecule localization microscopy (SMLM) have been well-investigated, while the research on the aberrations in structured illumination microscopy (SIM) is not sufficient, the researchers always poured attention into aberrations only in the detection path. In this paper, we investigate the aberrations in SIM in a comprehensive manner, and their causes and effects on both the illumination and the detection paths are discussed. The aberrations in the illumination path may distort illumination patterns, and deteriorate the final images, together with the aberrations in the detection path. In addition, several non-aberration-related factors, especially the misalignment of the incident beams with respect to the objective pupil, can also dramatically influence the performances of SIM. The analysis provides the theoretical basis and for optimizing a SIM system.

**Keywords: fluorescence microscopy, structured illumination, aberrations, adaptive optics, Zernike polynomials**

***Edited by:***
*Chao Tian,*
*University of Science and Technology of China, China*

***Reviewed by:***
*Ming Lei,*
*Xi'an Jiaotong University (XJTU), China*
*Meng Lu,*
*University of Cambridge, United Kingdom*
*Baoli Yao,*
*Xian Institute of Optics and Precision Mechanics (CAS), China*

***Correspondence:***
*Xiang Hao*
*haox@zju.edu.cn*

***Specialty section:***
*This article was submitted to Optics and Photonics, a section of the journal Frontiers in Physics*

***Received:*** *29 October 2019*
***Accepted:*** *30 December 2019*
***Published:*** *22 January 2020*

***Citation:***
*Liu X, Tu S, Xu Y, Song H, Liu W, Liu Q, Kuang C, Liu X and Hao X (2020) Aberrations in Structured Illumination Microscopy: A Theoretical Analysis. Front. Phys. 7:254. doi: 10.3389/fphy.2019.00254*

## INTRODUCTION

Fluorescence microscopy is widely used for the visualization of microstructures and dynamic processes in cells. However, owing to the diffraction limit, the best resolution is only about a half wavelength of the fluorescence [1] when the conventional fluorescence microscope is applied. Nevertheless, the state-of-the-art super-resolution microscopy can break the diffraction limit. These methods include, but are not limited to the single-molecule localization microscopy (SMLM) that stochastically activates single molecules in the full-field [2–5], the stimulated emission depletion (STED) microscopy using a depletion doughnut focal spot to reduce the size of the effective point spread function (PSF) [6–8], and the structured illumination microscopy (SIM) illuminating the sample with a periodic pattern [9–11]. Among them, SIM is exceedingly significant for live-cell imaging, providing double spatial resolution than that of the conventional wide-field microscopy. In this method, a one-dimensional sinusoidal illumination pattern is produced in the focal plane of the objective lens. A series of images, when the sample is illuminated by the patterns with different phases and orientations, are acquired by a camera. Using the specific SIM reconstruction algorithms [12–15], the super-resolution image of the sample can be obtained.

In super-resolution optical microscopes, aberrations compromise the image performances by worsening its resolution and reducing its contrast. The aberrations in SMLM and STED microscopy have been investigated sufficiently in previous works [16–18]. However, for SIM, researchers always poured attention only into the aberrations in the detection path, or assume that the aberrations are identical in the two paths [19, 20]. The discussion regarding the illumination path is insufficient. Yet, the quality of the illumination pattern is also crucial for the imaging performance of SIM. To fully optimize the final images of SIM, it is essential to create a model to describe the aberrations in SIM more comprehensively and figure out how they affect both the illumination pattern and the detection PSF.

In this paper, a strategy is developed for quantifying aberration effects in SIM. We build a mathematical model to analyze how the aberrations affect the illumination pattern and the detection PSF. As the systematic aberrations can be minimized during the design, only the sample-induced aberrations are considered. In addition, several non-aberration-related factors, especially the misalignment of the incident beams with respect to the objective pupil, are also discussed.

## THEORY

In SIM, a sinusoid pattern is used to excite the sample. The image obtained by a camera can be expressed as:

$$i(\mathbf{r}) = [e(\mathbf{r}) \cdot o(\mathbf{r})] \otimes h(\mathbf{r}) \tag{1}$$

where $e(\mathbf{r}) = 1 + \cos(\mathbf{k_e} \cdot \mathbf{r} + \varphi)$ is the intensity distribution of the illumination pattern, $o(\mathbf{r})$ is the spatial distribution of the sample labeled with fluorophores, and $h(\mathbf{r})$ is the point spread function (PSF) of the detection path.

In the Fourier domain, Equation (1) can be expressed as:

$$\begin{aligned} \tilde{i}(\mathbf{k}) &= [\tilde{e}(\mathbf{k}) \otimes \tilde{o}(\mathbf{k})] \cdot \tilde{h}(\mathbf{k}) \\ &= [\tilde{o}(\mathbf{k}) + \frac{1}{2}\tilde{o}(\mathbf{k} - \mathbf{k_e}) \cdot e^{i\varphi} + \frac{1}{2}\tilde{o}(\mathbf{k} + \mathbf{k_e}) \cdot e^{-i\varphi}] \cdot \tilde{h}(\mathbf{k}) \end{aligned} \tag{2}$$

where $\tilde{i}(k)$, $\tilde{e}(k)$, $\tilde{o}(k)$, and $\tilde{h}(k)$ are the Fourier transform of $i(\mathbf{r})$, $e(\mathbf{r})$, $o(\mathbf{r})$, and $h(\mathbf{r})$, respectively. $\mathbf{k}$ represents the spatial frequency. Inducing structured illumination pattern, SIM can move the high spatial frequency information originally blocked by the optical system into the passband, which expands the size of the optical transfer function (OTF) of the system.

Equations (1) and (2) demonstrate that the image obtained by SIM is in close connection with the illumination pattern, the spatial distribution of the sample, and the PSF of the detection path. Therefore, we took both the illumination path and the detection path into consideration to analyze the aberrations in SIM. To simplify the discussion, only the sample-induced aberrations were considered, since the systematic aberrations are always minimized during the design. For the illumination path, the excitation pattern is generated by the interference of two beams, which can be expressed as:

$$e(\mathbf{r}) = [\mathbf{A_1} \exp(i\mathbf{k_1} \cdot \mathbf{r} + \varphi) + \mathbf{A_2} \exp(i\mathbf{k_2} \cdot \mathbf{r})]^2 \tag{3}$$

where $\mathbf{A_1}$ and $\mathbf{A_2}$ are the amplitudes of the two coherent incident beams, respectively. $\mathbf{k_1}$ and $\mathbf{k_2}$ are the wave vectors, respectively, and $\varphi$ is the phase difference between the two beams. To simplify the discussion, the two beams can be assumed to be s-polarized and $\varphi = 0$ [21], plus $|\mathbf{A_1}| = |\mathbf{A_2}|$. For the detection path, the PSF can be calculated using the vectorial diffraction theory [22, 23]. Moreover, in our simulation, the illumination beam and the detection beam are both linear polarized.

A mathematical model is built to analyze the effects of the aberrations. As depicted in **Figure 1**, the illumination beam exits the objective, propagates into the immersion medium layer, and then passes through the coverslip into the sample medium. On the other hand, in the detection path, following the reversibility principle of the beam path, the fluorescence emitted from the sample medium can be treated as the light focused by the same objective. The refractive indices (RI) of the three layers of media (immersion liquid, cover glass, and the sample) are represented as $n_1$, $n_2$, and $n_3$, respectively, while the thickness of the coverslip is $h$. The incident angles of the illumination beam on each media interface are $\theta_1$, $\theta_2$, and $\theta_3$, respectively, while the angles are $\alpha_1$ and $\alpha_2$ for the detection path. In our simulation, the objective is plan-apochromatic by default [24].

A Cartesian coordinate system ($x$, $y$, $z$) is built for the description of the position information (**Figure 1A**). The orientations of the unit vectors $x$ and $z$ are defined by the layer interface and the optical axis, respectively. The origin of the coordinate system is consistent with the position of the Gaussian focus in the absence of stratified media (no sample medium, **Figure 1B**), and the subscript $i$ denotes the ideal values [24]. Following the above definitions, the lower surface of the coverslip is located at $z = 0$, while the upper one at $z = -h$. To quantitatively test the aberration effects, we set the excitation and fluorescence wavelengths as 488 and 532 nm, respectively.

Aberrations are usually measured by the deviation of the practical wavefront from its ideal shape and can be expressed as:

$$\begin{aligned} \delta = {} & |\mathbf{k}| \cdot [-z_l \cdot n_3\cos\theta_3 + (z_l\text{-}z_u) \cdot n_2\cos\theta_2 + z_u \cdot n_1\cos\theta_1 \\ & - (h_i \cdot n_{2i}\cos\theta_{2i} - h_i \cdot n_{1i}\cos\theta_{1i})] \end{aligned} \tag{4}$$

where $z_l$ and $z_u$ are the $z$-coordinates of the lower and upper surface of the coverslip for simulation, respectively. Notably, $\delta_i = h_i \cdot (n_{2i}\cos\theta_{2i} - n_{1i}\cos\theta_{1i})$ is used to compensate for the aberrations induced by the RI difference between the immersion medium and the coverslip during the objective's design [24].

## RESULTS AND DISCUSSION

The results with no aberrations are shown in **Figure 1**. Different numerical apertures (NA) were applied during the simulations, and the specific parameters in each simulation are presented in **Table 1**. Combining the excitation patterns and the PSFs of the detection path, the images of SIM were reconstructed using the inverse matrix-based phase estimation algorithm (**Figure 1E**) [15], and the resolution was estimated using the parameter-free image resolution estimation method [25]. As what we expect, the comparisons between **Figures 1C–G** illustrate that using the objective with a larger NA generates a smaller PSF and a denser

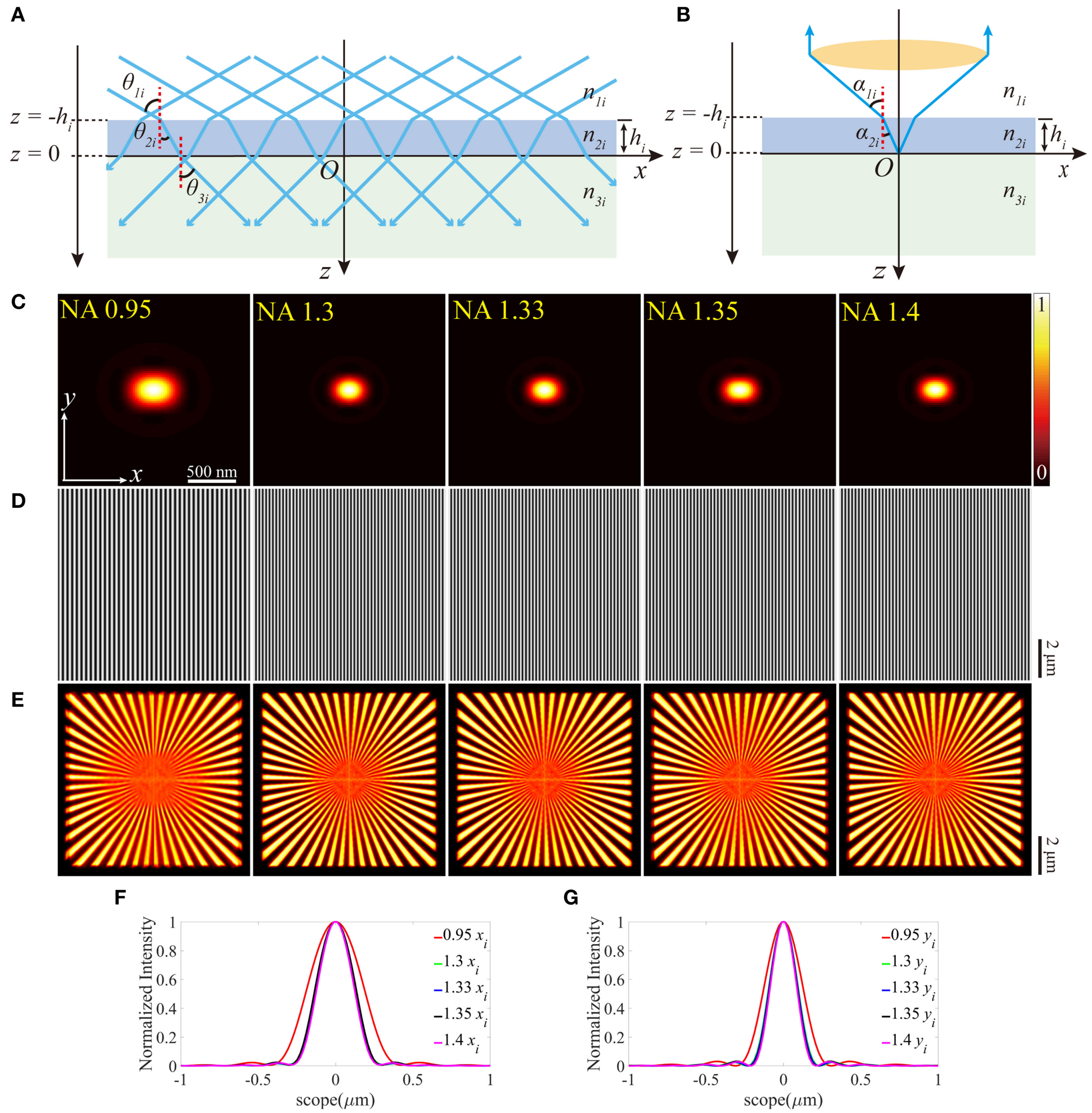

**FIGURE 1 |** SIM with no aberrations for objectives with different NAs. **(A)** The illumination beam path. **(B)** The fluorescence is inversely collected by the same objective using the classic epifluorescence architecture. **(C)** The PSFs on the plane $z = 0$ (ideal focal plane). **(D)** The excitation patterns calculated from different objectives using the same parameters in **(C)**. **(E)** The reconstructed images of SIM from the objectives with different NAs. From left to right, the resolutions are 164, 128, 125, 125, and 120 nm. **(F,G)** are profiles of the ideal PSFs in **(C)** on the x and y-direction, respectively.

sinusoid pattern, thereby achieving a better resolution. In our simulation, the ideal interference angle of the two beams is determined by $\theta_{1i} = \sin^{-1}(\mathrm{NA}/n_{1i})$.

We further investigated the effects of the aberrations when the value of the RI of the coverslip deviates from the desired one, which is depicted in **Figure 2**. In **Figures 2A,B**, the incident angles $\theta$ and $\alpha$ change in response to the varied RI of the coverslip. Similar to the above simulations, a series of different RIs were considered to discuss the effects in a more comprehensive manner, and **Figures 2C–I** are simulated in $n_2 = 1.521$ for detail.

As depicted in **Figure 2C**, the pupil functions of the detection path were calculated using the ray tracing. Moreover, to quantify the aberrations, we decomposed these pupil functions into Zernike polynomials [26, 27] from 0th to 14th modes, which are shown in **Figure 2D**. The piston (0th) mode holds the most part, which has no visible effect on the PSF, while the remainders are the defocus mode (4th) that simply makes the PSF out of focus and the primary spherical mode (12th) which increases the size of the PSF (**Figures 2E,F**). The profiles (**Figure 2H**) indicate that the aberrations induced in **Figure 2A** have little effects on the excitation patterns (**Figure 2G**) owing to the constant NA.

**TABLE 1** | Parameters in the ideal case.

| NA | $n_{1i}$ | $n_{2i}$ | $n_{3i}$ | $z_{li}$ (μm) | $z_{ui}$ (μm) |
|---|---|---|---|---|---|
| 0.95 | 1 | 1.515 | 1.38 | 0 | −170 |
| 1.3 | 1.518 | 1.515 | 1.38 | 0 | −170 |
| 1.33 | 1.53 | 1.515 | 1.38 | 0 | −170 |
| 1.35 | 1.406 | 1.518 | 1.38 | 0 | −170 |
| 1.4 | 1.518 | 1.518 | 1.38 | 0 | −170 |

The reconstructed images are shown in **Figure 2I**, which are blurred by the larger PSFs (**Figure 2E**), compared with the images in **Figure 1E**. In order to further detail the effects of the aberrations, the correlation coefficients of the reconstructed images are presented in **Figure 2J**. The simulated values of $n_2$ are set to be larger than the desired ones, otherwise, the light emitted from the sample cannot be collected by the objective effectively.

On the other hand, we investigated how the aberrations affect SIM images when the objective focuses deeper into the sample. As shown in **Figures 3A,B**, this case can be treated as the location shift of the coverslip along the optical axis. The $z$-coordinates of the lower and the upper surfaces ($z_l$ and $z_u$) of the coverslip change a value $a$, while the other parameters remain constant. A series of different $z_l$ are considered, and an example is given in **Figures 3C–I** ($z_l = -0.2\,\mu\text{m}$). The pupil functions are shown in **Figure 3C**, specifically, when NA $= 1.4$, the value on the edge of the pupil function is complex due to the total internal reflection (TIR), which reduces the effective size of pupil (**Figure 3J**) and the effective NA. The decomposition of the pupil function (**Figure 3D**) shows that the main aberration modes are the piston (0th), defocus (4th), and primary spherical (12th). The aberrated PSFs and the corresponding profiles are shown in **Figures 3E,F**, which are larger than that in the ideal case. The excitation patterns and the local profiles are illustrated in **Figures 3G,H**, and as a result of TIR, the intensity of the excitation pattern for NA $= 1.4$ is lower than that in the ideal case. However, the image is well-reconstructed with satisfactory contrast, for the reason that the contrast of the excitation pattern is the same as the ideal ones. Similarly, the images of SIM and the corresponding correlation coefficients are shown in **Figures 3I,K**.

Similarly, the thickness change of the coverslip, which may also induce aberrations can be treated as the offset of $z$-coordinate of the upper surface, while the lower surface still locates at $z = 0$ (**Figures 4A,B**). For objective that $n_1$ is smaller than $n_2$, the thickness should not be thinner than the ideal value, otherwise, the light emitted from the sample cannot be collected by the objective effectively. In contrast, the thicker coverslip is not valid if $n_1$ is larger than $n_2$. To make the discussion complete, different thicknesses of the coverslip are considered, and **Figures 4C–I** is an example for $h = 170.8\,\mu\text{m}$ (above the black dashed line) and $h = 169.25\,\mu\text{m}$ (below the black dashed line), respectively. **Figures 4J,K** indicate that the offset of the thickness affects the objective for NA $= 0.95$ more critically, and the increase of thickness is more serious than the reduction of that. No visible effects are induced in objective for NA $= 1.4$ because the aberrations have little effect on the pupil function and the excitation pattern.

All three cases discussed above can induce aberrations to some extent. However, these aberrations are symmetrical about the optical axis. Therefore, only the symmetric Zernike polynomials, e.g., defocus and spherical aberrations appear. The condition becomes more complicated when the symmetry is broken. As an example, we can give a small slope angle $\beta$ to the coverslip (**Figures 5A,B**). The direct consequence of the tilted coverslip is the re-organization of the incident angles $\theta$ and $\alpha$, which eventually results in the accumulation of the aberrations. It's paramount to be clear that the aberrations vary with the field of view along the $x$-axis, as a result of the various optical length difference. Therefore, the PSF is location dependent, and the final image is blurred by these variable PSFs. During the simulation, the slop angle $\beta$ varied within a range of $0\sim0.3^\circ$, and **Figures 5C–I** is an example when $\beta = 0.3^\circ$. The pupil functions were then calculated and decomposed into the first 15 Zernike modes, and the major modes now are tip (2nd) and coma (8th) aberration. Notably, in our simulation, the tilted coverslip has effects on the size of pupil function when NA $= 1.4$ (**Figure 5J**), as a result of the TIR induced by the tilt. Moreover, the intensity of the excitation pattern decreases with $x$ increasing, and the periods of these patterns change. The scope is different from that in the above cases because the sample only exists in the side $x > 0$ on the plane $z = 0$. Subsequently, the reconstructed images were obtained with deviation from the center of the scope, and the contrast reduced.

The correlation coefficients between the distorted images and that with no aberrations are shown in **Figure 5K**. Generally speaking, it descends with the slope angle $\beta$ increasing. However, for NA $= 0.95$, the correlation coefficient decreases first and then increases.

Based on the above results, the aberrations induced by the mismatched RIs, the increase of the focal depth, and the biased thickness of the coverslip have little effects on the excitation patterns. However, the PSFs are more affected, which is shown in the larger size caused by the defocus and the primary spherical aberrations. The immediate effect of these aberrations is the more blurred reconstructed images of SIM. Moreover, the aberrations induced by the tilted coverslip change the period of the excitation pattern, and result in the non-uniform contrast, on the other hand, the PSF of the detection path is stretched and biased in the $x$-$y$ plane. Correspondingly, the reconstructed images of SIM are biased, and the contrasts are non-uniform, as shown in **Figure 5I**. In particular, as for the objective with a larger NA (e.g., NA $=$ 1.4), the reduction of the coverslip thickness and the tilted case not only induce aberrations but also reduce the effective size of the pupil in the detection path.

In previous research, the aberrations on the pupil plane of the illumination path are investigated [28], however, the offset of the excitation beam with respect to the BFP of the objective, can also intensely affect the reconstructed images of SIM. In the optical system of the illumination path, the excitation pattern can be treated as the Fourier transform of two edge points on the pupil plane. As depicted in **Figure 6A**, one of the two edge points shifts toward the center point of the size-normalized pupil plane, $m$ represents the distance between the edge point and the center. Furthermore, the amplitude on the corresponding pupil function of the detection path is shown in

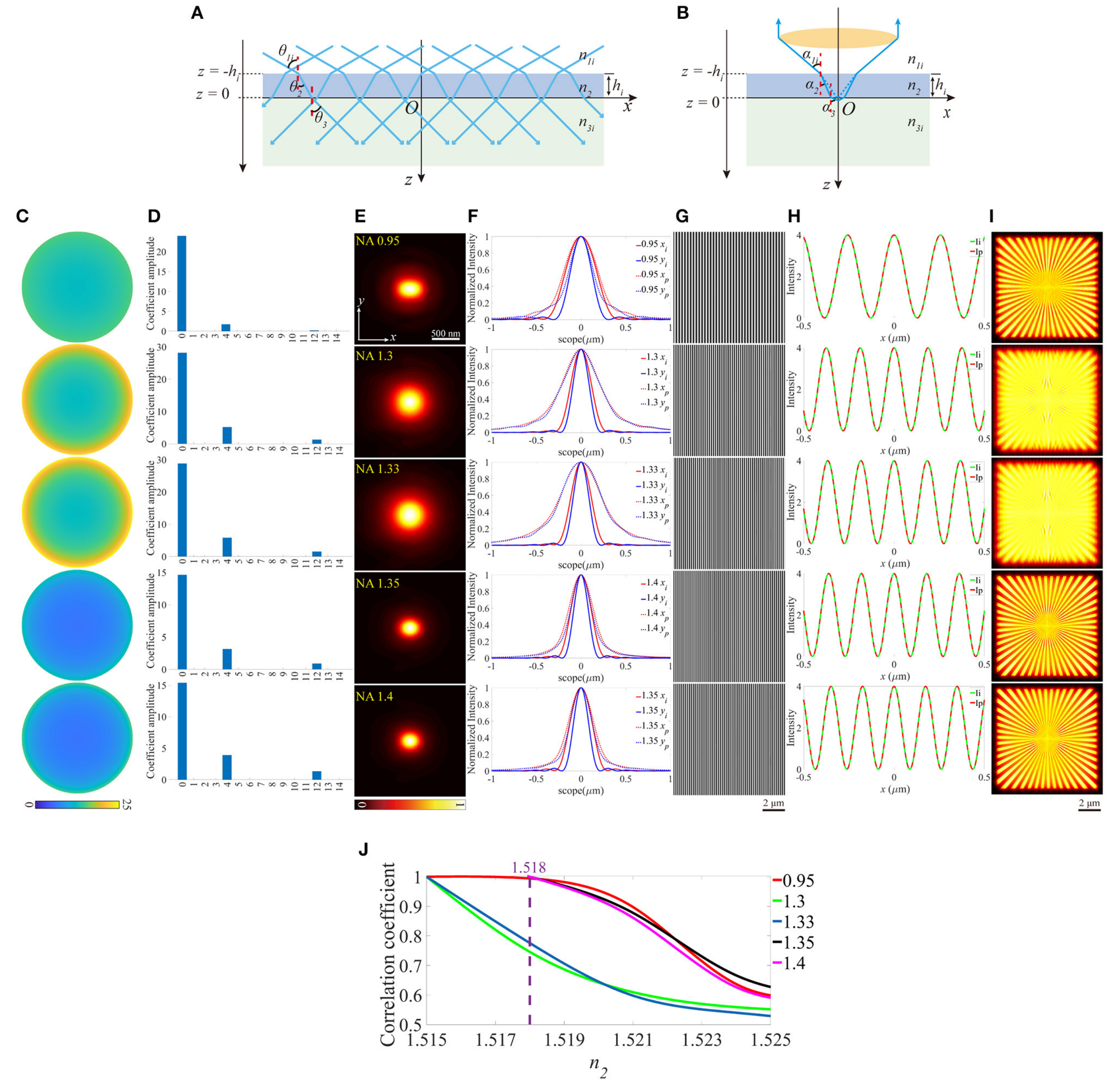

**FIGURE 2 |** The aberrations induced by the deviation of the RI of the coverslip. **(A,B)** The RIs between the immersion medium and the coverslip mismatch for the illumination path and the detection path, respectively. **(C)** The pupil functions calculated from the case depicted in **(B)**. **(D)** Zernike decomposition of the pupil functions shown in **(C)**. **(E)** The PSFs on the plane $z = 0$, calculated from the corresponding pupil functions. **(F)** The profiles of the ideal (solid line) and biased (dashed line) PSFs in **(E)**. **(G)** The excitation patterns affected by these biased RIs. **(H)** The local profiles of the corresponding excitation patterns shown in **(G)**. The red dashed line Ip presents the biased case and the green solid line Ii presents the ideal case, respectively. The scope is $-0.5 \sim 0.5\,\mu$m. **(I)** The corresponding reconstructed images of SIM. **(J)** The correlation coefficients of SIM images with different $n_2$and NAs. The purple dashed line corresponds to $n_2 = 1.518$.

**Figure 6B**. **Figures 6C–G** is an example for $m = 0$, therefore, the PSFs (**Figure 6C**) distorted to more elliptical shapes. The excitation patterns and profiles are depicted in **Figures 6E,F**, in which the periods of the patterns show an intense difference from the ideal counterparts. The reconstructed images show that the images include a lot of ghost parts in higher NA objectives (**Figure 6G**). The correlation coefficients are calculated and plotted in **Figure 6H**. The quality of the images declines with the distance between the edge point and the center of the pupil plane increasing for all objectives.

The aberration modes we built include the biased working condition of the objective (as discussed above, the illumination path has a stable performance, however, the PSFs are expanded in the detection path, and the resolution of the reconstructed

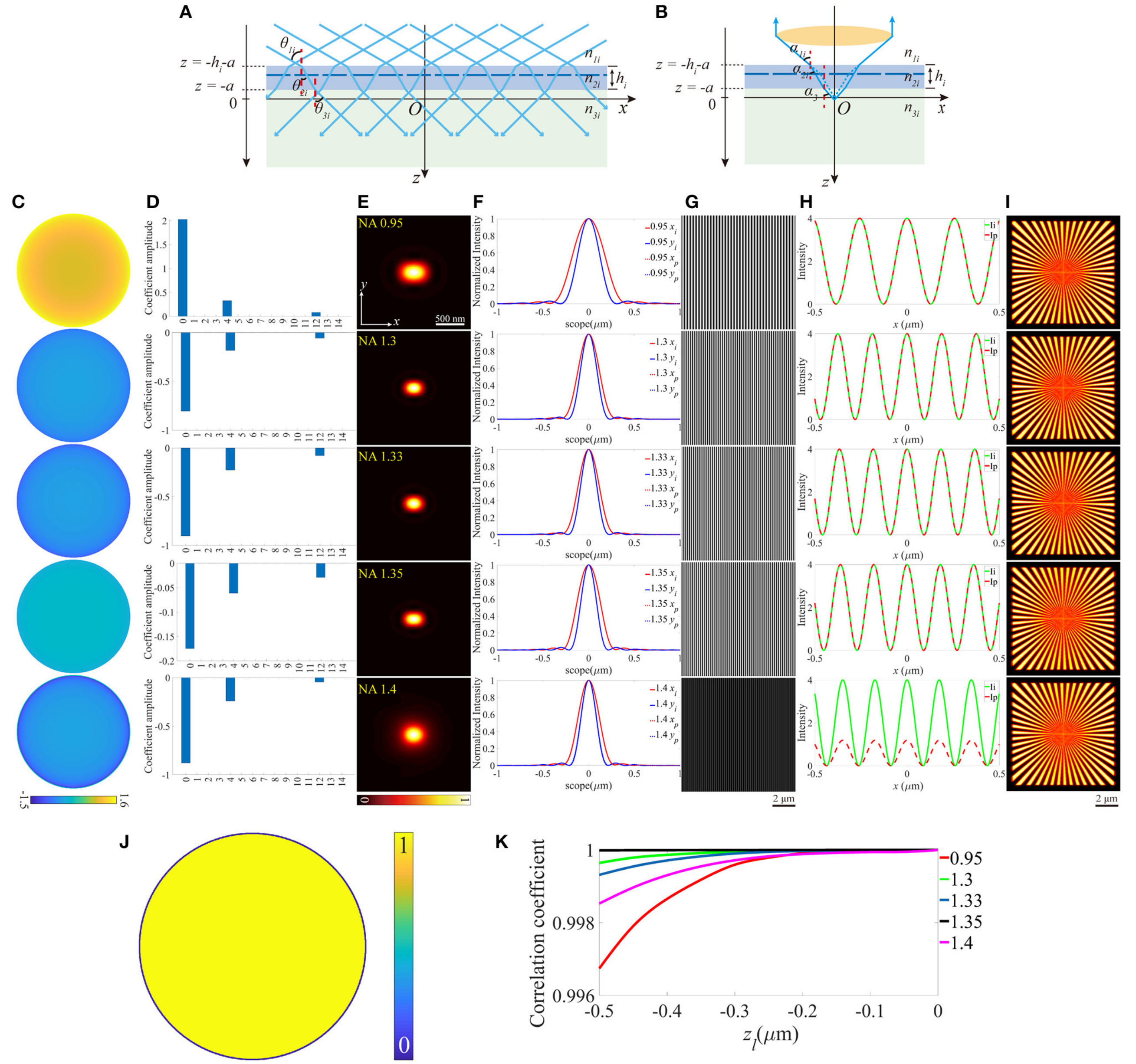

**FIGURE 3 |** The aberrations induced by the increase of the focal depth. **(A,B)** The case that objective focuses deeper into the sample medium. **(C)** The pupil functions calculated from the case depicted in **(B)**. **(D)** Zernike decomposition of the pupil functions shown in **(C)**. **(E)** The PSFs on the plane $z = 0$, calculated from the corresponding pupil functions. **(F)** The profiles of the ideal and biased PSFs in **(E)**. **(G)** The excitation patterns affected by biased $z_l$. **(H)** The local profiles of the corresponding excitation patterns shown in **(G)**, the scope is $-0.5 \sim 0.5\,\mu$m. **(I)** The corresponding reconstructed images of SIM. **(J)** The effective pupil for NA = 1.4. **(K)** The correlation coefficients of SIM images with different $z_l$.

images is reduced) and the tilted coverslip, which induce the non-uniform contrast and the offset from the center of the reconstructed images. These modes are very beneficial to the analysis for the aberrations induced by the immersion medium and the coverslip, and have potential application in the adaptive optics for SIM. Additionally, the distance between the two edge points on the BFP of the objective is taken into account, which leads to a tremendous change of the excitation patterns from the ideal counterparts, and PSFs are just like being squished on the vertical direction, therefore, the reconstructed images include a lot of ghost parts. It's necessary to comprehend these effects for further optimizing a SIM system, for example, if the reconstructed images contain ghost parts, the researchers can analyze the source of the damage by reference to the aberration mode of misaligned pupil. However, in practical experiments, the noise and background

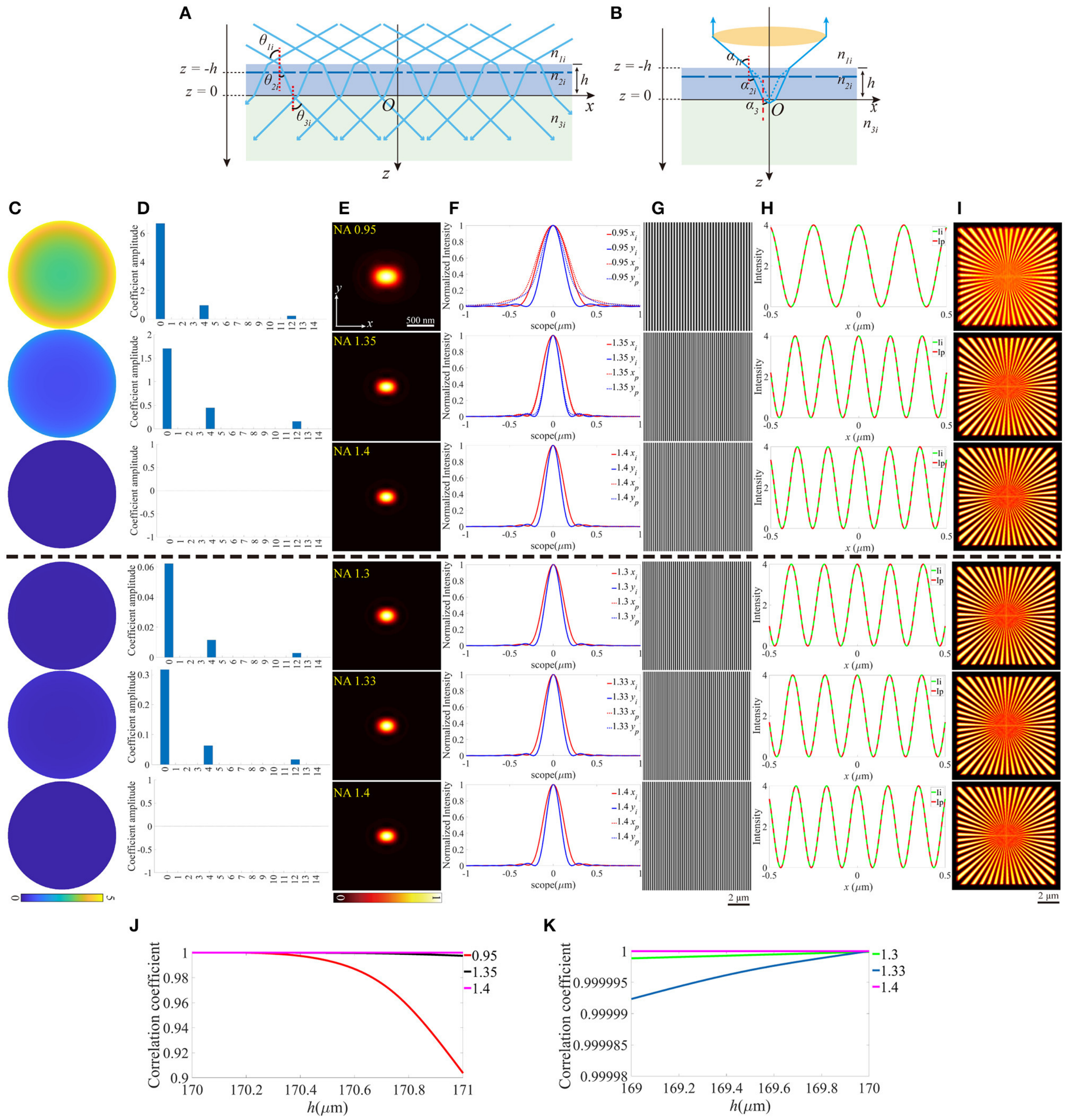

**FIGURE 4 |** The aberrations induced by the deviation of the thickness of the coverslip. **(A,B)** The thickness of the coverslip has a biased value for the illumination path and the detection path. **(C)** The pupil functions calculated from the case depicted in **(B)**. **(D)** Zernike decomposition of the pupil functions shown in **(C)**. **(E)** The PSFs on the plane $z = 0$, calculated from the corresponding pupil functions. **(F)** The profiles of the ideal and biased PSFs in **(E)**. **(G)** The excitation patterns affected by the biased *h*. **(H)** The local profiles of the corresponding excitation patterns shown in **(G)**, the scope is $-0.5 \sim 0.5\,\mu$m. **(I)** The corresponding reconstructed images of SIM. **(J,K)** The correlation coefficients of SIM images with different *h* for $n_1 \leq n_2$ and $n_1 \geq n_2$, respectively.

intensity must be taken into consideration, which aggravates the quality of images more intensely. Moreover, with the increase of the imaging depth, not only do the aberrations increase, but also the influence of scattering and absorption should be paid more attention.

## SUMMARY

In conclusion, we have built modes for the mismatched RIs, the increase of the focal depth, and the biased thickness of the coverslip, the tilted coverslip, and the misalignment of incident

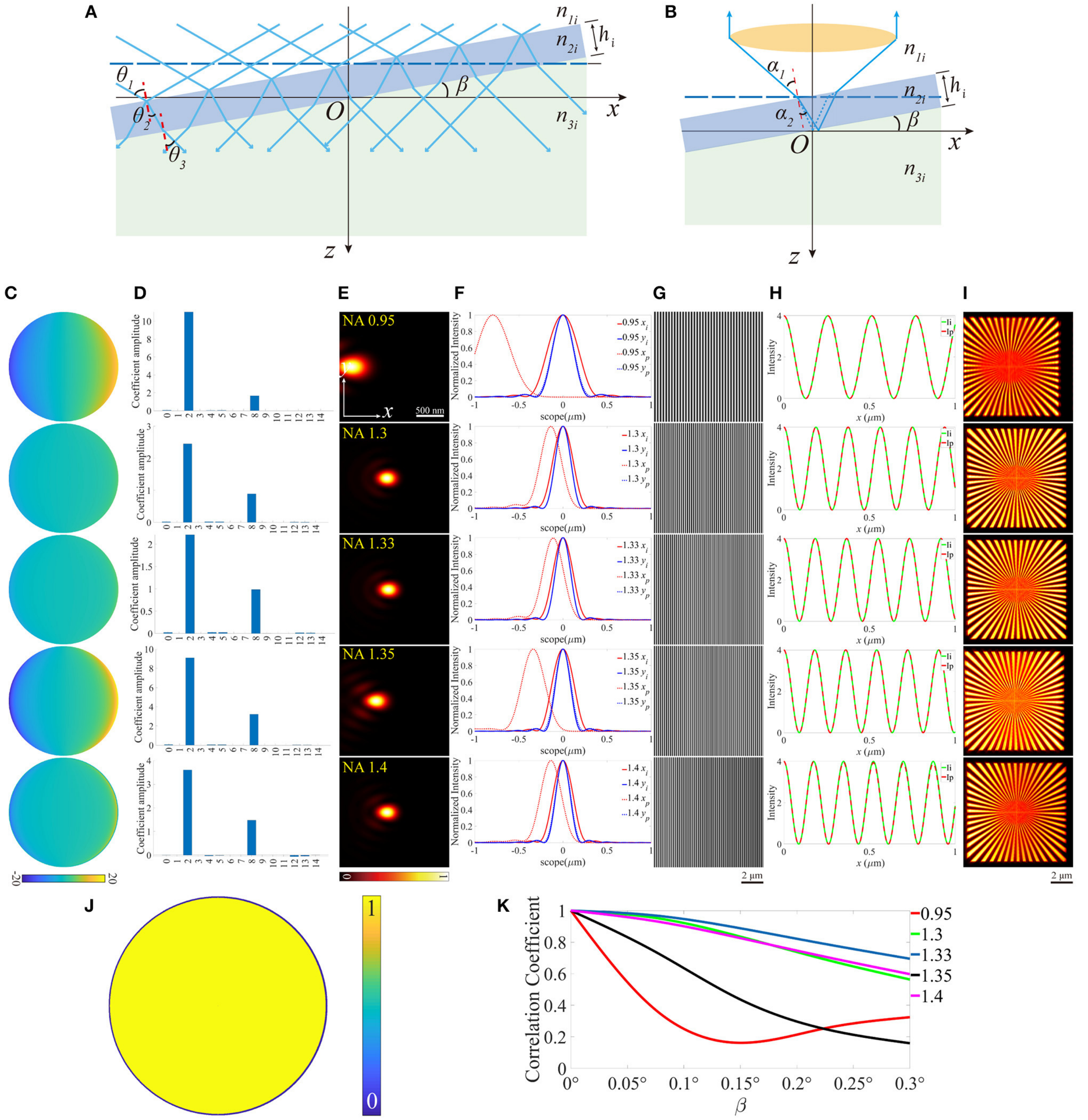

**FIGURE 5 |** The diagrams of the illumination path and the detection path for a tilted coverslip, and the corresponding results for $\beta = 0.3°$. **(A,B)** The tilted coverslip mode in the illumination path and the detection path. **(C)** The pupil functions calculated from the case depicted in **(B)**. **(D)** Zernike decomposition of the pupil functions shown in **(C)**, the first 15 orders of modes are used. **(E)** The PSFs on the plane $z = 0$, calculated with the pupil functions shown in **(C)**. **(F)** The profiles of the ideal and biased PSFs in **(E)**. **(G)** The excitation patterns affected by the aberrations. **(H)** The profiles of the excitation pattern shown in **(G)**, the scope is $0 \sim 1\,\mu$m. **(I)** The reconstruction images of SIM. **(J)** The effective pupil for NA = 1.4. **(K)** The correlation coefficients of the reconstructed images and the corresponding slope angle $\beta$.

beams with respect to the BFP of the objective, respectively. In these modes, the excitation patterns are calculated based on the principle of two beams interference. In the first four modes, the pupil functions of the detection path are calculated using the ray tracing and are decomposed into the first 15th Zernike polynomials to obtain a quantified analysis, however, for the misalignment of incident beams, the pupil is not filled in the detection path. Consequently, the PSF of the detection path is distorted as a result of the corresponding pupil function, and combined with the excitation pattern, the reconstructed images

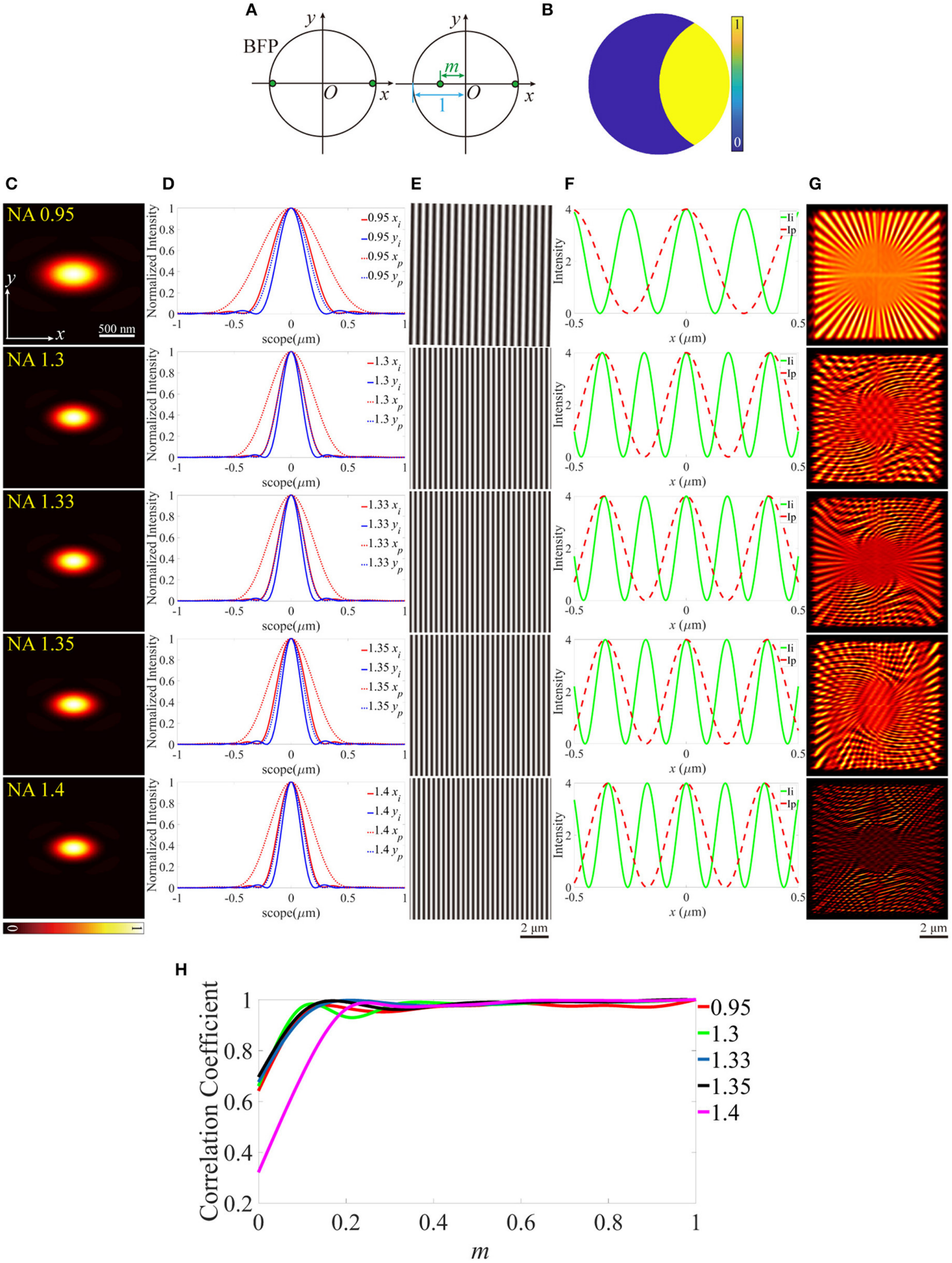

**FIGURE 6 |** Effects of the off-centered excitation beam. **(A)** The back focal plane (BFP) of the objectives. **(B)** The pupil function of the detection path. **(C)** PSFs on the plane $z = 0$, calculated from the pupil function in **(B)**. **(D)** The profiles of the ideal and biased PSFs in **(C)**. **(E)** The excitation patterns. **(F)** The local profiles of the corresponding excitation patterns shown in **(E)**, the scope is $-0.5 \sim 0.5\,\mu$m. **(G)** The reconstructed images of SIM. $m = 0$ for all objectives. **(H)** The correlation coefficients of the biased reconstructed images and the corresponding $m$.

are affected at different levels in these cases. The quantified descriptions for these modes can assist in monitoring and compensating the aberrations by adaptive optics, and a more completed reference for the correction of the SIM systems can be obtained.

This model is beneficial for the estimation and the correction of the aberrations in SIM, giving a guideline to further improve the performance of the SIM microscopes. In addition, this model is generally applicable to the systems that use structured illumination, e.g., such as multi-beams interference illumination.

## DATA AVAILABILITY STATEMENT

All datasets generated for this study are included in the article/supplementary material.

## AUTHOR CONTRIBUTIONS

XH conceived the idea. XiL, ST, and YX did the simulation. HS, WL, and QL gave the guide for analysis. XH, CK, and XuL supervised the project. All the authors contributed to the discussion on the results for this manuscript.

## FUNDING

This work was financially supported by the grants from National Key R&D Program of China (2018YFA0701400), the Fundamental Research Funds for the Central Universities (2019QNA5006), and ZJU-Sunny Photonics Innovation Center (2019-01).

## REFERENCES

1. Abbe E. Beiträge zur Theorie des Mikroskops und der mikroskopischen Wahrnehmung. *Archiv Mikrosk Anat*. (1873) **9**:413–68. doi: 10.1007/BF02956173
2. Betzig E, Patterson GH, Sougrat R, Lindwasser OW, Olenych S, Bonifacino JS, et al. Imaging intracellular fluorescent proteins at nanometer resolution. *Science*. (2006) **313**:1642–5. doi: 10.1126/science.1127344
3. Rust MJ, Bates M, Zhuang X. Sub-diffraction-limit imaging by stochastic optical reconstruction microscopy (STORM). *Nat Methods*. (2006) **3**:793–5. doi: 10.1038/nmeth929
4. Folling J, Bossi M, Bock H, Medda R, Wurm CA, Hein B, et al. Fluorescence nanoscopy by ground-state depletion and single-molecule return. *Nat Methods*. (2008) **5**:943–5. doi: 10.1038/nmeth.1257
5. Thompson MA, Lew MD, Badieirostami M, Moerner WE. Localizing and tracking single nanoscale emitters in three dimensions with high spatiotemporal resolution using a double-helix point spread function. *Nano Lett*. (2010) **10**:211–8. doi: 10.1021/nl903295p
6. Hell SW, Wichmann J. Breaking the diffraction resolution limit by stimulated emission: stimulated-emission-depletion fluorescence microscopy. *Opt Lett*. (1994) **19**:780–2. doi: 10.1364/OL.19.000780
7. Rittweger E, Han KY, Irvine SE, Eggeling C, Hell SW. STED microscopy reveals crystal colour centres with nanometric resolution. *Nat Photon*. (2009) **3**:144–7. doi: 10.1038/nphoton.2009.2
8. Nagerl UV, Willig KI, Hein B, Hell SW, Bonhoeffer T. Live-cell imaging of dendritic spines by STED microscopy. *Proc Natl Acad Sci USA*. (2008) **105**:18982–7. doi: 10.1073/pnas.0810028105
9. Gustafsson MG. Surpassing the lateral resolution limit by a factor of two using structured illumination microscopy. *J Microsc*. (2000) 198(Pt 2):82–7. doi: 10.1046/j.1365-2818.2000.00710.x
10. Gustafsson MG. Nonlinear structured-illumination microscopy: wide-field fluorescence imaging with theoretically unlimited resolution. *Proc Natl Acad Sci USA*. (2005) **102**:13081–6. doi: 10.1073/pnas.0406877102
11. Heintzmann R, Jovin TM, Cremer C. Saturated patterned excitation microscopy–a concept for optical resolution improvement. *J Opt Soc Am A Opt Image Sci Vis*. (2002) **19**:1599–609. doi: 10.1364/JOSAA.19.001599
12. Wicker K, Mandula O, Best G, Fiolka R, Heintzmann R. Phase optimisation for structured illumination microscopy. *Opt Expr*. (2013) **21**:2032–49. doi: 10.1364/OE.21.002032
13. Wicker K. Non-iterative determination of pattern phase in structured illumination microscopy using auto-correlations in Fourier space. *Opt Expr*. (2013) **21**:24692–701. doi: 10.1364/OE.21.024692
14. Muller M, Monkemoller V, Hennig S, Hubner W, Huser T. Open-source image reconstruction of super-resolution structured illumination microscopy data in ImageJ. *Nat Commun*. (2016) **7**:10980. doi: 10.1038/ncomms10980
15. Cao R, Chen Y, Liu W, Zhu D, Kuang C, Xu Y, et al. Inverse matrix based phase estimation algorithm for structured illumination microscopy. *Biomed Opt Expr*. (2018) **9**:5037–51. doi: 10.1364/BOE.9.005037
16. Coles BC, Webb SE, Schwartz N, Rolfe DJ, Martin-Fernandez M, Lo Schiavo V. Characterisation of the effects of optical aberrations in single molecule techniques. *Biomed Opt Expr*. (2016) **7**:1755–67. doi: 10.1364/BOE.7.001755
17. Deng S, Liu L, Cheng Y, Li R, Xu Z. Effects of primary aberrations on the fluorescence depletion patterns of STED microscopy. *Opt Expr*. (2010) **18**:1657–66. doi: 10.1364/OE.18.001657
18. Deng S, Liu L, Cheng Y, Li R, Xu Z. Investigation of the influence of the aberration induced by a plane interface on STED microscopy. *Opt Expr*. (2009) **17**:1714–25. doi: 10.1364/OE.17.001714
19. Debarre D, Botcherby EJ, Booth MJ, Wilson T. Adaptive optics for structured illumination microscopy. *Opt Expr*. (2008) **16**:9290–305. doi: 10.1364/OE.16.009290
20. Thomas B, Wolstenholme A, Chaudhari SN, Kipreos ET, Kner P. Enhanced resolution through thick tissue with structured illumination and adaptive optics. *J Biomed Opt*. (2015) **20**:26006. doi: 10.1117/1.JBO.20.2.026006
21. O'Holleran K, Shaw M. Polarization effects on contrast in structured illumination microscopy. *Opt Lett*. (2012) **37**:4603–5. doi: 10.1364/OL.37.004603
22. Richards B, Wolf E, Gabor D. Electromagnetic diffraction in optical systems, II. Structure of the image field in an aplanatic system. *Proc R Soc Lond Ser A Math Phys Sci*. (1959) **253**:358–79. doi: 10.1098/rspa.1959.0200
23. Hao X, Kuang C, Wang T, Liu X. Effects of polarization on the de-excitation dark focal spot in STED microscopy. *J Opt*. (2010) **12**:115707. doi: 10.1088/2040-8978/12/11/115707
24. Nasse MJ, Woehl JC. Realistic modeling of the illumination point spread function in confocal scanning optical microscopy. *J Opt Soc Am A Opt Image Sci Vis*. (2010) **27**:295–302. doi: 10.1364/JOSAA.27.000295

25. Descloux A, Grussmayer KS, Radenovic A. Parameter-free image resolution estimation based on decorrelation analysis. *Nat Methods*. (2019) **16**:918–24. doi: 10.1038/s41592-019-0515-7
26. Zernike VF. Beugungstheorie des schneidenver-fahrens und seiner verbesserten form, der phasenkontrastmethode. *Physica*. (1934) **1**:689–704. doi: 10.1016/S0031-8914(34)80259-5
27. Born M, Wolf E, Bhatia AB, Clemmow PC, Gabor D, Stokes AR, et al. *Principles of Optics.* Cambridge: Cambridge University Press (1999).
28. Booth M, Andrade D, Burke D, Patton B, Zurauskas M. Aberrations and adaptive optics in super-resolution microscopy. *Microscopy*. (2015) **64**:251–61. doi: 10.1093/jmicro/dfv033

**Conflict of Interest:** The authors declare that the research was conducted in the absence of any commercial or financial relationships that could be construed as a potential conflict of interest.

frontiers in Physics

ORIGINAL RESEARCH
published: 08 April 2020
doi: 10.3389/fphy.2020.00097

# Rapid Classification of Single Bacterium Based on Backscattering Microscopic Spectrum—A Pilot Study

**Cheng Wang[1], Bin Liu[1], Sen Li[2], Qing Liu[2], Minghui Chen[1], Gang Zheng[1], Songlin Zhuang[3], Dawei Zhang[3]* and Xunbin Wei[4,5]***

[1] Key Lab of Medical Optical Technology and Instrument, Ministry of Education, Institute of Biomedical Optics and Optometry, University of Shanghai for Science and Technology, Shanghai, China, [2] Institute of Food Microbiology, School of Medical Instruments and Food Engineering, University of Shanghai for Science and Technology, Shanghai, China, [3] Key Laboratory of Modern Optical System, Engineering Research Center of Optical Instrument and System, Ministry of Education, University of Shanghai for Science and Technology, Shanghai, China, [4] School of Biomedical Engineering, Med-X Research Institute, Shanghai Jiao Tong University, Shanghai, China, [5] School of Physics, Foshan University, Foshan, China

**Edited by:**
Chao Tian,
University of Science and Technology of China, China

**Reviewed by:**
Liwei Liu,
Shenzhen University, China
Delong Zhang,
Zhejiang University, China
Wei Gong,
Zhejiang University, China

***Correspondence:**
Dawei Zhang
dwzhang@usst.edu.cn
Xunbin Wei
xwei01@sjtu.edu.cn

**Specialty section:**
This article was submitted to Optics and Photonics, a section of the journal Frontiers in Physics

**Received:** 09 November 2019
**Accepted:** 13 March 2020
**Published:** 08 April 2020

**Citation:**
Wang C, Liu B, Li S, Liu Q, Chen M, Zheng G, Zhuang S, Zhang D and Wei X (2020) Rapid Classification of Single Bacterium Based on Backscattering Microscopic Spectrum—A Pilot Study. Front. Phys. 8:97. doi: 10.3389/fphy.2020.00097

Rapid detection of foodborne pathogens is one of the most effective ways to solve food safety problems. To achieve rapid and noninvasive detection and classification of foodborne pathogens, we modified a fiber confocal backscattering micro-spectral system to suit an extremely small biological sample, that is, a bacterium. This system offers single-bacterium level, label-free, convenient, and environmentally friendly characterization. Three categories of common foodborne pathogens (*Salmonella typhimurium*, *Escherichia coli*, and *Staphylococcus aureus*) were measured. The scattering spectrum ranging from 450 to 900 nm was selected, and by the model of principal component analysis (PCA) and error back propagation algorithm of back propagation neural network (BPNN), the backscattering microscopic spectra of three categories of pathogens were dimensionally reduced, identified, and classified. The results showed that the identification accuracy of three categories of pathogens was above 90%, under neutral, acidic, and alkaline culturing conditions, respectively. The preliminary results demonstrated the feasibility of using confocal backscattering microscopic spectra combined with PCA and BPNN algorithm to identify and classify single bacterium in a rapid, noninvasive, and label-free manner.

**Keywords: foodborne pathogens, elastic scattering, scattering spectra, classification, principal component analysis**

## INTRODUCTION

At present, foodborne illness poses a serious public health threat. Foodborne pathogens are the major cause of foodborne illness [1]. According to World Health Organization (WHO) estimates, pathogenic microorganisms are responsible for 70% of the world's foodborne disease patients [2]. In the worldwide, there are 1.5 billion diarrhea cases caused by biocontamination of food every year, of which about 3 million resulted in death among children <5 years old [3]. Contaminants are widely distributed in nature, coming from air, water, or the feces of animals. Moreover, they are difficult to eliminate because some of them often adhere to the surface of food or medical devices and form a biofilm that resists sterilization. For instance, *Staphylococcus aureus* is commonly associated with device-related infections after an implantation or operation [4]. Hence, the detection of foodborne pathogens is an effective first step in controlling food safety and reducing clinical infection rates.

In recent years, numerous methods of detecting foodborne pathogens have been deployed, for example, enzyme-linked immunosorbent assay (ELISA) [5], bioluminescence detection [6], gene chip technology, and polymerase chain reaction (PCR) technology [7]. However, conventional pathogen detection methods for the detection and identification of different bacteria still have some defects. For example, if the marker of a gene probe is a radioactive group, it may harm the human body, with its subsequent treatment relatively difficult. An adenosine triphosphate (ATP) luminescence detection technology can detect the total number of microorganisms contained in food but cannot specifically detect a target microorganism. Enzyme-linked immunity usually has a high false-positive rate, which affects the accuracy of detection, and is time-consuming and laborious. In addition, traditional detection methods do not apply to many clinical instruments. Therefore, at present, in the field of rapid detection of foodborne pathogens, optical means are playing an increasingly important role [8]. Raman spectroscopy has been found to have increasing applications in the field of foodborne pathogen detection due to its rapid and ultra-sensitive properties [9, 10]. Pan et al. reported a near infrared (NIR) laser scattering imaging system for rapid and noninvasive classification of foodborne pathogens [11]. The study results explored the potential of this system combined with multivariate calibrations for classifying three categories of common bacteria. Wilson and Vigil proposed a dark-field imaging technique capable of automated identification of individual bacterium [12]. Various reports in the literature have demonstrated that strategies using optical methods are potentially able to identify foodborne pathogens noninvasively, in real time, and *in vivo*.

Optical scattering is the main form of the interaction of a tiny particle and light, while the characteristics of the scattered light are directly related to the characteristics of the scattering particles [13]. It is used to detect the structural variations of mitochondria, measurements of macromolecular dipole moments, structural changes in cells, mechanisms of swelling, and lysis of isolated mitochondria, among other applications [14–17]. All of these studies are based on scattering theory, that is, the principle that structural differences may cause scattering differences. The optical detection method based on elastic scattered light can measure and analyze the internal structure distribution and changes of living cells in a natural state without introducing an external medium. Backscattering spectra carry structural and chemical component information from inside the bacterial cell.

Here, a pilot study was carried out to identify three categories of label-free bacteria using a fiber confocal backscattering micro-spectrometer (FCBS). Every bacterial smear was measured by the FCBS. The collected spectra were dimensionally reduced based on principal component analysis (PCA), identified and classified based on back propagation neural network (BPNN) algorithm. Because artificial neural network algorithm has strong nonlinear mapping function, which the representative model is BPNN [18]. It is a multilayer feedforward network trained by an error back propagation algorithm and can get good prediction results.

# MATERIALS AND METHODS

## Experimental Device

The FCBS is a combination of optical fiber confocal and elastic scattering to obtain the single-cell backscattering spectrum. This method has been published in our earlier study and was used for classification and identification of cancerous cells in previous studies [15]. Here, we introduced mainly a slight modification on FCBS suitable for bacteria detection. We improved the original optical fiber confocal backscattering spectrum system to reduce its light field diameter to fit small biological samples. The detailed improved methods are as following. The light is coupled by Port 3 of the fiber coupler to the optic probe, which is made up of a flat-field apochromatic (PLAN Apo) objective (NA = 0.4, 20X, Olympus, Japan) as a collimator and another PLAN Apo objective (NA = 0.65, 40X, Olympus, Japan) as an objective. The diameter of the optical field for the modified FCBS is about 3.5 μm.

## Bacterial Samples

The cell samples for this experiment were *Salmonella typhimurium* (*S. typhimurium*, ATCC14028), *Escherichia coli* (*E. coli*, ATCC25922), and *S. aureus* (*S. aureus*, ATCC6538). All bacterial samples were obtained from the Laboratory of Microbiology, University of Shanghai for Science and Technology. All cytological samples were free of sedimentation. The experiment was completed within 24 h at room temperature.

The bacteria were separated in the following manner: The three strains were cultured in a nutrient broth for 16 h, fixed with 1% methanol (v/v), and then made the bacteria smear. The procedure steps are as following: firstly, 200 μL of the bacteria were placed in the Eppendorf centrifuge tube and centrifuged for 5 min at 5,000 rpm. Secondly, the supernatant was removed. Thirdly, the precipitated part was resuspended with 1mL of deionized water to make the bacteria suspension. These procedures were repeated three times before the bacteria were finally resuspended in 500 μL of deionized water. After the clean oil-free slides were baked on an alcohol lamp, 20 μL of bacterial suspension were smeared on the prepared slide using a sterilized coating rod.

## Spectral Collection and Pretreatment

We used a silicon slice whose reflectivity was about 30% in the visual and NIR range as the standard reflector for all bacteria backscattering spectral analyses to accurately obtain the true spectral characteristics of the measured samples. *S. typhimurium, E. coli*, and *S. aureus* were individually placed on the microscope slide, while the stage was manually adjusted to move along the surroundings so that the spot of convergence could be scanned in all directions. The microscopic information of the sample at this point was measured at the single bacterium level.

## Analysis and Identification Method

In the spectrum range from 450 to 800 nm, the dimensionality of spectrum is too high, making analysis and automatic identification very difficult. Principal component analysis (PCA) method is a multivariate statistical analysis technique. The core idea is to compress and extract the data, compress the linearly dependent variables into a few linearly independent comprehensive variables. The new obtained comprehensive variables contain most of the information of original variables. The PCA method is used to reduce the dimensionality. The main characteristics of the data are extracted by data decorrelation [19]. Then the main information is included in the first few principal components (PCs). In the process of comprehensive analysis, the first few PCs with the largest variance are selected and can be used in preliminary treatment for other machine learning methods [20].

The basic idea of BPNN is to use the steepest descent method to obtain the constant adjustment of the network weight and threshold through back propagation, so as to obtain the smallest square error of network error. To identify and classify the spectra of three categories of pathogens, the samples of the test set are pre-processed by PCA. The principal component vectors of cumulative contributions over 85% are inputted into the BPNN model are extracted for prediction. We set the deviation of prediction results within ±0.15 as the correct prediction. Conversely, there are two types of misjudgments: [1] when the prediction value is not in the setting value range, the misjudgment is occurred. However it is not recognized as another type of bacteria; [2] when the prediction value is in another bacteria value range, it will be recognized as other bacteria. The number of trainings used is 5,000 and the target error is 0.01.

# EXPERIMENTAL RESULTS UNDER NEUTRAL CULTURING CONDITIONS

In this experiment, the backscattering micro-spectra of *S. typhimurium*, *E. coli,* and *S. aureus* that were cultured under neutral condition, were measured using the modified FCBS.

## Three Bacterial Spectra

The light scattering spectra of the three kinds of foodborne pathogens were obtained and demonstrated by using BWspec software. The experimental data for the backscattering micro-spectra of the three kinds of bacteria are shown in **Figure 1**.

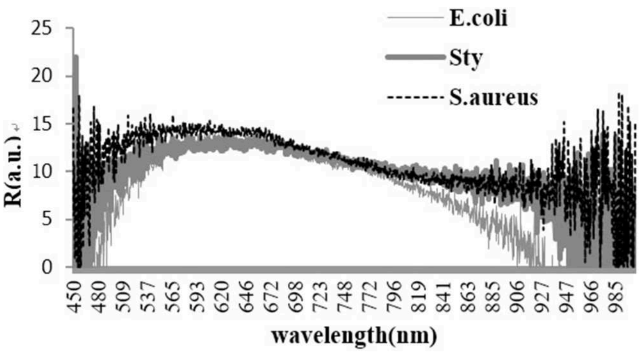

**FIGURE 1 |** Backscattering micro-spectra of three kinds of bacteria.

In the spectra range of 450 to 800 nm, the contribution rate and cumulative contribution rate of variance for the first five principal components calculated by PCA are shown in **Table 1**. The cumulative contribution rate of the first two principal components (PC1 and PC2) reaches 99.39%, indicating that they already contain the primary information of the original variables.

**TABLE 1 |** Contribution rate and cumulative contribution rate of the first five principal components.

| Main ingredient | Contribution rate | Cumulative contribution rate |
|---|---|---|
| PC1 | 91.3729 | 91.3729 |
| PC2 | 8.0163 | 99.3892 |
| PC3 | 0.3897 | 99.7789 |
| PC4 | 0.0874 | 99.8663 |
| PC5 | 0.0354 | 99.9017 |

A PCA scatter diagram based on the first two principal component scores, PC1 and PC2, is shown in **Figure 2**. Fifty spectral data for each of the three kinds of bacteria are used in the PCA. This result has demonstrated that the micro-spectra of *S. typhimurium*, *E. coli*, and *S. aureus* obtained using the modified FCBS can be distinguished by the first two principal components in the PCA.

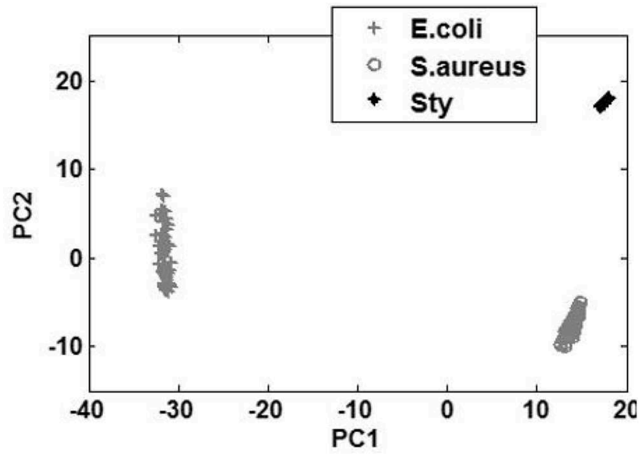

**FIGURE 2 |** Discrimination of the spectra of the three kinds of bacteria by PCA.

## Identification Results by BPNN

Spectral data of 150 samples were collected as prediction set samples, 1–50, 51–100, and 101–150 cases were *S. typhimurium, E. coli,* and *S. aureus* spectral data, respectively. The effective spectral components of the microscopic spectra of bacteria collected after the data dimension of spectra were reduced by PCA method. The first and second principal component vectors were selected as the input of the BPNN model for testing. The classification and identification results have been shown in **Table 2** for 150 prediction sample sets. The experimental results have shown that the identification rate of all three bacteria is above 90%.

**TABLE 2 |** Classification results.

| Strain | Output samples | Correct samples | Recognition accuracy (%) |
|---|---|---|---|
| Sty | 50 | 45 | 90 |
| *E. coil* | 50 | 47 | 94 |
| *S. aureus* | 50 | 48 | 96 |
| Total | 150 | 140 | 93% |

## EXPERIMENTAL RESULTS UNDER DIFFERENT CULTURING CONDITIONS

During the actual detection process, the growth of foodborne pathogens will also change with the external environment. The use of back scattering spectroscopy for label-free classification and identification of foodborne pathogens is an ongoing research. To prove the ability of classification and identification of the modified FCBS, it is necessary to consider the backscattering of foodborne pathogens in on-site detection. The same three foodborne pathogens are selected. Most of the oils and fats are weakly alkaline, while most of the eggs and milk foods are weakly acidic. Therefore, two pH values (pH = 6.6, pH = 8.4) culturing condition are designed. The backscattering spectra of three foodborne pathogens are studied by spectroscopy combined with statistical methods, chemometric methods, and deep learning algorithms.

### Spectra of Three Foodborne Pathogens Under Two pH Conditions

The experimental data of the backscattering micro-spectra of the three kinds of bacteria under two conditions of pH value are shown in **Figure 3**.

The contribution rate and cumulative contribution rate of the variance of two pH value conditions for the first five principal components calculated by PCA are shown in **Tables 3**, **4**. In the spectra range of 450 to 800 nm, the cumulative contribution of the first two principal components (PC1 and PC2) reaches 86.179 and 98.6%, respectively, indicating that they already contain the primary information of the original variables.

Under two conditions of pH values, PCA plots based on the first two principal component scores, PC1 and PC2, are presented in **Figures 4**, **5**, respectively. A total of 50 samples of spectral data for each of the three kinds of bacteria are used in the PCA. This result has demonstrated that under acidic and alkaline culturing conditions, the micro-spectra of *S. typhimurium*, *E. coli*, and *S. aureus* obtained using the modified FCBS can be distinguished by the first two principal components in the PCA.

### Identification Results by BPNN Under Two pH Conditions

Under each of two pH conditions, spectral data of 150 samples are collected as prediction set samples respectively. Same as under neutral culturing conditions, the samples of the test set are also pre-processed by PCA, while the first two principal component input BPNN model are extracted for testing. The classification and identification result have been shown in **Tables 5**, **6**. The experimental results have

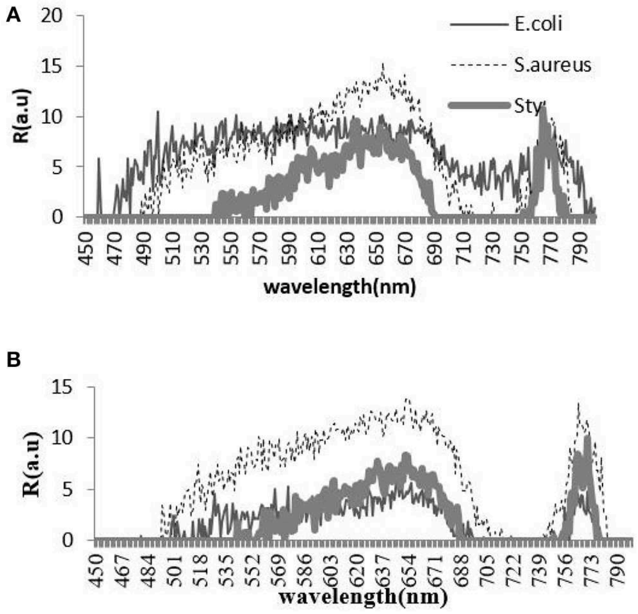

**FIGURE 3 |** Backscattering micro-spectra of three kinds of bacteria under acidic condition **(A)** and alkaline condition **(B)**.

**TABLE 3 |** Contribution rate and cumulative contribution rate of the first five principal components (acidic condition).

| Main ingredient | Contribution rate | Cumulative contribution rate |
|---|---|---|
| PC1 | 67.551 | 67.551 |
| PC2 | 18.628 | 86.179 |
| PC3 | 7.474 | 93.653 |
| PC4 | 1.833 | 95.486 |
| PC5 | 0.682 | 96.168 |

**TABLE 4 |** Contribution rate and cumulative contribution rate of the first five principal components (alkaline condition).

| Main ingredient | Contribution rate | Cumulative contribution rate |
|---|---|---|
| PC1 | 72.647 | 72.647 |
| PC2 | 22.488 | 95.135 |
| PC3 | 2.882 | 98.017 |
| PC4 | 0.310 | 98.327 |
| PC5 | 0.284 | 98.611 |

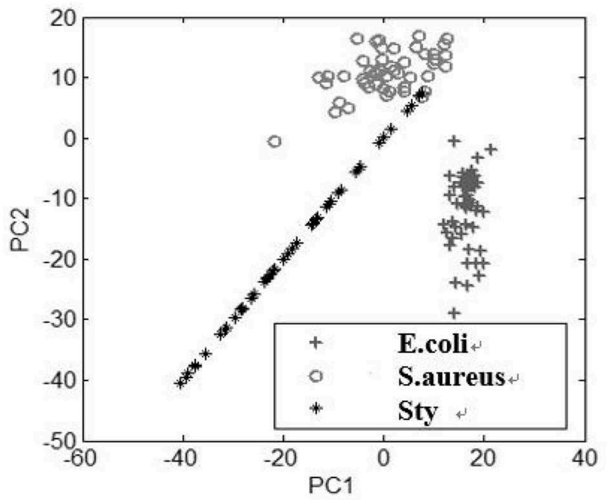

**FIGURE 4 |** Discrimination of the spectra of the three kinds of bacteria under acidic condition by PCA.

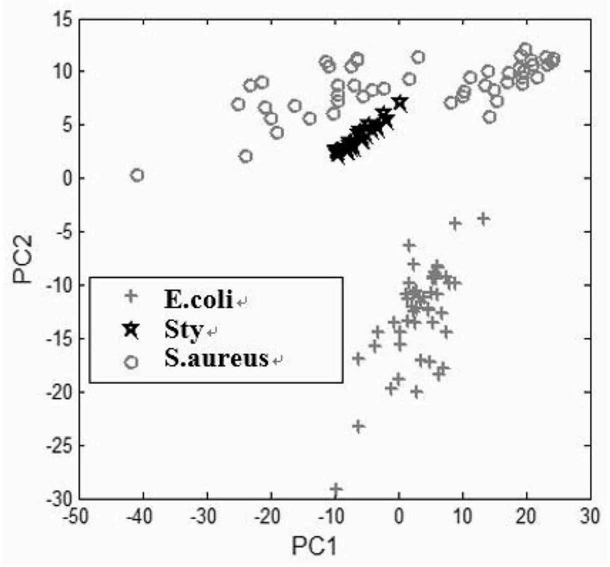

**FIGURE 5 |** Discrimination of the spectra of the three kinds of bacteria under alkaline condition by PCA.

**TABLE 5 |** Classification results (acidic condition).

| Strain | Output samples | Correct samples | Recognition accuracy (%) |
|---|---|---|---|
| Sty | 50 | 48 | 96 |
| *E. coil* | 50 | 48 | 96 |
| *S. aureus* | 50 | 48 | 96 |
| Total | 150 | 144 | 96 |

shown that the identification rates of all three bacteria are above 94%.

**TABLE 6 |** Classification results (alkaline condition).

| Strain | Output samples | Correct samples | Recognition accuracy (%) |
|---|---|---|---|
| Sty | 50 | 48 | 96 |
| *E. coil* | 50 | 48 | 96 |
| *S. aureus* | 50 | 47 | 94 |
| Total | 150 | 143 | 95 |

## DISCUSSIONS AND CONCLUSION

Food safety issues are associated with the national economy and people livelihood. Traditional techniques of bacterial identification are time-consuming and offer poor detection sensitivity. Our proposed test method here is noninvasive and label free. It can extract the spatial information of the bacterial cells into the spectral information and obtain the scattering characteristics of various bacterial cells without complicated pre-processing. By extracting the characteristic of the scattering spectrum, different cells can be identified and classified. Compared with the backscattering detection technology, such as the Raman spectrum, the elastic light scattering spectrum can better describe the cell morphological characteristics. Our method has a number of advantages, such as the simplicity of the system, good repeatability, and high precision of spectral signals. Moreover, the system is more conductive to the design and construction of portable detection equipment, thereby meeting the requirements of detection *in-situ*. Backscattering micro-spectral data from *S. typhimurium*, *E. coli*, and *S. aureus* are collected from three foodborne pathogens based on our modified FCBS. By utilizing PCA and BPNN algorithm, the three kinds of bacteria were classified and identified, with good results obtained. At the same time, the identification accuracy was improved, which provided a new method for cell identification. The results have shown that the identification accuracy of three categories of common foodborne pathogens under neutral, acidic and alkaline culturing conditions were all above 90%. In addition, it could be observed that the spectral curves of the same species of bacteria were significantly different under different culture conditions. In response to this phenomenon, we speculate that the morphological characteristics of bacteria changed under acidic and alkaline culturing conditions, compared with neutral culturing condition. Thus the elastic light scattering spectrum changed [21].

With a greater understanding of food microorganisms, we believe that additional foodborne pathogen analysis methods and detection techniques can be applied in real-life situations. In future, we will continue to optimize the identification algorithm and collect a larger number of samples to confirm our current data before establishing a database of bacterial feature information. In addition, miniaturization equipment can provide guarantee for *in-situ* rapid detection. However, considerable work remains to be done in the future for applying the discrimination of the bacteria based on the modified FCBS. Given the complicated effect of the variety of foodborne pathogens that usually exist in food, automatic classification of mixed bacteria and its application for clinical detection and treatment needs further research. Full detection of pathogenic bacteria in food cannot be accomplished using a single method and requires a combination of various techniques to enhance detection sensitivity and reduce detection time. With the rapid development of microbiology, biochemistry, molecular biology, and other disciplines, the development of various multifunctional microbial detection systems has become an important topic. Combining the optical technology with other detection techniques can achieve accurate and efficient detection of foodborne pathogens and requires further research.

## DATA AVAILABILITY STATEMENT

The raw data supporting the conclusions of this article will be made available by the authors, without undue reservation, to any qualified researcher.

## AUTHOR CONTRIBUTIONS

DZ and XW guided our work. CW and SZ designed the experiments. SL and QL provided the bacteria samples. MC and GZ improved the equipment. BL carried out experiments and analyzed the data. CW and BL wrote the manuscript.

## FUNDING

This work was supported by grants from the National Natural Science Foundation of China Nos. 61775140 and 81771850, and the SJTU Medicine Engineering Interdisciplinary Research Fund No. YG2017MS19.

## ACKNOWLEDGMENTS

We thank LetPub (www.letpub.com) for its linguistic assistance during the preparation of this manuscript.

## REFERENCES

1. Nyachuba DG. Foodborne illness: is it on the rise? *Nutr Rev*. (2010) **68**:257–69. doi: 10.1111/j.1753-4887.2010.00286.x
2. Groundwater PW, Todd A, Worsley AJ, Anderson RJ. The technology and techniques used in the detection of pathogenic bacteria. *Pharm J*. (2009) **283**:281–2. Available online at: https://www.pharmaceutical-journal.com/files/rps-pjonline/pdf/pj_20090912_detection.pdf
3. Li HM, Xu HY, Xiong YH. Research progress on the application of immunochromatographic test strip technology in foodborne pathogen detection. *Food Sci*. (2011) **32**:380–3. doi: 10.1111/j.1759-6831.2010.00113.x
4. Lian YZ, Xue D, Yong L, Yue L, Jing A, Xin L. Study on measuring rapidly bacterium in water with ATP bioluminescence technique. *Chin J Health Lab Technol*. (2007) **17**:1859–60.
5. Galikowska E, Kunikowska D, Tokarska-Pietrzak E, Dziadziuszko H, Łoś JM, Golec P, et al. Specific detection of *Salmonella enterica* and *Escherichia coli* strains by using ELISA with bacteriophages as identification agents. *Eur J Clin Microbiol Infect Dis*. (2011) **30**:1067–73. doi: 10.1007/s10096-011-1193-2
6. Zulkiply NA, Sjafri FR, Ismail A, Ismail A. An in-house multiplex PCR for detection of *S. typhi* and *S. paratyphi* A: a comparison between detection method by agarose gel electrophoresis and lateral flow assay. *Int J Infect Dis*. (2012) **16**:395. doi: 10.1016/j.ijid.2012.05.526
7. Arbault P, Buecher V, Poumerol S, Sorin ML. Study of an ELISA method for the detection of *E. coli* O157 in food. *Prog Biotechnol*. (2000) **17**:359–68. doi: 10.1016/S0921-0423(00)80093-3
8. Jo Y, Jung J, Kim MH, Park H, Kang SJ, Park Y. Label-free identification of individual bacteria using Fourier transform light scattering. *Optics Exp*. (2015) **23**:15792–805. doi: 10.1364/OE.23.015792
9. Duan N, Chang B, Zhang H, Wang Z, Wu S. *Salmonella typhimurium* detection using a surface-enhanced raman scattering-based aptasensor. *Int J Food Microbiol*. (2016) **218**:38–43. doi: 10.1016/j.ijfoodmicro.2015.11.006
10. Wang P, Pang S, Chen J, McLandsborough L, Nugen SR, Fan M, et al. Label-free mapping of single bacterial cells using surface-enhanced Raman spectroscopy. *Analyst*. (2016) **141**:1356–62. doi: 10.1039/C5AN02175H
11. Pan W, Zha J, Chen Q. Classification of foodborne pathogens using near infrared (nir) laser scatter imaging system with multivariate calibration. *Sci Rep*. (2015) **5**:9524. doi: 10.1038/srep09524
12. Wilson BK, Vigil GD. Automated bacterial identification by angle resolved dark-field imaging. *Biomed Opt Exp*. (2013) **4**:1692. doi: 10.1364/BOE.4.001692
13. Wyatt PJ. Identification of bacteria by differential light scattering. *Nature*. (1969) **221**:1257–8. doi: 10.1038/2211257a0
14. Li S, Hu P, Malmstadt N. Confocal imaging to quantify passive transport across biomimetic lipid membranes. *Anal Chem*. (2010) **82**:7766–71. doi: 10.1021/ac1016826
15. Wang C, Guo XD, Fang B, Song C. Study of back-scattering micro-spectrum for stomach cells at single cell scale. *J Biomed Opt*. (2010) **15**:040505. doi: 10.1117/1.3469782
16. Murugova TN, Solodovnikova IM, Yurkov V, Gordeliy VI, Kuklin AI, Ivankov O, et al. Potentials of small-angle neutron scattering for studies of the structure of "Live" mitochondria. *Neutron News*. (2011) **22**:11–14. doi: 10.1080/10448632.2011.598800
17. Zhang Lu, Qin Y, Li KX, Zhao X, Xing YF, Zhao H, et al. Light scattering properties in spatial planes for label free cells with different internal structures. *Opt Quantum Electr*. (2015) **47**:1005–25. doi: 10.1007/s11082-014-9957-4
18. Zhang Y, Yunxiang LI, Quan Q. Prediction model of PM_(2.5) based on attribute reduction and BP neural network. *Environ Sci Technol*. (2017) **40**:341–6.
19. Wang C, Wen M, Bai L, Zhang T. Auto-classification for confocal back-scattering micro-spectrum at single-cell scale using principal component analysis. *Optik*. (2015) **127**:1007–10. doi: 10.1016/j.ijleo.2015.10.066
20. Mao ZH, Zhang XX, Yue-Chao WU, Yin JH, Xia Y. Fourier transform infrared microscopic imaging and fisher discriminant analysis for identification of healthy and degenerated articular cartilage. *Chin J Anal Chem*. (2015) **43**:518–22. doi: 10.1016/S1872-2040(15)60816-7
21. Katz A, Alimova A, Xu M, Rudolph E, Shah MK, Savage HE, et al. Bacteria size determination by elastic light scattering. *IEEE J Select Top Quant Electr*. (2003) **9**:277–87. doi: 10.1109/JSTQE.2003.811284

**Conflict of Interest:** The authors declare that the research was conducted in the absence of any commercial or financial relationships that could be construed as a potential conflict of interest.

frontiers in Physics

ORIGINAL RESEARCH
published: 21 April 2020
doi: 10.3389/fphy.2020.00118

# Super-Resolution Structured Illumination Microscopy Reconstruction Using a Least-Squares Solver

**Jintao Luo [1], Chuankang Li [1], Qiulan Liu [1], Junling Wu [2], Haifeng Li [1], Cuifang Kuang [1,3,4]*, Xiang Hao [1] and Xu Liu [1,3,4]**

[1] State Key Laboratory of Modern Optical Instrumentation, College of Optical Science and Engineering, Zhejiang University, Hangzhou, China, [2] Texas Instruments Semiconductor Technologies (Shanghai) Co., Ltd, Pudong, China, [3] Ningbo Research Institute, Zhejiang University, Ningbo, China, [4] Collaborative Innovation Center of Extreme Optics, Shanxi University, Taiyuan, China

Super-resolution microscopy enables images to be obtained at a resolution higher than that imposed by the diffraction limit of light. Structured illumination microscopy (SIM) is among the fastest super-resolution microscopy techniques currently in use, and it has gained popularity in the field of cytobiology research owing to its low photo-toxicity and widefield modality. In typical SIM, a fluorescent sample is excited by sinusoidal patterns by employing a linear strategy to reconstruct super-resolution images. However, this strategy fails in cases where non-sinusoidal illumination patterns are used. In this study, we propose the least-squares SIM (LSQ-SIM) approach, which is an efficient super-resolution reconstruction algorithm in the framework of least-squares regression that can process raw SIM data under both sinusoidal and non-sinusoidal illuminations. The results obtained in this study indicate the potential of LSQ-SIM for use in structured illumination microscopy and its various application fields.

**Keywords: super-resolution imaging, structured illumination microscopy, reconstruction algorithm, optimization, least squares**

OPEN ACCESS

**Edited by:**
*Chao Tian,*
*University of Science and Technology of China, China*

**Reviewed by:**
*Jae-Byum Chang,*
*Korea Advanced Institute of Science and Technology, South Korea*
*Gao Peng,*
*Xidian University, China*

***Correspondence:**
*Cuifang Kuang*
*cfkuang@zju.edu.cn*

**Specialty section:**
*This article was submitted to Optics and Photonics, a section of the journal Frontiers in Physics*

**Received:** 12 February 2020
**Accepted:** 25 March 2020
**Published:** 21 April 2020

**Citation:**
*Luo J, Li C, Liu Q, Wu J, Li H, Kuang C, Hao X and Liu X (2020) Super-Resolution Structured Illumination Microscopy Reconstruction Using a Least-Squares Solver. Front. Phys. 8:118. doi: 10.3389/fphy.2020.00118*

## INTRODUCTION

The resolution of a fluorescence microscope is limited by the optical diffraction effect, which can be described by Abbe's Equation [1]. Several super-resolution fluorescence microscopy techniques have been previously developed, such as stochastic optical reconstruction microscopy (STORM) [2], stimulated emission depletion fluorescence microscopy (STED) [3], and structured illumination microscopy (SIM) [4]. SIM features low photo-toxicity and a relatively high imaging speed, and has been widely applied in the field of biological sciences to study cellular and subcellular dynamics and mechanisms [5, 6]. SIM employs sinusoidal illumination patterns with different directions and initial phases to downshift the high-frequency component of the fluorescence signals of a specimen into the scope of the optical transfer function (OTF), which is otherwise filtered in conventional microscopic optics, leading to resolution loss. The high- and low-frequency components are then unmixed using the solution of a set of linear equations and shifted to their correct positions in the reciprocal domain. With this expanded spectrum, the resulting resolution is almost twice that of widefield fluorescence microscopy. The resolution enhancement provided by SIM can be further improved if the nonlinear characteristics of fluorescent labels are utilized, such as saturation [7] and photo-switching [8, 9], depending on the strength of the high-frequency signal and level of noise corruption in the system.

In super-resolution reconstruction of SIM data, the parameters of sinusoidal illumination patterns (e.g., the frequency vectors and initial phases) must be precisely known. However, this knowledge is difficult and even impossible to obtain if the illumination patterns are distorted due to aberrations caused by the observed specimen, especially in the case of thick biological tissue [10]. Mudry et al. [11] developed a structured illumination microscopy approach using unknown speckle illumination (referred to as blind SIM), in which both the object and speckle patterns are estimated by conjugate gradient descent. With the grain size of speckle being close to the diffraction limit, the resolution of blind SIM is comparable to that of classical structured illumination microscopy [11]. In addition to speckle, multi-foci has also been applied as structured illumination to realize a doubling in resolution and optical sectioning with an extra digital pinhole [12]. Unfortunately, the reconstruction algorithm of original structured illumination microscopy is unable to process the raw data from these novel SIM techniques. Various reconstruction methods have been invented to deal with SIM data under non-sinusoidal illumination, though these approaches are both iterative and time consuming [13–15].

In this paper, we propose a highly efficient reconstruction method for use with SIM images under general structured illumination (sinusoidal and non-sinusoidal). As reported in the previous literature, the reconstruction of an object is formulated in terms of an optimization problem [11]. This optimization problem lacks an analytical solution owing to the convolution operator in the SIM imaging model, which is also ill-conditioned. We introduce a pre-deconvolution step for simplification, so a direct solution to this problem is available that can be instantly calculated through least-squares fitting. Furthermore, our method is conducted mainly in the spatial domain, which makes it faster because it requires fewer computationally intensive Fourier transformation operations.

In section Method, we present the SIM imaging forward model that we exploit in the least-squares algorithmic framework for super-resolution reconstruction of objects. The principles of our method are demonstrated and reconstruction results obtained using simulated data are shown. Section Results and Discussion describes the validation of our approach using open-access SIM data under sinusoidal and non-sinusoidal illumination.

## METHOD

In two-dimensional (2D) SIM, the relation of an object $\mathbf{f}$ illuminated by an excitation pattern $\mathbf{p}$ and a captured image $\mathbf{g}$ can be described by:

$$\mathbf{g} = (\mathbf{f} \times \mathbf{p}) \otimes \mathbf{psf}, \tag{1}$$

where $\otimes$ denotes the 2D convolution operator, and $\mathbf{psf}$ the point spread function. For convenience, the magnification is assumed to equal 1 here, without loss of generality. In the frequency domain, Equation (1) becomes:

$$\mathbf{G} = (\mathbf{F} \otimes \mathbf{P}) \times \mathbf{OTF}, \tag{2}$$

where $\mathbf{OTF}$ denotes the optical transfer function, and $\mathbf{G}$, $\mathbf{F}$, and $\mathbf{P}$ are the 2D Fourier transformations of $\mathbf{g}$, $\mathbf{f}$, and $\mathbf{p}$, respectively. As the OTF is band-limited, spectrum information at frequencies higher than the cutoff frequency is filtered and unrecoverable after imaging if the illumination pattern is uniform, as in the case of widefield microscopy, which leads to resolution degradation. Through pulse function decomposition, Equation (2) becomes:

$$\mathbf{G}(\mathbf{k_x},\mathbf{k_y}) = \int\int \mathrm{P(u,v)F(k_x - u, k_y - v)OTF(k_x, k_y)dudv} \tag{3}$$

where $\mathbf{k}_\mathrm{x}$ and $\mathbf{k}_\mathrm{y}$ denote frequency coordinates corresponding to spatial coordinates $\mathbf{x}$ and $\mathbf{y}$, respectively, and $\mathbf{u}$ and $\mathbf{v}$ are integration variables. This implies that a high-frequency component is coded into the frequency domain within the range of the OTF weighted by the spectrum of the illumination pattern. As a specific case of SIM, the integration in Equation (3) is replaced with a discrete summation of the spectrum of the object filtered by the OTF and its shifted copies. It can be seen that the essence of super-resolution SIM consists of accessible high-frequency information resulting from structured illumination. SIM illumination patterns are usually generated through the same objective in the detection path, which restricts their spatial frequency below its cutoff frequency, so the resolution improvement is at most 2-fold. The resolution enhancement of SIM can be further extended if certain nonlinear processes of fluorescence dyes are applied to effectively excite higher-order harmonics [7–9].

The task of reconstructing an object from SIM data can be viewed as an optimization problem, for which the cost function to be minimized is

$$\mathbf{L_1(f)} = \sum_{\mathbf{i=1}}^{\mathbf{N}} \left\| \mathbf{g_i} - (\mathbf{f} \times \mathbf{p_i}) \otimes \mathbf{psf} \right\|_2^2, \tag{4}$$

where $\mathbf{N}$ is the total number of illumination patterns. There is no direct solution to this optimization problem as a result of the convolution operator. Considering the band-limiting nature of the point spread function, minimization of $\mathbf{L_1(f)}$ is equivalent to that of

$$\mathbf{L_2(f)} = \sum_{\mathbf{i=1}}^{\mathbf{N}} \left\| \mathbf{deconwnr(g_i)} - \mathbf{S_{cutoff}(f \times p_i)} \right\|_2^2, \tag{5}$$

where $\mathbf{deconwnr}$ denotes the Wiener deconvolution and $\mathbf{S}_{\mathrm{cut-off}}$ is a frequency-bound constraint function that sets spectrum values outside the cutoff bound of $\mathbf{OTF}$ to zero. The analytical solution for the minimization of $\mathbf{L_2(f)}$ is then described by Tian et al. [16]

$$\mathbf{f_{lsq}} = \frac{\sum_{\mathbf{i=1}}^{\mathbf{N}} \mathbf{deconwnr(g_i)} \times \mathbf{p_i}}{\sum_{\mathbf{i=1}}^{\mathbf{N}} \mathbf{p_i^2}}, \tag{6}$$

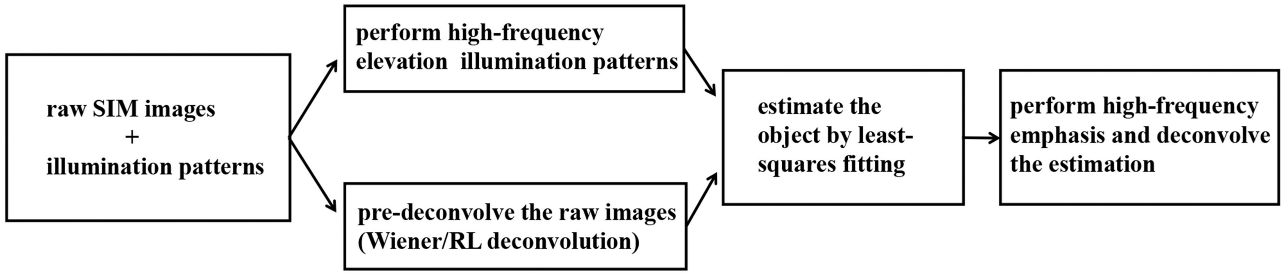

**FIGURE 1 |** Block diagram showing the proposed LSQ-SIM algorithm.

which is also a least-squares estimation. To avoid division by zero, a small positive constant acting as the Tikhonov regularization is added to the denominator in Equation (6) when applied to the SIM data. We find that Wiener deconvolution causes obvious artifacts and noise amplification, especially when the sample is bead-like, which leads to significant corruption of the reconstruction results. This issue can be solved by simply replacing the Wiener deconvolution through using Richardson-Lucy deconvolution in this pre-deconvolution step. We also implement high-frequency elevation for each illumination pattern before applying Equation (6), and deconvolve $\mathbf{f}_{\mathrm{lsq}}$ after high-frequency emphasis with an point spread function that corresponds to a doubled numerical aperture, to strengthen the contrast of the final reconstruction result. With high-frequency elevation for illumination patterns, the weight of low frequency components in final reconstruction can be reduced so out-of-focus background is suppressed, which benefits thick biological tissue imaging. A block diagram describing our approach is shown in **Figure 1**.

We use a simulated Siemens Star target [$o(r,\theta)=1+\cos 32\theta$ in polar coordinates] to test our method. The numerical aperture for simulation is set to 0.7 and five types of two-dimensional illumination patterns are used: sinusoidal fringes, quadratic lattice, hexagonal lattice, multi-spots, and pseudo-random speckles. In 2D SIM, sinusoidal fringes are usually generated through the interference of two coherent beams or projection of the light field on a digital micromirror device (DMD) [17, 18]. The quadratic lattice, which contains two more peaks in the reciprocal domain compared to the sinusoidal fringe, is produced with two pairs of coherent orthogonal beams. The hexagonal lattice is generated in a similar manner, with three pairs of light beams with a high degree of coherence [19]. Due to increased sparsity, the quadratic and hexagonal lattices bear higher modulation depth than sinusoidal fringes in a thick sample, which can yield better reconstruction results.

Multi-spots and pseudo-random speckle have also been used to achieve super-resolution SIM, both of which can be created with the economical DMD [20, 21]. Due to the flexibility of DMD, which is digitally controlled, the properties of illumination patterns, such as quantity and sparsity, can be appropriately designed. In our simulation, the multi-spots pattern scans the target uniformly and the speckle patterns are generated using a pseudo-random algorithm, as such, the sum of SIM images forms a complete widefield frame of the target, which promotes unbiased reconstruction [22]. Note that the speckle illumination applied in blind SIM [11] is produced by placing a mechanically driven optical diffuser in the excitation path, which leads to a high required number of captured images to obtain an unbiased reconstruction.

**Figure 2** shows the simulation results for these different types of structured illumination. The outer blue dashed circle indicates the resolution that is limited by optical diffraction, and the inner one indicates resolution doubling. The area inside the outer circle is still blurred after pure deconvolution. In the case of the reconstructions obtained using our method (**Figures 2D–H**), the details between the two circles of the target are clearly distinguishable, with some slight ambiguity close to the inner circle, which suggests that a nearly 2-fold resolution enhancement is achieved. It is noteworthy that the resolution enhancement of image reconstruction in the case of pseudo-random speckle illumination is slightly weaker than those of the other examples, which may result from the irregularity of the speckle.

To assess the performance of our method, contrasts at different circular spatial periods are calculated, as shown in **Figure 3**. For the widefield and deconvolved images, the contrast falls close to zero at a spatial period of $\boldsymbol{\lambda/2\mathrm{NA}}$, in accordance with the theoretical diffraction limit. In the case of reconstructions obtained using the proposed LSQ-SIM method, the contrast remains comparatively high, at spatial periods ranging between 0.5 and 1 times $\boldsymbol{\lambda/2\mathrm{NA}}$, which verifies the resolution improvement. As shown in **Figure 3**, the reconstructions of lattice-illuminated images present much higher contrasts within the middle of the super-resolution region compared with the other reconstructions, which reveals the superiority of lattice-structured illumination.

## RESULTS AND DISCUSSION

We validate our LSQ-SIM reconstruction algorithm on two open-accessible experimental data sets (Laser Analytics Group), and compare it with joint Richardson-Lucy deconvolution, an iterative method that has been used to successfully reconstruct

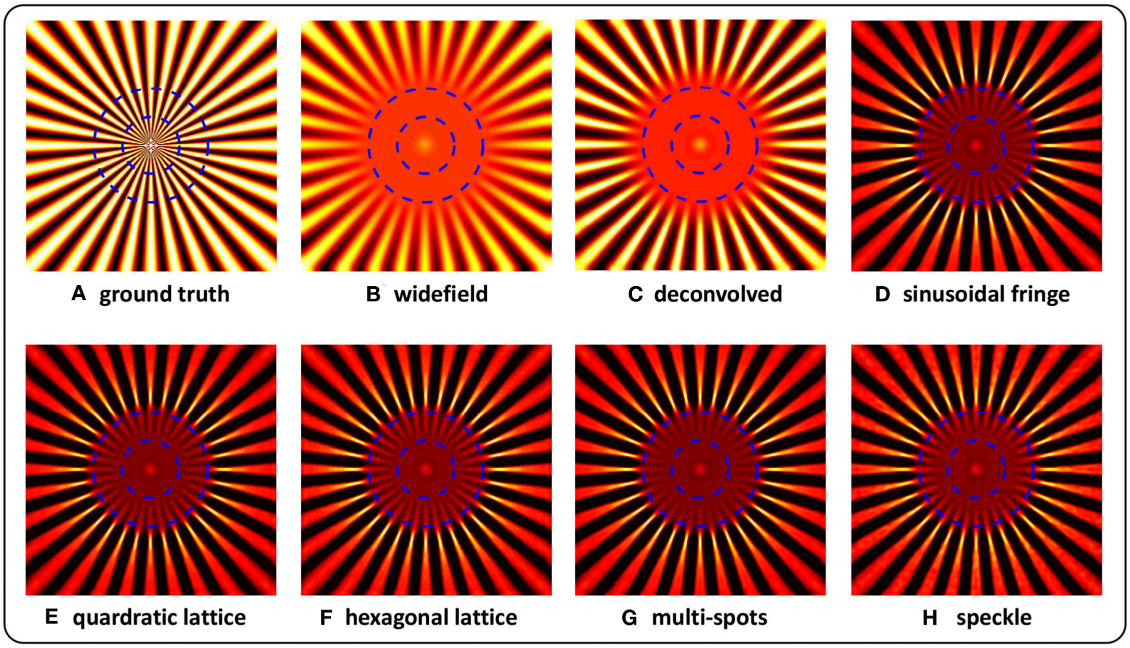

**FIGURE 2 |** Reconstructions of simulated Siemens Star targets imaged under structured illuminations of sinusoidal fringe **(D)**, quadratic lattice **(E)**, hexagonal lattice **(F)**, multi-spots **(G)**, and speckle **(H)**. The ground truth **(A)**, together with widefield **(B)**, and deconvolved **(C)** images is also shown. The outer blue dashed circle indicates the resolution limited by optical diffraction, and the inner circle denotes resolution doubling.

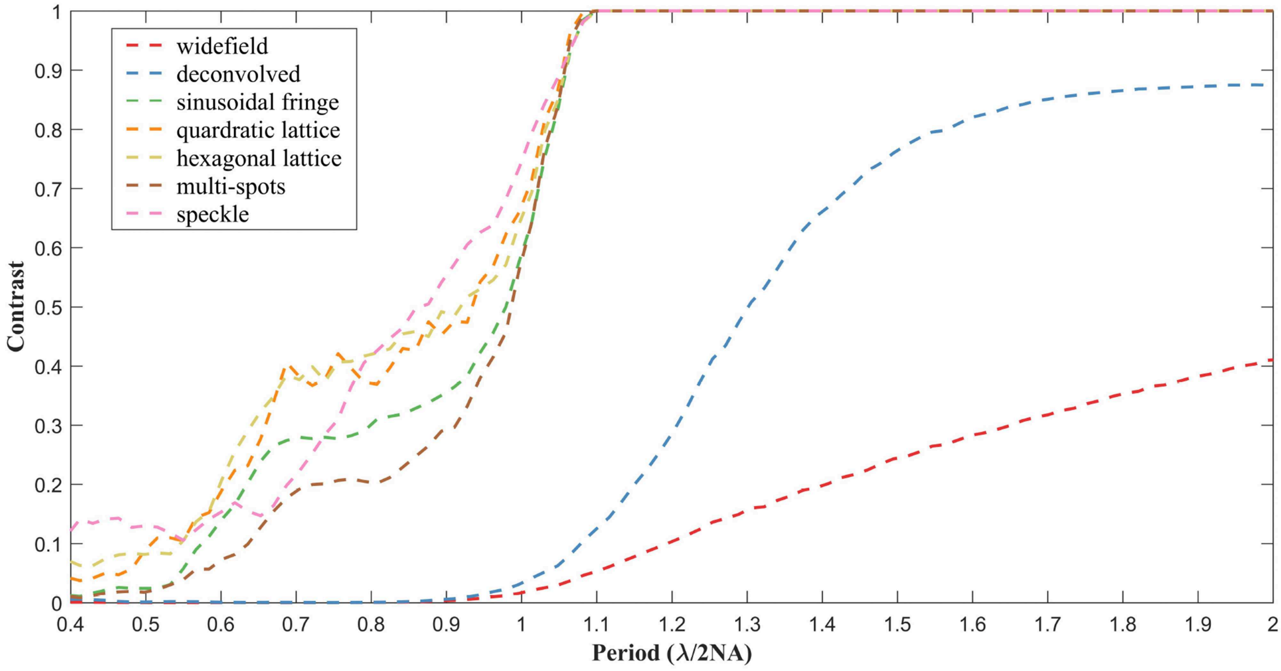

**FIGURE 3 |** Contrast degradation curves of the reconstructed simulated target under different types of structured illumination.

SIM images by sinusoidal and multi-focal excitation (jRL-SIM) [13, 23]. The jRL-SIM approach originates from the Richardson-Lucy (RL) deconvolution used in image restoration, the idea of which is to get an estimation of the object to maximize the likelihood of the observation under the Poisson noise model by multiplicative iteration [24, 25]. In

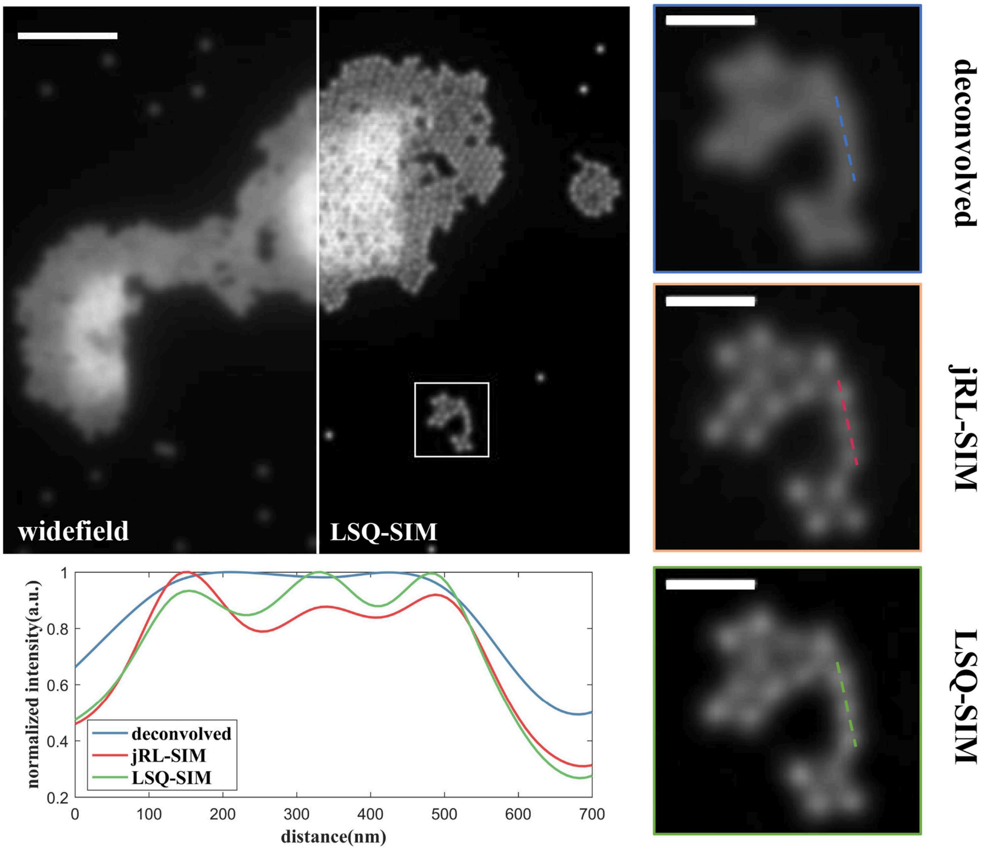

**FIGURE 4 |** Comparison of reconstructions of fluorescent beads under sinusoidal illumination using the jRL-SIM and LSQ-SIM methods. Scale bar: 2 μm for full-frame image and 0.5 μm for the zoomed region.

RL deconvolution, the blurring convolution kernel (e.g., the point spread function) is regarded as a linear operator. While in jRL-SIM, this convolution operator is modified to be a mixed operator that combines convolution and structured excitation operations. As a result of this iteration approach, jRL-SIM is particularly time consuming for large numbers of raw SIM images.

All the reconstructions described in this study were conducted on a personal computer equipped with a 2.9 GHz i5-9400 CPU. The first data set contains SIM images of fluorescent beads (Tetraspeck, Thermo Fisher Scientific) with a nominal diameter of 100 nm by sinusoidal excitation at the wavelength of 488 nm [23]. The widefield image is acquired by summing all the raw images on which deconvolution is subsequently implemented. The number of iterations for jRL-SIM reconstruction is chosen to be 30 to guarantee sufficient convergence and prevent intolerable artifacts and noise amplification. At the pre-deconvolution step of our LSQ-SIM reconstruction, we use iterative RL deconvolution rather than instant Wiener deconvolution because we find that Wiener deconvolution leads to obvious ringing artifacts that severely corrupt the reconstruction result. **Figure 4** shows a comparison of jRL-SIM and LSQ-SIM reconstructions for fluorescent beads. In the widefield image, fluorescent beads that are lying in proximity cannot be discriminated (pure deconvolution also fails to distinguish these) although the contrast is boosted. Both the jRL-SIM and LSQ-SIM reconstruction methods successfully resolve these neighboring beads, while the latter partially presents a slightly higher contrast, according to the intensity profile shown in **Figure 4**.

To further compare the resolution improvement provided by the proposed LSQ-SIM method and jRL-SIM, we study their capacity to compress the full width at half maximum (FWHM) of a sub-diffraction object [18]. The intensity profiles of a single bead are plotted in **Figure 5**. The FWHM value for the single bead in the widefield image is approximately 250 nm, whereas the FWHMs for jRL-SIM and LSQ-SIM reconstructions were ∼120 nm and ∼140 nm, respectively. Although the FWHM confinement of LSQ-SIM is a little lower than that of jRL-SIM, a reduction of the FWHM by nearly one half is still realized.

The efficacy of the proposed LSQ-SIM method is also assessed using a data set consisting of sample images from multi-focal SIM (MSIM). The target sample is a microtubule structure labeled by Alexa Fluor 488 in a fixed cell imaged under a 60× TIRF objective with NA1.45 [12]. The reconstruction results of jRL-SIM and LSQ-SIM are shown in **Figure 6**. For the pre-deconvolution step in LSQ-SIM reconstruction, an easily performed quasi-Wiener deconvolution is applied by replacing the signal-to-noise (SNR) regularization term in the standard Wiener deconvolution with a small positive constant (referred to as Tikhonov regularization). We find that the proposed LSQ-SIM method provides sample reconstruction that is similar to that of jRL-SIM, with a clearer background but without the post-deconvolution procedure mentioned earlier in this section, revealing two closely nestling branches that are nevertheless obscured in the deconvolved widefield images. Employing the post-deconvolution process described above in LSQ-SIM reconstruction provides clear resolution enhancement, as well as significant contrast improvement.

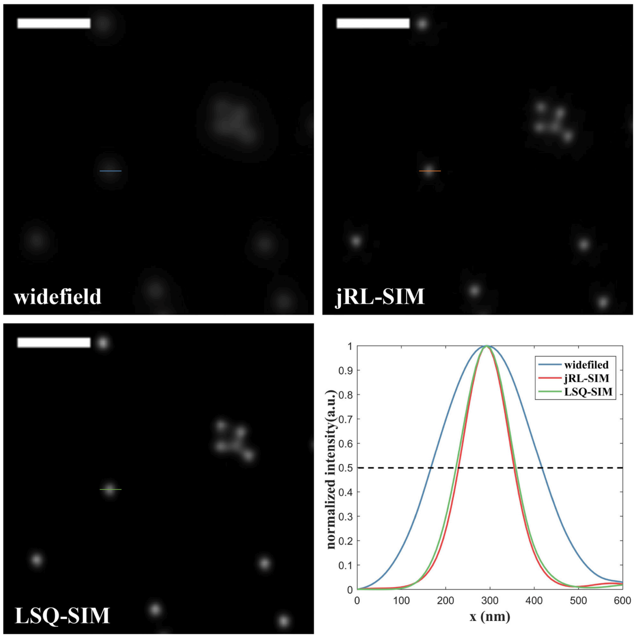

**FIGURE 5 |** Comparison of the intensity profile of a single fluorescent bead reconstructed using jRL-SIM and LSQ-SIM. Scale bar: 1 µm.

The frequency spectra of jRL-SIM and LSQ-SIM reconstructions are also compared, as shown in **Figure 7**. The inner red dashed circle indicates the experimentally calibrated widefield cut-off at a spatial frequency of 1/280 nm$^{-1}$, while the outer circle indicates a cutoff of 1/145 nm$^{-1}$. The spectrum of jRL-SIM reconstruction is expanded and almost fills the area bounded by the outer circle, which is consistent with the result of the previous study [12]. Without post-deconvolution, the spectrum expansion of LSQ-SIM reconstruction is slightly weaker than that of jRL-SIM, which is compensated for by the proposed post-deconvolution method.

With regards to computation time, the jRL-SIM reconstruction of fluorescent beads requires 48.1 s in contrast to the 16.7 s required by the proposed LSQ-SIM method, which is nearly three times faster. For the reconstruction of the microtubule sample, jRL-SIM requires 14.2 s to reconstruct a super-resolution image, while the proposed LSQ-SIM method requires 0.69 and 0.71 s with and without post-deconvolution,

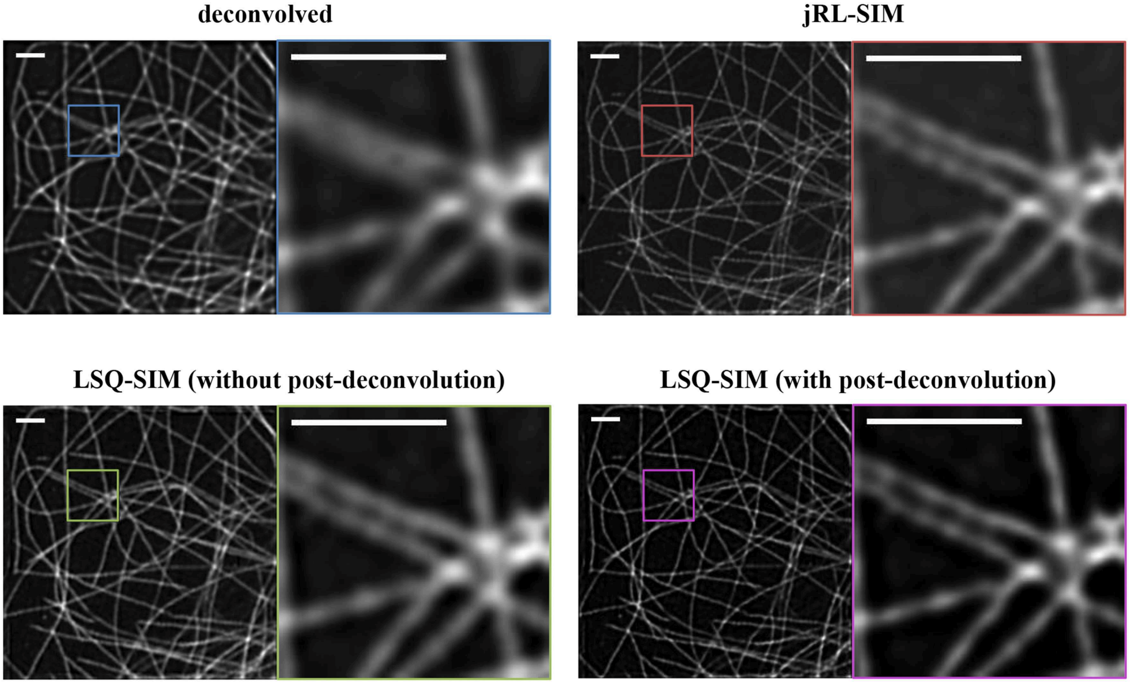

**FIGURE 6 |** Reconstruction results of the microtubule sample, obtained using widefield, jRL-SIM, and proposed LSQ-SIM methods without and with post-deconvolution. Scale bar: 1.5 µm.

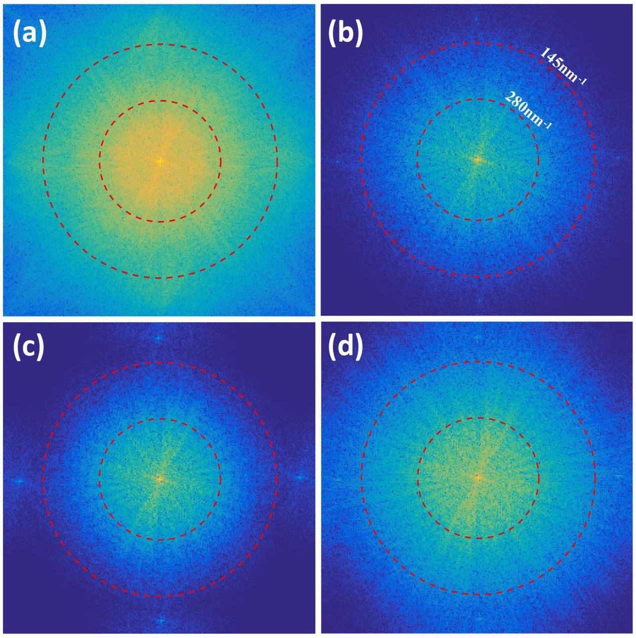

**FIGURE 7 |** Comparison of frequency spectral of the reconstructions of the microtubule sample. The spectra of the deconvolved image **(a)**, jRL-SIM reconstruction **(b)**, and LSQ-SIM reconstruction without **(c)** and with **(d)** post-deconvolution are displayed.

respectively. The speed improvement obtained by the LSQ-SIM algorithm is dramatically increased to over 25 times because of the fast quasi-Wiener deconvolution utilized at the pre-deconvolution step of microtubule reconstruction.

## CONCLUSION

We propose a novel super-resolution image reconstruction algorithm in the least-squares regression framework to efficiently process SIM data under both sinusoidal and non-sinusoidal structured illumination. Our method is conducted mainly in the spatial domain, which greatly reduces the computation time required for an individual reconstruction. The super-resolution capability of the proposed LSQ-SIM approach is verified both *in silico* and *in vitro*. The performance of our method is assessed on two open-access experimental data sets, giving results that are comparable to those of the jRL-SIM method. Our findings indicate that the proposed LSQ-SIM method has the potential for use in biological applications.

## DATA AVAILABILITY STATEMENT

The datasets generated for this study are available on request to the corresponding author.

## AUTHOR CONTRIBUTIONS

JL contributed to conception of this work, accomplished the simulation, performed the analysis of results, and wrote the first draft of the manuscript. All authors contributed to manuscript revision, read, and approved the submitted version.

## FUNDING

This research was funded by the National Natural Science Foundation of China (61827825 and 61735017), Fundamental Research Funds for the Central Universities (2019XZZX003-06), and Zhejiang Lab (2018EB0ZX01 and 2020MC0AE01).

## REFERENCES

1. Abbe E. Beitirage zur theorie des mikroskops und der mikroskopischen Wahrnehmung. *Arch Mikroskopische Anat*. (1873) **9**:413–8. doi: 10.1007/BF02956173
2. Rust MJ, Bates M, Zhuang X. Sub-diffraction-limit imaging by stochastic optical reconstruction microscopy (STORM). *Nat Methods*. (2006) **3**:793–5. doi: 10.1007/978-3-642-02597-6_20
3. Hell SW, Wichmann J. Breaking the diffraction resolution limit by stimulated emission: stimulated-emission-depletion-fluorescence microscopy. *Opt Lett*. (1994) **19**:780–92. doi: 10.1364/OL.19.000780
4. Gustafsson MG. Surpassing the lateral resolution limit by a factor of two using structured illumination microscopy. *J Microsc*. (2010) **198**:82–7. doi: 10.1046/j.1365-2818.2000.00710.x
5. Guo Y, Li D, Zhang S, Yang Y, Liu JJ, Wang X. Visualizing intracellular organelle and cytoskeletal interactions at nanoscale resolution on millisecond timescales. *Cell*. (2018) **175**:1–13. doi: 10.1016/j.cell.2018.09.057
6. Huang X, Fan J, Li L, Liu H, Chen L. Fast, long-term, super-resolution imaging with hessian structured illumination microscopy. *Nat Biotechnol*. (2018) **36**:451–9. doi: 10.1038/nbt.4115
7. Gustafsson GLM. Nonlinear structured-illumination microscopy: wide-feld fuorescence imaging with theoretically unlimited resolution. *Proc Natl Acad Sci USA*. (2005) **102**:13081–6. doi: 10.1073/pnas.0406877102
8. Li D, Shao L, Chen BC, Zhang X, Zhang M, Moses B. Extended-resolution structured illumination imaging of endocytic and cytoskeletal dynamics. *Science*. (2015) **349**:aab3500. doi: 10.1126/science.aab3500
9. Rego EH, Shao L, Macklin JJ, Winoto L, Gustafsson MGL. Nonlinear structured-illumination microscopy with a photoswitchable protein reveals cellular structures at 50-nm resolution. *Proc Natl Acad Sci USA*. (2011) **109**:E135–43. doi: 10.1073/pnas.1107547108
10. Aurélie J, Tolstik E, Feldmann P, Wicker K, Sentenac A, Heintzmann R. Optical sectioning and high resolution in single-slice structured illumination microscopy by thick slice blind-sim reconstruction. *PLOS ONE*. (2015) **10**:e0132174. doi: 10.1371/journal.pone.0132174
11. Mudry E, Belkebir K, Girard J, Savatier E, Moal C, Nicoletti C. Structured illumination microscopy using unknown speckle patterns. *Nat Photon*. (2012) **6**:312–5. doi: 10.1038/nphoton.2012.83
12. York AG, Parekh SH, Nogare DD, Fischer RS, Temprine K, Mione M. Resolution doubling in live, multicellular organisms via multifocal structured illumination microscopy. *Nat Methods*. (2012) **9**:749–54. doi: 10.1038/nmeth.2025
13. Ströhl F, Kaminski CF. A joint richardson—lucy deconvolution algorithm for the reconstruction of multifocal structured illumination microscopy data. *Methods Appl Fluoresc*. (2015) **3**:014002. doi: 10.1088/2050-6120/3/1/014002
14. Dong S, Nanda P, Shiradkar R, Guo K, Zheng G. High-resolution fluorescence imaging via pattern-illuminated fourier ptychography. *Opt Exp*. (2014) **22**:20856–70. doi: 10.1364/OE.22.020856

15. Chakrova N, Rieger B, Stallinga S. Deconvolution methods for structured illumination microscopy. *J Opt Soc Am A*. (2016) 33:B12. doi: 10.1364/JOSAA.33.000B12
16. Tian L, Li X, Ramchandran K, Waller L. Multiplexed coded illumination for fourier ptychography with an led array microscope. *Biomed Opt Exp*. (2014) **5**:2376–89. doi: 10.1364/BOE.5.002376
17. Florian S, Kaminski CF. Frontiers in structured illumination microscopy. *Optica*. (2016) **3**:667–77. doi: 10.1364/optica.3.000667
18. Dan D, Lei M, Yao B, Wang W, Winterhalder M, Zumbusch A, et al. DMD-based LED-illumination super-resolution and optical sectioning microscopy. *Sci Rep*. (2013) **3**:1116. doi: 10.1038/srep01116
19. Ingerman EA, London RA, Heintzmann R, Gustafsson MGL. Signal, noise and resolution in linear and nonlinear structured-illumination microscopy. *J Microscopc*. (2018) **273**:3–25. doi: 10.1111/jmi.12753
20. Yeh LH, Tian L, Waller L. Structured illumination microscopy with unknown patterns and a statistical prior. *Biomed Opt Exp*. (2016) **8**:695–711. doi: 10.1364/BOE.8.000695
21. Chakrova N, Heintzmann R, Rieger B, Stallinga S. Studying different illumination patterns for resolution improvement in fluorescence microscopy. *Opt Exp*. (2015) **23**:31367–83. doi: 10.1364/OE.23.031367
22. Dong S, Liao J, Guo K, Bian L, Suo J, Zheng G. Resolution doubling with a reduced number of image acquisitions. *Biomed Opt Exp*. (2015) **6**:2946–52. doi: 10.1364/BOE.6.002946
23. Ströhl F, Kaminski C. Speed limits of structured illumination microscopy. *Opt Lett*. (2017) **42**:2511–4. doi: 10.1364/OL.42.002511
24. Richardson WH. Bayesian-based iterative method of image restoration. *J Opt Soc Am*. (1972) **62**:55–9. doi: 10.1364/JOSA.62.000055
25. Lucy LB. An iterative technique for the rectification of observed distributions. *J Astron*. (1974) **79**:745–54. doi: 10.1086/111605

**Conflict of Interest:** JW was employed by the company Texas Instruments Semiconductor Technologies (Shanghai) Co., Ltd.

The remaining authors declare that the research was conducted in the absence of any commercial or financial relationships that could be construed as a potential conflict of interest.

frontiers in Physics

ORIGINAL RESEARCH
published: 28 April 2020
doi: 10.3389/fphy.2020.00110

# Compact Dual-Channel (Hyperspectral and Video) Endoscopy

*Fuhong Cai*[1], *Min Gao*[1], *Jingwei Li*[2], *Wen Lu*[3,4]* and *Chengde Wu*[5]*

*[1] Mechanical and Electrical Engineering College, Hainan University, Haikou, China, [2] State Key Laboratory for Modern Optical Instrumentation, Centre for Optical and Electromagnetic Research, Zhejiang University, Hangzhou, China, [3] Department of Biochemistry and Molecular Biology, Hainan Medical University, Haikou, China, [4] Key Laboratory of Emergency and Trauma of Ministry of Education, Hainan Medical University, Haikou, China, [5] Department of Cardio-Thoracic Surgery, Haikou People's Hospital, Central South University Xiangya School of Medicine Affiliated Haikou Hospital, Haikou, China*

The combining of reflected endoscopic imaging with spectral data has recently attracted much attention. In this study, we used an optical fiber bundle probe, a galvo-scanning module and an imaging spectrometer module to realize a dual-channel endoscope that is capable of simultaneously acquiring real-time video data and high-throughput hyperspectral data. The frame per second of the video channel is 30, and the wavelength range in the hyperspectral channel is 400–750 nm, with a 3 nm spectral resolution at 547 nm. To achieve fast hyperspectral imaging, we extracted the region of interest (ROI) from the video channel and utilized it as guidance to drive the galvo-scanning module to obtain the hyperspectral data in the ROI. In this way, the hyperspectral imaging speed for a selected ROI area can be reduced to about 1 second, making it possible to achieve rapid detection. Utilizing this system, we acquired the hyperspectral image of fingerprints, dorsum of the hand, and skin melanin nevus, demonstrating that compact dual-channel endoscopy has broad implications for research and therapeutics.

**Keywords: optical fiber bundle probe, galvo-scanning module, dual-channel, region of interest, hyperspectral**

OPEN ACCESS

***Edited by:***
*Chao Tian,*
*University of Science and Technology of China, China*

***Reviewed by:***
*Jiaxin Yu,*
*University of Shanghai for Science and Technology, China*
*Hao He,*
*Shanghai Jiao Tong University, China*

****Correspondence:***
*Wen Lu*
*swkxlw@163.com*
*Chengde Wu*
*chengdewu@yeah.net*

***Specialty section:***
*This article was submitted to Medical Physics and Imaging, a section of the journal Frontiers in Physics*

***Received:*** *12 February 2020*
***Accepted:*** *23 March 2020*
***Published:*** *28 April 2020*

***Citation:***
*Cai F, Gao M, Li J, Lu W and Wu C (2020) Compact Dual-Channel (Hyperspectral and Video) Endoscopy. Front. Phys. 8:110. doi: 10.3389/fphy.2020.00110*

## INTRODUCTION

The importance of histopathological evaluation for disease remains critical. However, the acquisition and recognition of traditional pathological data are time-consuming and must be obtained by a well-trained observer. In order to achieve rapid intraoperative diagnosis, examination of frozen pathological sections from patients during operation has been developed and widely used in the clinical field. However, some dysplasia is invisible, inevitably leading to misdiagnosis. To circumvent this problem, some *in vivo* diagnostic techniques based on endoscopic tools have been developed [1–3]. For example, Qiu et al. [3] utilized light scattering endoscopic imaging for esophageal precancer diagnosis. Their work demonstrated that spectral technology is compatible with endoscopic diagnosis. In order to obtain high-throughput spectral information, hyperspectral endoscopy has been developed [4–6]. In hyperspectral imaging, the spectrum of each pixel in the image can be obtained, and then the chemical components of various kinds of tissue can be analyzed through spectral information [7, 8], which helps to improve the accuracy of diagnosis [9–14]. Nevertheless, motion artifacts during medical endoscopy may affect clinical diagnosis. From the perspective of imaging, increasing the imaging speed contributes to reducing motion artifacts. Hence, imaging speed is important for accuracy in clinical applications [15]. In general, a straightforward way to improve the imaging speed is to reduce the integral time of the sensor. However, the signal-to-noise ratio (SNR) is usually poor, with short integral time. At present, it is critical to resolve the issue of reducing spectral resolution to improve the SNR of spectral data in order to develop a fast-spectral detection system with less exposure time. Another way to improve imaging speed is to reduce the spectral resolution of the system. However, in the visible and near-infrared band, the absorption spectra of different biomolecules usually overlap. This reduces the reconstruction accuracy of biomolecules' content. Higher spectral resolution data can help to distinguish different biomolecules and contribute to a more accurate medical/chemical analysis [16]. Thus, a hyperspectral endoscopy system with high imaging speed and rich spectral information is required to perform accurate clinical diagnoses.

In our previous work [17], we developed a fiber bundle probe-based hyperspectral endoscope that utilized a galvo mirror to achieve spatial scanning. This hyperspectral endoscope is relatively cost-efficient and portable, making it suitable for field use. However, the previous endoscopic prototype required several tens seconds to obtain one three-dimensional (3D, 2D spatial, and 1D spectral) spectral image cube, which certainly limits its clinical application during operation. Additionally, the spectral image cube obtained suffered because of severe motion artifacts. In this study, we developed a compact dual-channel endoscope to accomplish rapid hyperspectral imaging in order to obtain a hyperspectral image of a region of interest (ROI) in about 1 s. This rapid imaging undoubtedly expanded its use in the histopathological evaluation. The system combines a traditional endoscopic imaging system and galvo-scanning imaging spectrometer to generate two channels of imaging data, i.e., high-speed two-dimensional (2D) spatial video data and a 3D hyperspectral cube. These two channels both detect the same target through endoscope imaging. Utilizing the high-speed spatial image and an image processing algorithm, ROIs can be rapidly located. By controlling the scanning angle of the galvo mirror, we can acquire fast-spectral imaging on the ROI. In the present study, the system was used to detect fingerprints, dorsum of hand, and skin melanin nevus, demonstrating its broad implications for research and therapeutics.

## MATERIALS AND METHODS

In this work, a dual-channel endoscope was assembled to simultaneously acquire video and hyperspectral imaging data. **Figures 1a,b** shows the optical schematic diagram and photo of the dual-channel endoscope, respectively. A fiber bundle probe was used to transmit an image of the sample. When detecting the spectra of samples, an imaging lens was used to focus the image of the sample onto the far end face of the fiber bundle, while the proximal end face of the fiber bundle was in the focal plane of the objective. In this way, the real image of the sample was relayed to the detection module. After passing through the objective (RMS10X, THORLABS), the sample's real image was divided into two paths by a beam splitter (BSX10, THORLABS). After lens focusing (AC254-050-A, THORLABS), one path was captured by a custom video camera, thus obtaining the spatial image of the sample. The other path was first reflected by the galvo mirror (GVS001, THORLABS) and then focused into the homemade imaging spectrometer by another doublet lens (AC254-050-A, THORLABS). The homemade imaging spectrometer consisted of a custom slit with a 30 $\mu$m width, a collimating lens (AC254-050-A, THORLABS), a custom prism-grating-prism module, a focusing lens (AC254-050-A, THORLABS), and a CMOS camera. By changing the angle of the galvo mirror with the help of a data acquisition/generation card (USB6008, NI), the real image was scanned across the slit. For each angle, a spectral image was captured by the camera of the imaging spectrometer. A hyperspectral image cube of the sample was formed by combining a sequence of spectral images [18]. By outputting voltage with different values from USB6008, we controlled the angle of the galvo mirror. Both the video camera and spectral camera were connected to a computer using USB 3.0 cables. Through the USB cables, camera control and data transfer were accomplished. Notably, this compact dual-channel endoscope—including the driver circuit, data acquisition card, wire box, and a power outlet—can be contained in a suitcase whose size is 68 cm × 32 cm × 17 cm.

We then performed the spectral calibration by utilizing a custom-made mercury lamp. Inset of **Figure 1c** was a spectral image captured by the camera of imaging spectrometer. The horizontal axis indicated spectral axis, while the vertical axis represented spatial axis, which was also perpendicular to the scanning direction. According to reporting by Das et al. [8], the wavelength of the spectrometer was assumed to be a polynomial function of the pixel index of the spectral axis. Thus, a least squares polynomial fit method was employed to investigate the relationship between wavelength and pixel index. Here, the wavelength of the calibration source at 406, 437, 547, 579, 620, 699 nm [19], and their corresponding pixel indexes at 1,136, 1,047, 741, 654, 611, 541, 333 were utilized in the fitting process. The solid line of **Figure 1c** shows the relationship between the wavelength and pixel index derived from the fitting result. **Figure 1d** is the spectrum of the calibration source obtained by our homemade spectrometer, with approximate 3 nm spectrometer at 547 nm. The wavelength range of this homemade imaging spectrometer was 400–750 nm.

## RESULTS AND DISCUSSION

We first presented the imaging results of a test fiber bundle to check the consistency of the spatial image and hyperspectral image. A collimated LED lamp was adopted to illuminate the far end face of the fiber bundle probe. The spectrum of the LED lamp was shown in **Figure 2a**. The radiance of the LED lamp was about 500 lumens. The LED was driven by an electrical signal, so that the LED was turned on during the hyperspectral scanning process. With this working mode, we were able to avoid the heating problem of LED caused by long-time illumination. In the test experiment, a uniform white board was selected as an imaging sample, whose spatial image and hyperspectral cube were acquired synchronously. **Figure 2b** shows the image obtained by the video channel. Herein, there were several flaw pixels in the fiber bundle, since some region of the fiber bundle could not deliver the LED light. A hyperspectral cube

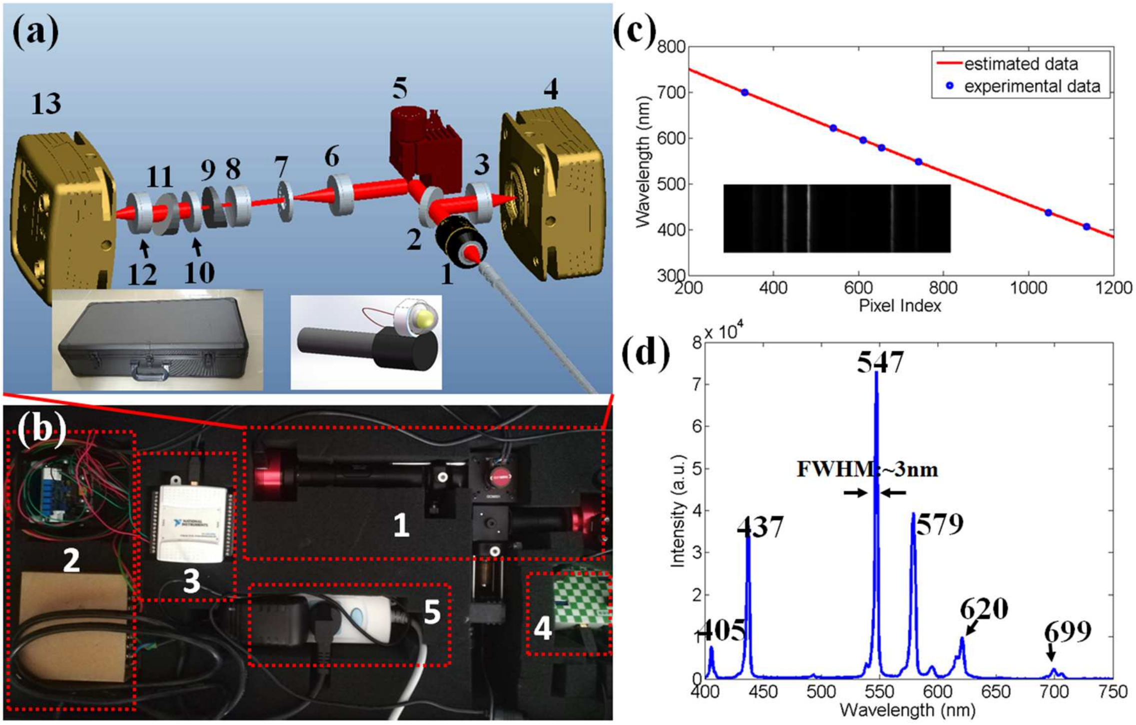

**FIGURE 1 | (a)** Schematic drawing of the compact dual-channel endoscopy. 1, microscopic object; 2, beam splitter; 3, lens; 4, video camera; 5, galvo mirror; 6, imaging lens; 7, slit; 8, collimating lens; 9, prism; 10, grating; 11, prism; 12 doublet lens; 13, CMOS camera. One inset is the enclosing capsule, which is used to contain the compact dual-channel endoscopy. Another inset shows the far end face of the fiber bundle. **(b)** Photo of the compact dual-channel endoscopy. 1, compact dual-channel endoscopy; 2, driver circuit of the galvo mirror; 3, data acquisition/generation card; 4, wire box; 5, power outlet. **(c)** Relationship between the pixel index of CMOS camera and the calibrated wavelength. Inset is the spectral image of the calibration source. **(d)** Spectrum of the calibration source measured by our system.

was synchronously acquired from the spectral channel. The spatial image extracted from the hyperspectral cube is shown in **Figure 2c**. Observing the flaw pixels region, we found the spectral channel had good spatial consistency with the imaging result of the video channel.

Second, we attempted to demonstrate that the scanning result of the spectral channel was linearly related with the control voltage from USB6008. For this purpose, we performed a spectral scanning experiment with six voltage ranges (i.e., 2.5–3.0 v, 2.0–2.5 v, 1.5–2.0 v, 1–1.5 v, 0.5–1 v, 0–0.5 v). Six spectral cubes were acquired after six scanning experiments, and the corresponding six spatial images are shown in **Figures 2d–i**. The combination of these six pictures is consistent with that of **Figure 2c**, indicating that the regional scan is consistent with global scan. This result shows that we can scan the region of interest through appropriate voltage output. By analyzing the spectral image of the end face of the fiber bundle probe in **Figures 2d–i**, the corresponding driving voltages to the left and right edge were 2.87 and 0.09 v, respectively. Meanwhile, the width of the spatial image of **Figure 2b** was 1,280 pixels, and the width of proximal end face of the fiber bundle was 1,264 pixels. Therefore, we can get the relationship between the driving voltage and the horizontal pixel index of the image by the following formula: *driving voltage* $= -0.0022 \times$ pixel position + 2.87.

Next, we utilized this system to image the hand of the first author. The LED lamp described above was used as an illumination source. **Figures 3a,b** shows spatial images derived from the video and spectral channel, respectively, when the fiber probe was aimed at human fingerprints. **Figure 3c** presents the average spectrum of fingerprints inside the red circle in **Figure 3b**. Two absorption bands, caused by the absorption of hemoglobin, can be seen near 543 and 580 nm [indicated by two arrows in the **Figure 3c**]. **Figure 3d** presents images of the finger at three spectral channels (543, 580, and 606 nm). Among the three images, the image brightness at 580 nm channel is the weakest due to the absorption of hemoglobin. Similarly, **Figures 3e,f** shows spatial images of the dorsum of the human hand derived from the video and spectral channel, respectively. **Figure 3g** presents the average spectrum of the blue circle in **Figure 3f**. Compared with the spectrum of the fingerprint, only the absorption band at 580 nm can be seen [indicated by the arrow in the **Figure 3g**], indicating that the hemoglobin content in the dorsum of the hand is less than that in the fingerprint. **Figure 3h** presents images of dorsum of the hand at three spectral channels (543, 580, and 606 nm).

It is worth nothing that for each spectral image, the exposure time of the camera was 20 ms and that 300 spectral images were collected during the experiment. Hence, the overall scanning

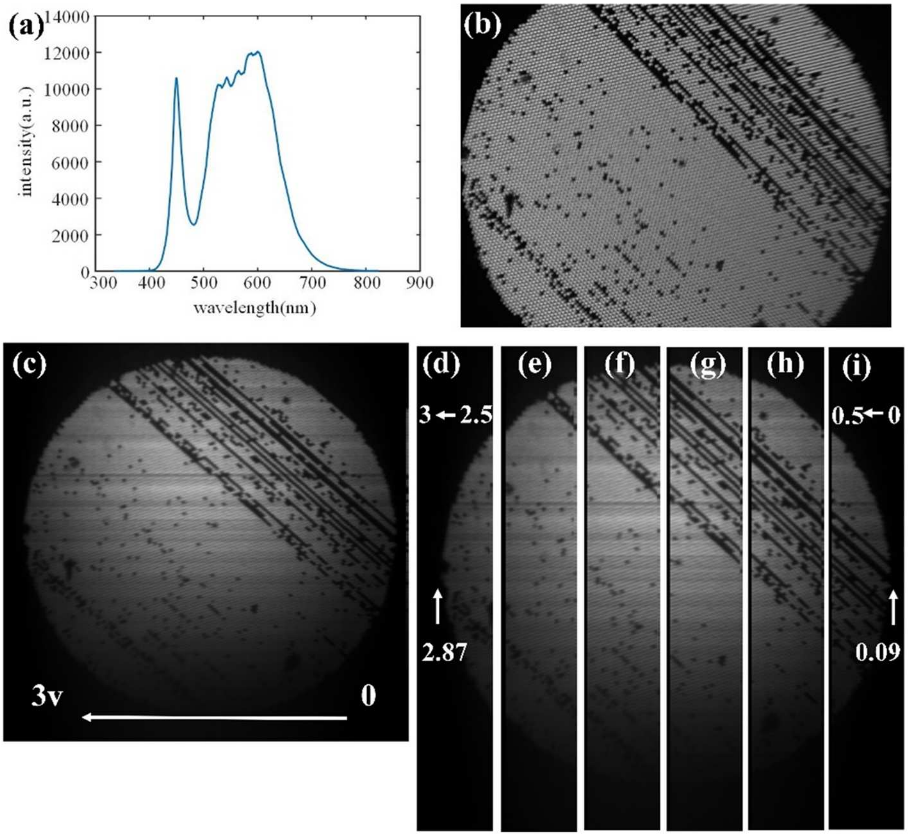

**FIGURE 2 | (a)** The spectrum of the LED source. **(b)** Spatial image of the fiber bundle end face derived from video channel. **(c)** Spatial image of the fiber bundle end face, extracted from the spectral cube from spectral channel with 0–3 v driving voltage. **(d–i)** The corresponding relationship between driving voltage of galvanometer and pixel position of hyperspectral image, indicating regional scan is consistent with global scan.

time was about 6 s. During the scanning process, the spectral images were stored in the computer memory, rather than in a hard disk, to reduce the data storage time. While the computer was collecting spectral images, a new thread was created in the program to deal with the spectral data in the memory of the computer. All the programs were written in C# code.

However, even though the carrying out of the scan and the processing of spectral images occurred simultaneously by creating dual threads in the program, the total processing time, 6 s, is impractical for *in vivo* application since it is quite slow. By analyzing hyperspectral images, we found that we often paid more attention to a key area rather than the whole area when processing hyperspectral data. In order to further improve the scanning speed, we determined the ROI by spatial image first. Then, we scanned the region of interest by setting the initial voltage and the end voltage of galvanometer scanning because there was a linear relationship between the driving voltage and the horizontal pixel index of the intensity image. **Figure 4a** shows the spatial image of a melanin nevus on the skin's surface of the first author. It took 6 s to obtain the reflection hyperspectral image of this area according to the system described earlier in this article. A melanin nevus in the middle of the image is visible. If the reflectance spectrum of this region is only necessary, the spectral data of skin tissue outside the nevus prove redundant. By processing the spatial image, we extracted the ROI and used it to generate the appropriate driving voltage of the galvo mirror to scan the region. In this way, the scanning time was reduced to a great extent. In order to extract the location of melanin, we used the expansion function in MATLAB to process **Figure 4a** and obtained **Figure 4b**. **Figure 4b** was an intensity image. In order to identify the melanin nevus, we used the binary algorithm to process the image. In the binary algorithm, pixels with intensity greater than a threshold value were set to digital 1, and the pixels below the threshold were set to the digital 0. In our work, the binarization function in MATLAB was used to binarize the image, and the binary image is thusly shown in **Figure 4c**. In the binary image, the white region represented the common skin tissue, and the black region inside the white region represented the melanin nevus area. In this study, it took about 0.5 s to complete this image processing. In **Figure 4c**, we obtained the pixel index range of the black region in the middle, which presented a range of 680 to 810. The original width of the image was 1,280, and the extracted width was ∼10% of the original width. According to the relationship driving voltage = −0.0022 × pixel position + 2.87, the corresponding voltage range of the black area is

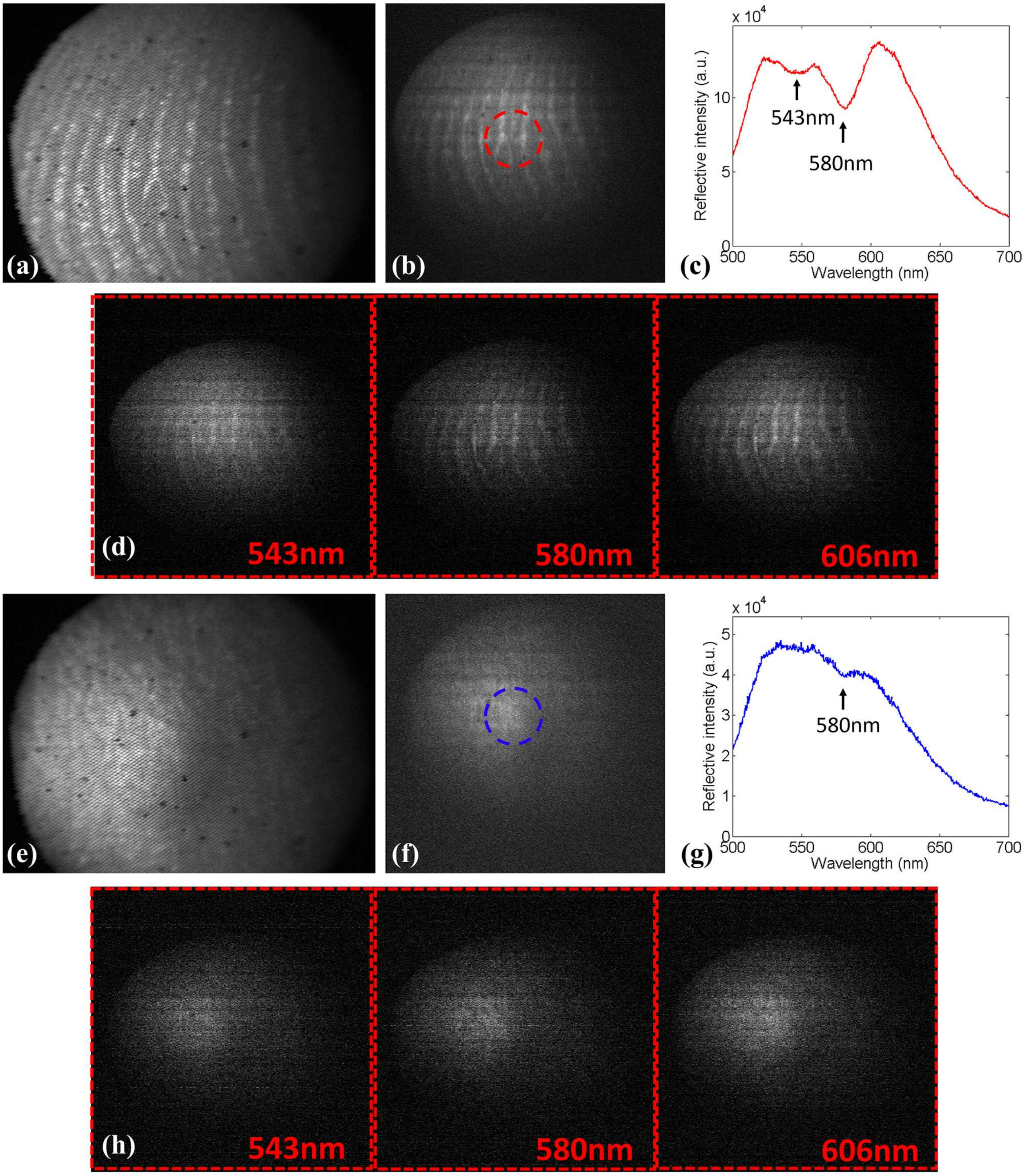

**FIGURE 3 | (a)** Spatial image of finger derived from video channel. **(b)** The corresponding spatial image extracted from the spectral cube from the spectral channel. **(c)** The average spectrum of the finger inside the red circle. **(d)** Images of finger at three spectral channels (543, 580, and 606 nm). **(e)** The spatial image of dorsum of the hand. **(f)** The corresponding spatial image extracted from the spectral cube from the spectral channel. **(g)** The average spectrum of dorsum of hand inside the blue circle. **(h)** Images of dorsum of the hand at three spectral channels (543, 580, and 606 nm).

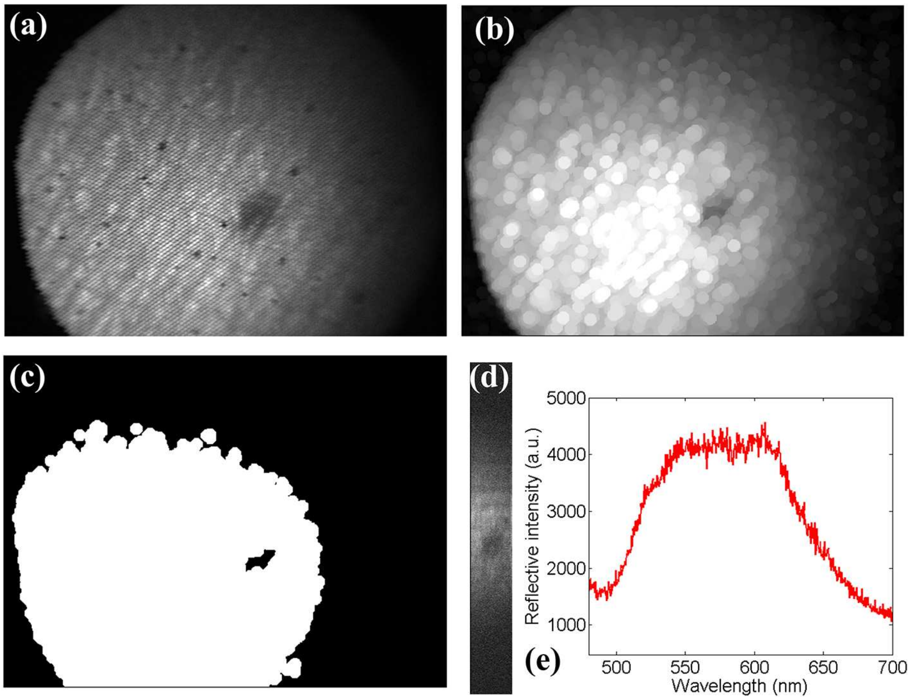

**FIGURE 4 | (a)** The spatial image of skin. **(b)** The corresponding spatial image extracted from the spectral cube from spectral channel. **(c)** The intensity image after threshold segmentation. **(d)** The spectral image of hyperspectral image of a ROI (skin melanin nevus). **(e)** The spectrum of skin melanin nevus.

1.0880 to 1.3740. By setting the driving voltage range of the galvo mirror, it enabled a rapid scan of the melanin nevus. The hyperspectral image of the melanin nevus is shown in **Figure 4d**. With the same exposure time, the scanning time reduced to ∼0.6 s, indicating much less scanning time by focusing on the ROI. The entire scanning process was about 1.1 s when the image processing time is also considered. If multithreading is used to perform the image processing in the future, this time can be further shortened. **Figure 4e** shows the spectrum of melanin nevus. Compared with the reflective spectrum of common skin, whose hemoglobin's characteristic absorption peak was at 580 nm, the absorption drop at 580 nm was absent in the reflective spectrum of melanin nevus. We can distinguish the melanin region from common skin region based on this characteristic. Meanwhile, the SNR of the melanin nevus was lower than those in **Figure 3** due to the strong absorption in the visible light band of melanin.

## DISCUSSION

In this study, a compact dual-channel endoscope was presented, and *in vivo* biomedical applications of the endoscopy were explicated. In the system, the image of the sample was relayed to the detection module, which consists of a video camera and homemade imaging spectrometer by a custom fiber bundle probe. The frame rate of the video camera was 30 per second, and the wavelength range of the imaging spectrometer was 400–750 nm, with an approximate 3 nm spectral resolution at 547 nm. This hyperspectral endoscope enables the obtainment of real-time video data and high-throughput hyperspectral data simultaneously. More importantly, by utilizing the spatial image captured by video camera to locate the ROI, this system is able to accomplish hyperspectral imaging of an ROI in about 1 s, giving it great potential to be used in clinical applications. We first demonstrated the spatial consistency between the video channel and the hyperspectral channel by acquiring the spatial image and hyperspectral cube of the end face of the fiber bundle. Thereafter, we investigated the relationship between the input voltage of the galvo mirror and the pixel index of the spatial image, which exhibited a linear relationship between them. Using a LED lamp as an illumination source, we obtained the hyperspectral cube of fingerprints and dorsum of the hand. The result apparently indicates different hemoglobin content in fingerprints and dorsum of the hand. To note, it takes 6 s to acquire the whole hyperspectral cube. In order to increase the speed of hyperspectral imaging, using the spatial image as guidance and extracting the pixel index of the ROI, we obtained the hyperspectral cube of the skin melanin nevus within 0.6 s, which demonstrates the system's capability of rapid detection. In the future, we can adopt more professional image segmentation methods [20] to obtain accurate ROI. Therefore, we believe this compact dual-channel (hyperspectral and video) endoscope is promising for biomedical applications in disease diagnosis. In addition, our system can also be extended to a double-fiber bundle, combined with binocular vision technology [21, 22], and the system can be extended to a four-dimensional (3D spatial and 1D spectral) detection system.

## DATA AVAILABILITY STATEMENT

All datasets generated for this study are included in the article/supplementary material.

## ETHICS STATEMENT

The studies involving human participants were reviewed and approved by the Medical Ethics Committee of Hainan Medical University and the Medical Ethics Committee of Hainan University.

## AUTHOR CONTRIBUTIONS

WL and CW conceived the study. FC designed the optical system. MG and JL performed the experiments and analyzed data. FC developed the algorithm. JL, WL, and CW wrote the paper. All authors reviewed the results and approved the final version of the manuscript.

## FUNDING

The work was supported by the high level talent support project of basic and applied basic research plan (Natural Science Field) of Hainan Province (2019RC080 to FC), the National Natural Science Foundation of China (31600863 to WL), the Scientific Research Fund of Hainan University (KYQD1653,) and the start-up fund of Hainan Medical University to WL.

## REFERENCES

1. Waterhouse DJ, Fitzpatrick CRM, di Pietro M, Bohndiek SE. Emerging optical methods for endoscopic surveillance of Barrett's oesophagus. *Lancet.* (2018) **3**:349–62. doi: 10.1016/S2468-1253(18)30030-X
2. Lan L, Xia Y, Li R, Liu K, Mai J, Medley JA, et al. A fiber optoacoustic guide with augmented reality for precision breast-conserving surgery. *Light Sci Appl.* (2018) **7**:2. doi: 10.1038/s41377-018-0006-0
3. Qiu L, Chuttani R, Pleskow DK, Turzhitsky V, Khan U, Zakharoy YN, et al. *Light Sci. Appl.* (2018) **7**:17174. doi: 10.1038/lsa.2017.174
4. Akbari H, Uto K, Kosugi Y, Kojima K, Tanaka N. Cancer detection using infrared hyperspectral imaging. *Cancer Sci.* (2011) **102**:852–7. doi: 10.1111/j.1349-7006.2011.01849.x
5. Zhang H, Yuan J, Fu L. Imaging Fourier transform endospectroscopy for *in vivo* and *in situ* multispectral imaging. *Opt Express.* (2012) **20**:23349–60. doi: 10.1364/OE.20.023349
6. Kester RT Bedard N, Gao L, Tkaczyk TS. Real-time snapshot hyperspectral imaging endoscope. *J Biomed Opt.* (2001) **16**:056005–12. doi: 10.1117/1.3574756
7. Yao X, Cai F, Zhu P, Fang H, Li J, He S. Non-invasive and rapid pH monitoring for meat quality assessment using a low-cost portable hyperspectral scanner. *Meat Sci.* (2009) **152**:73–80. doi: 10.1016/j.meatsci.2019.02.017
8. Das AJ, Wahi A, Kothari I, Raskar R. Ultra-portable, wireless smartphone spectrometer for rapid, non-destructive testing of fruit ripeness. *Sci Rep.* (2016) **6**:32504. doi: 10.1038/srep32504
9. Halicek M, Fabelo H, Oretega S, Callico GM, Fei B. *In-vivo* and *ex-vivo* tissue analysis through hyperspectral imaging techniques: revealing the invisible features of cancer. *Cancers.* (2019) **11**:756. doi: 10.3390/cancers11060756
10. Halicek M, Little JV, Wang, X, Chen AY, Fei, B. Optical biopsy of head and neck cancer using hyperspectral imaging and convolutional neural networks. *J Biomed Opt.* (2019) **24**:036007. doi: 10.1117/1.JBO.24.3.036007
11. Steelman ZA, Ho DS, Chu KK, Wax A. Light-scattering methods for tissue diagnosis. *Optica.* (2019) 6:479–89. doi: 10.1364/OPTICA.6.000479
12. Wu IC, Syu HY, Jen CP, Lu, MY, Chen YT, Wu MT, et al. Early identification of esophageal squamous neoplasm by hyperspectral endoscopic imaging. *Sci Rep.* (2018) **8**:13797. doi: 10.1038/s41598-018-32139-1
13. Luthman AS, Water house DJ, Ansel-Bollepalli L, Yoon J, Gordon GSD, Joseph J, et al. Bimodal reflectance and fluorescence multispectral endoscopy based on spectrally resolving detector arrays. *J Biomed Opt.* (2018) **24**:031009. doi: 10.1117/1.JBO.24.3.031009
14. Yoon J, Joseph J, Waterhouse DJ, Luthman AS, Gordon GSD, Pietro M, et al. A clinically translatable hyperspectral endoscopy (HySE) system for imaging the gastrointestinal tract. *Nat Commun.* (2019) **10**:1902. doi: 10.1038/s41467-019-09484-4
15. Fabelo H, Ortega S, Ravi D, Kiran BR, Sosa C, Bulters D, et al. Spatio-spectral classification of hyperspectral images for brain cancer detection during surgical operations. *PLoS ONE.* (2018) **13**:e0193721. doi: 10.1371/journal.pone.0193721
16. Hair JW, Hostetler CA, Cook AL, Harper DB, Ferrare RA, Mack TL, et al. Airborne high spectral resolution lidar for profiling aerosol optical properties. *Appl Opt.* (2008) **47**:6734–52. doi: 10.1364/AO.47.006734
17. Cai F, Wang Y, Gao M, He S. The design and implementation of a low-cost multispectral endoscopy through galvo scanning of a fiber bundle. *Opt Commun.* (2018) **428**:1–6. doi: 10.1016/j.optcom.2018.07.044
18. Li Q, He X, Wang Y, Liu H, Xu D, Guo F. Review of spectral imaging technology in biomedical engineering: achievements and challenges. *J Biomed Opt.* (2013) **18**:100901. doi: 10.1117/1.JBO.18.10.100901
19. Sansonetti CJ, Salit ML, Reader J. Wavelengths of spectral lines in mercury pencil lamps. *Appl Opt.* (1996) **35**:74–7. doi: 10.1364/AO.35.000074
20. Kharmyssov C, Ko MWL, Kim JR. Automated segmentation of optical coherence tomography images. *Chin Opt Lett.* (2019) **17**:041701. doi: 10.3788/COL201917.011701
21. Yu N, Wang S. Enhanced autonomous exploration and mapping of an unknown environment with the fusion of dual RGB-D sensors. *Engineering.* (2019) **5**:164–72. doi: 10.1016/j.eng.2018.11.014
22. Cai F, Wang T, Wu J, Zhang X. Handheld four-dimensional optical sensor. *Optik.* (2020) **203**:164001. doi: 10.1016/j.ijleo.2019.164001

**Conflict of Interest:** The authors declare that the research was conducted in the absence of any commercial or financial relationships that could be construed as a potential conflict of interest.

frontiers
in Physics

ORIGINAL RESEARCH
published: 30 April 2020
doi: 10.3389/fphy.2020.00091

# Therapeutic Assessment of High-Intensity Focused Ultrasound for Vulvar Lichen Sclerosus by Active Dynamic Thermal Imaging and Hyperspectral Imaging—A Preliminary Study

*Yingjie Qu[1], Yuquan Meng[2], Sui Feng[1], Maoyu Liu[3], Linlin Xiao[3], Xiaoyuan Zhang[3], Jinjin Zheng[1], Shufang Chang[3]* and Ronald X. Xu[1,4]**

*[1] Department of Precision Machinery and Precision Instrumentation, University of Science and Technology of China, Hefei, China, [2] Department of Thermal Science and Energy Engineering, University of Science and Technology of China, Hefei, China, [3] Department of Obstetrics and Gynecology, Second Affiliated Hospital of Chongqing Medical University, Chongqing, China, [4] Department of Biomedical Engineering, The Ohio State University, Columbus, OH, United States*

***Edited by:***
*Jun Xia,*
*University at Buffalo, United States*

***Reviewed by:***
*Ramy Abdlaty,*
*McMaster University, Canada*
*Depeng Wang,*
*Duke University, United States*

***Correspondence:***
*Shufang Chang*
*shfch2005@163.com*
*Ronald X. Xu*
*xu.ronald@hotmail.com*

***Specialty section:***
*This article was submitted to*
*Medical Physics and Imaging,*
*a section of the journal*
*Frontiers in Physics*

***Received:*** *25 December 2019*
***Accepted:*** *12 March 2020*
***Published:*** *30 April 2020*

***Citation:***
*Qu Y, Meng Y, Feng S, Liu M, Xiao L, Zhang X, Zheng J, Chang S and Xu RX (2020) Therapeutic Assessment of High-Intensity Focused Ultrasound for Vulvar Lichen Sclerosus by Active Dynamic Thermal Imaging and Hyperspectral Imaging—A Preliminary Study. Front. Phys. 8:91.*
*doi: 10.3389/fphy.2020.00091*

Vulvar lichen sclerosus (VLS) is a common inflammatory condition associated with an increased risk of developing vulvar carcinoma. Recently, high-intensity focused ultrasound (HIFU) has been identified as a promising treatment modality for VLS in several clinical trials. However, in HIFU therapy, therapeutic outcome is routinely assessed visually by an expert using standardized grading criteria. Furthermore, such a therapeutic assessment cannot be made until at least 3 months after treatment. Therefore, an objective and timely method capable of quantitatively evaluating HIFU treatment effectiveness is desired, which may help identify patients whose treatment is insufficient promptly and prevent delay in re-treatment. The purpose of this study is to investigate the feasibility of using active dynamic thermal imaging (ADT) and hyperspectral imaging (HSI) as two individual objective and non-invasive optical methods for prompt quantitative assessment of the therapeutic response to HIFU treatment in VLS. From December 2018 to March 2019, 20 female VLS patients who underwent HIFU treatment were evaluated using both the ADT and HSI methods. The effective damage rate from the ADT method and the entropy of feature index from the HSI method were used to develop a multivariate linear discriminant classification model for grading the effectiveness of HIFU treatment in comparison with clinical evaluation gold standard. It was found that ADT was able to correctly differentiate ineffective treatments from effective ones with a sensitivity of 100% and specificity of 100%, while the sensitivity and specificity of HSI were 75 and 87.5%, respectively. The classification results demonstrate the clinical potential of the ADT and HSI methods for timely non-invasive and quantitative assessment of HIFU treatment for VLS.

**Keywords: vulvar lichen sclerosus, focused ultrasound, therapeutic assessment, ADT, hyperspectral imaging**

# 1. INTRODUCTION

Vulvar Lichen Sclerosus (VLS) is a chronic mucocutaneous disorder, which is likely to lead to impairment in sexual function and the potential for malignant transformation [1–4]. Early diagnosis, prompt treatment, and appropriate follow-up are extremely important to prevent these negative sequelae [4–6].

Since the etiology of VLS has not yet been fully explained, effective treatments are lacking [7]. Current treatment for VLS mostly focuses on symptomatic relief [7]. Potent corticosteroids applied topically are generally considered as the first-line treatment [8, 9]. When properly administered, these can help to resolve the symptoms of pruritus. However, safety concerns exist regarding long-term use [10, 11]. As this standard treatment can cause side effects, such as atrophy, and has a high recurrence rate, new effective alternatives should be studied for clinical practice.

Considering the serious side effects of traditional treatment, high-intensity focused ultrasound (HIFU) treatment, which uses ultrasound as a carrier of energy, has gradually gained popularity as an alternative treatment for VLS [2, 4, 12–16]. Propagating harmlessly, HIFU causes a sufficient local rise in temperature for the thermal destruction of target tissues without damaging surrounding or overlying tissues [17]. Due to its non-invasive nature, this technology has been used for the ablation of solid tumors [18]. Furthermore, HIFU has been used for several other therapeutic applications [13, 19]. Recently, several clinical trials have shown that HIFU treatment could relieve itching of the vulva and recover the vulvar skin's elasticity and appearance [12–16]. HIFU appears to be a promising treatment modality for vulvar diseases, including VLS. Today, this technique is regularly used for treating this condition in many centers of China.

Although HIFU treatment is recognized as an effective therapy for VLS, there is a lack of quick, quantitative assessment methods for therapeutic response to HIFU in VLS. In clinical settings, patient symptoms, including pruritus and skin appearance, were investigated by a questionnaire before and after the treatment [20–22]. The scores on the questionnaire were used to evaluate effectiveness [12, 14], but these are subjective and may cause mis-assessment. Since this assessment method is based on symptoms, evaluation of therapeutic effectiveness cannot be carried out until at least 3 months after treatment, which is time-consuming and may lead to delayed re-treatment. Thus, it is important to find a new non-invasive and quantitative assessment method to help the gynecologist evaluate therapeutic response in a timely manner.

Ultrasound interacts with biological tissue through both thermal and mechanical mechanisms [23–25]. The biological effects of ultrasound pulses are determined by both ultrasound beam parameters and tissue property alterations [26]. Considering the changes of thermal and optical properties during HIFU treatment, infrared (IR)-thermography-based methods and spectral imaging-based methods are expected to serve as viable solutions for quantitative assessment of HIFU-induced tissue injuries.

Classical IR-thermography has been widely applied for medical diagnostics of burns and wounds by measuring the surface temperature distribution of the target area [27–30]. However, the distribution of temperature on a patient may be strongly affected by physiological and environmental conditions. In active dynamic IR thermal imaging (ADT), an external excitation source is used to induce thermal transient processes in a tested object in order to retrieve the thermal properties of tissue, such as its conductivity, diffusivity, and equivalent thermal time constant, with reduced artifacts of temperature fluctuations [27, 28]. Since the main mechanisms of HIFU treatment for VLS are thermal effects, which cause temperature increase in the vulvar skin [23, 24], the ADT method, which shows changes in tissue thermal properties instead of changes in temperature distribution, can be used for quantitative objective assessment of HIFU treatment efficacy.

In addition to measuring the changes in thermal properties by the ADT method, detecting the changes in optical properties by a spectral imaging method seems to be a promising alternative to evaluate the efficacy of HIFU treatment for VLS. Hyperspectral imaging (HSI) is an emerging technique that can provide both spatial and spectral information for an object. Recently, it has been widely used for measurements of specific chromophores within skin tissue for thermal injury assessment [31–33]. During HIFU treatment, both optical scattering and absorption coefficients increase as heat is applied to tissue [34]. HSI combines high spatial and spectral resolution in one modality, giving optical information on the target area. This makes it a promising tool for quantifying the changes in the optical properties of vulvar skin before and after HIFU treatment for therapeutic assessment.

In this paper, we investigate the feasibility of ADT with cold excitation and HSI as two individual objective and non-invasive optical methods for quick non-invasive assessment of the therapeutic response to HIFU in VLS based on the changes caused in tissue properties by HIFU treatment. To our knowledge, we are the first to propose such a prompt, non-invasive, and quantitative method for evaluation of HIFU treatment effectiveness in VLS patients.

# 2. MATERIALS AND METHODS

HIFU therapy is a treatment in which ultrasound is applied to the target skin, i.e., infected area. During this process, low-level thermal injury occurs so that parts of unhealthy tissues are destroyed. Thus, the treatment will change the physical properties of the target skin area, e.g., its thermal conductance, specific heat capacity, and absorption spectrum [34, 35]. Hence, by quantifying the difference between the values of the physical properties before and after HIFU treatment, the therapeutic response to HIFU treatment can be accessed. The study overview is shown in **Figure 1**.

## 2.1. Theory

### 2.1.1. Physical Principles of Focused Ultrasound Therapy

The working mechanisms of HIFU therapy can be divided into two categories: mechanical effects and thermal effects [23–25, 36]. Those two effects play equally important roles in the ablation of solid tumors. However, in the HIFU treatment for VLS, the

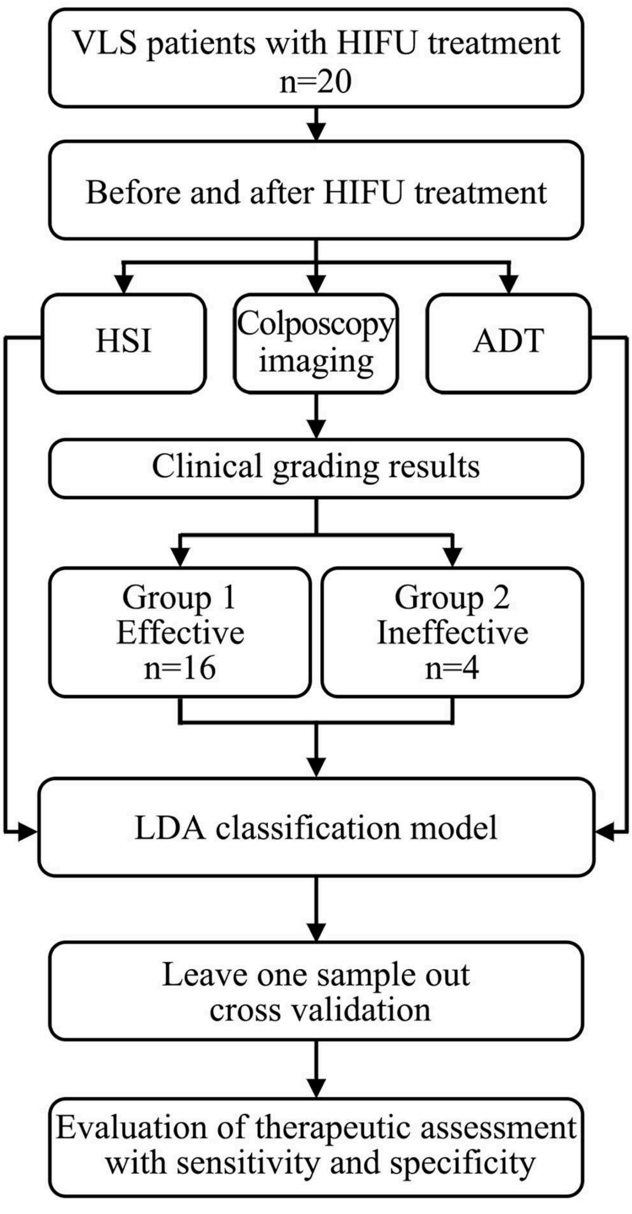

**FIGURE 1 |** Flow chart of this study, in which we explored the feasibility of the ADT and HSI methods for non-invasive and quantitative assessment of HIFU treatment for VLS.

focused intensity is much lower than that in regular HIFU treatment for cancers. The dominant effects may alter due to the reduction in sound intensity. To quantify the therapeutic outcome, it is necessary to identify the dominant physical effects during HIFU treatment for VLS.

### 2.1.2. Thermal Effects

When ultrasound is transmitted through tissue, the sound energy is absorbed by the medium and converts to thermal energy of the tissue. The heat generated can be expressed as ter Haar and Coussios [23]:

$$q = 2aIt \tag{1}$$

where $q$ is the heat generated (W/cm$^3$), $I$ is the intensity (W/cm$^2$), $a$ is the sound pressure absorption coefficient (cm$^{-1}$), and $t$ is the exposure time (s).

The relationship between $a$ and sound frequency $f$ can be approximated by the formula:

$$a = 0.026f^{1.1} \tag{2}$$

where the units of $f$ and $a$ are MHz and cm$^{-1}$, respectively.

Consequently, we have:

$$q = 0.052f^{1.1}It \tag{3}$$

The thermal effects are a function of the frequency of ultrasound. Under exposure to high-intensity ultrasound for a certain time, the temperature of tissue increases dramatically, which contributes to the denaturation of proteins and permanent damage of the focal zone so that lesions or tumor cells are killed. Consequently, the physical properties of the tissue, e.g., thermal conductivity, density, and heat capacity, alter owing to the thermal damage.

### 2.1.3. Mechanical Effects

The mechanical effect of ultrasound in a biomedical context is mainly a cavitation effect, which is ascribed to rapid changes in sound pressure [37]. During this process, the formation and blast of cavitation bubbles cause mechanical damage, and hence tissue ablations. To quantify the damage caused by the cavitation effect, the mechanical index ($MI$) is usually adopted [37]:

$$MI = P_{ra}/\sqrt{f_c} \tag{4}$$

where $P_{ra}$ is the peak negative pressure (MPa) and $f_c$ is the central frequency of the ultrasound wave (MHz).

A lower $MI$ indicates a lower degree of cavitation effect. A value lower than 0.5 is considered to indicate no bubble growth [37, 38], whereas 1.9 is considered to be the maximal threshold of no bioeffects, which is a value that is also adopted by the Food and Drug administration in its regulation for diagnostic ultrasound [37]. In regular HIFU treatment for cancers, which utilizes a high intensity of ultrasound, the cavitation effect plays an important role in curing lesions. However, the focal intensity of ultrasound in the VLS application is usually intermediate, as the goal is merely to stimulate the reconstruction and growth of tissues. To estimate the cavitation effect, 1,000 W/cm$^2$ of underwater intensity or 4.6 MPa of subsurface pressure is chosen. The derated peak negative pressure is then formulated as [39]:

$$P_{ra} = P_r exp(-0.0345f_c z) \tag{5}$$

where $P_r$ is measured peak negative sound pressure, which is usually assessed underwater, -0.0345 Np/(cm· MHz) is the attenuation factor used to obtain the approximate pressure in tissue, and $z$ is the distance from the transducer.

In the HIFU treatment for VLS, the *MI* of ultrasound is estimated to be 1.5, which is less than the threshold of noticeable bioeffect. Therefore, in VLS treatment, the cavitation effect can be ignored. The treatment efficacy is mainly ascribed to the thermal effect of ultrasound. Therefore, the quantified thermal effect is applied as the index of treatment performance in the rest of this paper.

### 2.1.4. Active Dynamic Thermal Imaging (ADT)

It has been widely accepted that thermal damage is dependent on duration of exposure to the heat source and radiation power. Henriques utilized an Arrhenius equation to describe damage to the tissues [40]:

$$\omega = Aexp(-\frac{E}{RT}) \tag{6}$$

$\omega$ is the reaction rate, $A$ is frequency factor, $E$ is activation energy, $R$ is the universal gas factor, and $T$ is temperature. The total degree of tissue injury $\Omega$ is the integration of $\omega$:

$$\Omega = A\int_0^t exp(-\frac{E}{RT})dt \tag{7}$$

Since skin treated by HIFU suffers thermal injury, the variation of thermal properties can be implemented to quantify how effective the treatment. In our case, we first exert cold excitation to the target area and then remove the cold source and have the skin warm up. The advantage of taking this approach is that such a procedure is a routine in HIFU therapy of VLS. Therefore, no redundant steps are added during treatment. The general governing equation for heat transfer in this process is described by Pennes' equation [41]:

$$\frac{\partial T(x,t)}{\partial t} = \nabla(k\nabla T) + q_s + q_p + q_m \tag{8}$$

In our case, Buettner simplifies the equation by assuming [42, 43]:

1) The temperature is just a function of depth and time.
2) Heat convection to the air is negligible.
3) Material constants are uniform in time and space.
4) There is a linear temperature profile at the skin surface before the cold source is removed.
5) The temperature at depth $d$ remains constant.

Then, the equation is simplified as 1-D heat transfer equation:

$$\frac{\partial T(x,t)}{\partial t} = \frac{k}{\rho c}\frac{\partial^2 T}{\partial x^2} \tag{9}$$

with the boundary condition:

$$T(x,0) = T_0 - T_s(1-\frac{x}{d}), \text{ where t = 0, x} \leq \text{d} \tag{10}$$

$$T(d,t) = T_0, \text{ where t} \geq 0 \tag{11}$$

$$\frac{\partial T}{\partial x}(0,t) = 0, \text{ where t} \geq 0 \tag{12}$$

By plugging in the boundary condition and using an inverse Fourier transformation, we finally obtain:

$$T(x,t) = T_0 - \frac{8T_s}{\pi^2}\sum_{n=0}^{\infty} exp(-\frac{(2n+1)^2\pi^2\frac{k}{\rho c}}{4d^2}t)cos(\frac{(2n+1)\pi}{2d}x) \tag{13}$$

In our study, we only investigate the superficial temperature response after removing the cold source, and, for ease of analysis, only three terms of the series survive. That is:

$$T(0,t) = T_0 - \frac{8T_s}{\pi^2}(exp(-\frac{t}{\tau}) + \frac{1}{9}exp(-\frac{9t}{\tau}) + \frac{1}{25}exp(-\frac{25t}{\tau})) \tag{14}$$

where,

$$\tau = \frac{4d^2\rho c}{\pi^2 k} \tag{15}$$

Here, we use $\tau$ to represent the time it takes for the skin surface temperature to stabilize. This depends on the density, thermal conductivity, heat capacity, and depth of the target skin domain. However, since the before-mentioned parameters vary considerably among patients, it does not suffice to infer the treatment level just by measuring post treatment $\tau$. An alternative is to use the difference between pre-treatment and post-treatment $\tau$. In our study, we adopt effective damage rate $e$:

$$e = \frac{\tau_{ref} - \tau}{\tau_{ref}} \tag{16}$$

where $\tau_{ref}$ is $\tau$ of the affected vulvar area before treatment as a reference to calculate the effective damage rate $e$ and $\tau$ corresponds to the affected area after treatment. To reduce the noise of raw data, the following model is utilized:

$$G(0,t) = \int_0^t \frac{T(0,\hat{t})}{t} d\hat{t} \tag{17}$$

i.e.,

$$G(0,t) = T_0 - \frac{8T_s\tau}{\pi^2 t}((1-exp(-\frac{t}{\tau})) + \frac{1}{81}(1-exp(-\frac{9t}{\tau})) + \frac{1}{625}(1-exp(-\frac{25t}{\tau}))) \tag{18}$$

To fit the model, we take the average of raw data to time, then input the post-processed data into Equation (18).

### 2.1.5. Hyperspectral Imaging (HSI)

Reflection, scattering, and absorption are the optical properties affecting the nature of the interaction of ultrasound with biological tissues [34]. In this paper, we used the visible range for measurement, in which melanin and different types of hemoglobin are mainly considered to identify the optical properties of skin tissue [44–48]. Changes in the content of these absorbents will affect the diffuse reflectance of the skin tissue [49]. Thus, by analyzing the diffuse reflectance spectrum of the skin tissue before and after HIFU treatment, it is possible to determine how the content of different components changes in the skin tissue, which will be a potential tool for therapeutic assessment. According to the characteristic peaks of the spectra of the treated areas before and after HIFU treatment, oxy-hemoglobin(HbO2), deoxy-hemoglobin(Hb), and methemoglobin (mHb) were used as the three main absorption components for further analysis.

The absorption spectrum $A(\lambda)$ in a skin model of N chromophores would be Equation (19) [17, 50]:

$$A(\lambda) = \sum_{i=1}^{N} C_i a_i(\lambda) + G(\lambda) \tag{19}$$

where $a_i$ is the absorption spectrum of each chromophore in tissues, $C_i$ is the corresponding contribution of each chromophore, and $G(\lambda)$ is used to take into account attenuation due to scattering. The average content of each component, defined as the feature index ($FI$), can then be calculated as Equation (20).

$$FI_i = \frac{\overline{C_i a_i}}{\bar{A}} \tag{20}$$

where $\overline{C_i a_i}$ is the average absorption contributed by component $i$ and $FI_i$ is the corresponding contribution feature index ($FI$).

#### 2.1.6. Patients and HIFU Treatment

This clinical trial was conducted in the Second Affiliated Hospital of Chongqing Medical University according to the protocol approved by the Institutional Review Board (IRB) of the Second Affiliated Hospital of Chongqing Medical University (IRB No: 2018KLS092). Each participant signed an informed consent document before enrolment. From December 2018 to March 2019, 20 female participants aging from 19 to 51 years with histological diagnoses of VLS were included in the study. Their disease duration was from 2 months to 4 years. No participant had received any treatment in the 3 months preceding HIFU treatment. Women who were pregnant or who had accompanying gynecologic diseases were excluded from the study.

The HIFU machine used was a Model CZF-300 manufactured by Chongqing Haifu Medical Technology Co., Ltd., Chongqing, China. It comprised a user console, the main system, a water cabinet, an electric control part, and a therapeutic transducer, as described by [12]. The frequency of the transducer is from 8 to 12 MHz, and its power ranges from 3.0 to 4.7 W. The probe was in contact with the lesion area via an ultrasound coupling and performed consecutive scanning at a speed of 3–5 mm/s. The treatment lasted from 15 to 30 min, depending on lesion size and skin reaction during treatment. For post-treatment management, ice packs were intermittently applied to affected skin (5 min ice application at 5 min intervals) within the first 24 h, and moist burn ointment was applied locally for a week.

## 2.2. Clinical Data Collection

Every patient's conditions, including itching and skin lesion appearance, were reported, and RGB images of the vulva were captured by colposcopy before and after HIFU treatment as clinical routines. In our experiment, before and immediately after the HIFU treatment, both the ADT and HSI methods were used for a quick quantitative evaluation of therapeutic response to HIFU. The full process is presented in **Figure 2**.

### 2.2.1. Active Dynamic Thermal Imaging (ADT)

To achieve high accuracy, the experiments were conducted in an air-conditioned operation room. The temperature and humidity in the room were respectively in the range of 22–23°C and 45–55%. An ice pack was applied to the entire vulva. Typically, the cooling phase lasted for 30–60 s, until the surface temperature of the vulva reached the temperature of the room. The self-warming phase equaled three times the cooling time. When the ice pack was removed from the vulva, a thermography IR camera (FLIR T460) with a high thermal resolution of 0.03 degrees was used to record the surface temperature of the vulva at a speed of 30 frames/s. Its thermal range for detection is 7.5–13 $\mu$m. The ice pack was only used once for cold excitation and was used again for the subsequent post-treatment management.

### 2.2.2. Hyperspectral Imaging (HSI)

A Brimrose hyperspectral imager (Brimrose, Sparks, Maryland) with a 500-Watt continuous white light source (Xenon Lamp Source, Beijing Optical Century Instrument Co., CHINA) was used to produce hyperspectral images of the target area from 450 to 650 nm with an internal of 2 nm [51, 52], as shown in **Figure 6A**.

## 2.3. Data Processing

### 2.3.1. Clinical Evaluation Method for HIFU Treatment Efficacy

Therapeutic response to HIFU was graded by a clinical scoring method, as shown in **Table 1** [20–22]. All patients were followed up on by the same gynecologist once per month for the next 3 months (defined as short term), and each patient's condition before and after treatment was reported as clinical scores. Then, the therapeutic index was obtained: [(score before the treatment-score after treatment)/score before treatment] ×100%. The results were as follows:

1) Cured (Therapeutic index $\geq$ 90%);
2) Effective (Therapeutic index: 21–89%);
3) Ineffective (Therapeutic index $\leq$ 20%);

### 2.3.2. Image Registration

Though all enrolled patients were required to keep still for the acquisition of images of the vulva during data collection, image shifting was expected, which could introduce errors into the subsequent data analysis. In this paper, we used an improved SIFT (Scale Invariant Feature Transform) registration algorithm for image registration.

The traditional SIFT algorithm proposed by Lowe [53] has been widely used in video stabilization. In the SIFT method, the criterion for selecting feature points is to detect blobs in a frame. In our case, we focus on slow and accumulated movement. Thus, each frame has the same importance in the frame reconstruction. For example, in frame I, we first get all the SIFT descriptors from encompassing blobbed points. Then, the

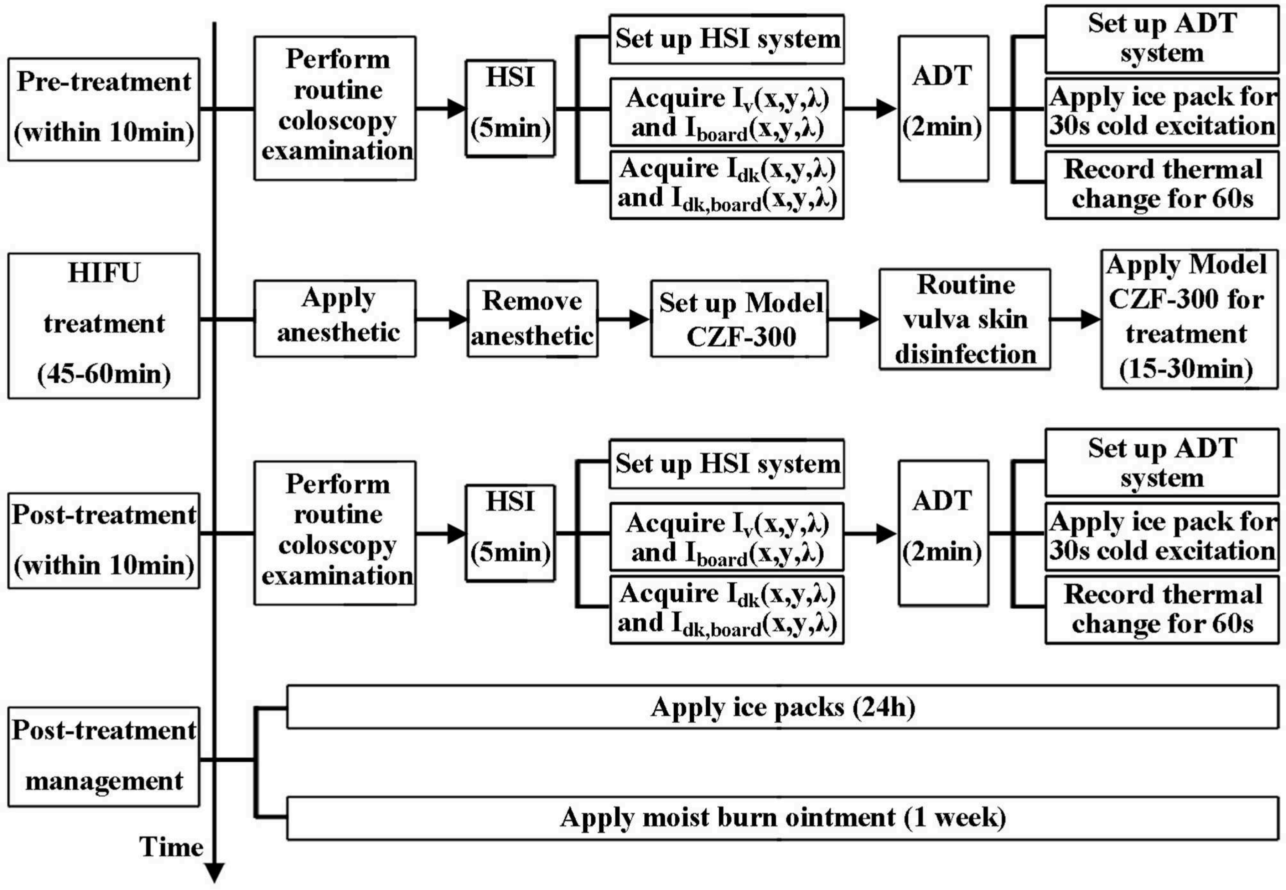

**FIGURE 2 |** Flow chart of the clinical data collection process.

**TABLE 1 |** Clinical evaluation method for HIFU treatment efficacy.

| Scores | Itch | Skin elasticity | Skin color |
|---|---|---|---|
| 0 | No | Good | Normal |
| 1 | Temporary | Ordinary | Depigmented |
| 2 | Ordinary | Bad | Pink |
| 3 | Severe | Chapped skin | White |

distances between those points to those in the previous frame are calculated. For each point, the point pairs with the least distance and less than a preset threshold will be preserved as matched feature points.

A flow chart showing the specifics of its implementation in this study is presented in **Figure 3** and comprised the following steps:

1) Calculating the Gauss convolution of the logarithms of the temperature frames to construct an image Pyramid.
2) Detecting the extremum of pixel interpolation in a 4 × 4 area and leaving out the low response points or the sharp points.
3) Describing feature points. **Figure 4A** shows an example of feature points in two frames.
4) Numerous feature points were found in each frame after step 1, step 2, and step 3. By adding a localization limitation that loosens as the time difference increases, we can get matched sets and their match degrees. The matched point sets are shown in **Figure 4B**.
5) Initializing the movement weight matrix as a null matrix.
6) Calculating the movement weight matrix from the best-matched point sets. If the movement exceeds $3\sigma$ of the expected movement, the set of points will be neglected. Using a linear insertion method to fill in the movement weight matrix.
7) Finally, rebuilding the frames with the movement weight matrix.

The result of the image registration is presented in **Figure 4**. **Figure 4C** shows the reconstructed temperature image after image registration. The number of feature points is not specified. The initial movement weight matrix is a null matrix, and the matched points change the weight matrix. Aside from the matched points, the weight matrix is filled by linear interpolation. If there was a frame with no matched point, its movement matrix would be evaluated by the linear interpolation between its prior and subsequent matrices.

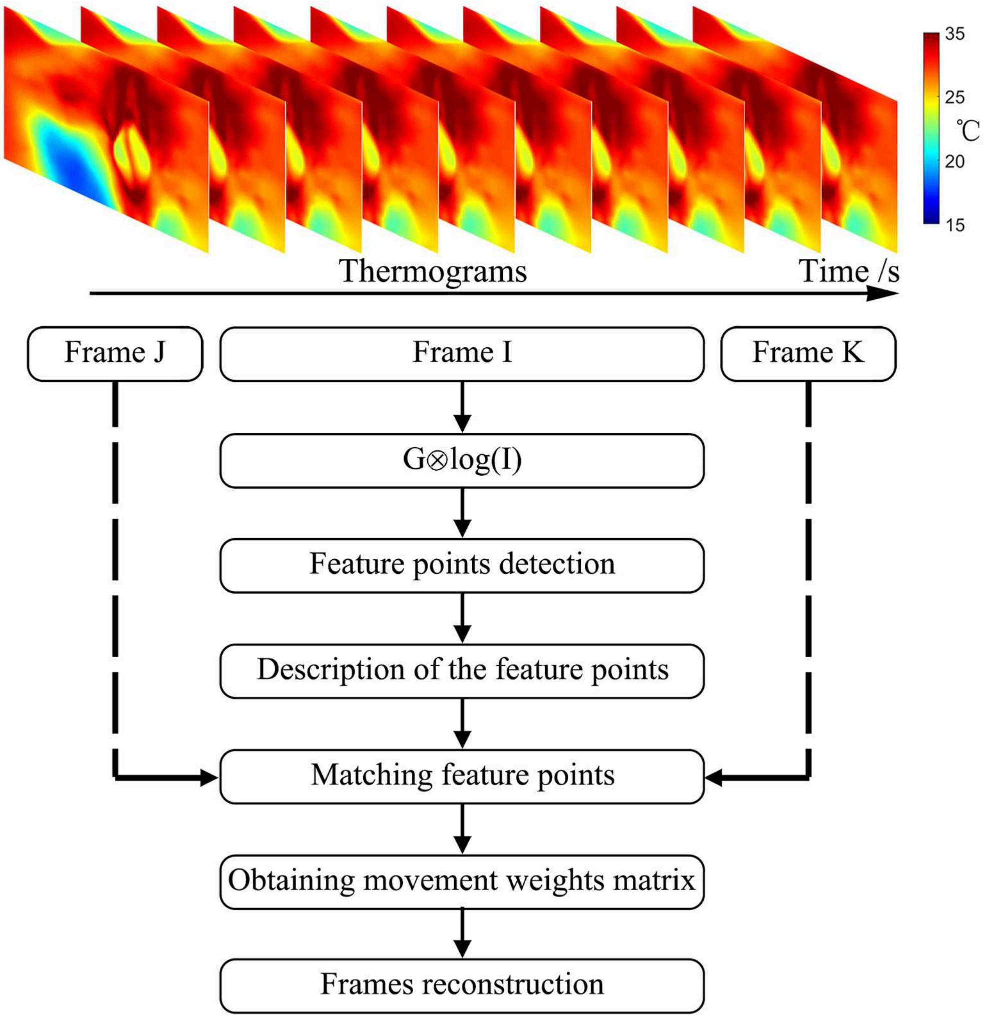

**FIGURE 3 |** Flow chart of imaging registration.

### 2.3.3. Effective Damage Rate *e* From Active Dynamic Thermal Imaging (ADT)

In the ADT method, after the image registration process, we traced the temperature in every 2×2 pixels ROI of the vulva surface for every frame for the treatment areas, taken during the self-heating phase (after the cooling phase). This procedure is illustrated in **Figure 5**.

1) Acquiring the raw temperature curve vs. time $T(0, t)$ for each ROI.
2) Reducing the noise of raw data by integrating as in Equation (17).
3) Calculating thermal time constant $\tau_{ref}$ for each ROt by fitting $G(0, t)$ as in Equation (18).
4) Calculating thermal time constant $\tau$ for each ROI by fitting $G(0, t)$ as in Equation (18).
5) Calculating effective damage rate $e$ for each ROI with Equation (16).
6) Plotting a histogram of the effective damage rate $e$ of the selected treatment areas.
7) Extracting effective damage rates $e$ less than a $3\sigma$ lower limit in the histogram and calculating the average of the extracted $e$.

### 2.3.4. Entropy of Feature Index [*H*(*FI*)] From Hyperspectral Imaging (HSI)

The absorption spectrum of the affected vulvar skin was extracted at every 1×1 pixel for each patient. The reflectance spectrum $R(x, y, \lambda)$ is corrected by a standard NIST traceable white diffuser (NIST, Gaithersburg, Maryland) with Equation (21), as shown in **Figures 6B,C**:

$$R(x, y, \lambda) = \frac{\bar{I}_v(x, y, \lambda) - I_{dk}(x, y, \lambda)}{\bar{I}_{board}(x, y, \lambda) - I_{dk,board}(x, y, \lambda)} \tag{21}$$

where $I_v(x, y, \lambda)$ is the reflection intensity of the skin in band $\lambda$ at point (x, y), and $I_{board}(x, y, \lambda)$ is the reflection intensity of a PTFE

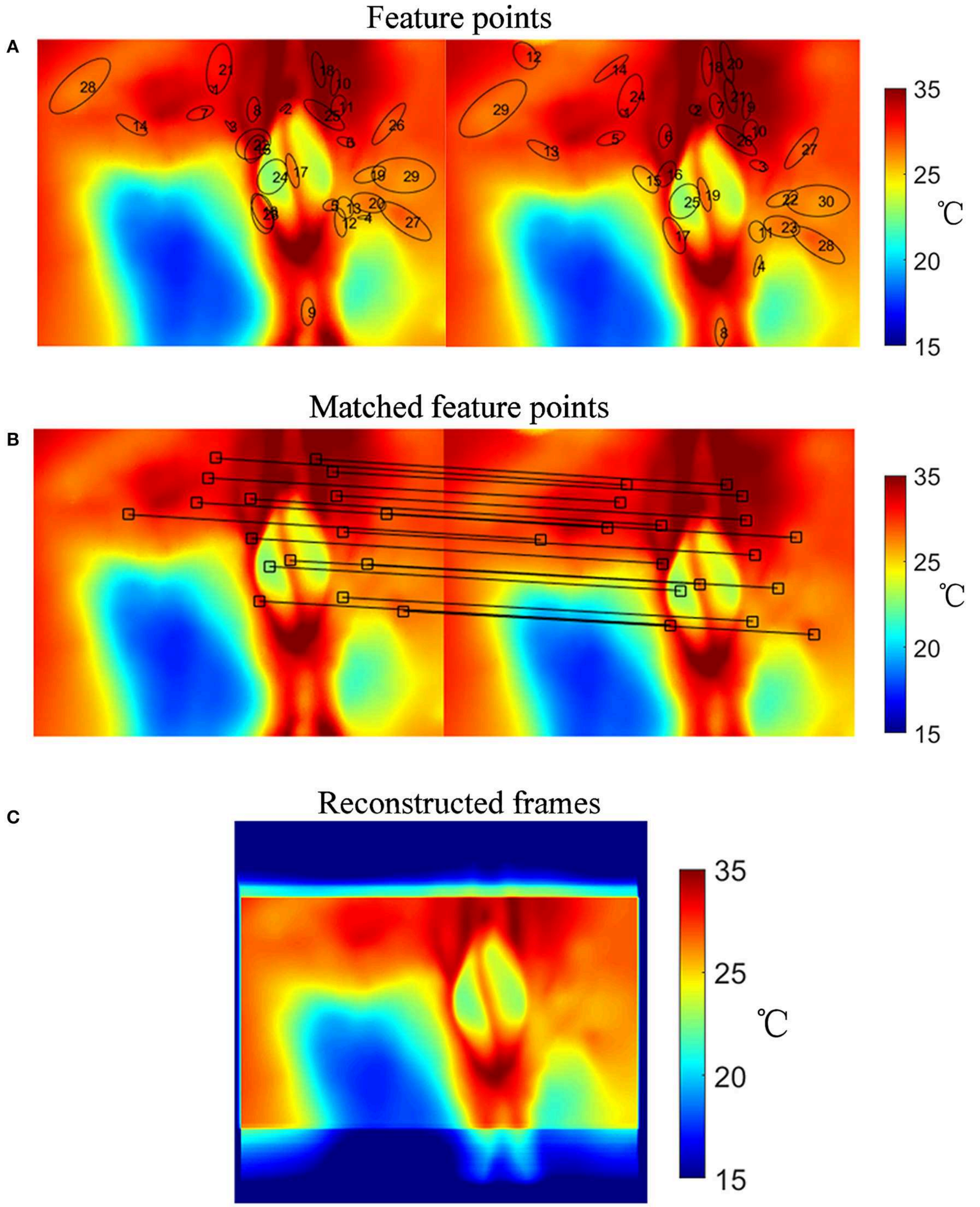

**FIGURE 4 |** Image registration procedure. **(A)** Selected feature points in frames. **(B)** Matched point sets. **(C)** Reconstructed temperature image after image registration.

board covering the skin in band λ at point (x, y). There are two ways of acquiring the dark frames for reflectance correction. One is to keep the lens covered during exposure [54] and the other is to switch off the light source [48]. In our study, the dark frames, $I_{dk}(x, y, \lambda)$ and $I_{dk,board}(x, y, \lambda)$, are measured with the light source switched off [48].

The absorption spectrum is given by Equation (22):

$$A_{x,y}(\lambda) = -\log_{10}\left(R_{x,y}(\lambda)\right) \tag{22}$$

For quantifying the difference in the absorption spectrum between the effective treatment group and the ineffective

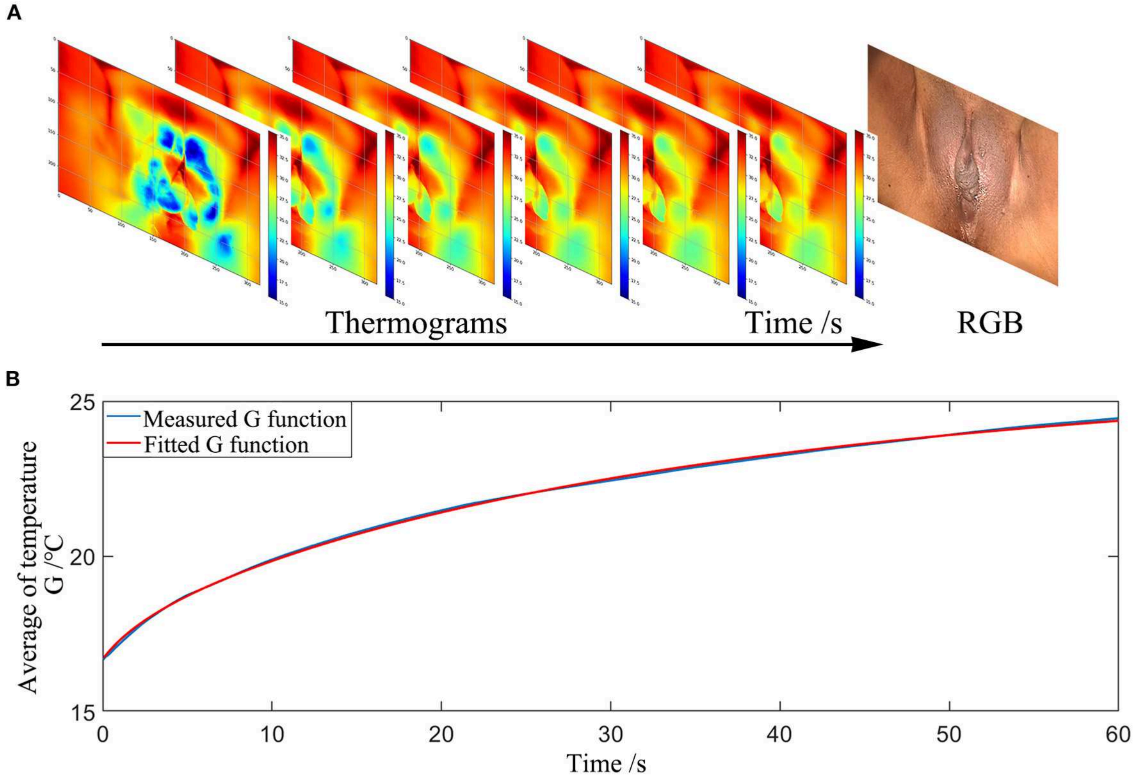

**FIGURE 5 |** Measurement procedures of the ADT method **(A)** Thermograms of the temperature distribution at the surface of the vulvar skin recorded over time. **(B)** The average temperature trend of a selected area during the self-warming phase.

treatment group, three independent features were selected according to the absorption curves of the treated areas before and after HIFU treatment. The index of each feature was calculated by the least-squares method as in Equations (19, 20). We used the entropy $H(FI)$ of each feature index for further classification, which calculates the amount of uncertainty of a random variable. It is defined as follows:

$$H(FI_i) = -\sum_{k=1}^{n} p\left(\mathrm{FI_{ik}}\right) \log_{10} p\left(\mathrm{FI_{ik}}\right) \tag{23}$$

### 2.3.5. Statistical Analysis

Data were analyzed using MATLAB software. We adopted a linear discriminant analysis (LDA) algorithm to classify the HIFU patient into two types: effective and ineffective treatment. The classification ability of both the ADT and HSI methods to detect whether the HIFU treatment was from a patient with effective treatment (group 1) or ineffective treatment (group 2) were evaluated using leave-one-out cross-validation to reduce the probability of a type 1 error (false positive). The statistical significance of any observed difference was analyzed by the Hotelling $T^2$-test. Statistical significance was defined as $P < 0.05$.

# 3. RESULTS

## 3.1. Clinical Evaluation for 20 HIFU Patients

A total of 20 patients with a 100% follow-up rate were followed up for 3 months. Complete data on the clinical therapeutic effects in all patients were obtained and are shown in **Table 2**: group 1 comprised 16 HIFU patients with effective HIFU treatment, and group 2 comprised 4 HIFU patients with ineffective HIFU treatment.

### 3.1.1. Thermal Time Constant $\tau$ Between Effective and Ineffective HIFU Treatment Groups

The statistical results of thermal time constant $\tau$ are presented in **Figure 7C**. $\tau_{ref}^{Effective}$, defined as $\tau$ measured before HIFU treatment in effective treatment group (group 1) showed statistical difference ($P < 0.05$) compared with $\tau^{Effective}$ measured immediately after HIFU treatment in group 1. However, for the ineffective treatment group (group 2), $\tau_{ref}^{Ineffective}$ and $\tau^{Ineffective}$ did not show statistical difference ($P > 0.1$).

### 3.1.2. Effective Damage Rate *e* Between Effective and Ineffective HIFU Treatment Groups

**Figure 7A** show histograms of $e$ between an effective HIFU patient $\mathrm{P}_{19}$ and an ineffective HIFU patient $\mathrm{P}_{15}$. Here, we used $e$ values less than a $3\sigma$ lower limit to calculate the average $e$. The

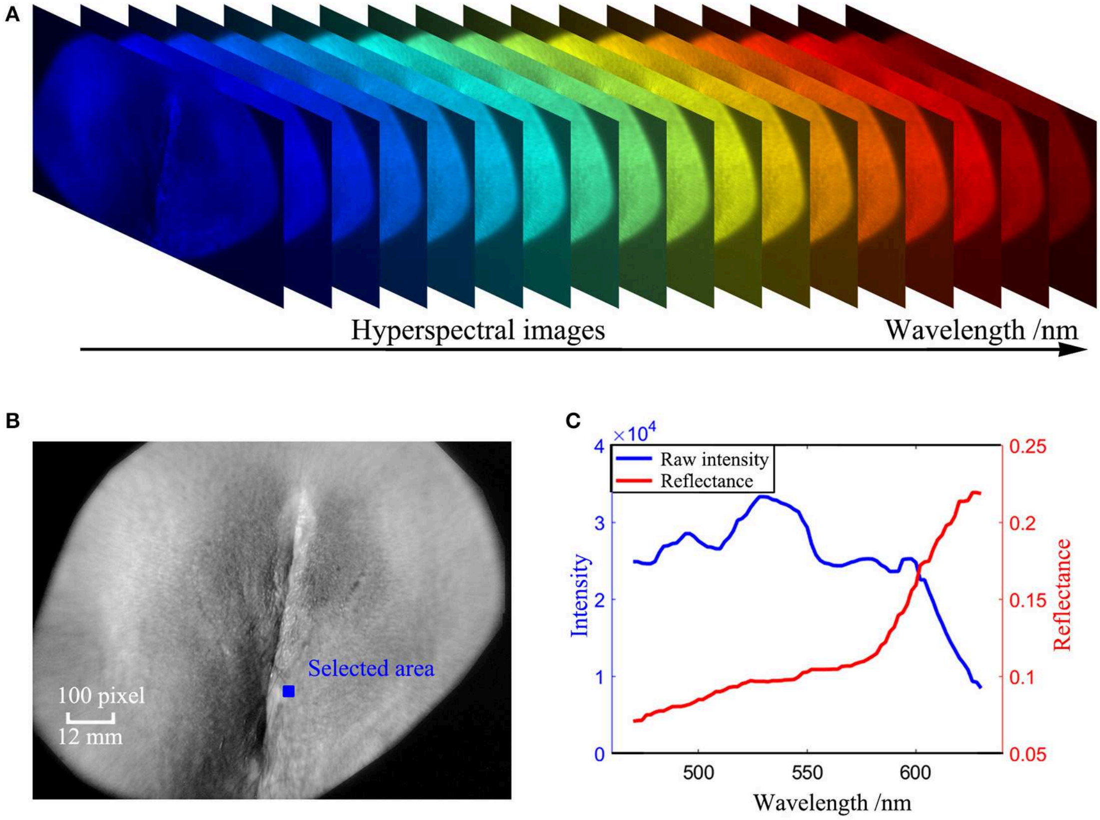

**FIGURE 6 |** Measurement procedures of the HSI method **(A)** Hyperspectral images of the vulva captured in the wavelength range 450 nm to 650 nm. **(B)** A hyperspectral image of the vulva at a single wavelength of 550 nm after image registration. **(C)** absorption spectrum retrieved from the blue area in **(B)**.

average *e* of effective treatments was significantly higher than that of ineffective treatment groups in **Figures 7B,C** ($P < 0.05$).

## 3.2. Hyperspectral Imaging (HSI) for 20 HIFU Patients

### 3.2.1. Reflectance Absorption Spectra Between Effective and Ineffective HIFU Treatment Groups

**Figure 8** shows the hyperspectral results of one effective HIFU treatment patient $P_{15}$ and one ineffective HIFU treatment patient $P_{19}$. **Figure 8A** shows an RGB image of $P_{15}$ captured by colposcopy and the corresponding hyperspectral image at a single wavelength of 550 nm before HIFU treatment. **Figure 8B** shows an RGB image of $P_{15}$ captured by colposcopy and the corresponding hyperspectral image at a single wavelength of 550 nm immediately after HIFU treatment. **Figure 8D** shows an RGB image of $P_{19}$ captured by colposcopy and the corresponding hyperspectral image at a single wavelength of 550 nm before HIFU treatment. **Figure 8E** shows an RGB image of $P_{19}$ captured by colposcopy and the corresponding hyperspectral image at a single wavelength of 550 nm immediately after HIFU treatment. The red cycles in **Figures 8A,B,D,E** were the general treatment areas marked by an experienced gynecologist. After image registration, the corresponding treatment areas were selected in every hyperspectral image from 450 to 650 nm with an interval of 2 nm, shown in **Figures 8A,B,D,E**. A few biases may occur between the marked ROI in colposcopy and the selected ROI in hyperspectral images. However, for VLS, the affected areas usually cover more than 80% of the whole vulva and so are not difficult to recognize. Despite the possible small differences, the ROI in the hyperspectral images has included most of the general treatment areas. In this paper, we explored the absorption spectrum of the affected labia majora. For further analysis, $6 \times 10^4$ ROIs of a size of $1 \times 1$ pixel within the treatment areas of the labia majora of every patient were selected randomly. **Figures 8C,F** show the reflectance absorption curves of all selected ROIs for $P_{15}$ and $P_{19}$. The blue curves are averaged reflectance absorption spectra of the $6 \times 10^4$ ROIs before HIFU treatment, and the red ones are averaged curves immediately after HIFU treatment. There is a new peak around 630 nm in the red curve after HIFU treatment compared with the blue one in both $P_{15}$ and $P_{19}$. However, the peak for $P_{15}$ is more recognizable than that for $P_{19}$.

### 3.2.2. Feature Index (*FI*) Between Effective and Ineffective HIFU Treatment Groups

The histograms of $(FI_1, FI_2, FI_3)$ extracted from absorption spectrum curves are shown in **Figure 9**. The blue histograms in **Figures 9A–F** are for $(FI_1, FI_2, FI_3)$ before HIFU treatment, and the red ones represent the results immediately after HIFU

**TABLE 2** | Clinical grading results of HIFU treatment.

| Patient | Age (years) | HIFU dose (J) | Pre-grading score before HIFU treatment | Post-grading score 3 months after HIFU treatment | Therapeutic index(%) | Therapeutic response |
|---|---|---|---|---|---|---|
| $P_1$ | 44 | 5,417 | 6 | 3 | 50% | Effective |
| $P_2$ | 36 | 3,215 | 5 | 3 | 40% | Effective |
| $P_3$ | 30 | 5,067 | 8 | 3 | 62.5% | Effective |
| $P_4$ | 19 | 4,292 | 6 | 3 | 50% | Effective |
| $P_5$ | 35 | 4,817 | 9 | 6 | 33.3% | Effective |
| $P_6$ | 30 | 4,557 | 8 | 6 | 25% | Effective |
| $P_7$ | 22 | 4,410 | 5 | 3 | 40% | Effective |
| $P_8$ | 51 | 4,807 | 7 | 5 | 28.6% | Effective |
| $P_9$ | 28 | 4,965 | 7 | 5 | 28.6% | Effective |
| $P_{10}$ | 20 | 4,045 | 7 | 3 | 57.1% | Effective |
| $P_{11}$ | 44 | 4,892 | 4 | 3 | 25% | Effective |
| $P_{12}$ | 35 | 4,865 | 6 | 4 | 33.3% | Effective |
| $P_{13}$ | 50 | 4,490 | 7 | 5 | 28.6% | Effective |
| $P_{14}$ | 42 | 4,790 | 4 | 3 | 25% | Effective |
| $P_{15}$ | 27 | 4,480 | 8 | 5 | 37.5% | Effective |
| $P_{16}$ | 26 | 4,705 | 7 | 4 | 42.9% | Effective |
| $P_{17}$ | 50 | 4,112 | 8 | 9 | 12.5% | Ineffective |
| $P_{18}$ | 51 | 3,047 | 4 | 4 | 0% | Ineffective |
| $P_{19}$ | 22 | 4,230 | 6 | 7 | 16.7% | Ineffective |
| $P_{20}$ | 31 | 4,012 | 5 | 4 | 20% | Ineffective |

treatment. The histogram of each index from $P_{15}$ immediately after HIFU treatment became wider than the histogram before the treatment and compared with $P_{19}$.

### 3.2.3. Entropy *H*(*FI*) Between Effective and Ineffective HIFU Treatment Groups

For additional analysis of the histograms, we calculated the entropy $H(FI)$ of the index histogram of each feature as $H(FI_1), H(FI_2)$, and $H(FI_3)$. **Figure 10** presents box plots of $[H(FI_1), H(FI_2), H(FI_3)]$ of all 20 HIFU patients before and immediately after HIFU treatment. The effective group was significantly different from the ineffective group after HIFU treatment ($P < 0.05$), while the two groups did not show significant difference before HIFU treatment ($P > 0.1$).

## 3.3. Therapeutic Assessment for 20 HIFU Patients by the ADT and HSI Methods

We used a leave-one-out LDA model to evaluate the performance of both the average $e$ and $[H(FI_1), H(FI_2), H(FI_3)]$ of all 20 patients for therapeutic assessment of HIFU treatment. The results were very promising, with a high sensitivity of 100% and specificity of 100% for the ADT method and of 75% and 87.5%, respectively, for the HSI method.

## 4. DISCUSSION

During HIFU treatment for VLS, the ultrasound beams are focused on the target about 4–6 mm under the skin. The vulvar skin can be easily damaged by this exposure. The main possible side effects due to exposure may be superficial local skin burns and superficial ulcers [16]. However, the estimation of damage is difficult because it requires subjective inspection by skillful physicians. Excessive thermal damage of tissue leads to tissue charring. Insufficient heat will lead to an increased risk of recurrence of VLS. During the HIFU treatment process, vulvar tissues undergo both microscopic and macroscopic changes in their structures and physiological properties. Monitoring such changes would be a direct means of estimating the extent of thermal damage. Thus, an objective index of skin properties is needed. Numerous factors (such as surface temperature and reflectance) are used to evaluate skin properties. In this study, we focus on both the absorption reflection and thermal time constant $\tau$ of affected vulvar skin for therapeutic assessment of HIFU for VLS.

For the ineffective treatment group, $\tau_{ref}^{Ineffective}$, defined as $\tau$ measured before HIFU treatment, showed no statistical difference ($P > 0.1$) from $\tau^{Ineffective}$, measured immediately after HIFU treatment. However, for the effective treatment group, $\tau^{Effective}$ decreased to a statistically different level ($P < 0.05$), compared with $\tau_{ref}^{Effective}$. These results indicated that different HIFU treatments led to a different extents of thermal damage for each patient, resulting in a distinct change in thermal properties.

Thus, we proposed a new parameter, effective damage rate $e$ (as in Equation 16), to quantify the degree of thermal damage for each HIFU treatment. The histogram of $e$ from an effectively treated patient was separated from that of an ineffectively treated patient, shown in **Figure 7A**. However, it was improper to use the average $e$ of the whole histogram to represent each HIFU treatment for effectiveness classification, because ineffective treatment of a patient does not imply that all

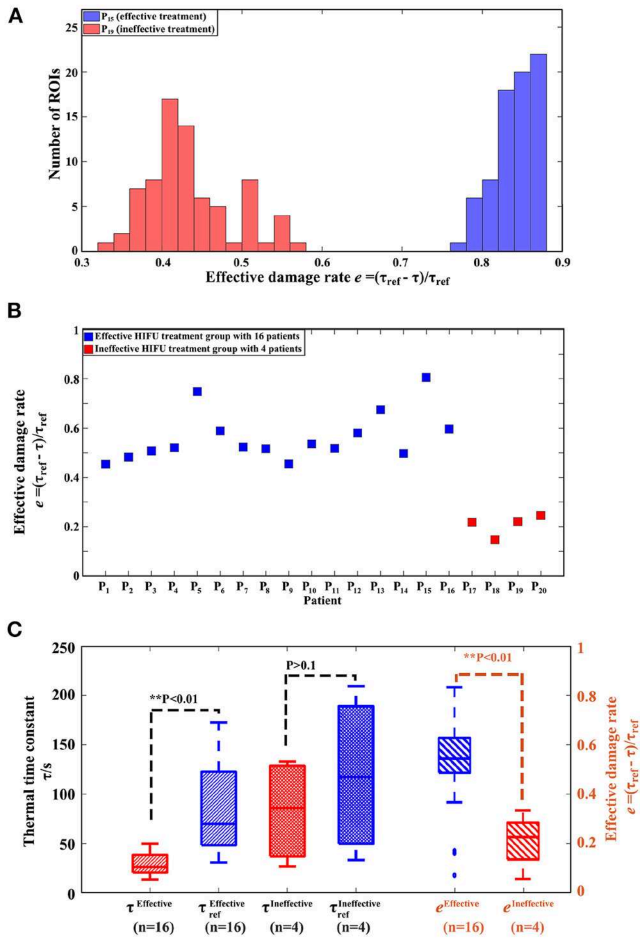

**FIGURE 7 |** Results of the ADT method. **(A)** Histogram of effective damage rate *e* from one patient ($P_{15}$) with effective treatment and one patient ($P_{19}$) with ineffective treatment. **(B)** Effective damage rate *e* of all patients. **(C)** Boxplot of the thermal time constant $\tau$, $\tau_{ref}$ and effective damage rate *e* from the effective treatment group with 16 patients and the ineffective treatment group with 4 patients. Note: $\tau_{ref}$ is the thermal time constant of the treatment area measured before HIFU treatment, while $\tau$ of the same area is measured immediately after HIFU treatment.

treated skin areas undergo insufficient HIFU treatment. In the ineffective case where 60–70% of the infected areas were treated effectively, the direct average *e* could also be large, which would be difficult to be distinguished from effective treatment. A better criterion is to use *e* from the relatively less-treated area instead of the whole treated area. Considering this, we took the average of *e* values smaller than a $3\sigma$ lower limit to represent the lower bound of the degree of thermal damage for each treatment so that the bias introduced by the areas with effective treatment in an ineffective treatment could be reduced. The effective treatment group had a larger average *e* than the ineffective treatment group at a statistically different level ($P < 0.05$), which showed that the index was positively related to the degree of thermal damage and could be used for therapy effectiveness classification.

Before HIFU treatment, the reflectance absorption spectra of the effective treatment group and the ineffective treatment group were similar. However, immediately after HIFU treatment, there was a new peak around 630 nm for both the effective treatment group and the ineffective treatment group, which did not appear in the absorption curves before treatment. The shoulder around the 630 nm region of absorption spectrum curves is specific to methemoglobin (mHb). The hemoglobin absorbance demonstrates a characteristic change following heat exposure. This change is partly due to oxidative reactions, with the formation of met-hemoglobin, and also by protein denaturation [55, 56], which may help in the study of the unclear etiology of VLS. In the HSI method, we used incident light in the visible wavelength range of 450–650 nm where melanin and different types of hemoglobin are dominant absorbers [44–48]. After comparing the reflectance spectra of the effective treatment group and the ineffective treatment group, we found that the primary spectral differences between these groups occur at the peak wavelength of oxy-hemoglobin ($HbO_2$), deoxy-hemoglobin (Hb), and methemoglobin (mHb). In order to simplify the analysis and highlight the spectral characteristics of effective treatment, we carried out absorption analysis in a human skin model with the assumption that HIFU-induced changes in scattering and other chromophores are secondary. We used $(H_1, H_2, H_3)$ extracted from the absorption curves to quantify the difference between an effective group and an ineffective group. There was no statistical difference in $[H(FI_1), H(FI_2), H(FI_3)]$ between the two groups before treatment ($P > 0.1$), which indicated that there was no significant difference in the optical properties of the enrolled 20 patients before HIFU treatment. However, they were significantly different after HIFU treatment ($P < 0.05$). Thus, the absorption properties of patients were changed differently by HIFU treatment, which can be utilized for treatment efficacy evaluation.

In our manuscript, a leave-one-out LDA model was used for classification, which is a relatively simple method for classifying both the ADT and HSI images and comparing the two imaging approaches quantitatively. Besides the LDA method, we have also tried SVM, K-means, and SAM for image classification with accuracies of 80, 100, and 80% for ADT and 80, 80, and 65% for his, respectively, which did not show better performance than LDA (100% for ADT and 85% for HSI). This lower performance is partially due to the unbalanced and relatively small dataset, which is suboptimal for implementing these machine learning methods. In order to enable those methods to be used, more data is necessary for future study and better classification performance.

Though the preliminary results are very encouraging, with a sensitivity of 100% and specificity of 100% for the ADT method and 75 and 87.5% for the HSI method, this study has several limitations. First, the sample size is small, and there is a lack of other vulvar diseases apart from VLS with HIFU treatment for comparison. Due to the limitation of sample size, the relatively high sensitivity and specificity results can only reveal the feasibility of the ADT and HSI methods for therapeutic assessment of HIFU treatment for VLS. More subjects will be recruited so that the sample size will be increased for further validation of their clinical performance in the future. Secondly, in

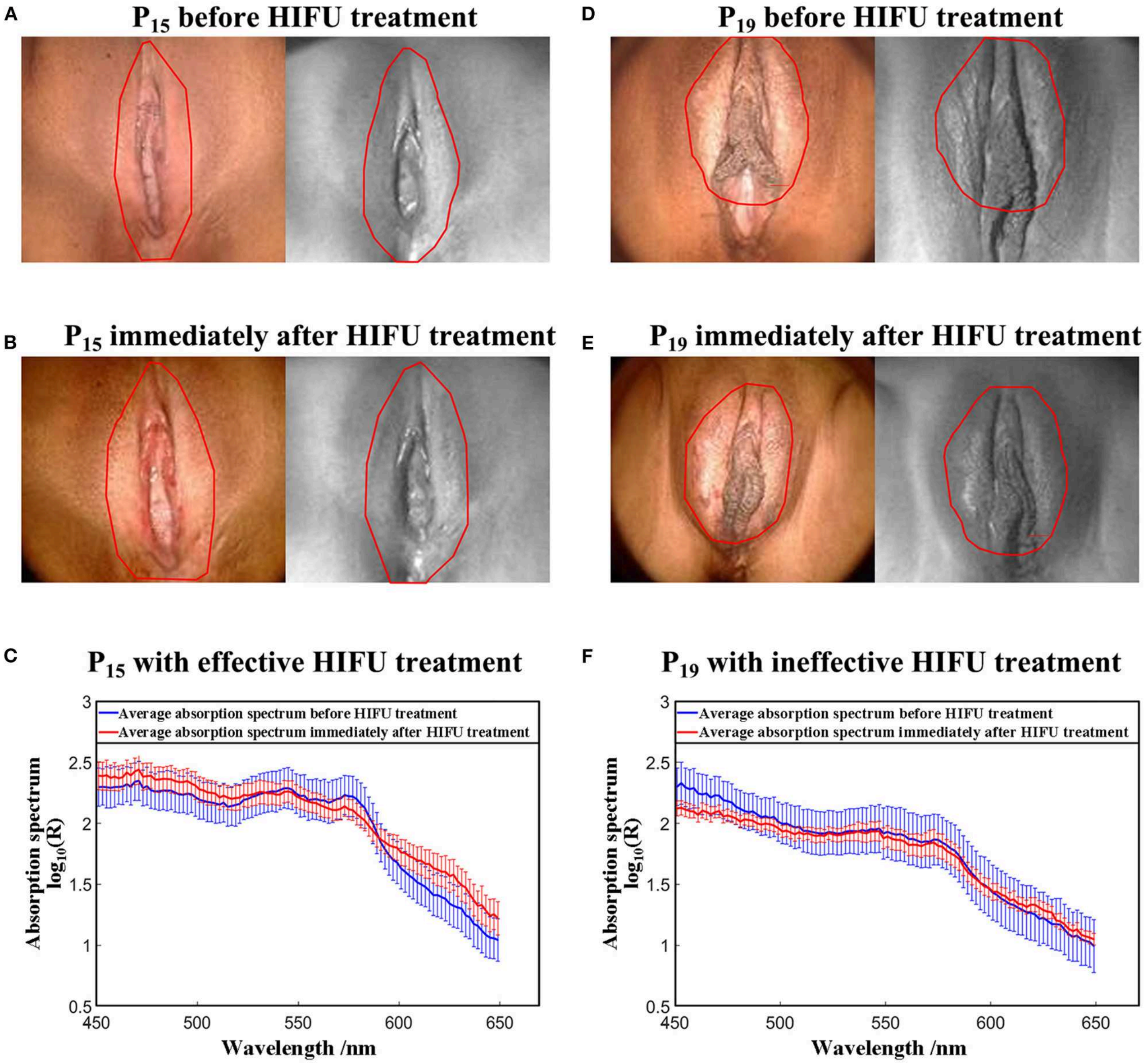

**FIGURE 8 |** Results of the HSI method. **(A)** RGB image of $P_{15}$ captured by coloscopy and the corresponding hyperspectral image at a single wavelength of 550 nm before HIFU treatment. **(B)** RGB image of $P_{15}$ captured by coloscopy and the corresponding hyperspectral image at a single wavelength of 550 nm immediately after HIFU treatment. **(C)** Average absorption spectrum from the affected areas of $P_{15}$ before and immediately after HIFU treatment. **(D)** RGB image of $P_{19}$ captured by coloscopy and the corresponding hyperspectral image at a single wavelength of 550 nm before HIFU treatment. **(E)** RGB image of $P_{19}$ captured by coloscopy and the corresponding hyperspectral image at a single wavelength of 550 nm immediately after HIFU treatment. **(F)** Average absorption spectrum from the affected areas of $P_{19}$ before and immediately after HIFU treatment. Note: The red outlines demarcate the general treatment areas marked by the same gynecologist.

the HSI method, we only used the visible range for measurement. A broader wavelength range, such as 400–1,000 nm, may provide more spectral information for improved assessment of therapeutic effect. The current wavelength range is limited by the hyperspectral imager used, which has a detection range from 400 to 700 nm. Considering that ADT is able to capture the thermal effect that plays a prominent role in the possible bioeffects and that visible light spectroscopy has been used for burning and wound assessment similar to HIFU-induced skin changes [31–33], our spectral measurements only cover the visible wavelength range. Since the classification outcome of the HSI method in the visible wavelength range is not optimal, we will carry out HSI data acquisition in a broader wavelength range to provide a fair comparison between the HSI and ADT methods in the future study. Thirdly, we chose one-time acquisition of post-treatment assessment data for 10 min instead of continuous monitoring of the treatment outcome. The current clinical practice of HIFU outcome assessment in

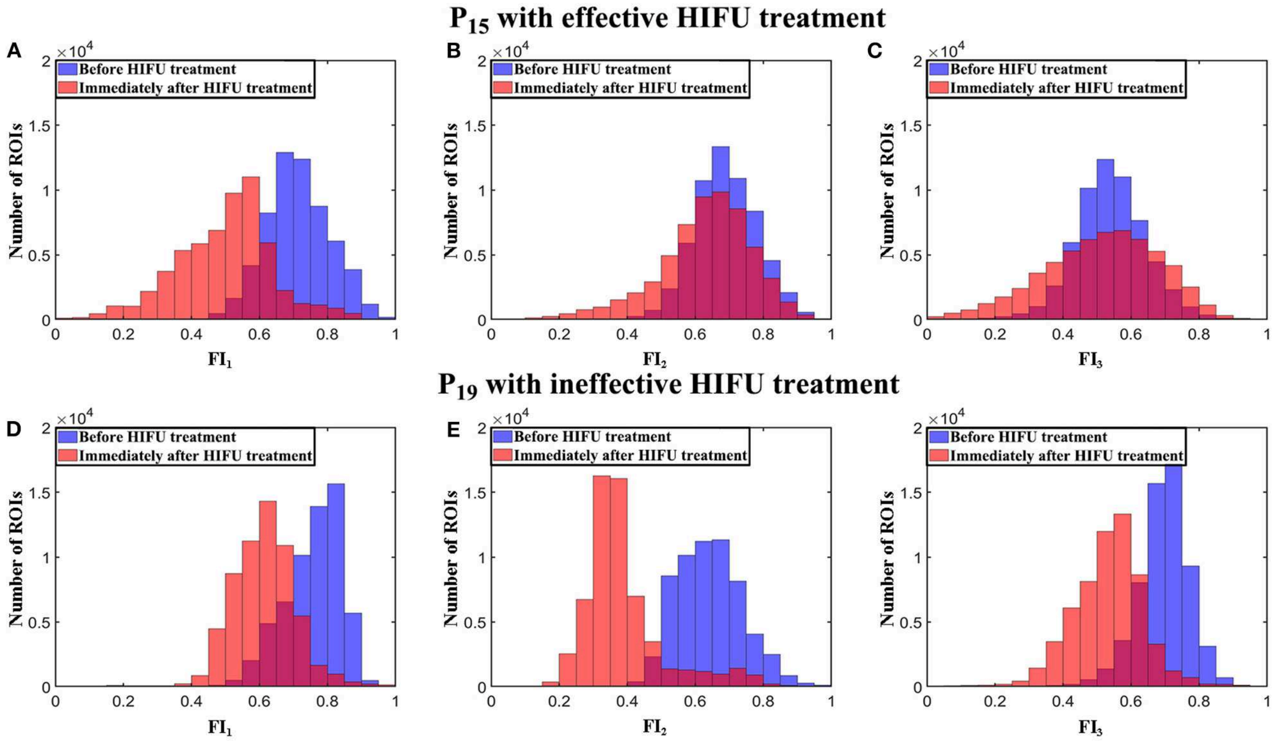

**FIGURE 9 |** Histograms of ($FI_1$, $FI_2$, $FI_3$) from $P_{15}$ and $P_{19}$ before and immediately after HIFU treatment. **(A-C)** ($FI_1$, $FI_2$, $FI_3$) from $P_{15}$. **(D-F)** ($FI_1$, $FI_2$, $FI_3$) from $P_{19}$.

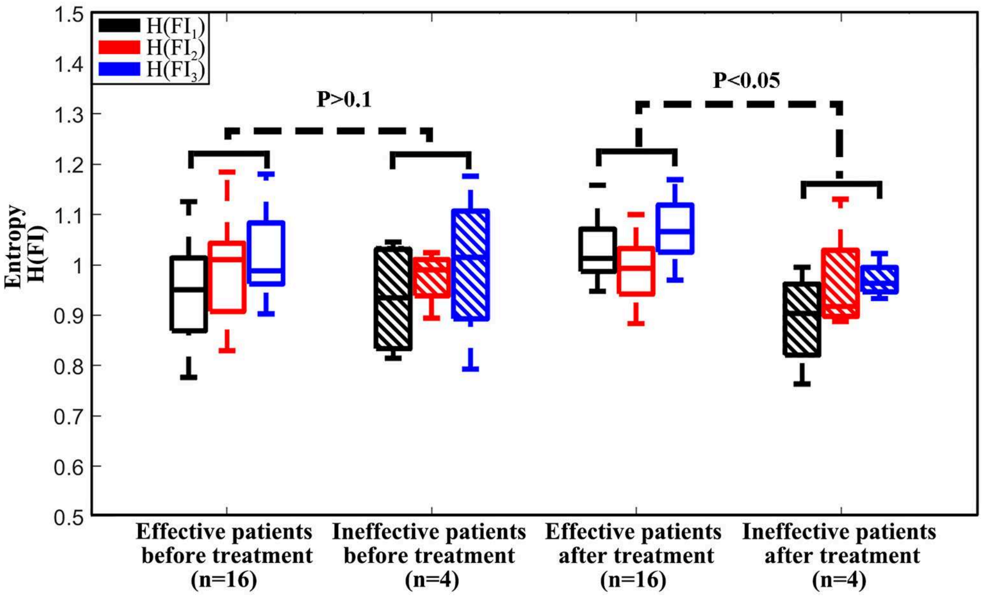

**FIGURE 10 |** Boxplot of ($H(FI_1)$, $H(FI_2)$, $H(FI_3)$) from the effective treatment group with 16 patients and the ineffective treatment group with 4 patients before and immediately after HIFU treatment.

VLS patients is subjective and cannot be carried out until 3 months post treatment. We propose to predict the therapeutic outcome by ADT and HSI evaluation of HIFU-induced tissue alternations and by establishing the correlation between these tissue alternations and the actual clinical outcome. Since the primary focus of this study is to predict the long-term outcome of HIFU therapy through post-treatment image analysis, we did not monitor the tissue changes over time. In the future, we may consider continuously monitoring the therapeutic responses over the course of a long recovery time in order to provide precise guidance for the treatment plan. Finally, the follow-up time was 3 months. Only the short-term efficacy of HIFU treatment for VLS was assessed. More studies with a larger sample size of HIFU treatment for different types of vulvar diseases and longer observation time are necessary to evaluate its long-term effects.

## 5. CONCLUSIONS

In this study, we focused on the use of two individual objective and non-invasive optical approaches, the ADT and HSI methods, to evaluate the therapeutic response to HIFU treatment in VLS, which can help identify patients with ineffective treatment promptly and prevent delay of re-treatment. Both the ADT and HSI modalities were used for HIFU outcome assessment because they provide complementary information closely relevant to the bioeffects of the therapy. On the one hand, ADT reveals the change of tissue thermal properties in response to HIFU. On the other hand, HSI reveals the tissue edema and perfusion properties relevant to HIFU-induced injury. Combinatory use of these two aspects of tissue properties may yield greater accuracy in the prediction of long-term therapeutic outcome. We are the first to study the technical feasibility of dual-modal ADT and HSI assessment of HIFU treatment in a small population of VLS patients. A large population of patients will be needed in future study in order to provide more effective evaluation of the proposed HIFU assessment technique with both accuracy and statistic power.

## DATA AVAILABILITY STATEMENT

The datasets generated for this study are available on request to the corresponding author.

## ETHICS STATEMENT

The studies involving human participants were reviewed and approved by The Institutional Review Board (IRB) of the Second Affiliated Hospital of Chongqing Medical University (IRB No: 2018KLS092) on the date of 12/07/2018. The patients/participants provided their written informed consent to participate in this study.

## CONSENT FOR PUBLICATION

Written informed consent was obtained from the from the individuals for the publication of any potentially identifiable images or data included in this article.

## AUTHOR CONTRIBUTIONS

Experiment design, data acquisition, and analysis, drafting of the manuscript, and final approval of the version to be published were carried out by YQ, YM, and SF. Data acquisition, final approval of the version to be published were contributed by ML, LX, XZ, and JZ. RX and SC were responsible for the initial concept and final review of the manuscript. YQ, YM, and SF are co-first authors.

## FUNDING

The study was partially supported by the Natural Science Foundation of China (Nos. 81271527 and 81327803), the Fundamental Research Funds for the Central Universities (WK2090090013), and Chongqing Health and Family Planning Committee (2015ZDXM010).

## ACKNOWLEDGMENTS

The authors thank the women who participated in the study and the clinicians who helped in the examinations.

## REFERENCES

1. Rodke G, Friedrich JE, Wilkinson E. Malignant potential of mixed vulvar dystrophy (lichen sclerosus associated with squamous cell hyperplasia). *J Reprod Med*. (1988) **33**:545–50.
2. Krapf JM, Goldstein AT. Vulvar dermatoses: diagnosis, management, and impact on sexual function. *Curr Sex Health Rep*. (2016) **8**:222–30. doi: 10.1007/s11930-016-0090-1
3. Bleeker MC, Visser PJ, Overbeek LI, van Beurden M, Berkhof J. Lichen sclerosus: incidence and risk of vulvar squamous cell carcinoma. *Cancer Epidemiol Prevent Biomark*. (2016) **25**:1224–30. doi: 10.1158/1055-9965.EPI-16-0019
4. Krapf JM, Mitchell L, Holton MA, Goldstein AT. Vulvar lichen sclerosus: current perspectives. *Int J Womens Health*. (2020) **12**:11. doi: 10.2147/IJWH.S191200
5. Maclean AB. Vulval cancer: prevention and screening. *Best Pract Res Clin Obstetr Gynaecol*. (2006) **20**:379–95. doi: 10.1016/j.bpobgyn.2005.11.001
6. Jensen LS, Bygum A. Childhood lichen sclerosus is a rare but important diagnosis. *Dan Med J*. (2012) **59**:A4424.
7. Zorlu C, Cobanoglu O. Medical treatment of squamous hyperplasia and lichen sclerosus of the vulva. *Int J Gynecol Obstetr*. (1995) **51**:235–8. doi: 10.1016/0020-7292(95)80012-3
8. Lorenz B, Kaufman R, Kutzner S. Lichen sclerosus. Therapy with clobetasol propionate. *J Reprod Med*. (1998) **43**:790–4.
9. Chi C, Kirtschig G, Baldo M, Brackenbury F, Lewis F, Wojnarowska F. Topical interventions for genital lichen sclerosus. *Cochrane Database Syst Rev*. (2011) **2011**:CD008240. doi: 10.1002/14651858.CD008240.pub2
10. Renaud-Vilmer C, Cavelier-Balloy B, Porcher R, Dubertret L. Vulvar lichen sclerosus: effect of long-term topical application of a potent steroid on the course of the disease. *Arch Dermatol*. (2004) **140**:709–12. doi: 10.1001/archderm.140.6.709
11. Smith YR, Haefner HK. Vulvar lichen sclerosus. *Am J Clin Dermatol*. (2004) **5**:105–25. doi: 10.2165/00128071-200405020-00005
12. Li C, Bian D, Chen W, Zhao C, Yin N, Wang Z. Focused ultrasound therapy of vulvar dystrophies: a feasibility study. *Obstetr Gynecology*. (2004) **104**:915–21. doi: 10.1097/01.AOG.0000139835.34168.b0
13. Zhou YF. High intensity focused ultrasound in clinical tumor ablation. *World J Clin Oncol*. (2011) **2**:8. doi: 10.5306/wjco.v2.i1.8

14. Wu C, Zou M, Xiong Y, Wang L, Chen H, Fan Y, et al. Short- and long-term efficacy of focused ultrasound therapy for non-neoplastic epithelial disorders of the vulva. *BJOG Int J Obstetr Gynaecol*. (2017) **124**:87–92. doi: 10.1111/1471-0528.14747
15. Ye M, Deng X, Mao S, Xue M. High intensity focused ultrasound treatment for non-neoplastic epithelial disorders of the vulva: factors affecting effectiveness and recurrence. *Int J Hyperther*. (2015) **31**:771–6. doi: 10.3109/02656736.2015.1053101
16. Ruan L, Xie Z, Wang H, Jiang J, Shi H, Xu J. High-intensity focused ultrasound treatment for non-neoplastic epithelial disorders of the vulva. *Int J Gynecol Obstetr*. (2010) **109**:167–70. doi: 10.1016/j.ijgo.2009.12.014
17. Kim Ys, Rhim H, Choi MJ, Lim HK, Choi D. High-intensity focused ultrasound therapy: an overview for radiologists. *Korean J Radiol*. (2008) **9**:291–302. doi: 10.3348/kjr.2008.9.4.291
18. Orsi F, Arnone P, Chen W, Zhang L. High intensity focused ultrasound ablation: a new therapeutic option for solid tumors. *J Cancer Res Therapeut*. (2010) **6**:414. doi: 10.4103/0973-1482.77064
19. Hsiao YH, Kuo SJ, Tsai HD, Chou MC, Yeh GP. Clinical application of high-intensity focused ultrasound in cancer therapy. *J Cancer*. (2016) **7**:225. doi: 10.7150/jca.13906
20. Cattaneo A, Bracco G, Maestrini G, Carli P, Taddei G, Colafranceschi M, et al. Lichen sclerosus and squamous hyperplasia of the vulva. A clinical study of medical treatment. *J Reprod Med*. (1991) **36**:301–5.
21. Carlson JA, Lamb P, Malfetano J, Ambros RA, Mihm JM. Clinicopathologic comparison of vulvar and extragenital lichen sclerosus: histologic variants, evolving lesions, and etiology of 141 cases. *Modern Pathol*. (1998) **11**: 844–54.
22. Clark T, Etherington I, Luesley D. Response of vulvar lichen sclerosus and squamous cell hyperplasia to graduated topical steroids. *J Reprod Med*. (1999) **44**:958–62.
23. ter Haar G, Coussios C. High intensity focused ultrasound: physical principles and devices. *Int J Hyperther*. (2007) **23**:89–104. doi: 10.1080/02656730601186138
24. Banerjee RK, Dasgupta S. Characterization methods of high-intensity focused ultrasound-induced thermal field. *Adv Heat Transf*. (2010) **42**:137–77. doi: 10.1016/S0065-2717(10)42002-X
25. Shehata IA. Treatment with high intensity focused ultrasound: secrets revealed. *Eur J Radiol*. (2012) **81**:534–41. doi: 10.1016/j.ejrad.2011.01.047
26. Wang Z, Bai J, Li F, Du Y, Wen S, Hu K, et al. Study of a "biological focal regio" of high-intensity focused ultrasound. *Ultrasound Med Biol*. (2003) **29**:749–54. doi: 10.1016/S0301-5629(02)00785-8
27. Renkielska A, Nowakowski A, Kaczmarek M, Ruminski J. Burn depths evaluation based on active dynamic IR thermal imaging–a preliminarystudy. *Burns*. (2006) **32**:867–75. doi: 10.1016/j.burns.2006.01.024
28. Kaczmarek M, Nowakowski A. Active IR-thermal imaging in medicine. *J Nondestruct Eval*. (2016) **35**:19. doi: 10.1007/s10921-016-0335-y
29. Jaspers ME, Carriare M, Meij-de Vries A, Klaessens J, van Zuijlen P. The FLIR ONE thermal imager for the assessment of burn wounds: reliability and validity study. *Burns*. (2017) **43**:1516–523. doi: 10.1016/j.burns.2017.04.006
30. Keenan E, Gethin G, Flynn L, Watterson D, O'Connor GM. Enhanced thermal imaging of wound tissue for better clinical decision making. *Physiol Meas*. (2017) **38**:1104. doi: 10.1088/1361-6579/aa6ea0
31. Calin MA, Parasca SV, Savastru R, Manea D. Characterization of burns using hyperspectral imaging technique-a preliminary study. *Burns*. (2015) **41**:118–24. doi: 10.1016/j.burns.2014.05.002
32. Clancy NT, Gurusamy K, Jones G, Davidson B, Clarkson MJ, Hawkes DJ, et al. Spectral imaging of thermal damage induced during microwave ablation in the liver. In: 40th Annual International Conference of the IEEE Engineering in Medicine and Biology Society (EMBC). Honolulu, HI: IEEE (2018). p. 3001–4. doi: 10.1109/EMBC.2018.8512901
33. Wang P, Cao Y, Yin M, Li Y, Lv S, Huang L, et al. Full-field burn depth detection based on near-infrared hyperspectral imaging and ensemble regression. *Rev Sci Instrum*. (2019) **90**:064103. doi: 10.1063/1.5034503
34. Raymond JL, Cleveland RO, Roy RA. HIFU-induced changes in optical scattering and absorption of tissue over nine orders of thermal dose. *Phys Med Biol*. (2018) **63**:245001. doi: 10.1088/1361-6560/aaed69
35. Song C, Marshall B, McLean D, Frank T, Cuschieri A, Campbell P, et al. Thermographic investigation of the heating effect of high intensity focused ultrasound. In: 2005 IEEE Engineering in Medicine and Biology 27th Annual Conference. IEEE (2006). p. 3456–8. doi: 10.1109/IEMBS.2005.1617222
36. Ahmed SE, Moussa HG, Martins AM, Abbas Y, Al-Sayah MH, Husseini GA. Factors affecting the acoustic *in vitro* release of calcein from PEGylated liposomes. *J Nanosci Nanotechnol*. (2019) **19**:6899–906. doi: 10.1166/jnn.2019.16646
37. en, T, Tüfekçiolu, O, Koza Y. Mechanical index. *Anatol J Cardiol*. (2015) **15**:334. doi: 10.5152/akd.2015.6061
38. Kollmann C, Ter Haar G, Dolezal L, Hennerici M, Salvesen K, Valentin L. Ultrasound output: thermal (TI) and mechanical (MI) indices. *Ultraschall in der Medizin*. (2013) **34**:422–34. doi: 10.1055/s-0033-1335843
39. Medicine AIoUi. Acoustic output measurement and labeling standard for diagnostic ultrasound equipment. (1992).
40. Henriques F Jr. Studies of themal injury, V. The predictability and significance of thermally induced rate processes leading to irreversible epidermal injury. *Arch Pathol*. (1947) **43**:489–502.
41. Pennes HH. Analysis of tissue and arterial blood temperatures in the resting human forearm. *J Appl Physiol*. (1948) **1**:93–122. doi: 10.1152/jappl.1948.1.2.93
42. Buettner K. Effects of extreme heat and cold on human skin. I. Analysis of temperature changes caused by different kinds of heat application. *J Appl Physiol*. (1951) **3**:691–702. doi: 10.1152/jappl.1951.3.12.691
43. Buettner K. Effects of extreme heat and cold on human skin. II. Surface temperature, pain and heat conductivity in experiments with radiant heat. *J Appl Physiol*. (1951) **3**:703–13. doi: 10.1152/jappl.1951.3.12.703
44. Vasefi F, MacKinnon N, Farkas D. Hyperspectral and multispectral imaging in dermatology. In: Hamblin MR, Avci P, Gupta GK, editors. *Imaging in Dermatology*. Boston, MA: Elsevier (2016). p. 187–201. doi: 10.1016/B978-0-12-802838-4.00016-9
45. Jakovels D, Spigulis J. 2-D mapping of skin chromophores in the spectral range 500-700 nm. *J Biophoton*. (2010). 3:125–9. doi: 10.1002/jbio.200910069
46. Chen X, Lin W, Wang C, Chen S, Sheng J, Zeng B, et al. *In vivo* real-time imaging of cutaneous hemoglobin concentration, oxygen saturation, scattering properties, melanin content, and epidermal thickness with visible spatially modulated light. *Biomed Optics Express*. (2017) **8**:5468–82. doi: 10.1364/BOE.8.005468
47. Tseng SH, Bargo P, Durkin A, Kollias N. Chromophore concentrations, absorption and scattering properties of human skin *in-vivo*. *Optics Express*. (2009) **17**:14599–617. doi: 10.1364/OE.17.014599
48. He Q, Wang RK. Analysis of skin morphological features and real-time monitoring using snapshot hyperspectral imaging. *Biomed Optics Express*. (2019) **10**:5625–38. doi: 10.1364/BOE.10.005625
49. Zonios G, Bykowski J, Kollias N. Skin melanin, hemoglobin, and light scattering properties can be quantitatively assessed *in vivo* using diffuse reflectance spectroscopy. *J Investig Dermatol*. (2001) **117**:1452–7. doi: 10.1046/j.0022-202x.2001.01577.x
50. Shimada M, Yamada Y, Itoh M, Yatagai T. Melanin and blood concentration in a human skin model studied by multiple regression analysis: assessment by Monte Carlo simulation. *Phys Med Biol*. (2001) **46**:2397. doi: 10.1088/0031-9155/46/9/309
51. Zheng W, Wang C, Chang S, Zhang S, Xu RX. Hyperspectral wide gap second derivative analysis for *in vivo* detection of cervical intraepithelial neoplasia. *J Biomed Optics*. (2015) **20**:121303. doi: 10.1117/1.JBO.20.12.121303
52. Wang C, Zheng W, Bu Y, Chang S, Zhang S, Xu RX. Multi-scale hyperspectral imaging of cervical neoplasia. *Arch Gynecol Obstetr*. (2016) **293**:1309–17. doi: 10.1007/s00404-015-3906-8
53. Lowe DG. Distinctive image features from scale-invariant keypoints. *Int J Comput Vis*. (2004) **60**:91–110. doi: 10.1023/B:VISI.0000029664.99615.94
54. Abdlaty R, Sahli S, Hayward J, Fang Q. Hyperspectral imaging: comparison of acousto-optic and liquid crystal tunable filters. In: *Medical Imaging*

*2018: Physics of Medical Imaging*. *Vol*. 10573. Houston, TX: International Society for Optics Photonics (2018). p. 105732P. doi: 10.1117/12.2282532

55. Randeberg L, Bonesrnning J, Dalaker M, Nelson J, Svaasand L. Methemoglobin formation during laser induced photothermolysis of vascular skin lesions. *Lasers Surg Med*. (2004) **34**:414. doi: 10.1002/lsm.20042
56. Randeberg LL, Hagen AJD, Svaasand LO. Optical properties of human blood as a function of temperature. In: *Lasers in Surgery: Advanced Characterization, Therapeutics, Systems XII*. *Vol*. 4609. San Jose, CA: International Society for Optics and Photonics (2002). p. 20–8. doi: 10.1117/12.437283

**Conflict of Interest:** The authors declare that the research was conducted in the absence of any commercial or financial relationships that could be construed as a potential conflict of interest.

frontiers in Physics

ORIGINAL RESEARCH
published: 24 July 2020
doi: 10.3389/fphy.2020.00266

# A Portable Ultrasound System for Detecting Food Sweetness Based on Chewing Dynamics: A Preliminary Investigation

**Ye Zhan[1], Jingwen Luo[2], Souransu Nandi[3], Lidai Wang[2], Tarunraj Singh[3] and Jun Xia[1]***

*[1] Optical and Ultrasonic Imaging Laboratory, Department of Biomedical Engineering, University at Buffalo, State University of New York, Buffalo, NY, United States, [2] Department of Biomedical Engineering, City University of Hong Kong, Hong Kong, China, [3] Control, Dynamics and Estimation Laboratory, Department of Mechanical and Aerospace Engineering, University at Buffalo, State University of New York, Buffalo, NY, United States*

Type 1 diabetes (T1D) is an incurable disease that affects 1. 25 million Americans. Diabetic patients typically rely on subcutaneous insulin infusions to regulate their glucose levels. A major contributor to their blood glucose levels is the amount of sugar intake, which cannot be easily tracked. While ultrasound imaging has been used to investigate the relationship between food characteristics and tongue movement, the technique utilized a bulky transducer array that cannot be translated into daily monitoring. Capitalizing on advanced electronics and data processing technologies, we developed a portable system that utilizes only a single ceramic disk to quantify the tongue movement in response to various levels of sweetness. After acquiring 32 subject datasets, we found a significant correlation between food sweetness and tongue movement. Our system can potentially be miniaturized into a wearable device for monitoring sugar intake, which will ultimately help T1D patients to better monitor and control their blood glucose levels and balance their diets accordingly.

**Keywords: ultrasound system, food sweetness, tongue movements, wearable sensor, portable device**

**Edited by:**
*Lorenzo Pavesi,*
*University of Trento, Italy*

**Reviewed by:**
*Chao Tao,*
*Nanjing University, China*
*Tamás Gábor Csapó,*
*Budapest University of Technology and Economics, Hungary*

***Correspondence:**
*Jun Xia*
*junxia@buffalo.edu*

**Specialty section:**
*This article was submitted to Optics and Photonics, a section of the journal Frontiers in Physics*

***Received:*** *16 January 2020*
***Accepted:*** *12 June 2020*
***Published:*** *24 July 2020*

**Citation:**
*Zhan Y, Luo J, Nandi S, Wang L, Singh T and Xia J (2020) A Portable Ultrasound System for Detecting Food Sweetness Based on Chewing Dynamics: A Preliminary Investigation. Front. Phys. 8:266. doi: 10.3389/fphy.2020.00266*

## INTRODUCTION

Type 1 diabetes (T1D) is an autoimmune disease that currently has no cure [1]. People with T1D typically rely on insulin pump therapy (subcutaneous insulin infusion) to control their blood glucose level. Before each meal, T1D patients are recommended to conduct a pre-bolus insulin injection, the amount of which is determined by the projected carbohydrates intake and the personal insulin-to-carb ratio. The pre-bolus approach can effectively avoid a sudden increase in blood glucose level after a meal [2]. However, because it is difficult to quantify the number of carbohydrates in the food, there are uncertainties resulting from this approach. If the dose of injected insulin is largely different from the actual need, the patient may be at risk of hyperglycemia or hypoglycemia. Therefore, there is an unmet clinical need for a portable device that can continuously monitor sugar intake.

The physical and chemical compositions determine the flavor of the food [3, 4], which is also reflected in the chewing behavior. In addition, the biomechanical properties determine the duration and the amount of oral processing before swallowing. For example, solid food is mixed with saliva and fragmented by teeth to form soft, coherent clumps [5]. Low viscosity liquids can be swallowed with minimal processing. But intense flavors, acidic, or icy liquids will remain in the mouth for a longer period of time to increase the pH of the buffer in the saliva and to equilibrate the product to body temperature for further dilution with saliva. Generally, after the start of oral processing, the swallowing process is divided into three-phase, oral transit phase, swallow phase, and clearance phase. Previous experimental results show that during oral transit time, there was a relatively significant movement of the tongue and food characteristics and tongue movement features are closely related [6–8]. Therefore, the texture and flavor of the food may both influence people's chewing behavior. In this research, we will focus on the same food consistency and investigate how different levels of sweetness affect oral processing.

Ultrasonic imaging is a powerful technique used to quantify oral processing [1]. This technique was demonstrated by de Wijk et al. [9] using a linear transducer array, which contained a row of piezoelectric crystals. The ultrasonic probe was placed under the subject's chin to receive the sagittal-view image of the tongue. The ultrasound probe can generate a video of tongue images through internal computer analysis. By processing temporal B-scan images, with the tongue as the region of interest, the magnitude of tongue movements can be quantified [10]. René's research investigated the taste attributes, specifically sweetness and bitterness [9]. However, this technique can be relatively bulky because a transducer array is required to capture the B-scan image.

To address this issue, we replaced the transducer array with a single ceramic disk and developed an algorithm to quantify the tongue movement based on A-line ultrasound data, which is also widely used in the medical field [11]. In terms of data acquisition, we used a smartphone-based recording system that is portable and more energy-efficient than the transducer arrays used in the previous study [12]. Our study indicates that there is a correlation between the tongue movement and food sweetness, and our design could potentially be translated into a wearable device for daily monitoring of sugar intake.

## MATERIALS

**Figure 1** shows a schematic drawing of our system. A 4.25 MHz ceramic disk with a diameter of 7 mm and thickness of 0.5 mm (Steminc) was used for ultrasound transmission and receiving. Ultrasound pulses were provided by an ultrasound pulse-receiver (Panasonic, Model 5070PR), which outputs 50 ns pulses at 100 Hz (repetition rate). Before the experiment, we applied ultrasound gel to the ceramic disk. We then attached it under the chin of the subject (about two fingers away from the tip of the chin) using adhesive tape. Since we used a planar transducer element with 7 mm diameter field of view, a slight shift in the transducer placement will not impact the result. The reflected ultrasound echo signal was detected by a portable oscilloscope (SmartScope) with a sampling frequency of 50 MHz. For each A-line, we acquired 2,048 points, which corresponds to 40 μs of data acquisition time. This time period corresponds to a 6 cm travel distance in tissue and is sufficient for the collection of reflected signals from the tongue. The SmartScope was connected to the smartphone through a USB cable and all acquisition parameters were controlled from the smartphone app. The received signals were displayed in real-time on the smartphone and saved in its memory for future analysis.

For phantom experiments, we placed the ceramic transducer inside a 10-mm-wide water tank. A metal plate was placed at the other side of the tank to serve as an acoustic reflector. The echo arrival time reveals the distance between the transducer

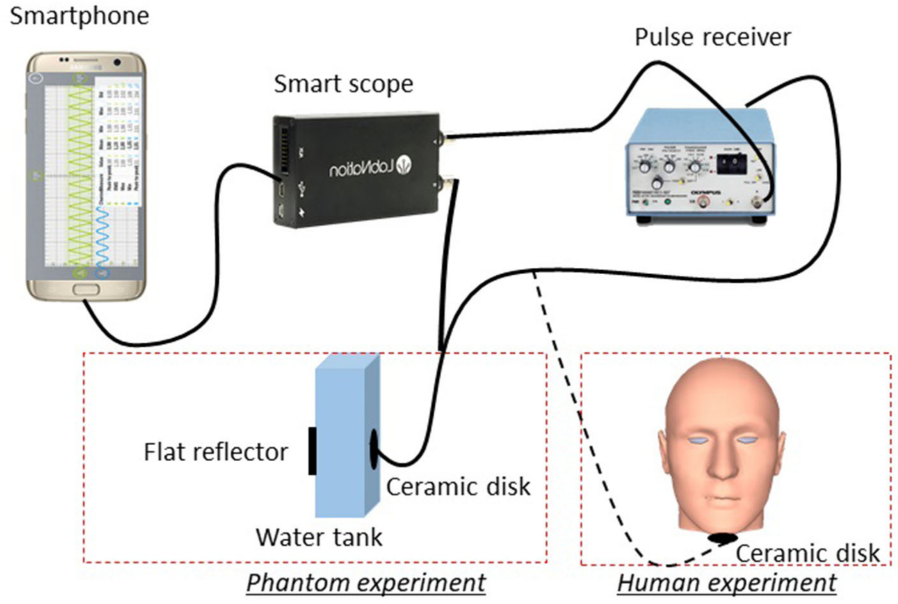

**FIGURE 1 |** A schematic drawing of the experimental set-up.

and the metal plate. To simulate the tongue motion, we used a voice-coil motor to move the reflector at different amplitudes and frequencies. The phantom experimental results will be used to verify whether our data processing method can reflect different motion states (vibration amplitudes and frequencies).

For human trials, our subjects' ages range between 19 and 30 years old, and the ratio of male to female was about 1:1. Based on visual assessment, all subjects are within the healthy body mass index (BMI) range (20–25). All experiments were conducted at room temperature (25°C). During the experiment, the ceramic transducer was placed under the chin, while the surface of the tongue acted as the reflector. To test the relationship between food sweetness and tongue movement, food with three different sweetness levels (high, middle, and low) were prepared based on a mixture of 300 ml skim milk and 15 g gelatin (Kraft Heinz Foods Company). Low-sweetness samples were prepared without sweetener, middle-sweetness samples were prepared by adding 10 g of sweetener (Truvia, Cargill, Inc.), and high-sweetness samples were prepared by adding 20 g of sweetener. Samples were then distributed into an ice cube maker (5 g/cube) and solidified in a freezer for 4 h. After solidification, the samples sat at room temperature for 20 min before the experiment [9]. To avoid influence from food attribute, each sample cube is identical in size, hardness, and smell. The subjects were given the samples (around 15 × 15 × 15 mm), and the process of chewing in the bulk phase was recorded for 7 s using the SmartScope. Recording started immediately at the beginning of chewing and ended 7 s later. This period covered the bulk phase (the first 5 s of oral processing), where oral movement is highly correlated with food characteristics [9]. During the experiment, the subjects were told to avoid speaking. No special instructions regarding oral movement and swallowing were provided. To avoid any interference between the contiguous measurements, subjects were asked to rinse their mouths with water before and after each experiment and between each trial. The procedure was repeated two times for each subject. Three food samples at three different sweetness levels were tested twice for each subject, generating 192 datasets (3 sweetness level × 2 tests × 32 subjects). These datasets will be processed and compared with the different sweetness levels of the food sample to evaluate their correlation.

## DATA PROCESSING METHODS

**Figure 2** shows an acoustic A-line acquired in the phantom experiment. The oscillation at time zero corresponds to acoustic firing. The reflected echo signal is shown at around 25 μs, which corresponds to the total travel time for the acoustic pulse. As we moved the reflector closer to the transducer, the peak (red) also shifted to the left accordingly. This result clearly indicates that the movement of the flat reflector can be precisely monitored by pulse-echo ultrasound. The same principle was used to capture tongue movement.

To quantify the movement of the reflector, we developed two algorithms: one was based on cross-correlation (CC), while the other was based on standard deviation (STD). The CC method has been widely used to quantify the shift between two plots by computing their cross-correlation coefficient [9]. In our case, each A-line signal records the instantaneous position of the tongue. The magnitude and frequency of the reflector movement can be calculated by cross-correlating the two neighboring A-lines [7]. If there was no movement, the correlation coefficient would be 1.00. Otherwise, the correlation coefficient would be <1.00. The larger the movement, the smaller the correlation coefficient. However, breathing and heartbeat can cause slight

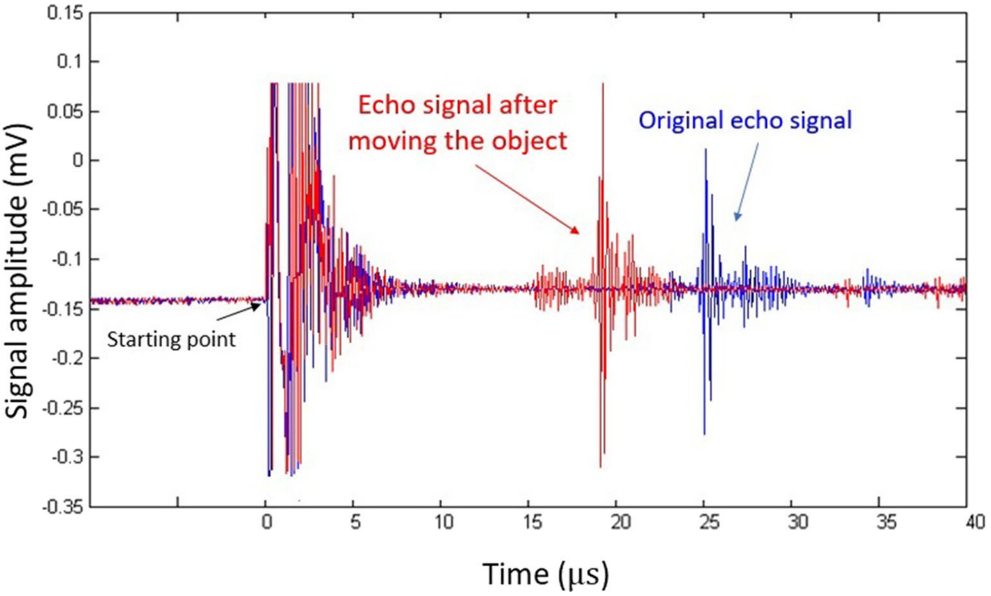

**FIGURE 2 |** Pulse-echo ultrasound signal acquired in the phantom experiment. The blue plot represents the original echo signal, while the red one represents signals acquired after the flat reflector was placed closer to the transducer.

fluctuations, which can influence the result of the correlation coefficient method. The STD approach may address this issue because it represents the volatility of tongue movements. STD focuses on the signal fluctuation within a specific window in the A-line (oral processing). The intense tongue movement creates a larger signal fluctuation, leading to a higher variation. Movements caused by respiration or heartbeat are much milder than that of the tongue, and therefore they have limited influence on the STD values. In contrast, any small shifts in the A-line may lead to a change in the CC value. Because all subjects are within the healthy BMI range, variations in the amount of adipose tissue in the chin are not significant. Nevertheless, for each subject, we manually verified the data processing window to ensure that it covers the tongue surface.

A quantitative score, named the fractal index (FI), is used to quantify the movement based on A-lines or STD values. FI reflects the sum of the first derivative of the CC or STD processed data. René's work [9] verified that the FI factor of the CC-processed data is positively correlated with the movement amplitude and intensity of the echo. In this study, we verified whether the STD-derived FI would offer similar or better results.

## RESULTS

The algorithms were first validated in the phantom. The movement was created by a voice coil actuator, which oscillates the reflecting metal plate. To mimic different magnitudes of tongue movement at the same frequency, we fixed the driving frequency at 10 Hz and increased the driving voltage from 3 to 9 V. Results from the correlation coefficient method are presented in **Figure 3A**, and the results from the STD method are presented in **Figure 3B**. The results show that the FI factor is positively correlated with the movement magnitude.

To mimic different tongue movement frequencies, we fixed the driving voltage at 5 V and increased the driving frequency from 10 to 100 Hz. Results from the correlation coefficient method are presented in **Figure 4A**, and the results from the STD method are presented in **Figure 4B**. These experiments show that

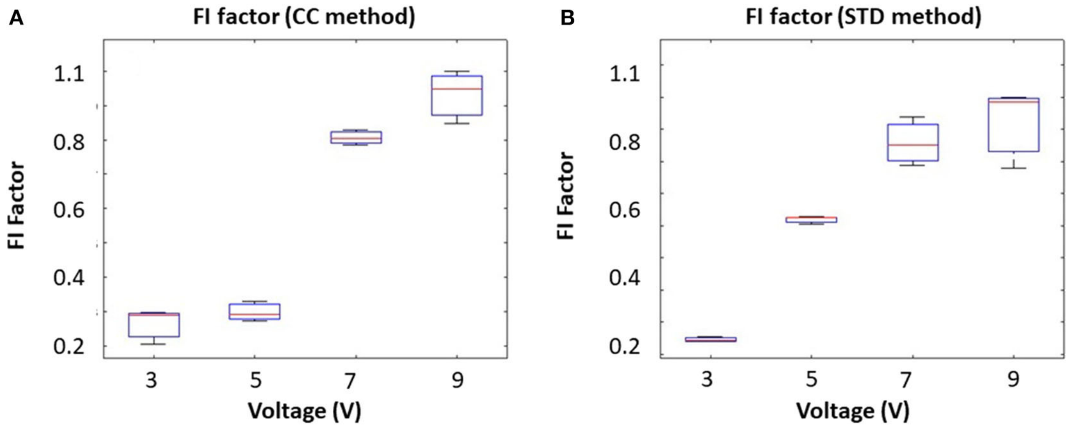

**FIGURE 3 |** Input voltage (Amplitude) corresponding to the FI factor based on different methods: **(A)** the correlation coefficient method and **(B)** the STD method.

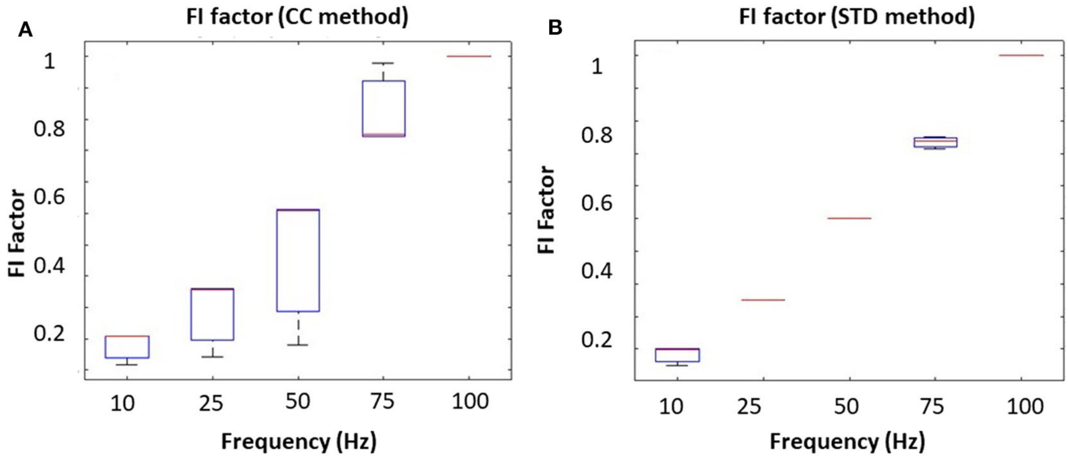

**FIGURE 4 |** The oscillating frequency corresponding to the FI factor base on different methods: **(A)** correlation coefficient method and **(B)** the STD method.

the FI factor is positively correlated with movement frequency. It should be noted that during the experiment, we observed a non-linearity correlation between voltage and oscillation magnitude, which might have caused the non-linearity in **Figures 3A**, **4A**. However, that won't affect our *in vivo* experiment result.

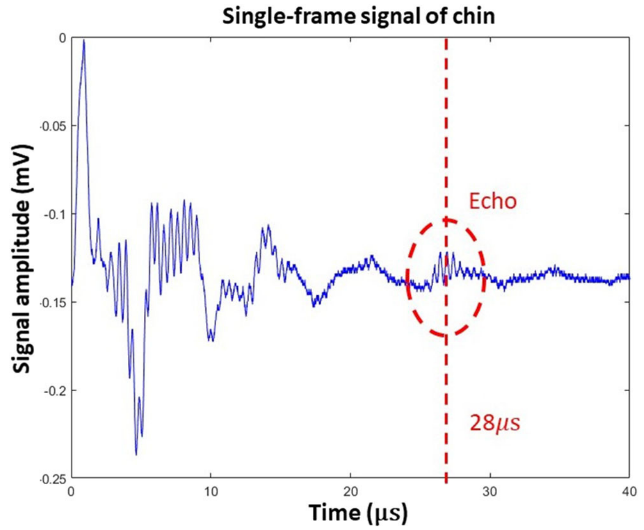

**FIGURE 5 |** A single A-line of human data acquired by a transducer placed under the chin.

**Figure 5** represents a single A-line acquired in the human trials. In this figure, ultrasound reflection can be seen at time 28 µs, which corresponds to a 42-mm round-trip distance. Based on human anatomy [13], this echo was generated by reflection from the bottom surface of the tongue. When the tongue moves, both the amplitude and delay time of the ultrasound echo will vary, and these parameters can be used to quantify oral movement. Because ultrasound echo from the tongue surface looks quite different from background signals, this feature was used to verify the location of tongue surface.

The CC and STD algorithms were also used to process human data, and the results are shown in **Figures 6**, **7**, respectively. **Figure 6A** shows the temporal correlation coefficient of 1,000 frames (acquired in 10 s). **Figure 6B** indicates correlation coefficient data after being smoothed by a moving-average filter with a 3-pixel window size [9]. The first deviation for the smoothed data is shown in **Figure 6C**. For better illustration, **Figure 6D** is a magnified image of **Figure 6C**, where every chewing cycle is clearly displayed.

**Figure 7A** shows the original STD data as a function of the frame number. **Figure 7B** indicates STD data after being smoothed by a 3-pixel window size moving-average filter. The first deviation for the smoothing data is demonstrated in **Figure 7C**. **Figure 7D** is a magnified image of **Figure 7C**, where each chewing cycle can be clearly seen. Based on the result in **Figure 7C**, we calculated the FI factor and compare it with the different levels of food sweetness.

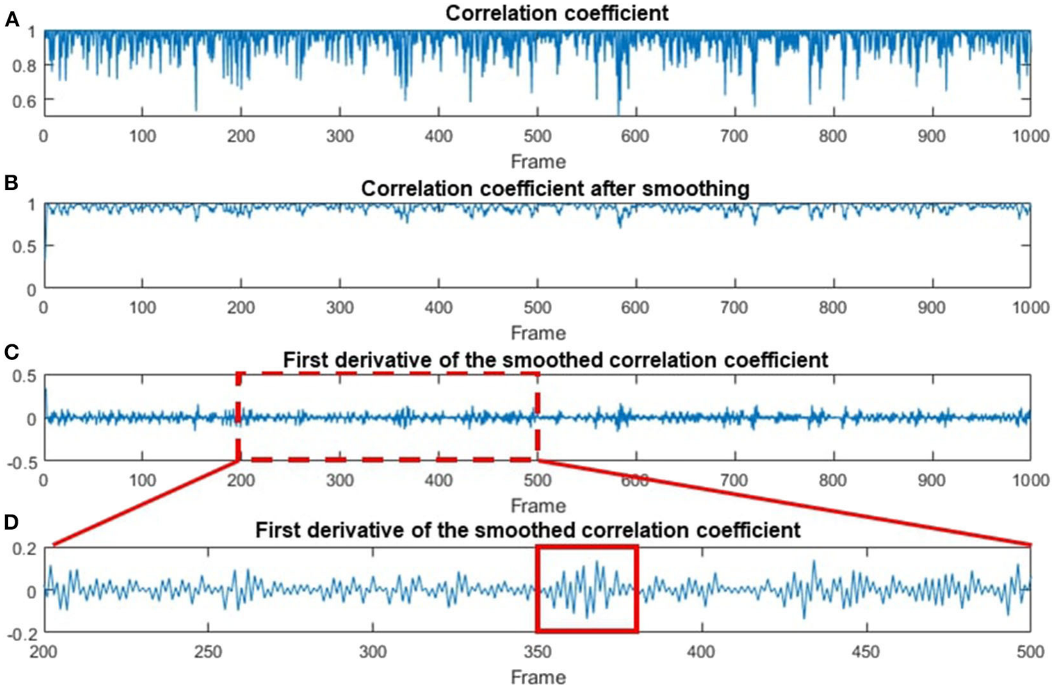

**FIGURE 6 |** Data processing steps based on the CC method. **(A)** The original CC-processed data as a function of the frame number. **(B)** The smoothing-processed plot of **(A)**. **(C)** The first deviation of the smoothed data in **(B)**. **(D)** A magnified plot of a section in **(C)**, where multiple chewing cycles can be clearly seen. A red solid line box is used to indicate one of the chewing cycles.

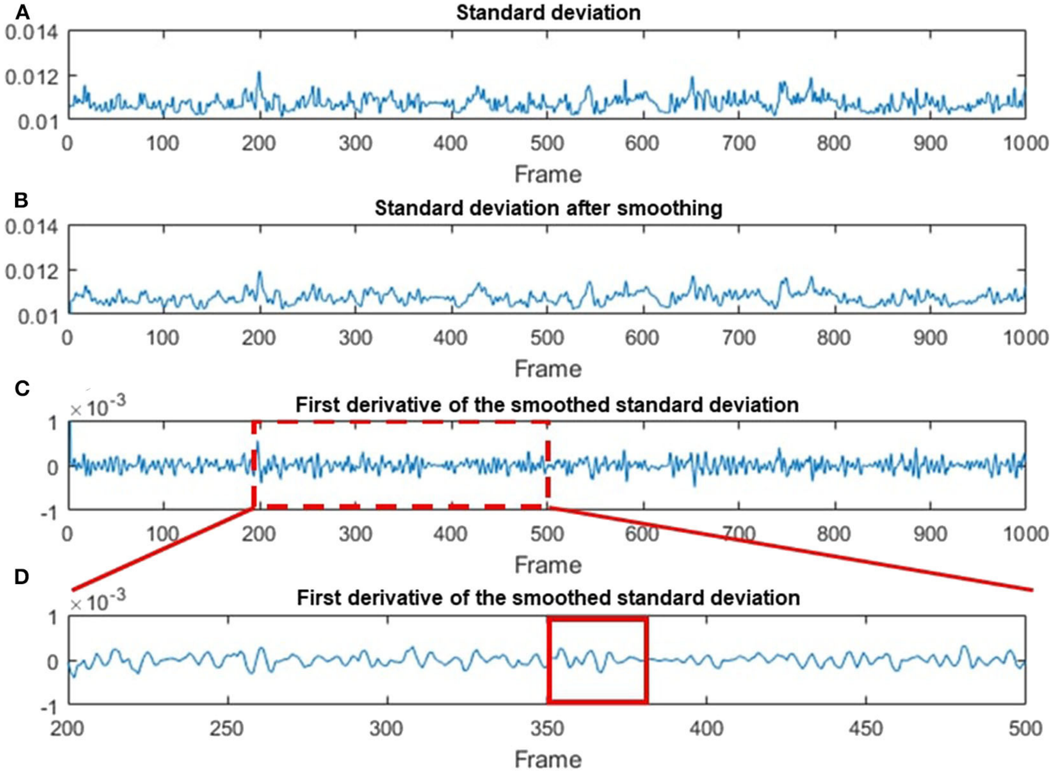

**FIGURE 7 |** Data processing steps based on the STD method. **(A)** The original STD-processed data as a function of the frame number. **(B)** The smoothing-processed plot of **(A)**. **(C)** The first deviation of the smoothed data in **(B)**. **(D)** A magnified plot of a section in **(C)**, where multiple chewing cycle can be clearly seen. A red solid line box is used to indicate one of the chewing cycles.

Analysis of variance (ANOVA) was used to verify whether there are significant differences in tongue movement among different food sweetnesses. The test was conducted with 32 subjects, each of whom was tested with three different sweetnesses and repeated three times for each sweetness. The results were presented in **Table 1**. ANOVA was then applied to the FIs to compare tongue movement for foods with different sweetnesses. ANOVA verified the significant differences among FIs of three different sweetnesses during the bulk phase (**Table 2**) [14]. The results showed an increased tongue activity for higher sweetness samples. We used a single sample *t*-test [15] to analyze the difference between the two conditions. Equation (1) is used in the *t*-test, where $\bar{d}$ is the mean of the differences between the FI of two different sweetness tests, n represents the sample size, $u_0$ is population mean, and s is the standard deviation of the difference. The FIs were multiplied by 1,000 in the *t*-test to avoid leading zeros in the sums of squares when ANOVA was applied [9].

$$t = (\bar{d} - u_0)/(s/\sqrt{n}) \tag{1}$$

For the high and middle sweetness (H-M) comparison, we found that the *P*-value was 7.19% in the CC method and 0.44% in the STD method. For the middle and low sweetness (M-L) comparison, the *P*-value was 7.19% in the CC method and 1.44% in the STD method. For the high and low (H-L) sweetness comparison, the *P*-value was <0.01% in both methods. These results indicate that the tongue movement varied significantly at different food sweetness levels. Also, the STD method performed better than the CC method in differentiating food sweetness. This occurred because the CC method is more susceptible to small changes, such as respiration and heartbeat, while the STD method is more sensitive to relatively large variations, like chewing and swallowing. Therefore, in this experiment, the STD method obtained relatively better results. Plots of FI distribution (**Figures 8**, **9**) further confirm the decreasing tendency of the FI with the reduction in sweetness.

Due to variations in different individual's chewing behavior, a direct comparison of the FI among subjects would render inaccurate results. To address this issue, we developed a self-calibration procedure, where each subject's FI factors are self-normalized by the mean FI of the same subject at three different sweetness levels. After normalization, the FI factors of different subjects would fall within a similar range for easy comparison. The results from 32 subjects using the data processing method described above are shown in **Figures 8**, **9**. Our conclusion was further validated by calculating the effect size [16], which is the ratio of the difference between two FI index means and their standard deviation. The result is shown in **Table 3**. Here, effect size >0.8, and 1.2 indicates a large difference between the two

**TABLE 1 |** Fractal index data for every experimental subject.

| Subject | High | Middle | Low |
|---|---|---|---|
| Fractal index of correlation coefficient | | | |
| 1 | 0.0231 | 0.0202 | 0.0208 |
| 2 | 0.0106 | 0.0093 | 0.0092 |
| 3 | 0.0273 | 0.0271 | 0.0152 |
| 4 | 0.0208 | 0.0145 | 0.0139 |
| 5 | 0.0204 | 0.0197 | 0.0237 |
| 6 | 0.052645 | 0.074657 | 0.067792 |
| 7 | 0.00739 | 0.00657 | 0.00847 |
| 8 | 0.00938 | 0.00388 | 0.00418 |
| 9 | 0.036633 | 0.036 | 0.019673 |
| 10 | 0.031488 | 0.031945 | 0.029863 |
| 11 | 0.007282 | 0.005438 | 0.005271 |
| 12 | 0.005156 | 0.00731 | 0.004778 |
| 13 | 0.065804 | 0.068976 | 0.065251 |
| 14 | 0.06473 | 0.052953 | 0.050516 |
| 15 | 0.052596 | 0.060794 | 0.051153 |
| 16 | 0.08435 | 0.07483 | 0.06492 |
| 17 | 0.05766 | 0.03768 | 0.04866 |
| 18 | 0.04604 | 0.04672 | 0.0429 |
| 19 | 0.06625 | 0.06705 | 0.06732 |
| 20 | 0.03465 | 0.02827 | 0.03008 |
| 21 | 0.03915 | 0.03999 | 0.03457 |
| 22 | 0.03842 | 0.03648 | 0.03753 |
| 23 | 0.04651 | 0.04385 | 0.0489 |
| 24 | 0.04279 | 0.0404 | 0.04101 |
| 25 | 0.029626 | 0.029118 | 0.026348 |
| 26 | 0.034175 | 0.026216 | 0.033972 |
| 27 | 0.052024 | 0.059062 | 0.059707 |
| 28 | 0.045822 | 0.033092 | 0.031527 |
| 29 | 0.024375 | 0.02126 | 0.023749 |
| 30 | 0.020734 | 0.016485 | 0.017439 |
| 31 | 0.019579 | 0.017653 | 0.015969 |
| 32 | 0.015595 | 0.017229 | 0.013636 |
| Fractal index of standard deviation | | | |
| 1 | 2.46E-05 | 2.37E-05 | 2.38E-05 |
| 2 | 2.2E-05 | 2.16E-05 | 1.93E-05 |
| 3 | 3.22E-05 | 3E-05 | 1.83E-05 |
| 4 | 1.92E-05 | 1.51E-05 | 1.48E-05 |
| 5 | 7.85E-05 | 7.82E-05 | 5.48E-05 |
| 6 | 8.44E-05 | 6.26E-05 | 5.92E-05 |
| 7 | 4.37E-05 | 4.61E-05 | 3.78E-05 |
| 8 | 7.37E-05 | 3.73E-05 | 3.44E-05 |
| 9 | 0.00016 | 0.000159 | 0.000127 |
| 10 | 0.000463 | 0.000476 | 0.000486 |
| 11 | 0.000644 | 0.000643 | 0.000639 |
| 12 | 0.000488 | 0.000487 | 0.000486 |
| 13 | 5.93E-05 | 6.28E-05 | 6.25E-05 |
| 14 | 0.000104 | 0.000104 | 9.65E-05 |
| 15 | 0.0001 | 8.91E-05 | 8.14E-05 |
| 16 | 0.000428 | 0.000385 | 0.000384 |
| 17 | 0.000489 | 0.000419 | 0.000475 |
| 18 | 0.000537 | 0.000518 | 0.000491 |
| 19 | 0.000172 | 0.000172 | 0.000177 |
| 20 | 0.000187 | 0.000159 | 0.000158 |
| 21 | 0.000168 | 0.000175 | 0.00014 |
| 22 | 0.000264 | 0.000222 | 0.000226 |
| 23 | 0.000254 | 0.000259 | 0.000201 |
| 24 | 0.000195 | 0.000205 | 0.00018 |
| 25 | 0.00013 | 0.000115 | 0.000103 |
| 26 | 0.00015 | 0.00011 | 0.000138 |
| 27 | 0.000173 | 0.000147 | 0.000134 |
| 28 | 0.000155 | 0.000129 | 9.36E-05 |
| 29 | 0.000152 | 0.000143 | 0.00013 |
| 30 | 0.000132 | 0.000124 | 0.000118 |
| 31 | 0.000135 | 0.000125 | 0.000128 |
| 32 | 0.000228 | 0.00027 | 0.000229 |

**TABLE 2 |** *P*-value of different comparison pairs.

| ***P*-value** | | | | |
|---|---|---|---|---|
| | **H-M** | **M-L** | **H-L** | **ANOVA** |
| Correlation coefficient | 0.071866 | 0.071866 | <0.0001 | 0.020831 |
| Standard deviation | 0.004412 | 0.014454 | <0.0001 | 0.000011 |

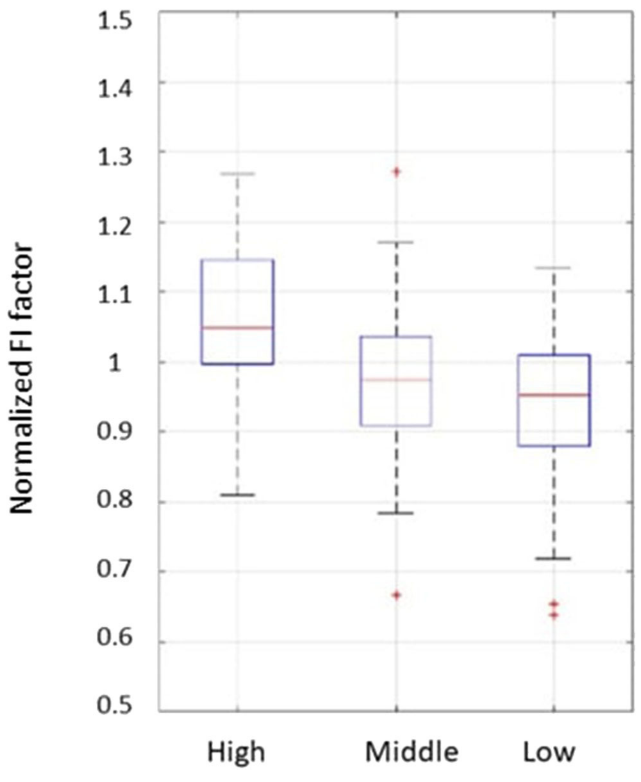

**FIGURE 8 |** Plots from the fractal index of correlation coefficient method. Each set of subject data was normalized by its mean value to eliminate fluctuations caused by different transducer positions.

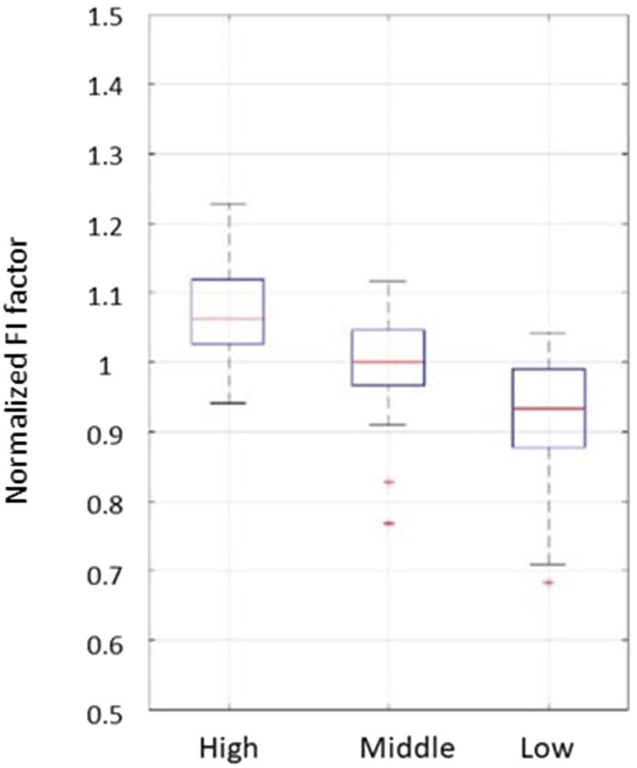

**FIGURE 9 |** Plots from the fractal index of standard deviation method. Each set of subject data was normalized by its mean value to eliminate fluctuations caused by different transducer positions.

**TABLE 3 |** Effect size of different comparison pairs.

| **Effect Size** | | | |
|---|---|---|---|
| | **H-M** | **M-L** | **H-L** |
| Correlation coefficient | 0.7325 | 0.3844 | 1.0933 |
| Standard deviation | 0.9410 | 0.9574 | 1.7012 |

groups. Based on the **Table 3**, the STD method is generally better than the CC method, and for both CC and STD methods, apparent differences can be seen between high and low sweetness levels.

From all these results, we can conclude that the sweetness of food has a significant correlation with oral processing behavior: the sweeter the food, the more intense the tongue moves. It should be noted that our device was designed to be used by the same subject and cross-subject comparison will not be needed for future applications.

## DISCUSSION AND CONCLUSION

In this study, we developed a portable ultrasound system that consists of a ceramic disk, an ultrasound pulser, and a smartphone-controlled smartscope. After each ultrasound pulse, the ceramic disk collects temporal data, which represents the position of the tongue. Multiple ultrasound pulses are associated with multiple sets of temporal data to track the oral process and tongue movement. Our results indicate that there is a positive correlation between the sweetness of food and tongue movement. We hope this approach could be used in the future to track sugar intake in patients with diabetes.

While we have demonstrated encouraging results, future improvements are still needed. First, although the size of the transducer and the oscilloscope have been significantly reduced, the ultrasound pulse generator is still relatively large. This issue can potentially be addressed by using a mobile ultrasound pulser chip, such as the ultrasonic signal processor and transducer driver produced by Texas Instruments with a size of 6 × 5 $\text{mm}^2$ [17]. Recent advances in smartphones also enabled mobile ultrasound systems [18], whose techniques might be implemented in our future design to make the system even more portable. Second, the position of transducer placement is not ideal. A potential solution is to integrate the sensor with an earbud and place it right under the ear to monitor jaw movement. This position will be more convenient for daily usage and the device can potentially also record the sound of chewing [19]. Third, the user interface needs to be optimized. Ideally, the software should be able to track patients' sugar intake from day to day and notify the patient if the intake is significantly higher than the typical value.

## DATA AVAILABILITY STATEMENT

All datasets generated for this study are included in the article/supplementary material.

## ETHICS STATEMENT

The studies involving human participants were reviewed and approved by the University at Buffalo Institutional Review Board (UB-IRB). The participants provided their written informed consent to participate in this study.

## AUTHOR CONTRIBUTIONS

YZ designed the experimental setup, processed the data, and wrote the article. JL collected and analyzed experimental data and participated in the manuscript writing. SN and TS offered guidance in data processing and manuscript revision. LW guided the experimental design and data processing. JX supervised the project and revised the manuscript. All authors contributed to the article and approved the submitted version.

## FUNDING

This project was partially supported by the University at Buffalo's IMPACT award.

# REFERENCES

1. Atkinson MA, *Eisenbarth* GS. Type 1 diabetes: new perspectives on disease pathogenesis and treatment. *Lancet.* (2001) **358**:221–9. doi: 10.1016/S0140-6736(01)05415-0
2. Kim S. *Calculating Insulin Dose*. (2019) Available online at: https://dtc.ucsf.edu/types-of-diabetes/type2/treatment-of-type-2-diabetes/medications-and-therapies/type-2-insulin-rx/calculating-insulin-dose/
3. Hutchings JB, Lillford P. The perception of food texture-the philosophy of the breakdown path. *J Texture Stud.* (1988) **19**:103–15. doi: 10.1111/j.1745-4603.1988.tb00928.x
4. Prinz J, Lucas P. Mastication and swallowing: an optimisation model. *Proc R Soc Lond B.* (1997) **264**:1715–21. doi: 10.1098/rspb.1997.0238
5. Liu L, Hammond EG. The role of particles in the perception of flavours. *J Food Qual.* (2000) **23**:521–8. doi: 10.1111/j.1745-4557.2000.tb00577.x
6. Chen J, Engelen L. *Food Oral Processing: Fundamentals of Eating and Sensory Perception.* Summit, NJ: John Wiley & Sons (2012). doi: 10.1002/9781444360943
7. Neyraud E, Peyron MA, Vieira C, Dransfield E. Influence of bitter taste on mastication pattern. *J Dent Res.* (2005) **84**:250–4. doi: 10.1177/154405910508400308
8. Engelen, L, de Wijk RA. Oral processing and texture perception. In: Chen J, Engelen L, editors. *Food Oral Processing: Fundamentals of Eating and Sensory Perception.* Oxford: Wiley-Blackwell. (2012) p. 159–76. doi: 10.1002/9781444360943.ch8
9. de Wijk RA, Wulfert F, Prinz JF.de Wijk RA, Wulfert F, Prinz JF. Oral processing assessed by M-mode ultrasound imaging varies with food attribute. *Physiol Behav.* (2006) **89**:15–21. doi: 10.1016/j.physbeh.2006.05.021
10. Prinz JF, Ng KW.Prinz JF, Ng KW. Characterization of sounds emanating from the human temporomandibular joints. *Arch Oral Biol.* (1996) **41**:631–9. doi: 10.1016/S0003-9969(96)00070-2
11. Erikson KR, Fry FJ, Jones JP. Ultrasound in medicine-a review. *IEEE Trans Sonics Ultrasonics.* (1974) **21**:144–70. doi: 10.1109/T-SU.1974.29810
12. Green JR, Wang YT.Green JR, Wang YT. Tongue-surface movement patterns during speech and swallowing. *J Acoustical Soc Am.* (2003) **113**:2820–33. doi: 10.1121/1.1562646
13. Netter FH, Colacino S. *Atlas of Human Anatomy*. 6th ed. East Hanover, NJ. (1989).
14. Stangroom J. *One-Way Repeated Measures ANOVA* Calculator (2019). Available online at: https://www.socscistatistics.com/contact3/
15. Stangroom J. *Single Sample T-Test* Calculator (2019). Available online at: https://www.socscistatistics.com/tests/tsinglesample/default.aspx
16. Cohen H. *Statistical Bower Analysis for Behavioral sciences.* Hillsdale, NJ: Lawrence Erlbaum Associates (1988).
17. Bageshwar DV, Pawar A, Khanvilkar VV, Kadam VJ. Photoacoustic spectroscopy and its applications–a tutorial review. *Eur J Anal Chem.* (2010) **5**:187–203.
18. Gummadi S, Eisenbrey JR, Li J, LI Z, Forsberg F, Lyschik A, et al. Advances in modern clinical ultrasound. *Adv Ultrasound Diagn Ther.* (2018) **2**:51–63. doi: 10.37015/AUDT.2018.180801
19. Zhang H, Song C, Wang A, Xu C, Li D, Xu W. PDVocal: towards privacy-preserving parkinson's disease detection using non-speech body sounds. In: *The 25th Annual International Conference on Mobile Computing and Networking.* Los Cabos: ACM (2019). doi: 10.1145/3300061.3300125

**Conflict of Interest:** The authors declare that the research was conducted in the absence of any commercial or financial relationships that could be construed as a potential conflict of interest.

frontiers in Physics

ORIGINAL RESEARCH
published: 31 July 2020
doi: 10.3389/fphy.2020.00283

# Parallelized Monte Carlo Photon Transport Simulations for Arbitrary Multi-Angle Wide-Field Illumination in Optoacoustic Imaging

*Tong Lu*[1], *Jiao Li*[1,2]*, *Tingting Chen*[1], *Shichao Miao*[1], *Shuai Li*[1], *Xinyang Xu*[1] and *Feng Gao*[1,2]

[1] *School of Precision Instruments and Optoelectronics Engineering, Tianjin University, Tianjin, China,* [2] *Tianjin Key Laboratory of Biomedical Detecting Techniques and Instruments, Tianjin University, Tianjin, China*

Optoacoustic imaging (OAI) or photoacoustic imaging can resolve the distribution of tissue chromophores and optical contrast agents deep inside tissue from the optoacoustic detection with multi-spectral illumination. The development of a fast and accurate modeling method for the photon transport in OAI is necessary to quantitatively evaluate the tissue optical parameters. This paper presents a parallelized Monte Carlo modeling method especially for OAI (MCOAI) to simulate photon transport in bio-tissues with arbitrary multi-angle wide-field illumination. The performance of the MCOAI method is verified by comparison with the graphics processing unit (GPU)-accelerated MCX method in the typical cases with the pencil beam and ring source illumination. The simulation results demonstrate the GPU-based MCOAI method has equivalent accuracy and significantly improved computation efficiency, compared to the MCX method. The simulations with cylindrical and hemispherical source illumination further illustrate that the MCOAI method can effectively implement three-dimensional photon transport simulation for typical illumination geometries of OAI systems. A cross-section of Digimouse is selected as a realistic heterogeneous phantom illuminated with six different light sources usually employed in OAI, in order to prove the necessity of establishing photon transport modeling in OAI for the quantitative visualization in deep tissues. The MCOAI method can provide a powerful tool to efficiently establish photon transport modeling with arbitrary illumination modes for OAI applications.

**Keywords: optoacoustic imaging, quantitative visualization, multi-angle wide-field illumination, Monte Carlo, graphics processing unit**

***Edited by:***
*Chao Tian,*
*University of Science and Technology of China, China*

***Reviewed by:***
*Zhen Yuan,*
*University of Macau, China*
*Xiaojing Gong,*
*Shenzhen Institutes of Advanced Technology (CAS), China*

***Correspondence:**
*Jiao Li*
*jiaoli@tju.edu.cn*

***Specialty section:***
*This article was submitted to Medical Physics and Imaging, a section of the journal Frontiers in Physics*

***Received:*** *15 April 2020*
***Accepted:*** *23 June 2020*
***Published:*** *31 July 2020*

***Citation:***
*Lu T, Li J, Chen T, Miao S, Li S, Xu X and Gao F (2020) Parallelized Monte Carlo Photon Transport Simulations for Arbitrary Multi-Angle Wide-Field Illumination in Optoacoustic Imaging. Front. Phys. 8:283. doi: 10.3389/fphy.2020.00283*

## INTRODUCTION

Optoacoustic imaging (OAI) or photoacoustic imaging is a hybrid imaging modality that can provide multi-scale optical visualization with high depth-to-resolution ratio in biological tissues [1–6]. The distribution of the initial acoustic pressure or absorbed light energy density $P_0$, is generally reconstructed from optoacoustic signals detected by ultrasonic transducers in traditional OAI methods. The initial acoustic pressure $P_0$ is the product of optical absorption coefficient and light fluence in the irradiated region [7, 8]. Since light fluence in the tissue is attenuated along the penetration depth, the result of traditional OAI, i.e., the distribution of $P_0$, cannot directly reflect the optical properties of deep tissues, such as optical absorption coefficient [9, 10]. To accurately reveal the optical functional information of deep tissues, a precise photon transport modeling approach is necessary to be developed for offering assistance to quantitative OAI methods.

As the gold standard for predicting distribution of light fluence in the biological tissue, the Monte Carlo (MC) simulation with strong applicability is preferred for the precise modeling with multi-angle wide-field illuminations usually employed in OAI systems. MC simulation methods have been widely developed for optical imaging modalities [11–16]. The MCML and MCXYZ methods by Wang et al. have been used to study light propagation in multi-layered tissues [11, 12]. Several light source modes have been realized including the pencil beam and the finite beam with a fixed incident direction, as well as the isotropic beam. An accelerated MCML has been developed to reduce the computation time based on graphics processing unit (GPU) [13]. The MMC and GPU-based MCX methods by Fang et al. provide more light source modes, containing the slit beam, the planar beam, and the cone beam, with the option of sinusoidal modulated amplitude [14, 15]. For the multi-angle wide-field illumination modes usually employed in OAI systems, the conventional MC methods can not simultaneously and randomly generate the initial angles and positions of emitted photons using the GPU framework. Thus, the number of initial angles and positions is limited due to the low computation efficiency of the central processing unit (CPU) framework. The limited number of initial positions produces great challenges for efficient light transport modeling of arbitrary multi-angle wide-field illumination modes in OAI systems, such as ring, cylindrical and hemispherical sources for typical OAI systems.

In this work, we present a MC approach based on GPU to quickly and accurately establish light transport modeling for OAI systems with arbitrary multi-angle wide-field illuminations, termed as MCOAI. The incident angles and positions of emitted photons can be simultaneously and randomly generated from their pre-set probability distributions in MCOAI, allowing its effective performance for simulating arbitrary light sources with GPU acceleration. By comparing with the MCX method, the accuracy of MCOAI method is verified in the simulation with the pencil beam illumination. Comparison results using the ring source mode in optoacoustic tomography indicate that the MCOAI method performs higher efficiency and greater precision than the MCX method. The proposed MCOAI method can also effectively achieve three-dimensional (3D) light transport simulation for cylindrical and hemispherical illumination modes usually employed in OAI systems. Finally, several illumination modes are set up for a cross-section of Digimouse, illustrating the necessity of MCOAI for the quantitative OAI.

# METHOD AND MODEL

## MCOAI Method

The MCOAI method can achieve simultaneous generation of both initial angles and positions of emitted photons by random numbers from pre-set probability distributions, or random selection from customized tables in the GPU framework. Owing to the sufficient number of initial angles and positions generated in the GPU framework, the MCOAI method can effectively conduct the precise photon transport modeling of arbitrary 3D media illuminated by arbitrary multi-angle wide-field light sources. In Cartesian coordinates, all objectives are uniformly divided into voxels. Optical properties of the media, such as absorption coefficient $\mu_a$, scattering coefficient $\mu_s$, scattering anisotropy factor g and refractive index n, are assigned to each voxel. The incident beam is simulated by emitting photon packets, whose trajectories are calculated in the media. Probability models and pseudorandom number generators are utilized to determine the initial position and direction, the path length between two adjacent scattering events, the scattering angle, transmission or reflection, as well as termination of the photon packet. As photons propagate from one voxel to the next, they deposit some energy ("weight") into the voxel, depending on absorption coefficient $\mu_a$ of the voxel. Photons are tracked until terminated in Russian roulette or escaping from the media boundary. The deposited energy is digitally accumulated in a 3D matrix, and is normalized to output power at the end of the simulation. **Figure 1** illustrates the flowchart of MCOAI for the multi-angle wide-field illumination mode.

In MCOAI, the random number is randomly generated in [0, 1]. For the ring source with the radius of $r$ in the plane of $z = z_0$, a random number $R_0$ is used to obtain the longitude angle $\phi = 2\pi R_0$ uniformly distributed in [0, 2π]. After an initialized direction $\phi$ is randomly generated, the initialized position $\mathbf{r_s}$ and the direction vector $\overrightarrow{v_s}$ can be expressed as

$$\begin{cases} \mathbf{r_s} = \left(r\cos(2\pi R_0), r\sin(2\pi R_0), z_0\right) \\ \overrightarrow{v_s} = \left(-\cos(2\pi R_0), -\sin(2\pi R_0), 0\right) \end{cases}. \tag{1}$$

For the cylindrical source with the radius of $r$ and the height of H, a random number $R_1$ is employed to produce the longitude angle $\phi = 2\pi R_1$, and another random number $R_2$ is used to compute the elevation position $h = HR_2$ randomly distributed in [0, H]. The initialized position $\mathbf{r_s}$ and the direction vector $\overrightarrow{v_s}$ can be expressed as

$$\begin{cases} \mathbf{r_s} = \left(r\cos(2\pi R_1), r\sin(2\pi R_1), HR_2\right) \\ \overrightarrow{v_s} = \left(-\cos(2\pi R_1), -\sin(2\pi R_1), 0\right) \end{cases}. \tag{2}$$

For the hemispherical source with the radius of $r$, two random numbers $R_3$ and $R_4$ are used to generate the longitude angle $\phi = 2\pi R_3$ and latitude angle $\theta = \pi R_4/2$, respectively. The initialized position $\mathbf{r_s}$ and direction vector $\overrightarrow{v_s}$ can be expressed as

$$\begin{cases} \mathbf{r_s} = \left(r\sin(\pi R_4/2)\cos(2\pi R_3), r\sin(\pi R_4/2)\sin(2\pi R_3),\right. \\ \left. r\cos(\pi R_4/2)\right) \\ \overrightarrow{v_s} = \left(-\sin(\pi R_4/2)\cos(2\pi R_3), -\sin(\pi R_4/2)\sin(2\pi R_3),\right. \\ \left. -\cos(\pi R_4/2)\right) \end{cases}. \tag{3}$$

For other types of source mode, the initial direction and position of emitted photon can be customized aforehand, and then the random extraction is adopted to randomly obtain these parameters based on the probability distributions. For light source models with uneven light intensity distribution, packet weights at different

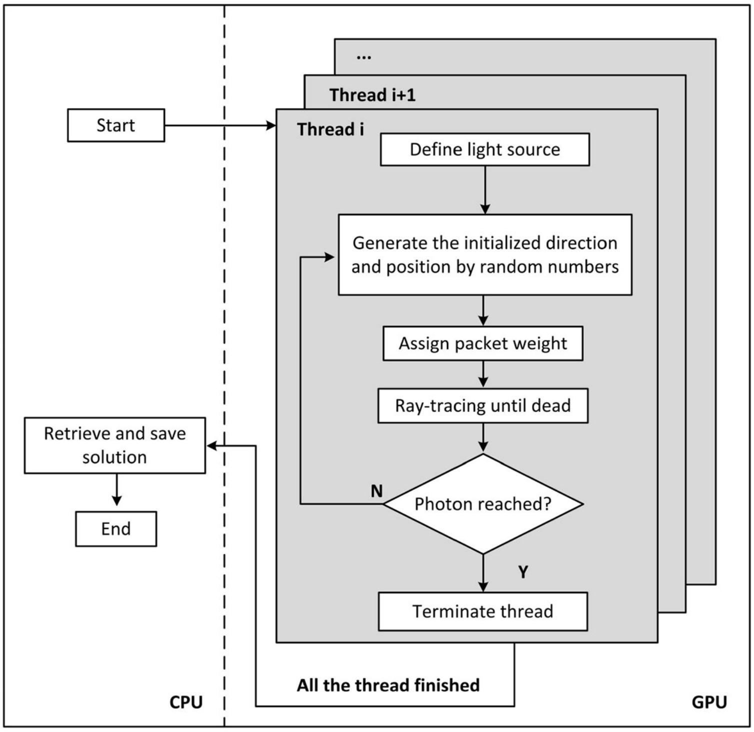

**FIGURE 1 |** Diagram of the MCOAI simulation for photon transport. The multi-angle wide-field illumination mode is established through randomly generating initialized direction and position for each emitted photon.

initialized positions can be prepared beforehand. The packet weight of emitted photon at a certain initialized position $\mathbf{r_s}$ is $W(\mathbf{r_s})$, depending on the light intensity at the position $\mathbf{r_s}$.

## Simulation Set-Up

A total of $10^8$ photons are launched in the simulation of the proposed MCOAI method. One hundred and twenty-eight threads are set for parallel calculation. Four simulated samples are employed to validate the performance of the MCOAI method. The optical properties of the samples are set as the representative values in the optical window [16]. The MCOAI and MCX methods are run on the same computer with an NVIDIA GTX 750 GPU with 64 GB memory.

*1) Sample 1: A homogeneous cube:* A cubic domain of 60 mm × 60 mm × 60 mm is simulated shown in **Figure 2**. The volume is from −3 to +3 cm in *x* and *y axis*, and from 0 to 6 cm in *z axis*, with the number of grids in each axis of 60. The pencil beam is located at $\mathbf{r_s} = (30,30,0)$ with an incident direction vector $\overrightarrow{v_s} = (0,0,1)$; the medium is homogeneous with the absorption coefficient $\mu_a = 0.01\ \text{mm}^{-1}$, the scattering coefficient $\mu_s = 10\ \text{mm}^{-1}$, the refractive index $n = 1.37$ and the anisotropy $g = 0.9$.
*2) Sample 2: A homogeneous cylinder:* A cylinder sample with the center located at (6, 6, 8) mm has a radius of 5 mm and a height of 6 mm. The voxel size is 50 µm × 50 µm × 50 µm to build the accurate curved boundary. The optical properties for the cylinder are $\mu_a = 0.1\ \text{mm}^{-1}$, $\mu_s = 10\ \text{mm}^{-1}$, $n = 1.37$ and $g = 0.9$. A ring source with the radius of 5 mm is located at the plane of $z = 8$ mm, shown in **Figure 3A**. **Figure 4A** illustrates a 3D cylindrical illumination distributed around the cylinder boundary.
*3) Sample 3: A homogeneous hemisphere:* A hemisphere sample centered at (6, 6, 6) mm has a radius of 5 mm. The voxel size and optical properties of the hemisphere are the same as those of the Sample 2. **Figure 4C** shows a hemispherical illumination distributed around the hemisphere surface.
*4) Sample 4: Cross-section of Digimouse:* A cross-section of the widely-used Digimouse atlas has been chosen as a more realistic tissue sample. $g = 0.9$ and $n = 1.37$ are set to be homogeneous in the sample. $\mu_a$ and $\mu_s$ of the sample are shown in **Table 1**. Several types of light sources are simulated, including the finite-width light-sheet illumination from one side (left, right, top, or bottom) and four sides, as well as ring light-sheet illumination.

## RESULTS AND DISCUSSION

To evaluate the accuracy of the MCOAI method, a comparison with the MCX method is implemented using the pencil beam to illuminate Sample 1. The fluence maps at the plane of $y = 30$ mm from the MCOAI and MCX results are presented in **Figures 2A,B**, respectively. The fluence contours with 10 dB spacing are also displayed in **Figure 2C**. The MCOAI result matches well with the MCX result in both fluence maps and

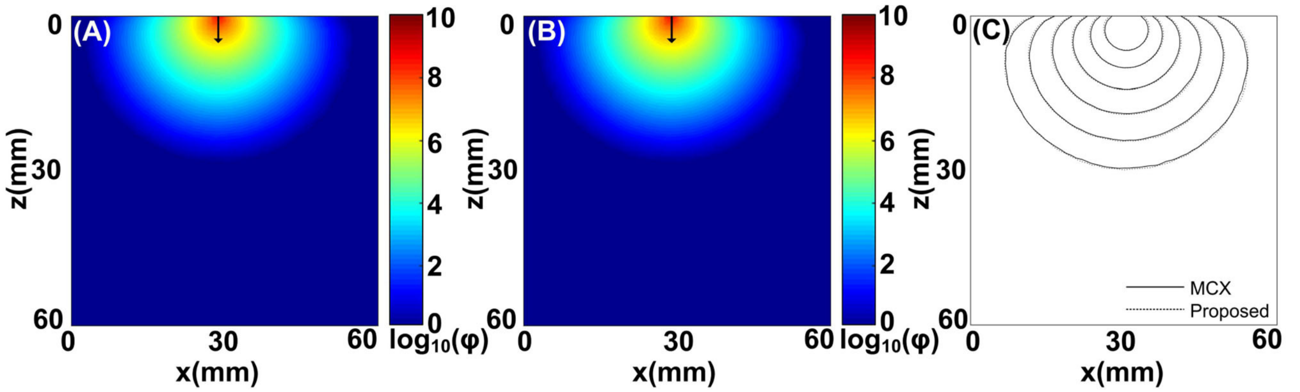

**FIGURE 2 |** Comparisons between the MCOAI and MCX methods using the pencil beam to illuminate a cube (Sample 1): **(A)** the fluence map along the plane of $y = 30$ mm from the MCOAI result, **(B)** the fluence map along the plane of $y = 30$ mm from the MCX result, and **(C)** the fluence contours with 10 dB spacing along the plane of $y = 30$ mm. $\phi$ is the light fluence.

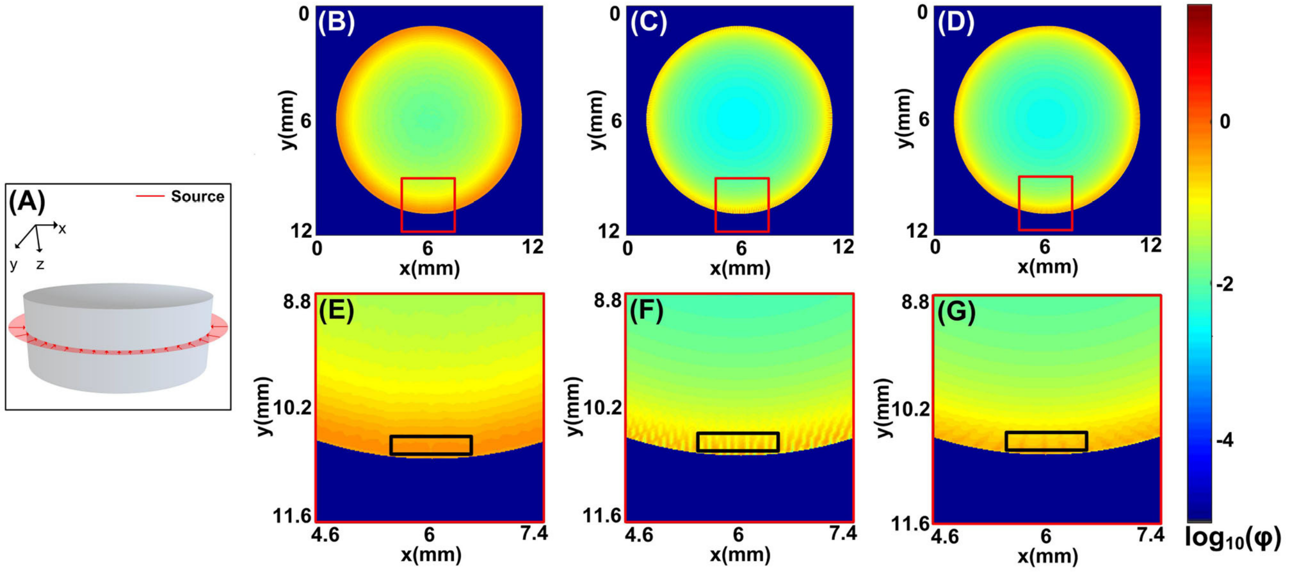

**FIGURE 3 |** Comparisons between the MCOAI and MCX methods using the ring source to illuminate the cylinder sample (Sample 2): **(A)** the ring source located at the plane of $z = 8$ mm, **(B)** the fluence map at the plane of $z = 8$ mm from the MCOAI result, **(C)** the fluence map at the plane of $z = 8$ mm from the MCX result of 360 sources, **(D)** the fluence map at the plane of $z = 8$ mm from the MCX result of 720 sources, **(E–G)** the enlarged details of the fluence map in **(B–D)**. $\phi$ is the light fluence.

contours, presenting the accurate performance of the MCOAI method. To quantitatively assess the accuracy of MCOAI result in **Figure 2**, the root mean square error (RMSE) has been calculated to show the difference between the MCOAI result and the MCX result. The RMSE is defined as

$$\mathrm{RMSE} = \sqrt{\sum_{n=1}^{N} \left(r_{\mathrm{MCX}}(n) - r_{\mathrm{MCOAI}}(n)\right)^2 \Big/ N}, \quad (4)$$

where $N$ is the total number of the image pixels, $r_{\mathrm{MCX}}(n)$ and $r_{\mathrm{MCOAI}}(n)$ are the values of fluence maps at the $n$th pixel in the MCX result and MCOAI result, respectively. The RMSE value between **Figures 2A,B** is 0.0008, indicating high consistency of the MCOAI result and the MCX result.

To demonstrate the fast and accurate modeling of the MCOAI method for the multi-angle wide-field illumination mode, a cylindrical sample (Sample 2) in **Figure 3A** has been chosen, with a ring source illumination usually employed in OAI. The calculation time of the MCOAI and MCX methods is illustrated in **Table 2**. The run time of MCOAI is 1.7 min. In the MCX method, amounts of pencil beam sources are set at the assigned positions around the cylinder boundary. The MCX simulations

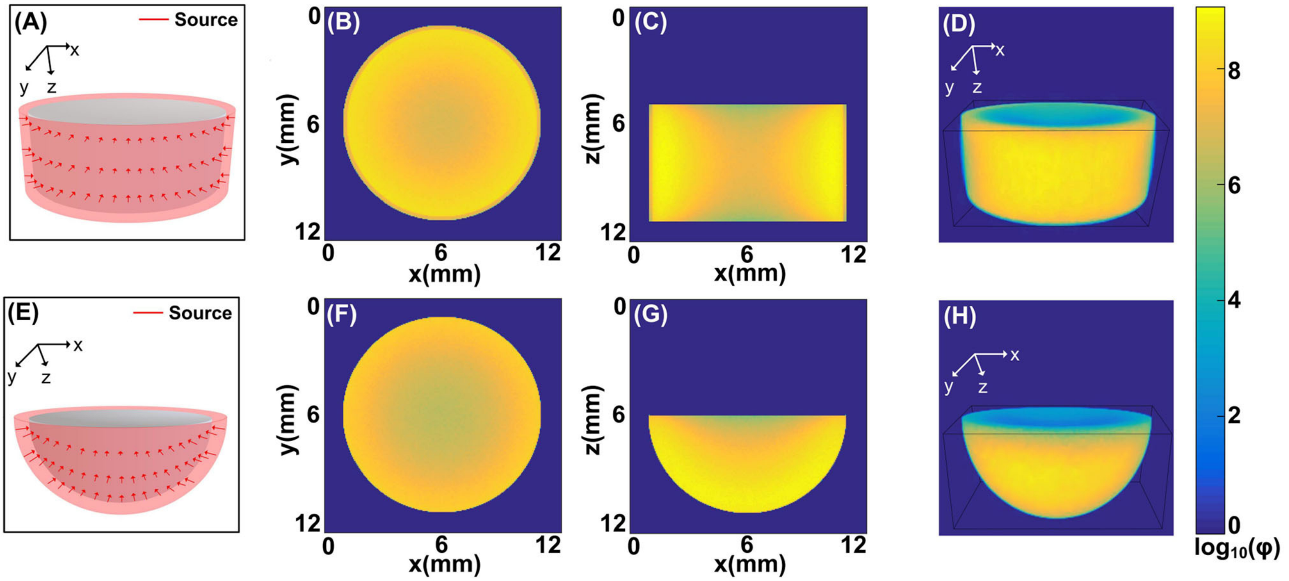

**FIGURE 4 |** The illumination modes achieved by the MCOAI method: **(A)** the cylindrical source mode to illuminate the cylinder sample (Sample 2), **(B)** the fluence map at the plane of $z = 9$ mm from the MCOAI result, **(C)** the fluence map at the plane of $y = 6$ mm from the MCOAI result, and **(D)** the corresponding 3D view of the fluence map; **(E)** the hemispherical source mode to illuminate the hemisphere sample (Sample 3), **(F)** the fluence map at the plane of $z = 6$ mm from the MCOAI result, **(G)** the fluence map at the plane of $y = 6$ mm from the MCOAI result, and **(H)** the corresponding 3D view of the fluence map.

**TABLE 1 |** Optical properties of Sample 4.

| Tissue ID | Tissue type | $\mu_a$(mm$^{-1}$) | $\mu_s$(mm$^{-1}$) |
|---|---|---|---|
| #1 | Skin | 0.0191 | 6.6 |
| #2 | Skeleton | 0.0136 | 8.6 |
| #3 | Liver | 0.072 | 5.6 |
| #4 | Pancreas | 0.072 | 5.6 |
| #5 | Kidneys | 0.050 | 5.4 |

**TABLE 2 |** Calculation time of the MCOAI and MCX methods.

| | Method | Time (Minute) |
|---|---|---|
| | MCOAI | 1.7 |
| MCX | 360 sources | 40 |
| | 720 sources | 80 |

with 360 and 720 pencil beam sources ($10^8$ photons for each beam) to form the ring illumination take the calculation time of 40 and 80 min, respectively. A total of $10^8$ photons are launched for the proposed MCOAI method. For each emitted photon, the initial angle and position are randomly generated. Thus, a total of $10^8$ initial angles and positions are randomly generated. With the sufficient number of photons (or the number of randomly generated initial angles and positions) and GPU acceleration, the computation time of the proposed MCOAI method is much faster than the MCX method.

The fluence maps at the plane of $z = 3$ mm from the MCOAI and MCX results are shown in **Figures 3B–D**. The zoom-in images at the curved boundary are, respectively, illustrated in **Figures 3E–G**. Although the distributions of fluence maps by the three MC simulations are generally similar in **Figures 3B–D,** the detailed image of fluence at the boundary in **Figure 3E** is obviously smoother and more authentic than the images in **Figures 3F,G**. Since $10^8$ photon packets are emitted at random initialized positions along the ring shape in the MCOAI method, the finite number of initialized positions set in the MCX method is much less than the number in the MCOAI method, resulting in the uneven fluence distributions at the boundary in the MCX results. The comparison results of the focused light illumination in **Figure S1** are consistent with the results of the ring source in **Figure 3**. The standard deviation (SD) has been calculated to analyze the regional uniformity of the MCOAI and MCX results indicated by the black squares in **Figures 3E–G**. The SD is defined as

$$\mathrm{SD}(r) = \sqrt{\sum_{n=1}^{N} (r(n) - r_{\mathrm{mean}})^2 \Big/ N}, \tag{5}$$

where $r(n)$ is the value of fluence map at the $n$th pixel and $r_{\mathrm{mean}}$ is the mean value in the black square. The SD values of the MCOAI result, the MCX result of 360 sources and the MCX result of 720 sources are 0.0142, 0.0828, and 0.0520, respectively. The lowest SD value of the MCOAI result indicates the highest uniformity. The higher fidelity and efficiency of the MCOAI method can be attributed to introducing the random generation approach for the incident angle and position of each emitted photon into

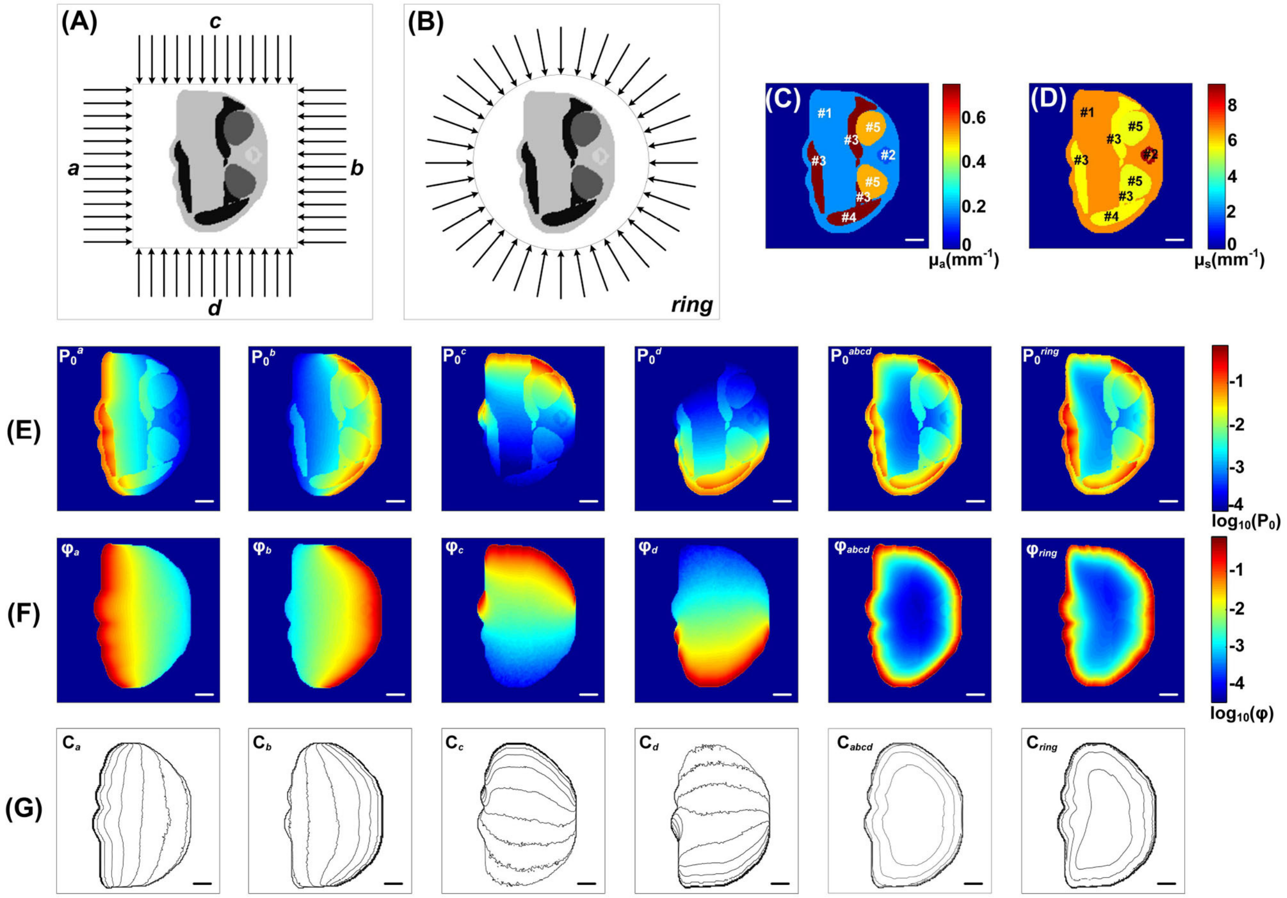

**FIGURE 5 |** Simulation of the Sample 4 under different light illumination modes by the MCOAI method: **(A)** finite-width light-sheet illumination from left (*a*), right (*b*), top (*c*), and bottom (*d*) side, as well as four sides (*abcd*); **(B)** ring light-sheet illumination; **(C)** pseudo-color image of the absorption coefficient $\mu_a$; **(D)** pseudo-color image of the scattering coefficient $\mu_s$; **(E)** images of initial acoustic pressure $P_0$ under the finite-width light-sheet illumination from each side as well as four sides, and under the ring light-sheet illumination; **(F)** images of fluence $\phi$ under the finite-width light-sheet illumination from each side as well as four sides, and under the ring light-sheet illumination; **(G)** the corresponding fluence contours (with 10 dB spacing). Scale bar, 2 mm.

the parallel computing framework. Therefore, MCOAI method is more appropriate to accurately and quickly establish multi-angle wide-field illumination modes for optoacoustic tomography.

Furthermore, two typical 3D source modes (**Figures 4A,E**) usually existed in OAI are illustrated by MCOAI method. For the cylindrical illumination mode, the fluence maps at the planes of $z = 9$ mm, $y = 6$ mm and 3D view are presented in **Figures 4B–D**. For the hemispherical illumination mode, the fluence maps at the planes of $z = 6$ mm, $y = 6$ mm and 3D view are displayed in **Figures 4F–H**. The boundary and interior distributions of fluence maps in two homogeneous media are smooth and authentic owing to the sufficient incident positions generated randomly. The results demonstrate the light transport modeling in 3D simulation with multi-angle wide-field illumination modes can be efficiently and accurately established by the proposed MCOAI method.

This MCOAI approach is further used to simulate various light illumination modes on a cross-section of Digimouse (Sample 4) shown in **Figure 5**. The optoacoustic tomography technology has been widely employed for the whole-body small-animal imaging by integrating lots of cross-section images. The cross-section of Digimouse containing several main organs listed in **Table 1** is selected.

The MCOAI method was further utilized to illustrate the necessity for quantitatively evaluating functional information of biological tissue from OAI results. **Figures 5C,D** present the grayscale images of $\mu_a$ and $\mu_s$ of Sample 4, indicating the heterogeneity in different organs. **Figure 5E** shows the images of initial acoustic pressure P of Sample 4 using six different illumination modes. As displayed in the first four columns of **Figure 5E** using one-sided illumination, the intensity distribution of targets and background in the P images plummet when moving away the light source. In the last two columns of **Figure 5E**, due to the illumination modes are both full-angle wide-field, the P images are closer to the $\mu_a$ images while still presenting obvious differences. The results show the P image cannot directly reflect accurate quantitative distributions of $\mu_a$ in the sample, affected by the light attenuation along tissue depth.

The fluence maps under these six different illumination modes are shown in **Figure 5F**, and the contours with 10 dB spacing are also displayed in **Figure 5G**. The light fluence ϕ in deep tissues is attenuated along the penetration depth, thus the fluence distributions in the region near the light source are higher than those in the region far from the light source. Under the finite-width light-sheet illumination modes only from one side, the heterogeneous distribution of ϕ is extremely evident. Under the four-sided light-sheet and ring light-sheet illumination modes, the Sample 4 receives full-angle wide-field irradiation, the fluence maps ϕ are attenuated from boundary to center. The results demonstrate the MCOAI method should be utilized to provide the fluence distribution of ϕ, in order to quantitatively recover the distribution of optical properties.

## CONCLUSION

To quantitatively evaluate the optical properties of the biological tissues, it becomes essential to develop an efficient and precise photon transport modeling method for multi-angle wide-field illumination modes usually employed in OAI systems. In this work, we present the MCOAI method to randomly generate the incident angles and positions of emitted photons based on parallel computing framework for efficiently simulating arbitrary wide-field light sources. The MCOAI method can offer the same accuracy in the simulation using pencil beam as the MCX method. However, the MCOAI method for the multi-angle wide-field light sources, such as the ring source, is capable of providing more accurate and authentic distributions of light fluence in a few tenths of the time, compared to the MCX method. The GPU framework has been utilized in both the MCX method and the MCOAI method for acceleration. For the pencil beam and planar beam in the MCX method, the initial angles and positions of emitted photons are generated in the GPU framework. However, for the multi-angle wide-field illumination modes usually employed in OAI systems, the MCX method can not simultaneously and randomly generate the initial angles and positions of emitted photons in the GPU framework. The proposed MCOAI method can achieve simultaneous generation of both initial angles and positions of emitted photons by random numbers in the GPU framework, greatly reducing the running time. If the optical properties of samples at the selected wavelength in visible or near-infrared spectrum can be determined, the light transport modeling at any selected wavelength can be achieved by the proposed MCOAI method. The proposed method has been demonstrated with typical illumination modes and uniform light intensity, which can be explored on user-defined illumination modes and uneven light intensity for further study. The MCOAI method is able to precisely conduct the light transport modeling for all typical OAI systems, having great potential of contributing to the further investigation of quantitative OAI methods. In this work, the MCOAI method focuses on providing an accurate light transport simulation for the forward modeling in quantitative OAI, not involving the inverse problems. The MCOAI method is designed to be an open source for user-friendly employment.

## DATA AVAILABILITY STATEMENT

Publicly available datasets were analyzed in this study. The data of this article will be made available by the authors to any qualified researcher.

## AUTHOR CONTRIBUTIONS

JL and FG guided the work. TL did the simulation. TC, SM, SL, and XX gave the guide for analysis. JL and TL wrote the manuscript. All authors contributed to the article and approved the submitted version.

## FUNDING

This work was supported by the grants from the National Natural Science Foundation of China (Grant Nos. 81771880, 81401453, 81671728, 81871393, and 81971656) and Tianjin Municipal Government of China (19JCQNJC12800).

## SUPPLEMENTARY MATERIAL

The Supplementary Material for this article can be found online at: https://www.frontiersin.org/articles/10.3389/fphy.2020.00283/full#supplementary-material

## REFERENCES

1. Wang LV, Yao J. A practical guide to photoacoustic tomography in the life sciences. *Nat Methods.* (2016) **13**:627–38. doi: 10.1038/nmeth.3925
2. Liu Y, Nie L, Chen X. Photoacoustic molecular imaging: from multiscale biomedical applications towards early-stage theranostics. *Trends Biotechnol.* (2016) **34**:420–33. doi: 10.1016/j.tibtech.2016.02.001
3. Zhou Y, Yao J, Wang LV. Tutorial on photoacoustic tomography. *J Biomed Opt.* (2016) **21**:061007. doi: 10.1117/1.JBO.21.6.061007
4. Wang LV. Multiscale photoacoustic microscopy and computed tomography. *Nat Photonics.* (2009) **3**:503–9. doi: 10.1038/nphoton.2009.157
5. Lu T, Wang Y, Zhang S, Li J. Photoacoustic mesoscopy:pushing toward the depth limit in the high-resolution optical imaging for biomedical applications and clinical potentials. *Instrumentation.* (2016) **3**:29–42.
6. Taruttis A, Ntziachristos V. Advances in real-time multispectral optoacoustic imaging and its applications. *Nat Photonics.* (2015) **9**:219–27. doi: 10.1038/nphoton.2015.29
7. Yuan Z, Jiang H. Quantitative photoacoustic tomography. *Philos Trans A Math Phys Eng Sci.* (2009) **367**:3043–54. doi: 10.1098/rsta.2009.0083
8. Cox B, Laufer JG, Arridge SR, Beard PC. Quantitative spectroscopic photoacoustic imaging: a review. *J Biomed Opt.* (2012) **17**:061202. doi: 10.1117/1.JBO.17.6.061202
9. Wang Y, He J, Li J, Lu T, Li Y, Ma W, et al. Toward whole-body quantitative photoacoustic tomography of small-animals with multi-angle light-sheet illuminations. *Biomed Opt Express.* (2017) **8**:3778–95. doi: 10.1364/BOE.8.003778
10. Zemp RJ. Quantitative photoacoustic tomography with multiple optical sources. *Appl Opt.* (2010) **49**:3566–72. doi: 10.1364/AO.49.003566

11. Wang LV, Jacques SL, Zheng L. MCML-Monte Carlo modeling of light transport in multi-layered tissues. *Comput Methods Programs Biomed.* (1995) **47**:131–46. doi: 10.1016/0169-2607(95)01640-F
12. Jacques SL. Coupling 3D Monte Carlo light transport in optically heterogeneous tissues to photoacoustic signal generation. *Photoacoustics.* (2014) **2**:137–42. doi: 10.1016/j.pacs.2014.09.001
13. Alerstam E, Svensson T, Andersson-Engels S. *CUDAMCML: User Manual and Implementation Notes*. Sweden: Department of Physics, Lund University (2009). p. 1–33.
14. Fang Q. Mesh-based Monte Carlo method using fast ray-tracing in Plücker coordinates. *Biomed Opt Express.* (2010) **1**:165–75. doi: 10.1364/BOE.1.000165
15. Fang Q, Boas DA. Monte Carlo simulation of photon migration in 3D turbid media accelerated by graphics processing units. *Opt Express.* (2009) **17**:20178–90. doi: 10.1364/OE.17.020178
16. Hong G, Antaris AL, Dai H. Near-infrared fluorophores for biomedical imaging. *Nat Biomed Eng.* (2017) **1**:1–22. doi: 10.1038/s41551-016-0010

**Conflict of Interest:** The authors declare that the research was conducted in the absence of any commercial or financial relationships that could be construed as a potential conflict of interest.

frontiers
in Physics

ORIGINAL RESEARCH
published: 29 October 2020
doi: 10.3389/fphy.2020.581519

# Perfluorocarbon-Loaded Hydrogel Microcapsules from Interface Shearing for Magnetic Guided Ultrasound and Laser Activation

*Zhiqiang Zhu*[1,2]*, Ming Zhang*[1,2]*, Yuanqing Zhu*[1,2]*, Fangsheng Huang*[1,2]*, Ting Si*[2,3]** and Ronald X. Xu*[1,2,4]

[1] *Department of Precision Machinery and Precision Instrumentation, University of Science and Technology of China, Hefei, China,* [2] *Key Laboratory of Precision Scientific Instrumentation of Anhui Higher Education Institutes, University of Science and Technology of China, Hefei, China,* [3] *Department of Modern Mechanics, University of Science and Technology of China, Hefei, China,* [4] *Department of Biomedical Engineering, The Ohio State University, Columbus, OH, United States*

Stimuli-responsive microcarriers have received considerable attention in a variety of fields, including disease diagnosis, drug delivery, sensing, and imaging. Here, we report the generation of multiple-responsive perfluorocarbon-loaded magnetic hydrogel microcapsules (PMHMs) with uniform size for magnetic controlled ultrasound (US) and laser activation. The PMHMs are fabricated by a novel coaxial interface shearing (CIS) method based on the mechanism of liquid bridge formation and fracture. Perfluorocarbon and iron oxide magnetic nanoparticles are used as US-responsive and photothermal absorption medium, respectively, and magnetic nanoparticles are also used for magnetic-controlled targeting. Moreover, the size, structure, and function of the prepared biocompatible PMHMs can be precisely controlled by adjusting the process parameters of CIS. It is indicated that the PMHMs have different US- and light-responsive characteristics, mainly because of the difference of their activation mechanisms. It is demonstrated that laser has better activation resolution and can achieve site-specific activation and drug release of PMHMs. The multiple-responsive features imply that the PMHMs fabricated by CIS may provide an effective drug release platform for biomedical and pharmaceutical applications.

**Keywords: microfluidics, microcapsule, drug delivery, ultrasound, laser activation**

***Edited by:***
*Zhaoyu Li,*
*University of Queensland, Australia*

***Reviewed by:***
*Yukun Ren,*
*Harbin Institute of Technology, China*
*Lingling Shui,*
*South China Normal University, China*

****Correspondence:***
*Ting Si*
*tsi@ustc.edu.cn*

***Specialty section:***
*This article was submitted to Medical Physics and Imaging, a section of the journal Frontiers in Physics*

***Received:*** *09 July 2020*
***Accepted:*** *22 September 2020*
***Published:*** *29 October 2020*

***Citation:***
*Zhu Z, Zhang M, Zhu Y, Huang F, Si T and Xu RX (2020) Perfluorocarbon-Loaded Hydrogel Microcapsules from Interface Shearing for Magnetic Guided Ultrasound and Laser Activation. Front. Phys. 8:581519. doi: 10.3389/fphy.2020.581519*

## INTRODUCTION

The advanced drug delivery system (DDS) can deliver drugs to the target organ, and effectively adjust the physicochemical properties of the drug, to improve treatment effect, reduce toxic and side effects, and save treatment cost [1–5]. As a novel DDS, stimuli-responsive microcarriers (SRMs) can release drugs on demand under stimuli, which can further manipulate drug release behaviors and improve therapeutic effect [4, 5]. The physicochemical properties of SRMs, such as size, structure, shape, and composition are vital for drug release process under stimuli. Commonly used stimuli methods include physical- (such as light, heat, electric field, and ultrasound) and chemical-based stimuli methods (such as enzymes, pH, and glucose). The emerging physical-based stimuli methods such as ultrasound (US) and laser offer a convenient and robust controlled drug release platform and have attracted extensive interest [6–13].

However, most existing SRMs lack precise structural and functional design and control. Meanwhile, the application of SRMs in biomedicine and other fields needs further exploration and research.

The emergence of microfluidic technology provides strong technical support for the preparation of complex emulsions with high controllability over size, structure, and properties, which offers excellent conditions for further preparation of advanced DDS (such as microparticles, microcapsules, and microgels) [14–18]. Generally, commonly used droplet microfluidic devices mainly include glass capillary- [19–24], PDMS- [25–30], metal capillary- [31–39], and 3D printing-based [40–43] devices. According to the mechanism of droplet generation, droplet generation methods are mainly divided into active and passive. Notably, in most commonly used passive droplet generation methods, the physicochemical parameters of the fluids and microfluidic devices all affect the size and uniformity of produced complex emulsions [44–47]. Therefore, it is of considerable significance to develop accurate and reliable methods to prepare SRMs and further explore their applications in biomedicine and other fields.

In this work, an active droplet generation method based on coaxial interface shearing (CIS) [48, 49] was proposed to prepare monodisperse multiple-responsive perfluorocarbon-loaded magnetic hydrogel microcapsules (PMHMs), as illustrated in **Figure 1**. Perfluorocarbon (PFC) was used as a kind of US-responsive agent, and iron oxide magnetic nanoparticles (MNPs) were used as magnetic attraction and light absorption medium in the PNIPAM hydrogel shell. The CIS experimental system was easy to set up and can prepare double emulsions quickly and stably at a very low cost. Based on interface shearing mechanism, the double emulsions were formed when the liquid bridge was pulled off. In addition, the size of the double emulsion was determined only by the flow rate and vibration frequency, and can be accurately controlled in a broad range. By adjusting the relevant experimental parameters, the PFC-loaded NIPAM core-shell droplet with different sizes and structures can be easily prepared. It has been demonstrated that the PMHMs can make directional movement under the control of the external magnetic field. Under the activation of ultrasound or laser, the PFC core underwent a liquid-gas phase transition and expanded rapidly and exploded. These multiple-responsive abilities of the PMHMs open up new possibilities for their practical application in the fields of biology and medicine.

# MATERIALS AND METHODS

## Materials and Reagents

N-isopropylacrylamide (NIPAM; Mw: 113 g/mol), N,N′-methylenebis (acrylamide) (MBA; Mw: 154 g/mol), 2,2′-azobis (2-methylpropionamidine) dihydrochloride (V50; Mw: 271 g/mol), 2,2-dimethoxy-2-phenylacetophenone (BDK; Mw: 256 g/mol) were purchased from Shanghai Aladdin Biochemical Technology Co., Ltd (Shanghai, China). Span 80, poly (vinyl alcohol) (PVA; Mw: 13,000–23,000 g/mol), Iron oxide (II, III) magnetic nanoparticle (MNPs; Mw: 231 g/mol, 20 nm) was purchased from Shanghai Macklin Biochemical Co., Ltd (Shanghai, China). 1,1,1,2,3,4,4,5,5,5-decafluoropentane (Mw: 252 g/mol, bp: 55°C) were purchased from Sigma-Aldrich LLC (St. Louis, MO, USA). Mineral oil was purchased from Sinopharm Chemical Reagent Co., Ltd (Shanghai, China). Ultrapure deionized water was generated by a Direct-Q® Water Purification System (Merck KGaA, Darmstadt, Germany).

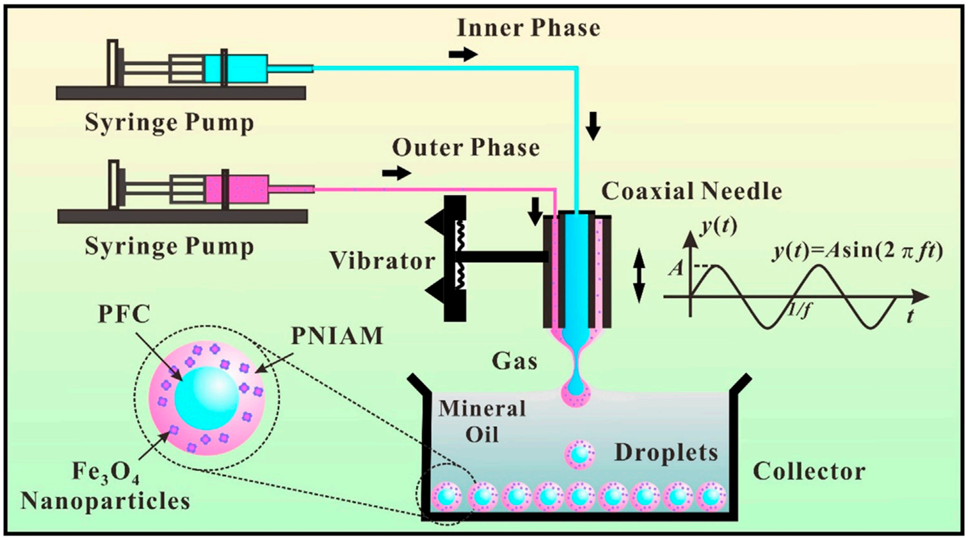

**FIGURE 1 |** Schematic illustration of an on-demand coaxial interface shearing (CIS) double emulsion generation system including a coaxial needle, two syringe pumps, an electric vibrator, and a collecting pool.

## Coaxial Interface Shearing Double Emulsion Generation System

The CIS process can be described as the formation and rupture of a compound liquid bridge for on-demand generation of multiple emulsions when a coaxial needle supplying liquids vibrates periodically across a free gas-liquid surface. Two precision injection pumps (LSP02-2A, Longer Precision Pump Co., Ltd, China) were used to provide inner and outer fluids to the coaxial needle, composed of an inner needle (28G) and an outer needle (21G). The two needles were adjusted to high concentricity under a microscope. A signal generator (DG1022U, RIGOL Electronic, China) was used to generate the excitation waveform, and a power amplifier (SA-PA080, Wuxi Shiao Technology Co., Ltd, China) was used to drive an electric vibrator (JZK-2, SHIAO, China) and the coaxial needle to vibrate. The NIPAM double emulsions were generated during the upward movement of the coaxial needle and sank into the bottom of the quartz pool due to high density. A CCD camera (DFK 23G274, The Imaging Source, LLC, USA) connected to a computer was used to monitor the NIPAM double emulsions generation process from one side of the quartz pool, and a strobe light (3 kHz, PN-01D, Hangzhou Pintoo Electronic Technology Co., Ltd, China) was used to illuminate from the other side of the quartz pool.

## Crosslinking Process and Morphology Analysis of Perfluorocarbon-Loaded Magnetic Hydrogel Microcapsules

After the generation of double emulsions, an UV LED light (DSX-UVP60, 365 nm, 9.9 W/cm$^2$, Shenzhen Deshengxing Electronics Co., Ltd, China) was used to crosslink the NIPAM outer shell. The distance between the light and the samples was set as 20 cm. The collected double emulsions were converted into PMHMs after the UV light irradiation crosslinking for 3 min. Optical images of the PMHMs were achieved by an optical microscope (SZX7, OLYMPUS Corp, Tokyo, Japan). Image-Pro and Origin 2017 software were used to analyze the size of the produced PMHMs. The polydispersity index (PDI) of the double emulsion was calculated by the standard deviation (SD) divided by the mean value of diameter.

## Magnetic Controlled Movement and Activation of Perfluorocarbon-Loaded Magnetic Hydrogel Microcapsules

For magnetic controlled movement of PMHMs, the produced PMHMs were placed into a glass rectangular slot (length: 12, width: 2, height: 1 mm) filled with mineral oil. Two cuboid NdFeB magnets (length: 40, width: 20, height: 5 mm) were used to control the movement of the PMHMs. The initial distance between the magnet and the microcapsule was 10 mm. The magnetic attraction process of the PMHMs under magnetic field was recorded by a microscope equipped with a CCD camera (MSX2-H, Mshot Photoelectric Technology Co., Ltd, China).

For US activation of PMHMs, several PMHMs were placed in a 96-well plate filled with mineral oil and coupling agent was applied to the bottom of the well plate. An ultrasonic therapeutic apparatus (UT1041, Shenzhen Dundex Technology Co., Ltd, China) with a probe of 5 cm$^2$ was used to activate the PMHMs.

For laser activation of PMHMs, several PMHMs were placed in a Petri dish filled with mineral oil. A near-infrared (NIR) laser (808 nm, 0.5 W, Shenzhen Fulei Laser Technology Co., Ltd, China) was used to active the PMHMs. A lens was used to focus the laser to increase the laser energy density, and the PMHM explosion process was also captured by the Mshot CCD.

# RESULTS AND DISCUSSION

## Coaxial Interface Shearing Process and Analysis

The on-demand CIS double emulsion generation system is illustrated in **Figure 1**. The experimental system mainly consists of three parts: the first part is liquid supply system, the second part is mechanical vibration system, and the last part is droplet generation and collection system. The initial position of the end of the coaxial needle is adjusted to be flush with the liquid level in the quartz pool. The vibration process of the coaxial needle meets the standard sine function, and the vibration amplitude and frequency can be precisely adjusted within a certain range. The double emulsions are generated during the process of the coaxial needle passing through the gas-liquid interface periodically. In a typical NIPAM double emulsions generation process, the inner phase is 1,1,1,2,3,4,4,5,5,5-decafluoropentane. The outer phase is 11.3% (w/v) monomer NIPAM, 10% (w/v) crosslinker MBA, 0.5% (w/v) initiator V50, and 2% (w/v) MNPs dissolved in 10% (w/v) PVA aqueous solution. The stationary phase is mineral oil with 11.3% (w/v) Span 80 and 0.5% (w/v) crosslinker BDK. When the process parameters such as inner and outer flow rates ($Q_i$, $Q_o$), vibration frequency ($f$), and amplitude ($A$) are suitable, double emulsions can be prepared stably (Supplementary Video 1). It is worth noting that other types of double emulsions (such as W/O/W, O/O/W, and W/W/O) can also be produced by the CIS process [48, 49].

When the coaxial needle contacts the stationary phase, a liquid bridge will be formed between them because of capillary force. The external envelope shape of the liquid bridge satisfies the Young-Laplace differential equation [49]. With the inner and outer phase fluids flowing through the coaxial needle, an inner meniscus and an outer meniscus are formed at the end of the coaxial needle and increase gradually. Before the fracture of the liquid bridge, the resultant force (capillary force, net buoyancy, viscous resistance, inertial force, and mass inertia force) of the droplet needs to satisfy the Newton's second law. As the capillary force is usually dominant, the droplet and the needle can move synchronously before the fracture of the liquid bridge [49]. As the coaxial needle leaves the initial position and rose gradually, the liquid bridge will shrink gradually and break at a certain height ($h$). The droplets will be produced along with the fracture of the liquid bridge. Theoretically, $h$ is the minimum value of height when the differential equation has no solution. In this experiment, the amplitude of the coaxial needle is set as 1.35 mm to ensure fracture of the liquid bridge. Under these conditions, the double emulsion can drop off the tip of the needle and sink to the bottom of the quartz pool because of the higher density. In addition, the vibration frequency, flow rate and other parameters need to be controlled within a certain range to ensure the steady operation of CIS process [49]. The produced double emulsions are collected at the bottom of the quartz pool and wait for subsequent processing and application.

## Generation and Characterization of Perfluorocarbon-Loaded Magnetic Hydrogel Microcapsules

**Figure 2A** shows the generation process of PFC-loaded NIPAM double emulsions in mineral oil. The black arrows in the image indicate the coaxial needle and the produced core-shell droplets. Due to the presence of surfactant in mineral oil, the double emulsions can be stably arranged at the bottom of the quartz pool without fusion. The optical microscopic image of the collected uniform double emulsions at the preparation parameters of $Q_o = 15\,\mu L/min$, $Q_i = 15\,\mu L/min$, and $f = 4\,Hz$ is shown in **Figure 2B**. The black arrows in the image indicate the inner PFC core and outer NIPAM shell before UV light irradiation, and the boundary between the two is evident. The average radii of the inner core and the outer shell are 267.8 and 327.1 μm, and polydispersity indexes are 2.0% and 1.8%, respectively, (**Figure 2C**). After the production of the PFC-loaded NIPAM double emulsions, the UV light is used to crosslink the NIPAM shell to form hydrogel microcapsules. The outer shell changes from colorless to gray, but the size of the double emulsion changes little after crosslinking (**Figure 2D**).

## Size Control of Double Emulsions

In a standard CIS process, the generation frequency of the double emulsions equals to the coaxial needle vibration frequency [48, 49]. The relationship between the double emulsion volume ($V$) and flow rates and frequency can be expressed as follows,

$$V = (Q_i + Q_o)/f,$$

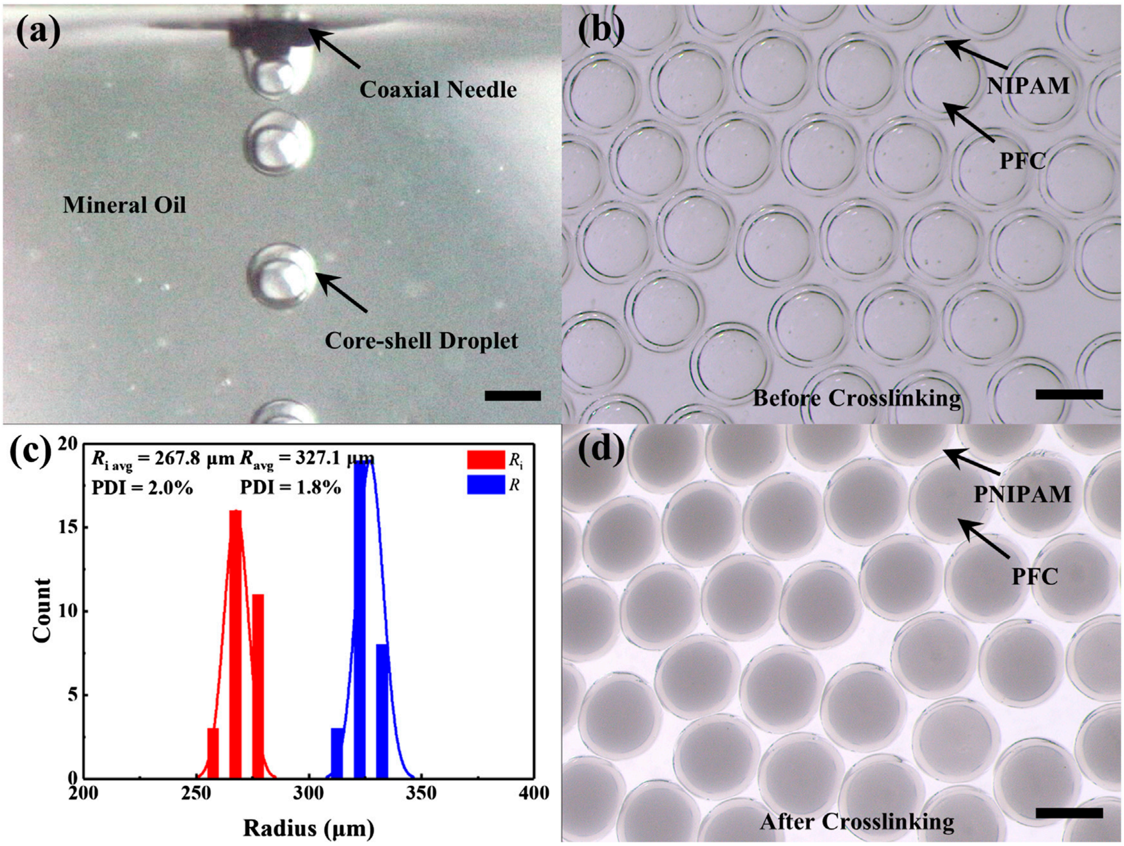

**FIGURE 2 |** The preparation of PFC-loaded NIPAM double emulsions. **(A)** Real-time CIS process during core-shell droplets formation. **(B)** Optical microscopic image of the produced PFC-loaded NIPAM double emulsions dispersed in mineral oil before crosslinking ($Q_o = 15\,\mu L/min$, $Q_i = 15\,\mu L/min$, $f = 4$ Hz). **(C)** Size distributions of the double emulsions inner core and outer shell in **(B)**. **(D)** The change of the double emulsion morphology after crosslinking ($Q_o = 15\,\mu L/min$, $Q_i = 15\,\mu L/min$, $f = 4$ Hz). Scale bar: 500 μm.

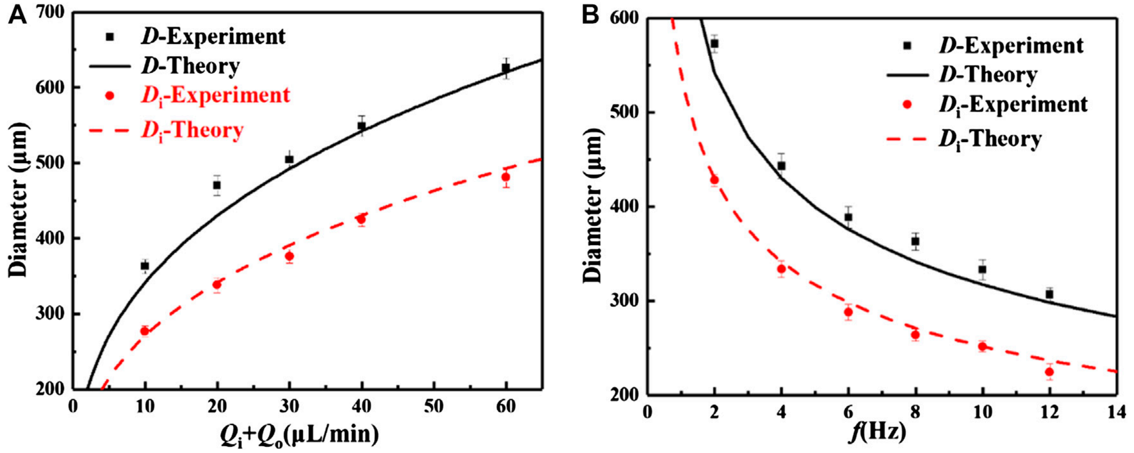

**FIGURE 3 |** Influence of experimental parameters on the size of the double emulsion. **(A)** The relationships between total flow rate and core and shell sizes ($f = 8$ Hz, $Q_i = Q_o$). **(B)** The relationships between vibration frequency and core and shell sizes ($Q_i + Q_o = 10$ μL/min, $Q_i = Q_o$).

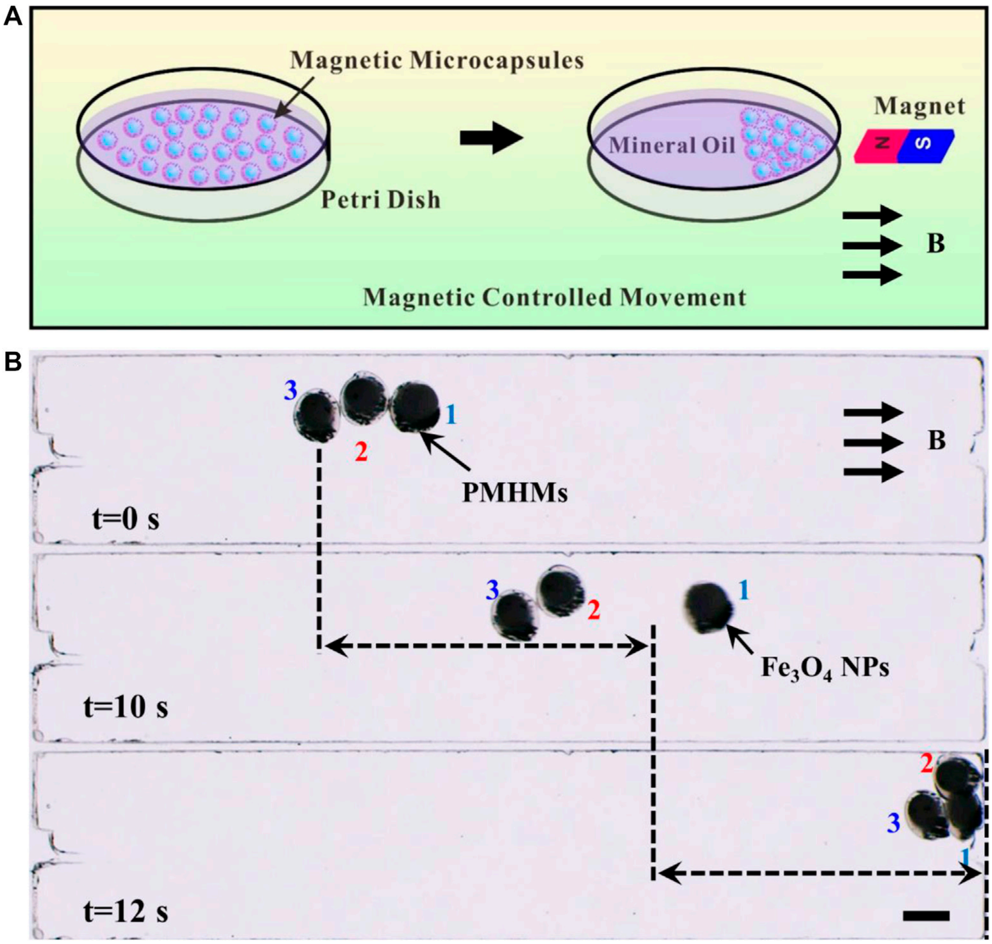

**FIGURE 4 | (A)** Schematic illustration of magnetic-guided PMHMs. **(B)** The positions of PMHMs at 0, 10, and 12 s under the action of the magnetic field. Scale bar: 500 μm.

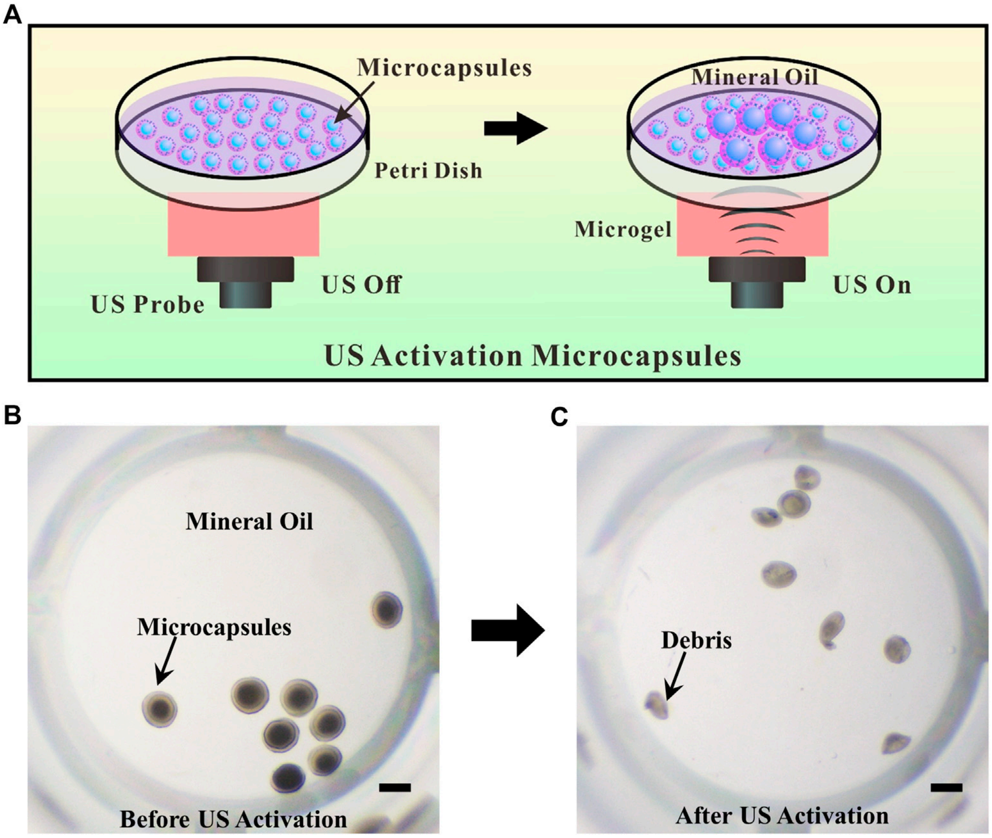

**FIGURE 5 | (A)** Schematic illustration of US activation of PMHMs. **(B)** Microscopic image of the produced PMHMs in a 96-well plate before US activation. **(C)** Microscopic image of the produced PMHMs after US activation. Scale bar: 500 μm.

Similarly, the relationship between the inner core volume ($V_i$) and flow rates and frequency can be expressed as follows,

$$V_i = Q_i/f,$$

Therefore, the double emulsion diameter ($D$) and the inner core diameter ($D_i$) can be calculated as,

$$D = \left[6\left(Q_i + Q_o\right)/\left(\pi f\right)\right]^{1/3},$$

$$D_i = \left[6Q_i/\left(\pi f\right)\right]^{1/3}.$$

From the above formulas, it can be found that the generated double emulsion size is determined only by the two fluids flow rates and vibration frequency, but not to the physicochemical parameters of the fluids and the experimental setup. Similarly, the size of the inner core of the double emulsions is only related to the inner flow rate and vibration frequency, but not to other parameters. The sizes and shapes of the double emulsions can be precisely adjusted in a broad range of experimental parameters, as shown in **Figures 3A,B**. The black and red dots indicate the experimental results of the double emulsion shell and core diameters, respectively. The black and red solid lines refer to the theoretical curves of the double emulsion shell and core diameters, respectively. When the vibration frequency and the ratio of inner and outer flow rates ($\varphi = Q_i{:}Q_o$) remain constant, the sizes of the double emulsion shell and core increase with the increase of the total flow rate of the two fluids (**Figure 3A**). When the total flow rate and the ratio of inner and outer flow rates remain constant, the sizes of the double emulsion shell and core decrease with the increase of the vibration frequency (**Figure 3B**). In the experiment, the amplitude of the exciter is kept the same at different vibration frequencies by adjusting the excitation voltage. The relationship between the frequency and the voltage is obtained by a laser distance sensor when the vibration amplitude keeps at a constant. The data indicate that the experimental and theoretical values are in good agreement. Here, the maximum frequency of droplet generation can be up to around 40 Hz. However, with the further increase of vibration frequency, the droplet will fall from the coaxial needle before the fracture of liquid bridge, resulting in the failure of the CIS process [48, 49]. The maximum vibration frequency can be increased to a certain extent by reducing the geometric parameters of the coaxial needle.

## Magnetic Guided Movement and Ultra Sound Activation of Perfluorocarbon-Loaded Magnetic Hydrogel Microcapsules

Iron oxide MNPs are dispersed in the shell of PMHMs which makes the hydrogel microcapsules can be attracted by the external magnetic field. **Figure 4A** illustrates the movement process of the PMHMs in mineral oil under magnetic field. **Figure 4B** shows the change of PMHMs position with time under magnetic field (0.4 T) in a rectangular glass slot. The movement speed of the PMHMs gradually increases with time, mainly due to the gradual increase of magnetic attraction. In the first 10 s, the droplet only moves about half of the distance, but the second half only takes 2 s. The content of the MNPs in the shell, the intensity of the magnetic field and the distance between the magnet and the PMHMs all affect the movement of the PMHMs. For the movement of PMHMs, a video clip is available as Supplementary data (Supplementary Video 2). Because the PNIPAM shell has excellent flexibility characteristics, a certain deformation will occur when the PMHMs hit the wall surface, and the PMHMs' morphology will return to the original state after the magnetic field is canceled. These experimental results show that the prepared PMHMs have excellent magnetic response characteristics, and are expected to be used in magnetic controlled drug delivery.

US activation PFC droplet mainly relies on negative pressure to make droplets vaporize rapidly, and the time dimension is usually millisecond [6, 49]. Because the ultrasonic probe is relatively large, multiple PMHMs will be activated simultaneously during the US activation process, as illustrated in **Figure 5A**. **Figures 5B,C** show the changes of PMHMs before

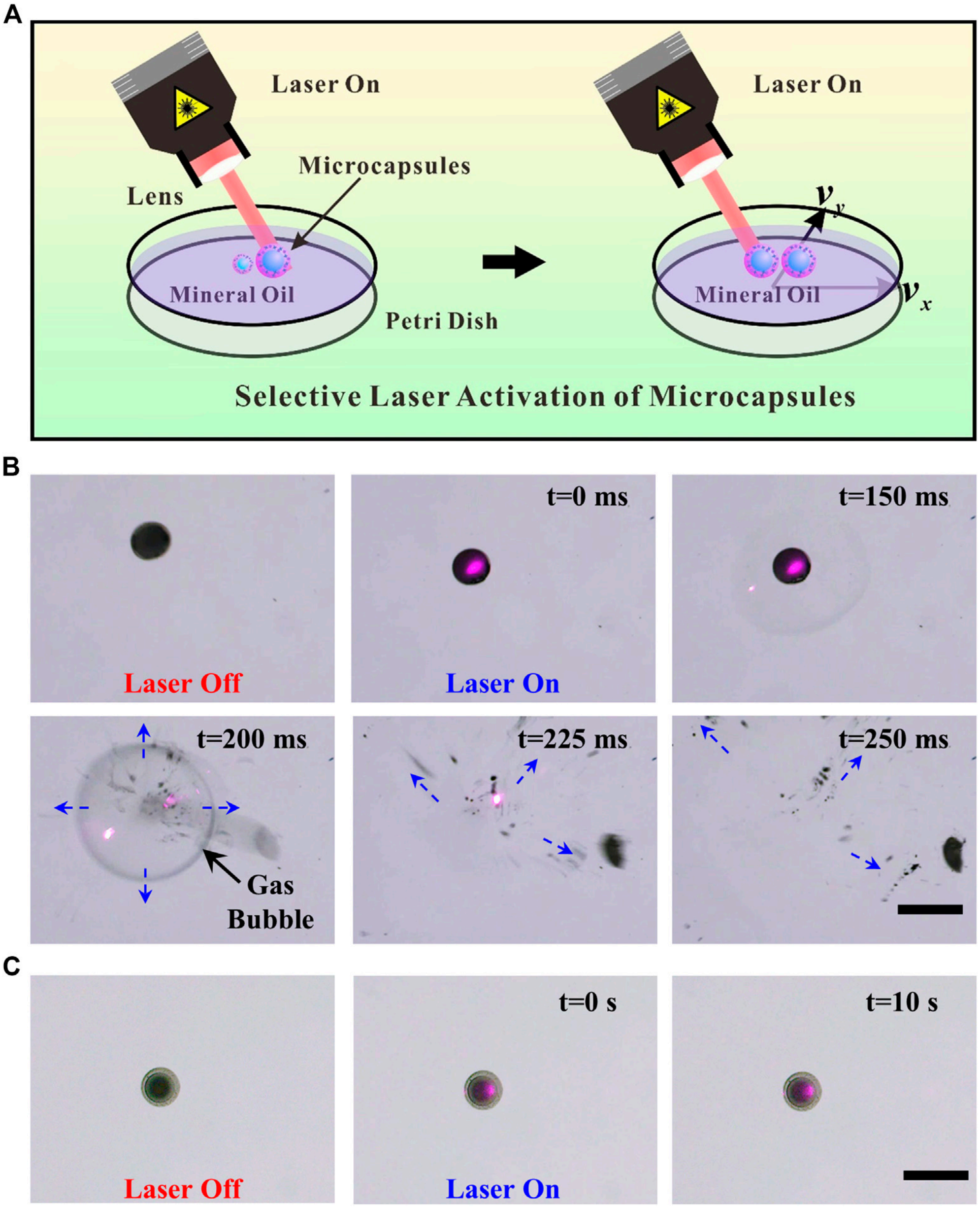

**FIGURE 6 | (A)** Schematic illustration of the laser activation of PMHMs. **(B)** Microscopic image of a single PMHM under NIR laser irradiation at different times. **(C)** Microscopic image of the produced PFC-loaded PNIPAM microcapsules without MNPs in the shell under NIR laser irradiation at different times. Scale bar: 500 μm.

and after US activation. Under the action of ultrasound (1 MHz, 45 s, 1.5 W/cm$^2$, duty cycle of 50%), the PNIPAM hydrogel shell breaks into debris as shown in **Figure 5C**. The experiment preliminarily verifies the feasibility of US activation of PMHMs, which lays a certain foundation for the application of the magnetic-controlled US responsive hydrogel microcapsules.

## Laser Activation of Perfluorocarbon-Loaded Magnetic Hydrogel Microcapsules

Because iron oxide MNP is a kind of light-absorbing medium, a NIR laser with a wavelength of 808 nm is chosen to activate PMHMs. Under the focusing effect of the lens, the laser spot becomes smaller than the droplet diameter, so the laser has a better activation resolution, as illustrated in **Figure 6A**. The diameter of the focused laser spot is about 8 μm and the laser intensity is calculated to be 7.8 × 10$^3$ W/mm$^2$. The temperature of the focusing part on the microcapsule would exceed the vaporization temperature of PFC (55°C). **Figure 6B** shows the time sequence of a single PMHM under laser irradiation. Under the laser irradiation, PFC droplets vaporize rapidly and explode, which break the PNIPAM shell. The laser activation process is recorded as Supplementary data (Supplementary Video 3). At 200 ms, the PFC bubble explodes to generate a violent shock wave, which causes the fluid around the microcapsule to flow outward. After the explosion, the surrounding fluids will return to fill the vacant position. The blue arrows indicate the direction of fluid movement. As a contrast, the PFC-loaded hydrogel microcapsules without iron oxide MNPs are prepared to observe the changes of the microcapsules under laser irradiation. No changes have occurred after 10 s of laser irradiation (**Figure 6C**), further

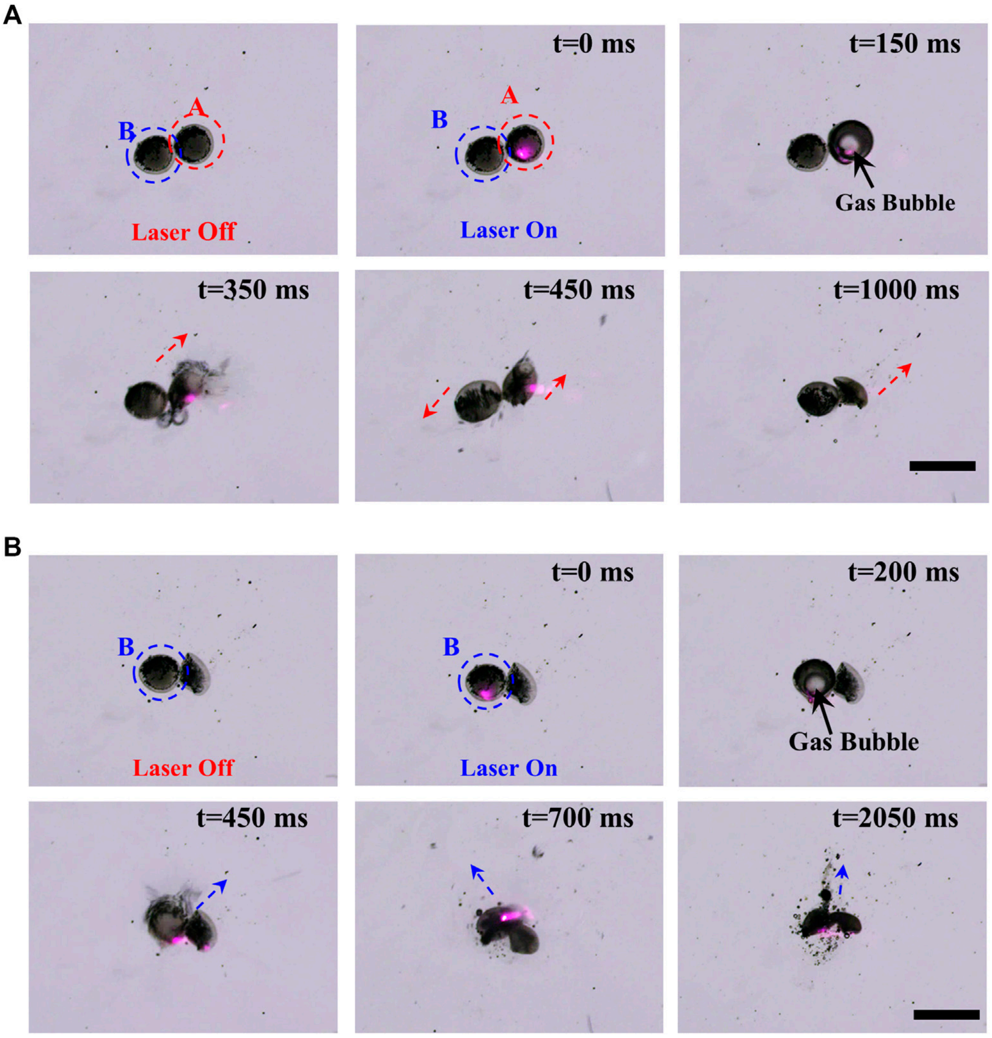

**FIGURE 7 |** Sequential laser activation of PMHMs. **(A)** NIR laser activation process of the first PMHM at different times. **(B)** NIR laser activation process of the second PMHM at different times. Scale bar: 500 μm.

confirming that the MNPs absorbing light energy and generating heat is the main reason for the vaporization of PFC core.

In the process of double emulsions crosslinking, if two droplets are very close together, they will adhere to each other after crosslinking. **Figures 7A,B** show the sequential laser activation process of two PMHMs attached to each other. The red and blue circles show the first and the second activated PMHMs. Because of the small laser spot, it is easy to realize the site-specific activation of the different PMHMs. The sequential laser activation process is recorded as Supplementary data (Supplementary Video 4). During the laser excitation process, the gas core is first generated in the PFC core and gradually increases and eventually ruptures [6], as indicated by the black arrows. The red and blue arrows indicate the different directions of debris movement. The experimental results show that the laser has the potential to achieve accurate drug delivery and release.

## CONCLUSION

In summary, a simple, facile, and low-cost CIS technique was proposed to prepare uniform PMHMs for magnetic guided US and laser activation. Herein, the outer shell of PMHMs is PNIPAM combined with MNPs and the inner core is US-responsive PFC liquid which makes the PMHMs have magnetic-, US-, and photothermal-responsive characteristics. Moreover, the PMHMs have the potential to synergistic delivery of multiple distinct drugs. Additionally, the size, structure of the PMHM can be precisely adjusted in a wide range by controlling the experimental parameters. US and laser activation of PMHMs have been verified by a series of experiments, US has the potential to quickly release multiple PMHMs, while laser has the ability to activate PMHMs more accurately. The PMHMs have excellent magnetic-response characteristics which can further improve the controllability of drug release. It can be concluded that the produced uniform PMHMs may have great application potential in biomedicine, engineering, chemistry, material science, and other fields.

## DATA AVAILABILITY STATEMENT

The original contributions presented in the study are included in the article/**Supplementary Material**, further inquiries can be directed to the corresponding author/s.

## AUTHOR CONTRIBUTIONS

ZZ designed and carried out the experiment, collected and analyzed the data and wrote the manuscript. MZ, YZ, and FH assisted the experiment. TS and RX guided the research and revised the manuscript. All authors contributed to manuscript revision, read, and approved the submitted version.

## FUNDING

This work was supported by the National Natural Science Foundation of China (Nos. 11722222, 11621202), the Strategic Priority Research Program of the Chinese Academy of Sciences (No. XDB22040403), the Anhui Provincial Natural Science Foundation (1908085QE200), the Youth Innovation Promotion Association CAS (No. 2018491), and the Fundamental Research Funds for the Central Universities.

## SUPPLEMENTARY MATERIAL

The Supplementary Material for this article can be found online at: https://www.frontiersin.org/articles/10.3389/fphy.2020.581519/full#supplementary-material

**Supplementary Video 1:** CIS double emulsions preparation process (MP4).

**Supplementary Video 2:** Magnetic controlled movement of PMHMs (MP4).

**Supplementary Video 3:** Laser activation of a single PMHM (MP4).

**Supplementary Video 4:** Sequential laser activation process of two PMHMs (MP4).

## REFERENCES

1. Zhao CX. Multiphase flow microfluidics for the production of single or multiple emulsions for drug delivery. *Adv Drug Deliv Rev* (2013) **65**(11–12):1420–46. doi:10.1016/j.addr.2013.05.009
2. He F, Zhang M-J, Wang W, Cai Q-W, Su Y-Y, Liu Z, et al. Designable polymeric microparticles from droplet microfluidics for controlled drug release. *Adv Mater Technol* (2019) **4**(6):1800687. doi:10.1002/admt.201800687
3. Lengyel M, Kallai-Szabo N, Antal V, Laki AJ, Antal I. Microparticles, microspheres, and microcapsules for advanced drug delivery. *Sci Pharm* (2019) **87**(3):20. doi:10.3390/scipharm87030020
4. Zhang Y, Yu J, Bomba HN, Zhu Y, Gu Z. Mechanical force-triggered drug delivery. *Chem Rev* (2016) **116**(19):12536–63. doi:10.1021/acs.chemrev.6b00369
5. Zhang A, Jung K, Li A, Liu J, Boyer C. Recent advances in stimuli-responsive polymer systems for remotely controlled drug release. *Prog Polym Sci* (2019) **99**: 101164. doi:10.1016/j.progpolymsci.2019.101164
6. Zhu Z, Wu Q, Li G, Han S, Si T, Xu RX. Microfluidic fabrication of stimuli-responsive microdroplets for acoustic and optical droplet vaporization. *J Mater Chem B* (2016) **4**(15):2723–30. doi:10.1039/c5tb02402a
7. Si T, Li G, Wu Q, Zhu Z, Luo X, Xu RX. Optical droplet vaporization of nanoparticle-loaded stimuli-responsive microbubbles. *Appl Phys Lett* (2016) **108**(11):111109. doi:10.1063/1.4944539
8. Duarte ARC, Ünal B, Mano JF, Reis RL, Jensen KF. Microfluidic production of perfluorocarbon-alginate core-shell microparticles for ultrasound therapeutic applications. *Langmuir* (2014) **30**(41):12391–9. doi:10.1021/la502822v
9. Soto F, Martin A, Ibsen S, Vaidyanathan M, Garcia-Gradilla V, Levin Y, et al. Acoustic microcannons: toward advanced microballistics. *ACS Nano* (2016) **10**(1):1522–8. doi:10.1021/acsnano.5b07080
10. Dwivedi P, Kiran S, Han S, Dwivedi M, Khatik R, Fan R, et al. Magnetic targeting and ultrasound activation of liposome-microbubble conjugate for enhanced delivery of anti-cancer therapies. *ACS Appl Mater Interfaces* (2020) **12**:23737–23751. doi:10.1021/acsami.0c05308

11. Sun Y, Wang Y, Niu C, Strohm EM, Zheng Y, Ran H, et al. Laser-activatible PLGA microparticles for image-guided cancer therapy in vivo. *Adv Funct Mater* (2014) **24**(48):7674–80. doi:10.1002/adfm.201402631
12. Wilson K, Homan K, Emelianov S. Biomedical photoacoustics beyond thermal expansion using triggered nanodroplet vaporization for contrast-enhanced imaging. *Nat Commun* (2012) **3**:618. doi:10.1038/ncomms1627
13. Gao D, Xu M, Cao Z, Gao J, Chen Y, Li Y, et al. Ultrasound-Triggered phase-transition cationic nanodroplets for enhanced gene delivery. *ACS Appl Mater Interfaces* (2015) **7**(24):13524–37. doi:10.1021/acsami.5b02832
14. Lee TY, Choi TM, Shim TS, Frijns RAM, Kim S-H. Microfluidic production of multiple emulsions and functional microcapsules. *Lab Chip* (2016) **16**(18): 3415–40. doi:10.1039/c6lc00809g
15. Shang L, Cheng Y, Zhao Y. Emerging droplet microfluidics. *Chem Rev* (2017) **117**(12):7964–8040. doi:10.1021/acs.chemrev.6b00848
16. Wang J, Eijkel JCT, Jin M, Xie S, Yuan D, Zhou G, et al. Microfluidic fabrication of responsive hierarchical microscale particles from macroscale materials and nanoscale particles. *Sensor Actuator B Chem* (2017) **247**:78–91. doi:10.1016/j.snb.2017.02.056
17. Li W, Zhang L, Ge X, Xu B, Zhang W, Qu L, et al. Microfluidic fabrication of microparticles for biomedical applications. *Chem Soc Rev* (2018) **47**(15): 5646–83. doi:10.1039/c7cs00263g
18. Zhao Q, Cui H, Wang Y, Du X. Microfluidic platforms toward rational material fabrication for biomedical applications. *Small* (2019) **16**(9): e1903798. doi:10.1002/smll.201903798
19. Utada AS, Lorenceau E, Link D, Kalpan PD, Stone HA, Weitz DA. Monodisperse double emulsions generated from a microcapillary device. *Science* (2005) **308**(5721):537–41. doi:10.1126/science.1109164
20. Bell RV, Parkins CC, Young RA, Preuss CM, Stevens MM, Bon SAF. Assembly of emulsion droplets into fibers by microfluidic wet spinning. *J Mater Chem* (2016) **4**(3):813–8. doi:10.1039/c5ta08917d
21. Chaurasia AS, Sajjadi S. Flexible asymmetric encapsulation for dehydration-responsive hybrid microfibers. *Small* (2016) **12**(30):4146–55. doi:10.1002/smll.201600465
22. Chen A, Ge X-h, Chen J, Zhang L, Xu J-H. Multi-functional micromotor: microfluidic fabrication and water treatment application. *Lab Chip* (2017) **17**(24):4220–4. doi:10.1039/c7lc00950j
23. Shang L, Wang Y, Yu Y, Wang J, Zhao Z, Xu H, et al.. Bio-inspired stimuli-responsive graphene oxide fibers from microfluidics. *J Mater Chem* (2017) **5**(29):15026–30. doi:10.1039/c7ta02924a
24. Meng Z-J, Zhang J, Deng X, Liu J, Yu Z, Abell C. Bioinspired hydrogel microfibres colour-encoded with colloidal crystals. *Mater Horiz* (2019) **6**: 1938–43. doi:10.1039/C9MH00528E
25. Anna SL, Bontoux N, Stone HA. Formation of dispersions using "flow focusing" in microchannels. *Appl Phys Lett* **82**(3):364–6. doi:10.1063/1.1537519
26. Chan HF, Zhang Y, Leong KW. Efficient one-step production of microencapsulated hepatocyte spheroids with enhanced functions. *Small* (2016) **12**(20):2720–30. doi:10.1002/smll.201502932
27. Li D, Li X, Chen C, Zheng Z, Chang H. Monodisperse water-in-oil-in-water emulsions generation for synthesising alginate hydrogel microspheres *via* locally hydrophobic modification to PMMA microchannels. *Sensor Actuator B Chem* (2018) **255**:1048–56. doi:10.1016/j.snb.2017.08.152
28. Zhang L, Chen K, Zhang H, Pang B, Choi C-H, Mao AS, et al. Microfluidic templated multicompartment microgels for 3D encapsulation and pairing of single cells. *Small* (2018) **14**(9):1702955. doi:10.1002/smll.201702955
29. Guerzoni LPB, Rose JC, Gehlen DB, Jans A, Haraszti T, Wessling M, et al. Cell encapsulation in soft, anisometric poly(ethylene) glycol microgels using a novel radical-free microfluidic system. *Small* (2019) **15**(20):e1900692. doi:10.1002/smll.201900692
30. Samandari M, Alipanah F, Javanmard SH, Sanati-Nezhad A. One-step wettability patterning of PDMS microchannels for generation of monodisperse alginate microbeads by in situ external gelation in double emulsion microdroplets. *Sens Actuators B Chem* (2019) **291**:418–25. doi:10.1016/j.snb.2019.04.100
31. Zhu Z, Si T, Xu RX. Microencapsulation of indocyanine green for potential applications in image-guided drug delivery. *Lab Chip* (2015) **15**(3):646–9. doi:10.1039/c4lc01032a
32. Si T, Yin C, Gao P, Ding H, Li GB, He XM, et al. Steady cone-jet mode in compound-fluidic electro-flow focusing for fabricating multicompartment microcapsules. *Appl Phys Lett* (2016) **108**(2):021601. doi:10.1063/1.4939632
33. Wu Q, Yang C, Liu G, Xu W, Zhu Z, Si T, et al. Multiplex coaxial flow focusing for producing multicompartment Janus microcapsules with tunable material compositions and structural characteristics. *Lab Chip* (2017) **17**(18):3168–75. doi:10.1039/c7lc00769h
34. Wu Q, Yang C, Yang J, Huang F, Liu G, Zhu Z, et al. Photopolymerization of complex emulsions with irregular shapes fabricated by multiplex coaxial flow focusing. *Appl Phys Lett* (2018) **112**(7):071601. doi:10.1063/1.5018207
35. Zhu Z, Wu Q, Han S, Xu W, Zhong F, Yuan S, et al. Rapid production of single- and multi-compartment polymeric microcapsules in a facile 3D microfluidic process for magnetic separation and synergistic delivery. *Sensor Actuator B Chem* (2018) **275**:190–8. doi:10.1016/j.snb.2018.08.044
36. Zhong F, Yang C, Wu Q, Wang S, Cheng L, Dwivedi P, et al. Preparation of pesticide-loaded microcapsules by liquid-driven coaxial flow focusing for controlled release. *Int J Polym Mater* (2019) **69**:840–7. doi:10.1080/00914037.2019.1617710
37. Yang C, Qiao R, Mu K, Zhu Z, Xu R, Si T, et al. Manipulation of jet breakup length and droplet size in axisymmetric flow focusing upon actuation. *Phys Fluids* (2019) **31**(9):091702. doi:10.1063/1.5122761
38. Liu G, Wu Q, Dwivedi P, Hu C, Zhu Z, Shen S, et al. Hemoglobin-laden microcapsules for simulating oxygen dynamics of biological tissue. *ACS Biomater Sci Eng* (2018) **4**(9):3177–84. doi:10.1021/acsbiomaterials.8b00830
39. Dwivedi P, Yuan S, Han S, Mangrio FA, Zhu Z, Lei F, et al. Core–shell microencapsulation of curcumin in PLGA microparticles: programmed for application in ovarian cancer therapy. *Artif Cells Nanomed Biotechnol* (2018) S481–91. doi:10.1080/21691401.2018.1499664
40. Martino C, Berger S, Wootton RCR, deMello AJ. A 3D-printed microcapillary assembly for facile double emulsion generation. *Lab Chip* (2014) **14**(21): 4178–82. doi:10.1039/c4lc00992d
41. Waheed S, Cabot JM, Macdonald NP, Lewis T, Guijt RM, Paull B, et al. 3D printed microfluidic devices: enablers and barriers. *Lab Chip* (2016) **16**(11): 1993–2013. doi:10.1039/c6lc00284f
42. Weisgrab G, Ovsianikov A, Costa PF. Functional 3D printing for microfluidic chips. *Adv Mater Technol* (2019) **4**(10):1900275. doi:10.1002/admt.201900275
43. Nielsen AV, Beauchamp MJ, Nordin GP, Woolley AT. 3D printed microfluidics. *Annu Rev Anal Chem* (2020) **13**(1):45–65. doi:10.1146/annurev-anchem-091619-102649
44. Gu H, Duits MHG, Mugele F. Droplets formation and merging in two-phase flow microfluidics. *Int J Mol Sci* (2011) **12**(4):2572–97. doi:10.3390/ijms12042572
45. Si T, Li F, Yin X-Y, Yin X-Z. Modes in flow focusing and instability of coaxial liquid-gas jets. *J Fluid Mech* (2009) **629**:1–23. doi:10.1017/s0022112009006211
46. Ganan-Calvo AM, Montanero JM, Martin-Banderas L, Flores-Mosquera M. Building functional materials for health care and pharmacy from microfluidic principles and flow focusing. *Adv Drug Deliv Rev* (2013) **65**(11-12):1447–69. doi:10.1016/j.addr.2013.08.003
47. Zhu P, Wang L, Passive and active droplet generation with microfluidics: a review. *Lab Chip* (2017) **17**(1):34–75. doi:10.1039/c6lc01018k
48. Huang F, Zhu Z, Niu Y, Zhao Y, Si T, Xu RX. Coaxial oblique interface shearing: tunable generation and sorting of double emulsions for spatial gradient drug release. *Lab Chip* (2020) **20**(7):1249–1258. doi:10.1039/d0lc00111b.
49. Zhu Z, Huang F, Yang C, Si T, Xu RX. On-demand generation of double emulsions based on interface shearing for controlled ultrasound activation. *ACS Appl Mater Interfaces* (2019) **11**(43):40932–43. doi:10.1021/acsami.9b15182

**Conflict of Interest:** The authors declare that the research was conducted in the absence of any commercial or financial relationships that could be construed as a potential conflict of interest.

ORIGINAL RESEARCH
published: 20 November 2020
doi: 10.3389/fphy.2020.600589

# Developing a Photoacoustic Whole-Breast Imaging System Based on the Synthetic Matrix Array

*Guangjie Zhang[1], Wenzhao Li[1], Meng Yang[2] and Changhui Li[1]**

*[1]Department of Biomedical Engineering, College of Engineering, Peking University, Beijing, China, [2]Department of Ultrasonography, Peking Union Medical College Hospital, Chinese Academy of Medical Sciences & Peking Union Medical College, Beijing, China*

In this study, we reported a photoacoustic (PA) imaging system for whole-breast imaging. Similar to the traditional X-ray mammography, this system slightly compressed the breast by a water tank. The PA signal is acquired via scanning a long unfocused ultrasonic linear array probe over the breast top surface, and the expanded high-energy laser pulses illuminate the breast bottom through a transparent supporting plate. Scanning the unfocused transducer probe is equivalent to a synthetic two-dimensional (2D) matrix array, which significantly increased the field of view (FOV) via a much easier way and at a much lower cost. Our phantom results demonstrated that this system has a great potential for clinical implementation.

**Keywords: photoacoustic imaging, breast imaging, mammography, 3D imaging, synthetic matrix array**

**Edited by:**
*Chao Tian,*
*University of Science and Technology of China, China*

**Reviewed by:**
*Lei Xi,*
*Southern University of Science and Technology, China*
*Hui Fang,*
*Shenzhen University, China*

***Correspondence:**
*Changhui Li*
*chli@pku.edu.cn*

**Specialty section:**
*This article was submitted to Medical Physics and Imaging, a section of the journal Frontiers in Physics*

**Received:** *30 August 2020*
**Accepted:** *19 October 2020*
**Published:** *20 November 2020*

**Citation:**
*Zhang G, Li W, Yang M and Li C (2020) Developing a Photoacoustic Whole-Breast Imaging System Based on the Synthetic Matrix Array. Front. Phys. 8:600589. doi: 10.3389/fphy.2020.600589*

## INTRODUCTION

Breast cancer is the most common cancer for women and ranks top of newly diagnosed cancers in 2018 [1]. Early detection and accurate diagnosis of breast cancer can substantially improve the survival rate [2–4]. Although X-ray mammography serves as the standard imaging method, it suffers lower sensitivity for dense breasts [5], and the radiation hazard also prevents it to be frequently used. Ultrasound (US) and magnetic resonance imaging (MRI) are also common imaging modalities adjunct to mammography [6–8]. However, MRI not only is expensive and complicated but also often requires exogenous contrast agent. US is the most convenient clinical imaging method, but it primarily depicts the structural information with relatively lower specificity, as well as its diagnosis accuracy highly depends on the physician's personal experience. Over the past decade, the emerging photoacoustic (PA) breast imaging method gained increasing attention with promising clinical study results [9, 10].

Based on the PA effect, PA imaging (PAI) combines the optical contrast and acoustic detection [11]. Via detecting US pressure waves generated through instant thermal expansion after certain tissue (optical absorber) absorbing the energy of the laser pulse, PAI can reconstruct images of those optical absorbers. Because angiogenesis and hypoxia are two typical hallmarks for breast cancer [12, 13] and the hemoglobin in blood is a strong endogenous optical absorber in the near infrared regime, most PA breast imaging systems target the abnormal vasculature, including morphology (such as the vessel density) and function (such as the oxygenation saturation).

Up to now, several PA breast imaging platforms have been developed, which can be classified into two types: local breast imaging based on handheld probes and whole-breast imaging. Owing to its familiarity to physicians, the PA handheld probe has been widely studied [14, 15]. Moreover,

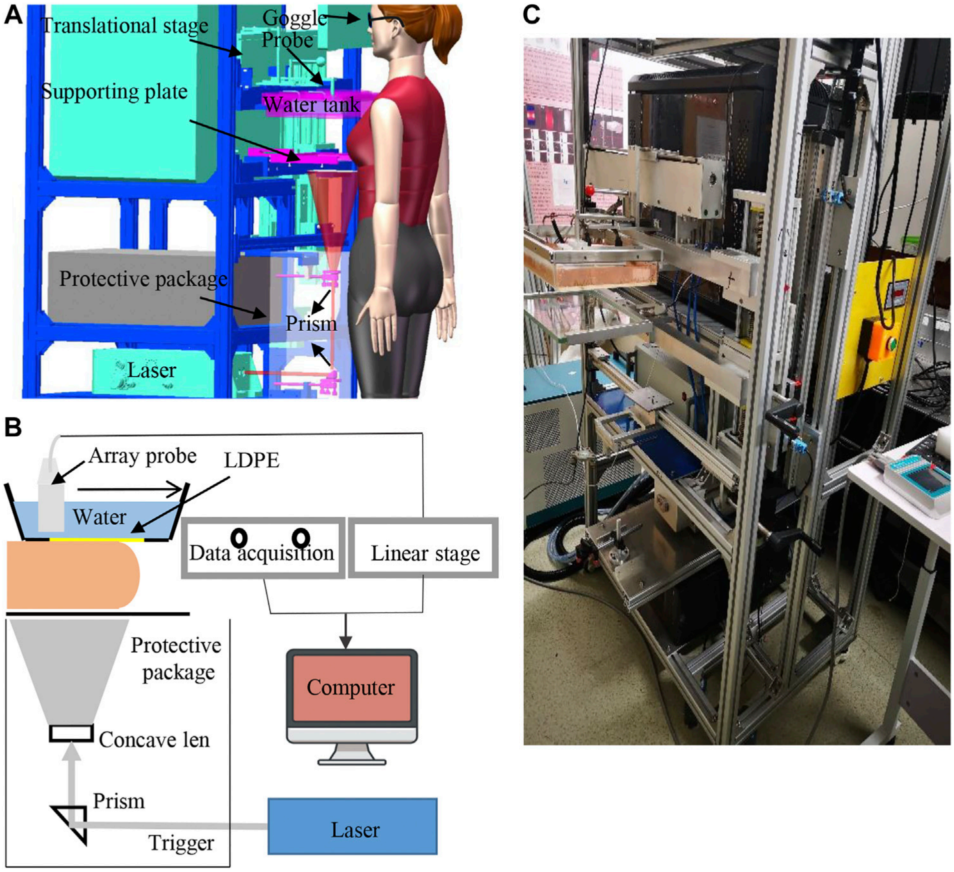

**FIGURE 1 |** System setup. **(A)** 3D interior structure presentation of the photoacoustic breast imaging system; **(B)** schematic diagram of the system design. **(C)** Photography of the prototype system.

commercial PA/US handheld products are also available [16, 17]. However, handheld probes only image limited part of the breast and suffers artifacts caused by limited-view issue. Therefore, PA whole-breast imaging also gains much attention [9, 18–20]. Most of the PA whole-breast imaging systems require patients to be in a prone position. Toi et al. [14] developed a system with a hemispherical-shaped detector array. Lin et al. [9] scanned the breast with a 220-mm-diameter, 512-element full-ring ultrasonic transducer array, whereas researchers in Twente University used an 80-mm-diameter, 590-element two-dimensional (2D) planar array [21]. Instead of prone position design, Zhixing et al. [19] reported a system similar to the X-ray mammographic geometry in which it employed a 572-element 2D planar array with a diameter of 80 mm lying under the compressed breast. Due to the technical complexity and cost, current 2D planar arrays used in PA breast imaging not only have limited data acquisition channels but also the element size is generally large, which sacrifices the spatial resolution. Compared to the 2D array probe, it is much easier to manufacture a linear array with smaller element size, as well as its parallel data acquisition system. Nikhila et al. [22] presented a dual scan mammoscope system by two focused array, and they employed the "virtual line" algorithm to successfully improve the elevation resolution. But the inherent focusing characteristic of this probe still limits its effective acquisition angle, making it difficult to image vertically obliquely aligned targets in 3D.

In this work, we presented a prototype PA whole-breast imaging system: photoacoustic synthetic matrix array tomography (PA-Smart). Our design employs the operation posture as in X-ray mammography, where patients stand (or sit) during the imaging procedure. Unlike the work reported in Refs. 19, 22, we scanned the breast with a one-dimensional (1D) unfocused linear probe over the upper surface of the breast. We have previously reported a method to realize a large-scale 2D planar array via scanning an unfocused linear array [23]. Based on this method, our system significantly increased the field of view (FOV) in a much easier way and at a much lower cost for PA breast imaging. At the same time, we used high-energy NIR laser illuminating the bottom of the breast over a large area to deliver enough photons into the breast within the safety limit. The phantom study demonstrated that our system can finish imaging an FOV of more than 10 cm × 10 cm × 4 cm within 33 s.

# METHODS

## System Setup

The PA-Smart imaging system is shown in **Figure 1A**. Similar to X-ray mammography, the subject stands in front of the system, and one of the patient's breasts was placed onto a transparent plate (made of glass) and was mildly compressed by the bottom of a water tank above the breast. Slight compression can not only reduce the breast thickness to facilitate light to penetrate but also reduce the tissue movement caused by breathing. An electrical translational stage drives a 1D unfocused linear US array to scan in the water tank at a speed of 3 mm/s. The bottom of the water tank is made by low-density polyethylene (LDPE) material that has a similar acoustic impedance with the breast tissue.

A Q-switched Nd: YAG laser (MQ/X, Beamtech Co., Ltd., China) provided 9-ns 1064-nm laser at a maximum pulse energy of 1.6 J/pulse and a repetition rate of 10 Hz to excite PA signals. The laser beam passed a concave lens and was expanded to be 10 cm in diameter onto the breast's bottom surface, guaranteeing the optical fluence on the tissue surface less than the American National Standards Institute (ANSI) safety limit at 1,064 nm (100 mJ/cm$^2$). To further ensure the safety, laser paths are confined in the protective package, and the only risk comes from the light leaking from the glass. Laser safety goggles are required for both the patient and the physician during examination. Also, the laser system specially designed a visible low-power red guiding light, which shares the same paths with the 1064-nm laser; then, we can double-check the laser alignment before each examination.

**Figure 2A** demonstrated the mechanism of constructing a synthetic large-scale 2D planar matrix array via scanning a long 1D unfocused array. The array used in this study, as shown in **Figure 2B**, consists of two identical customized unfocused linear array probes (TomoWave Inc., Houston, United States). Each subprobe has 48 elements of 1.0 mm × 1.0 mm, and the pitch is 1.35 mm. The array has a center frequency of 1.2 MHz and the bandwidth covering from 0.5 to 6.0 MHz. The theoretical acceptance angle for each unfocused element is about 45° at 1.5 MHz, guaranteeing to effectively detect PA signals from a large angle, which is essential for 3D reconstruction. The detected PA signal was amplified and recorded by a customized 12-bit data acquisition system (TomoWave Inc., Houston, United States) at a 25 MHz sampling rate.

In the following phantom study, we generally scanned the linear array about 10 cm. Considering the width of each element as 1 mm, scanning 10 cm corresponds to 100 columns of elements ($N = 100$) in **Figure 2A**. The equivalent large-scale 2D planar matrix array has 96 × 100 (~10 k) elements, leading to a substantially increased field of view (FOV). We employed the universal filtered back projection (FBP) algorithm [24] with a planar detection surface to do the 3D image reconstruction.

## Imaging Resolution of the System

The imaging resolution of the system is influenced by several factors, including array's characteristics (element size, pitch, and bandwidth) and the synthetic numerical aperture. We experimentally measured the spatial resolution by imaging three strands of black human hair buried in a scattering agar phantom, which had a thickness of 5 cm and consisted of 3% agar and 1% intra-lipid.

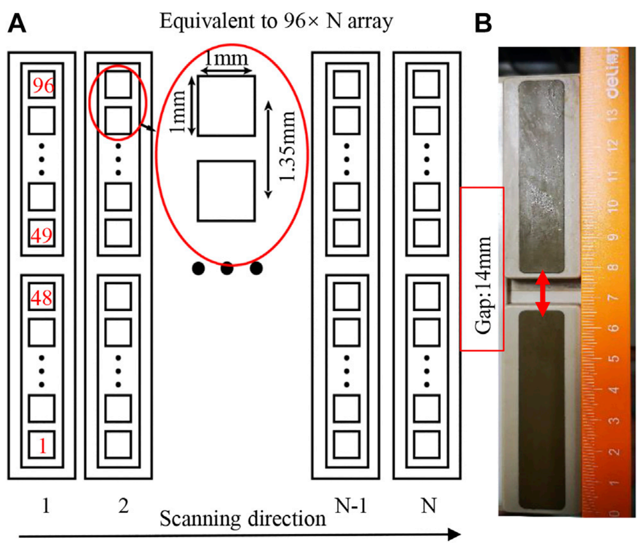

**FIGURE 2 | (A)** Schematic diagram of the probe as well as the scanning scheme; **(B)** photograph of the combined probe consisting of two linear probes.

The three hair strands were horizontally embedded in the agar phantom at depths of 12, 25, and 35 mm from the top surface of the phantom, respectively. **Figure 3A** showed a cross section of the reconstructed image with the Hilbert transform [25]. From these results, we use Gaussian fitting for the values along the three horizontal dashed lines and three vertical solid lines as shown in **Figure 3A**. **Figures 3 B and C** presented the fitting results at a depth of 12 mm. According to the results, the lateral resolutions were about 1.12, 1.37, and 1.57 mm at depths of 12, 25, and 35 mm, respectively. And the corresponding elevation resolutions at those three depths are about 0.60, 0.61, and 0.63 mm, respectively.

## Simulation Study of the Light Fluence

Considering the significant decrease in light fluence inside the thick breast tissue, we also studied the light fluence distribution inside a breast model by numerical simulation with COMSOL (COMSOL Inc., Sweden). As shown in **Figure 4A**, the breast tissue model is approximated to be a half cylindroid with a thickness of 5 cm. The cylindroid long and short axes are 20 and 15 cm, respectively. The model composes of the skin layer (~3 mm thick) and adipose layer, with the corresponding optical absorption and scattering coefficients being ($\mu_{a1} = 0.1\text{cm}^{-1}$, $\mu_{s1}^{'} = 10\text{cm}^{-1}$) and ($\mu_{a2} = 0.091\text{cm}^{-1}$, $\mu_{s2}^{'} = 6\text{cm}^{-1}$), respectively [26, 27]. The pattern of the expanded laser illuminating onto the bottom of the breast is approximated to be a uniform circle with a 10-cm diameter.

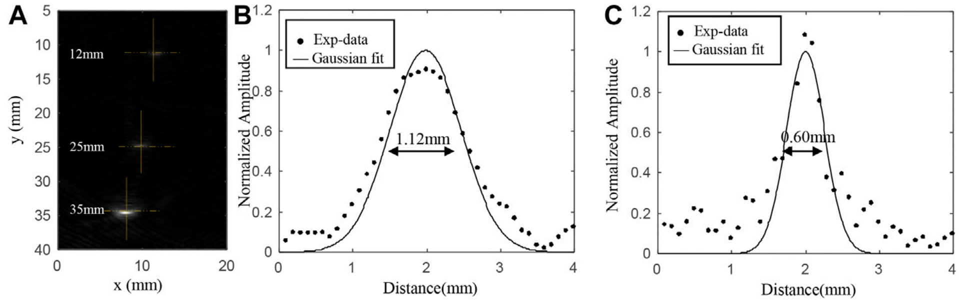

FIGURE 3 | **(A)** Cross section of the reconstructed imaging with the Hilbert transform; **(B)** reconstructed PA values along the horizontal yellow line at the depth of 12 mm; **(C)** reconstructed PA values along the vertical yellow line at the depth of 12 mm.

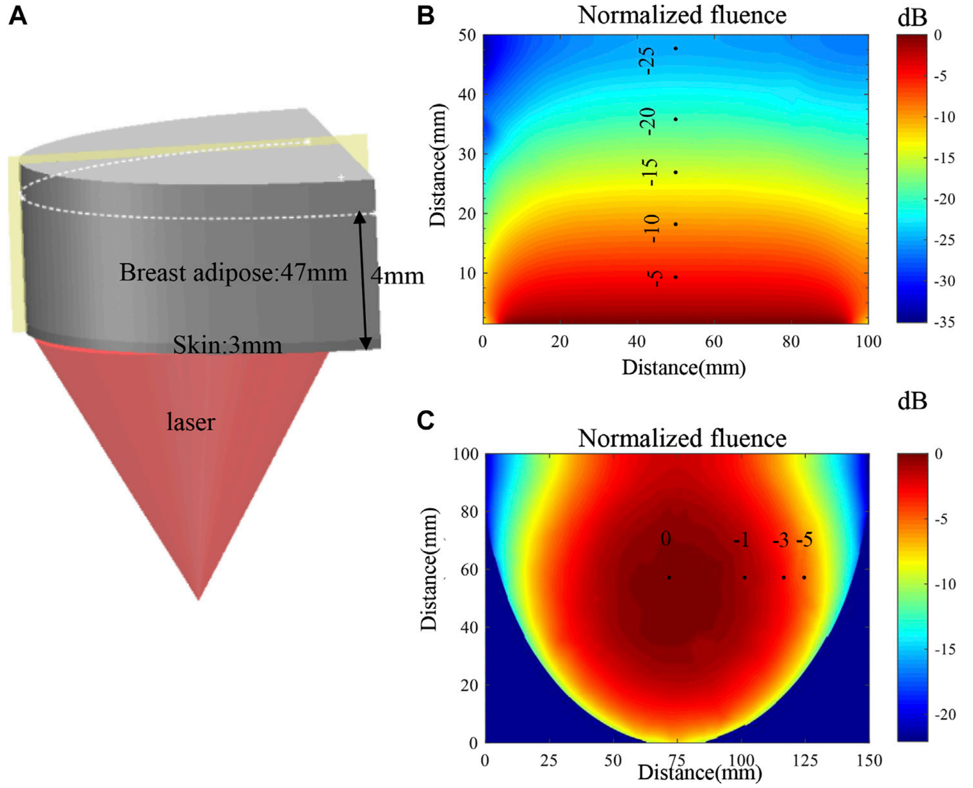

FIGURE 4 | **(A)** Schematic diagram of the simulation model and the illumination setup. **(B)** Map of the optical fluence along the vertical section marked by the yellow plane. **(C)** Map of the optical fluence at the horizontal section marked by the white dashed line.

The simulation of the light fluence distribution is based on the diffusion equation for the global region as in **Eq. 1**, which has been widely employed in PA imaging study [28],

$$-\frac{1}{\mu_{eff}^2}\nabla^2\phi+\phi=0, \tag{1}$$

where $\phi$ is the light fluence rate and $\mu_{eff}$ is the effective attenuation coefficient. The calculated normalized optical fluence in the central cut plane (marked as a yellow plane in **Figure 4A** is shown in **Figure 4B**. **Figure 4C** presents the calculated normalized optical fluence distributions over a horizontal plane (marked as a white dashed line in **Figure 4A**, 4 cm from the illuminated bottom surface. The color bar scale of all the fluences is in dB scale. The simulation results implicit that the light fluence could be decreased to two orders less after penetrating 4 cm in the breast, which will definitely influence the reconstructed PA values. Therefore, fluence compensation algorithms are desired, and we will demonstrate it in the phantom study.

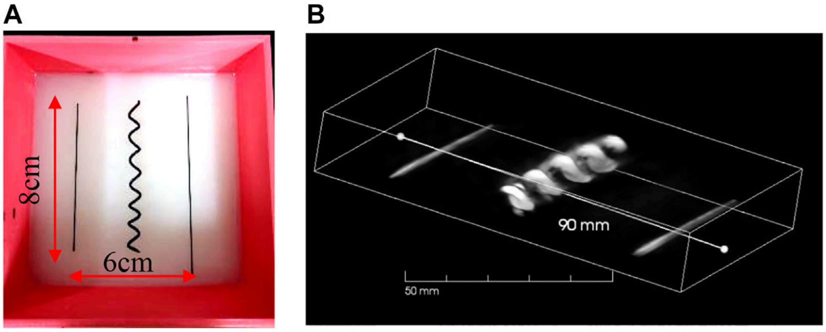

**FIGURE 5 | (A)** Photograph of carbon rods and helix in scattering medium in phantom study; **(B)** 3D result of carbon rods and helix.

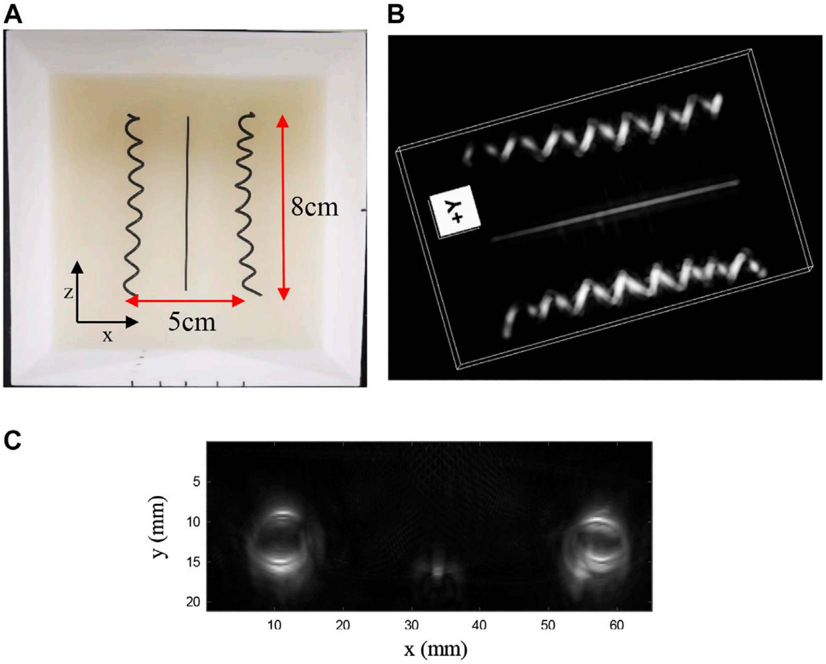

**FIGURE 6 | (A)** Photograph of carbon rods and helixes in scattering medium in phantom study; **(B)** 3D result of carbon rods and helixes; **(C)** MAP imaging of one period of the helix.

## RESULTS AND DISCUSSION

To validate the system's FOV and the capability of imaging complicated targets, we did two phantom experiments, in which all the imaged targets were buried in the agar phantom made of 3% agar and 1% intra-lipid. In the first phantom, we embedded two carbon rods (0.7 mm in diameter) and one helix object (7 mm in diameter) made from a black strip in a 4-cm-thick agar phantom, as illustrated in **Figure 5A**. These objects were horizontally buried approximately 2.0 cm deep into the phantom, in which the helix was located at the center. The laser illuminated upwardly onto the bottom of the phantom. Then, within 34 s, the array continuously scanned a total length of 100 mm at a speed of 3 mm/s, leading to a large-scale equivalent matrix array of 100 mm × 130 mm in size and nearly 10k elements (100 × 96 = 9,600). The 3D reconstructed image is shown in **Figure 5B** with an online animation (movie01). According to the result, not only the two wires but also the helix was well-reconstructed.

To study the potential artifact caused by the limited-view issue, we made the second phantom in which two helix objects (both about 7 mm in diameter) and one carbon fiber (1 mm in diameter) were embedded. Unlike the first phantom, the carbon fiber lied in the center and two helixes lied close to the two side edges (also close to the edge of FOV), as shown in **Figure 6A**. The distance from the middle carbon fiber to the

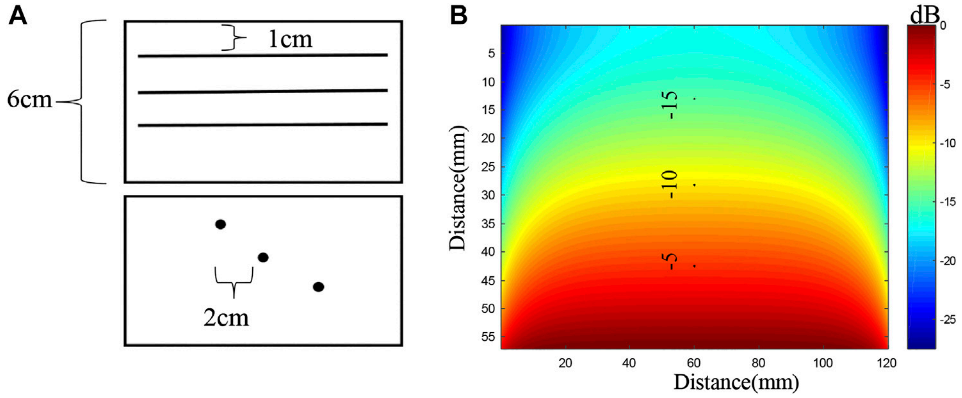

**FIGURE 7 | (A)** Structure of phantom; **(B)** $\phi$ map of the central cut plane.

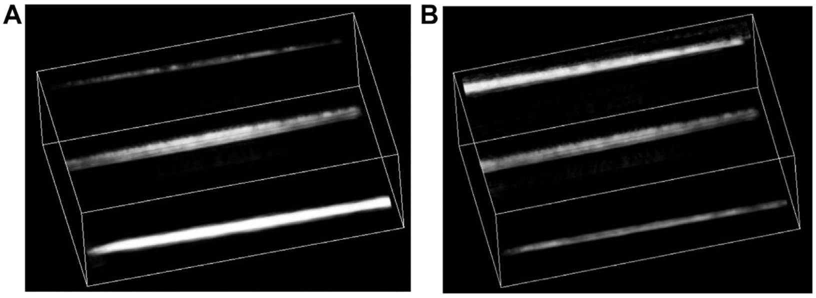

**FIGURE 8 | (A)** 3D result of three carbon rods without fluence compensation; **(B)** 3D result of three carbon fibers with fluence compensation.

center of the helix is approximately 25 mm. **Figure 6A** was the photograph of the phantom. We scanned a length of total 90 mm, leading to an equivalent large-scale matrix array with 90 × 106 (~9 k) elements. The 3D image reconstruction is shown in **Figure 6B** with an online animation (movie02). Owing to the large FOV and wide acceptance angle, both the helix and carbon fiber were well-reconstructed. In addition, the wide acceptance angle also helps recover oblique surface profile, as shown in **Figure 6C** in which we provide the MAP imaging of one period of the helix, except the middle part where the generated PA wave propagates parallel to the probe, which cannot be detected due to the limited view [29].

Next, to demonstrate the ability of deep imaging, we continued to image three carbon fibers (1 mm in diameter) at 1.0, 2.0, and 3.0 cm depths into the agar phantom, as shown **Figure 7A**. The imaging result is shown in **Figure 8A**. Due to the large difference in the light fluence as shown in **Figure 7B**, the fiber at the deeper location, that is, closer to the illumination source, would have much larger PA value, leading to an apparently thicker diameter in the 3D reconstructed images. Therefore, we applied fluence compensation, and the result is shown in **Figure 8B**.

## CONCLUSION

In this work, we developed a PA-Smart whole-breast imaging system. The proposed imaging posture is familiar to physicians and facilitates patients' examination. The large FOV of the system is achieved based on the synthetic matrix array method via scanning an unfocused linear array. Besides, the synthetic 2D array can have less reconstruction artifacts, which is crucial for whole-breast imaging. We did phantom experiments to validate the performance of the system. The clinical study is our next step to explore the power of this system.

However, there is relatively lower reconstruction quality of the side of the helix, which is caused by the "limited view" issue. In addition, the current resolution is about 1 mm, which is not suitable for imaging fine vasculature in breast tumor. Moreover, the 14-mm physical gap between two independent linear probes also degraded the imaging quality, especially for those just under the gap. We are working on a new probe with longer length and more elements with smaller element size. New reconstruction algorithms and machine learning will be applied to help solving problems with the limited view.

## DATA AVAILABILITY STATEMENT

The original contributions presented in the study are included in the article/supplementary material, further inquiries can be directed to the corresponding author.

## AUTHOR CONTRIBUTIONS

CL conceived the idea. GZ designed the system and did data analysis. All the authors contributed to the discussion on the results for this manuscript.

## FUNDING

This work was supported in part by the National Key Research and Development Program from the Ministry of Science and Technology of the People’s Republic of China (No.2017YFE0104200), Beijing Natural Science Foundation (JQ18023), the National Natural Science Foundation of China (No. 81421004, 81301268), and the National Key Instrumentation Development Project from the Ministry of Science and Technology of the People’s Republic of China (No. 2013YQ030651).

## REFERENCES

1. Siegel RL, Miller KD, Jemal A. Cancer statistics, 2018. *Cancer J Clinicians* (2018) 68(1):7–30. doi:10.3322/caac.21442.
2. Elmore JG, Armstrong K, Lehman CD, Fletcher SW. Screening for breast cancer. *J Am Med Assoc* (2005) 293(10):1245–56. doi:10.1001/jama.293.10.1245.
3. Bray F, McCarron P, Parkin DM. The changing global patterns of female breast cancer incidence and mortality. *Breast Canc Res* (2004) 6(6):229. doi:10.1186/bcr932.
4. Miller AB, Wall C, Baines CJ, Sun P, To T, Narod SA. Twenty five year follow-up for breast cancer incidence and mortality of the Canadian National Breast Screening Study: randomised screening trial. *Bmj* (2014) 348:g366. doi:10.1136/bmj.g366.
5. Freer PE. Mammographic breast density: impact on breast cancer risk and implications for screening. *Radiographics* (2015) 35(2):302–15. doi:10.1148/rg.352140106.
6. Madjar H. Role of breast ultrasound for the detection and differentiation of breast lesions. *Breast Care* (2010) 5(2):109–14. doi:10.1159/000297775.
7. Taylor KJW, Merritt C, Piccoli C, Schmidt R, Rouse G, Fornage B, et al. Ultrasound as a complement to mammography and breast examination to characterize breast masses. *Ultrasound Med Biol* (2002) 28(1):19–26. doi:10.1016/s0301-5629(01)00491-4.
8. Saslow D, Boetes C, Burke W, Harms S, Leach MO, Lehman CD, et al. American Cancer Society guidelines for breast screening with MRI as an adjunct to mammography. *Cancer J Clin* (2007) 57(2):75–89. doi:10.3322/canjclin.57.2.75.
9. Lin L, Hu P, Shi J, Appleton CM, Maslov K, Li L, et al. Single-breath-hold photoacoustic computed tomography of the breast. *Nat Commun* (2018) 9(1):2352. doi:10.1038/s41467-018-04576-z.
10. Becker A, Masthoff M, Claussen J, Ford SJ, Roll W, Burg M, et al. Multispectral optoacoustic tomography of the human breast: characterisations of healthy tissue and malignant lesions using a hybrid ultrasound-optoacoustic approach. *Eur Radiol* (2017) 28(2):602–609. doi:10.1007/s00330-017-5002-x.
11. Wang LV, Hu S. Photoacoustic tomography: *in vivo* imaging from organelles to organs. *Science* (2012) 335(6075):1458–62. doi:10.1126/science.1216210.
12. Folkman J. Angiogenesis in cancer, vascular, rheumatoid and other disease. *Nat Med* (1995) 1(1):27–30. doi:10.1038/nm0195-27.
13. Carmeliet P, Jain RK. Angiogenesis in cancer and other diseases. *Nature* (2000) 407:249. doi:10.1038/35025220.
14. Neuschler EI, Butler R, Young CA, Barke LD, Bertrand ML, Bohm-Velez M, et al. A pivotal study of optoacoustic imaging to diagnose benign and malignant breast masses: a new evaluation tool for radiologists. *Radiology* (2018) 287(2):398–412.
15. Diot G, Metz S, Noske A, Liapis E, Schroeder B, Ovsepian SV, et al. Multispectral optoacoustic tomography (MSOT) of human breast cancer. *Clin Cancer Res* (2017) 23(22):6912–22.
16. Zhou Y, Tripathi SV, Rosman I, Ma J, Hai P, Linette GP, et al. Noninvasive determination of melanoma depth using a handheld photoacoustic probe. *J Invest Dermatol* (2017) 137(6):1370–2. doi:10.1016/j.jid.2017.01.016.
17. Neuschmelting V, Burton NC, Lockau H, Urich A, Harmsen S, Ntziachristos V, et al. Performance of a multispectral optoacoustic tomography (MSOT) system equipped with 2D vs. 3D handheld probes for potential clinical translation. *Photoacoustics* (2016) 4(1):1–10. doi:10.1016/j.pacs.2015.12.001.
18. Toi M, Asao Y, Matsumoto Y, Sekiguchi H, Yoshikawa A, Takada M, et al. Visualization of tumor-related blood vessels in human breast by photoacoustic imaging system with a hemispherical detector array. *Sci Rep* (2017) 7:41970. doi:10.1038/srep41970.
19. Xie Z, Hooi FM, Fowlkes JB, Pinsky RW, Wang X, Carson PL. Combined photoacoustic and acoustic imaging of human breast specimens in the mammographic geometry. *Ultrasound Med Biol* (2013) 39(11):2176–84. doi:10.1016/j.ultrasmedbio.2013.05.018.
20. Asao Y, Hashizume Y, Suita T, Nagae K-i, Fukutani K, Sudo Y, et al. Photoacoustic mammography capable of simultaneously acquiring photoacoustic and ultrasound images. *J Biomedical Optics* (2016) 21(11):116009. doi:10.1117/1.jbo.21.11.116009.
21. Heijblom M, Piras D, Xia W, van Hespen JCG, Klaase JM, van den Engh FM, et al. Visualizing breast cancer using the Twente photoacoustic mammoscope: what do we learn from twelve new patient measurements? *Opt. Express* (2012) 20(11):11582–97. doi:10.1364/oe.20.011582.
22. Nyayapathi N, Takabe K, Xia J, Lim R, Zhang H, Zheng W, et al. Dual scan mammoscope (DSM) - a new portable photoacoustic breast imaging system with scanning in craniocaudal plane. *IEEE Trans Biomed Eng* (2019) 67(5):1321–1327. doi:10.1109/tbme.2019.2936088.
23. Tan Y, Xia K, Ren Q, Li C. Three-dimensional photoacoustic imaging via scanning a one dimensional linear unfocused ultrasound array. *Opt Express* (2017) 25(7):8022–8.
24. Xu M, Wang LV. *Universal back-projection algorithm for photoacoustic computed tomography* (2007) 1539–3755.
25. Li G, Li L, Zhu L, Xia J, Wang LV. Multiview Hilbert transformation for full-view photoacoustic computed tomography using a linear array. *J Biomed Opt* (2015) 20(6):066010. doi:10.1117/1.jbo.20.6.066010.
26. Cheong WF, Prahl SA, Welch AJ. A review of the optical properties of biological tissues. *IEEE J Quantum Electron* (1990) 26(12):2166–85. doi:10.1109/3.64354.
27. Sandell JL, Zhu TC. A review of *in-vivo* optical properties of human tissues and its impact on PDT. *J Biophot* (2011) 4(11-12):773–87. doi:10.1002/jbio.201100062.
28. Wang LV, Wu HI. *Biomedical optics: principles and imaging*. John Wiley & Sons (2012).
29. Xu Y, Wang LV, Ambartsoumian G, Kuchment P. Reconstructions in limited-view thermoacoustic tomography. *Med Phys* (2004) 31(4):724–33. doi:10.1118/1.1644531.

**Conflict of Interest:** The authors declare that the research was conducted in the absence of any commercial or financial relationships that could be construed as a potential conflict of interest.

frontiers
in Physics

ORIGINAL RESEARCH
published: 04 December 2020
doi: 10.3389/fphy.2020.600812

# High-Sensitive Multiwavelength Dynamic Diffuse Optical Tomography System: A Preliminary Investigation

**Limin Zhang [1,2]*, Bin Cao [1], Xiangdong He [1], Zhilong Sun [3], Jiao Li [1,2], Zhongxing Zhou [1,2] and Feng Gao [1,2]**

[1] College of Precision Instruments and Optoelectronics Engineering, Tianjin University, Tianjin, China, [2] Tianjin Key Laboratory of Biomedical Detecting Techniques and Instruments, Tianjin, China, [3] Tianjin International Engineering Institute, Tianjin University, Tianjin, China

Diffuse optical tomography (DOT) is a novel functional imaging technique that has the potential clinical application for breast cancer screening. Currently, an underexploited benefit of DOT is its ability to track and characterize dynamic events related to physiological progression, which can provide additional imaging contrast. In this work, we propose a novel 3-wavelength, 32-source–detector continuous-wave dynamic DOT system that allows relatively fast and high-sensitivity imaging by combining phase lock and photon counting technologies and obtains a balance between cost and effectiveness through series parallel measurement mode. To assess the effectiveness of the proposed system prototype, we systematically investigated the key specifications of the system, including stability, channel cross talk, and dynamic range. Furthermore, the static and dynamic phantom experiments validated the capability of the system to detect the target with low absorption contrast as well as track the changes in the target's absorption coefficient. These preliminary results indicate that the system has great application prospects in imaging of the low-contrast lesion as well as capturing the dynamic changes of hemodynamics in tumor tissue.

**Keywords: diffuse optical tomography, square-wave modulation, image reconstruction, phase-locked photon-counting, dynamic range, cross talk**

OPEN ACCESS

**Edited by:**
*Chao Tian,*
*University of Science and Technology of China, China*

**Reviewed by:**
*Du Le,*
*Florida International University, United States*
*David B. Stout,*
*Independent Researcher, Culver City, United States*

***Correspondence:**
*Limin Zhang*
*zhanglm@tju.edu.cn*

**Specialty section:**
*This article was submitted to Medical Physics and Imaging, a section of the journal Frontiers in Physics*

**Received:** *31 August 2020*
**Accepted:** *30 October 2020*
**Published:** *04 December 2020*

**Citation:**
*Zhang L, Cao B, He X, Sun Z, Li J, Zhou Z and Gao F (2020) High-Sensitive Multiwavelength Dynamic Diffuse Optical Tomography System: A Preliminary Investigation. Front. Phys. 8:600812. doi: 10.3389/fphy.2020.600812*

## 1. INTRODUCTION

Diffuse optical tomography (DOT) is a novel noninvasive technique that utilizes near infrared light to characterize the spatial distribution of optical properties in biological tissue [1]. It can generate images of the absorption or scattering properties of the tissue or other physiological parameters such as oxygenated and deoxygenated hemoglobin, lipid, and water by multiwavelength measurement. Compared with traditional imaging modalities including X-ray mammogram, ultrasound, and MRI, DOT is considered to be an ideal tool for breast cancer screening due to the merits of nonionizing radiation and low cost, as well as providing functional information [2].

After decades of development, significant advances in the field of DOT breast imaging have been made under a variety of ingenious designs [3–13]. Generally, there are three measurement modalities: time domain (TD), frequency domain (FD), and continuous wave (CW) [3–5]. TD systems can potentially provide absolute information regarding the light intensity as well as photon propagation time by means of measuring the temporal point spread function. FD systems can measure both the reduction in intensity and the phase shift of the light after it passes through tissue.

The wealth of information acquired in these two systems can be employed to distinguish the internal absorption and scattering properties of the tissue; however, the systems are expensive and require relatively long acquisition times, especially for time-domain modality. CW systems only measure the change in the amplitude of the light, which allows for a relatively simple, easy operational, and affordable technique. In addition, this approach enables fast data acquisition and the use of simple detectors and electronics, which makes it possible to monitor real-time dynamic changes of physiological signals [6–8].

Despite advances in DOT imaging techniques, an underexploited benefit of DOT is its ability to acquire data at high speed for real-time monitoring. This enables DOT to both recover static distributions of endogenous contrast resulting from tumor vascularization and track dynamic temporal events related to physiological progression. Previously, on the basis of CW diffuse optical tomography systems, some researchers have exploited the potential of imaging dynamic contrasts in breast tissue by disturbing physiological conditions such as breast compression [15, 16], respiratory maneuver [17], and injection of indocyanine green agent [14–20]. For example, several groups have reported the studies of imaging the hemodynamic response of the breast to compression, which is proved to induce differences in oxygen consumption between tumor and normal tissue [16, 17]; Schmitz and Flexman et al. explored the use of a breath hold for creating dynamic contrast to distinguish healthy from cancerous tissue [18, 19]. Intes et al. investigated the pharmacokinetics of indocyanine green agent in breast tumors, harnessing the characteristic that the tumor vessel demonstrates stronger permeability compared with normal vessel [20].

At present, achieving dynamic imaging using DOT is still an ongoing task. In order to capture the transient response process of physiological signals accurately, three main technical aspects should be carefully taken into account: the imaging system must have sufficient temporal resolution; high sensitivity is required to detect tiny changes in different states to provide meaningful additional information for diagnosis; large dynamic range of the system is necessary, since light in tissue is heavily attenuated with the increase of propagation distance; thus, the degree of detection signal may vary by orders of magnitude in different measurement positions, especially for large dimension biological tissues such as breast tissue.

Based on the above considerations, a dynamic three-wavelength (685, 785, and 830 nm) CW diffuse optical tomography system was built, using 20 sources with parallel excitation through phase-locked photon counting to significantly improve temporal resolution, sensitivity, and dynamic range. To evaluate the effectiveness and capabilities of the proposed system, a series of investigations with variable contrast signals were conducted using both static and dynamic phantoms. The goals were to detect the targets with low absorption contrast and validate the ability to track changes in the target absorption coefficients over time. The work involving investigation on the key specifications of the system and phantom imaging is a prerequisite for performing clinical studies.

## 2. INSTRUMENT AND METHODS

### 2.1. Dynamic Diffusion Optical Tomography System

A schematic of the dynamic continuous-wave DOT system is shown in **Figure 1**. The system has three source wavelengths, 685, 785, and 830 nm, which are widely considered to be an optimal combination for resolving *in vivo* changes of hemoglobin [21]. For each wavelength, 32 fiber-tailed laser diodes (10 mw, LSFLD685-10, LSFLD785-10, and LSFLD830-10, Beijing Lightsensing Technologies Ltd.) are driven by a self-designed constant power circuit and modulated for performing simultaneous illumination and rejection ambient light. The three-wavelength light sources are coupled to source fibers with a core diameter of 62.5 μm and a numerical aperture of 0.22, using wave division multiplexers (685/785/830-62.5/125, Oz Optics, Canada) to sequentially illuminate the imaging object. The transmission light on the boundary is collected via detection fiber with a core diameter of 500 μm and a numerical aperture of 0.37. The detection fibers are connected with an integrated module of programmable 4-1 × 8 multimode fiber switch so that the transmission light at four different positions is able to be probed in parallel at the same time. Subsequently, the photomultiplier tube (PMT) (H2859-02, Hamamatsu Photonics, Japan) counting head coupled to the fiber switch converts the light signals to electrical pulses which can be counted by using the photon count technique and synchronously demodulated in field programmable gate array. The demodulated data are sent to the computer through a serial port for optical image reconstruction.

To improve the dynamic capability and balance between cost and effectiveness, a square-wave modulation phase-locked photon-counting scheme and series parallel measurement mode are proposed in this system. In the following section, the principle and process of the measurement will be given in detail.

### 2.2. Square-Wave Modulation Phase-Locked Photon-Counting Strategy

To enable simultaneous multipoint illumination and distinguish the superposed source signals, a phase-locked photon-counting scheme was adopted. In this scheme, the sources are switched “on” and “off” by double-frequency orthogonal square-wave modulation signals with a duty cycle of 50%, and meanwhile, they are sent to the phase-locked photon-counting module as the reference signals of “ ± 1” weights for demodulation, which can be interpreted via a specific case as shown in **Figure 2**.

When four sources LD1, LD2, LD3, and LD4 are excited simultaneously, the signal $I$ detected in a certain period is the superposition of four source signals

$$I = I_{LD1} + I_{LD2} + I_{LD3} + I_{LD4}. \tag{1}$$

In order to separate the superposed signals, two sets of double-frequency orthogonal square-wave signals are utilized to modulate the four sources, where $f_{LD1}$ and $f_{LD2}$ as the first set

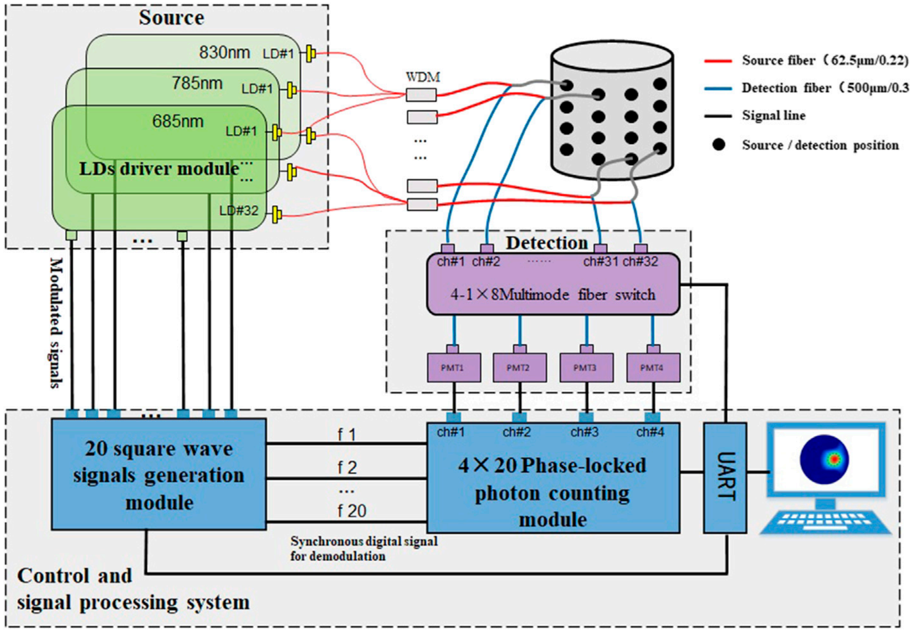

**FIGURE 1 |** Schematic of the CW dynamic diffuse optical tomography system.

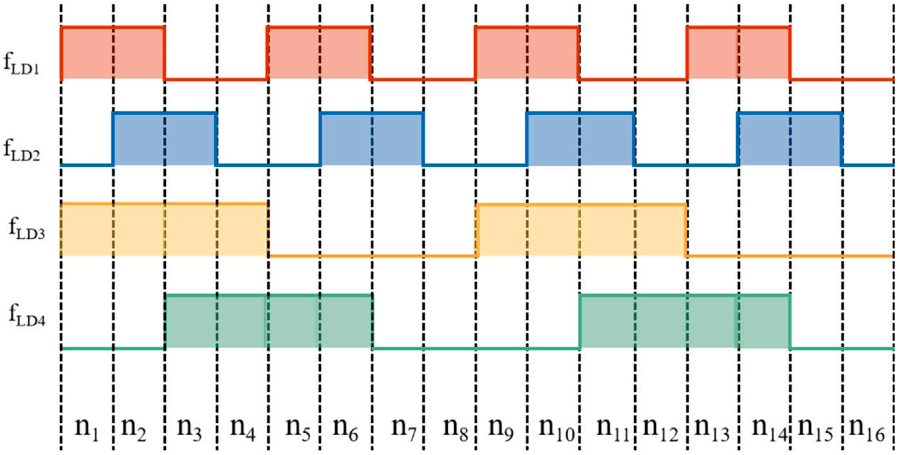

**FIGURE 2 |** Two sets of double-frequency orthogonal square-wave signals.

of orthogonal square wave modulated signals have the same frequency and are twice that of the second set ($f_{LD3}$ and $f_{LD4}$). In each cycle, the first and second sets of signals are divided equally into four and eight subintervals, respectively, represented by $n_i\,(i = 1, 2, 3 \ldots 16)$. During each subinterval, the detected signal $I_{n_i}\ (i = 1, 2, 3 \ldots 8)$ determined by switching on or off of the light source can be expressed in the following equations:

$$I_{n_1} = I_{LD1} + I_{LD3}\,, \tag{2}$$

$$I_{n_2} = I_{LD1} + I_{LD2} + I_{LD3}, \tag{3}$$

$$I_{n_3} = I_{LD2} + I_{LD3} + I_{LD4}, \tag{4}$$

$$I_{n4} = I_{LD3} + I_{LD4}, \tag{5}$$

$$I_{n5} = I_{LD1} + I_{LD4}, \tag{6}$$

$$I_{n_6} = I_{LD1} + I_{LD2} + I_{LD4}, \tag{7}$$

$$I_{n_7} = I_{LD2}, \tag{8}$$

$$I_{n_8} = 0\,. \tag{9}$$

Meanwhile, the light intensity of LD1, LD2, LD3, and LD4 is obtained by solving the above equations:

$$I_{LD1} = I_{n1} + I_{n2} + I_{n5} + I_{n6} - I_{n3} - I_{n4} - I_{n7} - I_{n8}, \tag{10}$$

$$I_{LD2} = I_{n2} + I_{n3} + I_{n6} + I_{n7} - I_{n1} - I_{n4} - I_{n5} - I_{n8}, \tag{11}$$

$$I_{LD3} = I_{n1} + I_{n2} + I_{n3} + I_{n4} - I_{n5} - I_{n6} - I_{n7} - I_{n8}, \tag{12}$$

$$I_{LD4} = I_{n3} + I_{n4} + I_{n5} + I_{n6} - I_{n1} - I_{n2} - I_{n7} - I_{n8}. \tag{13}$$

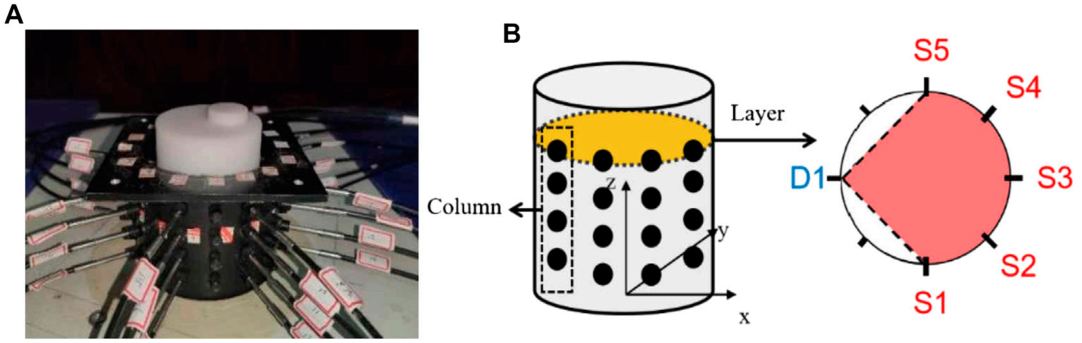

**FIGURE 3 |** Picture of the optical fiber distribution around imaging chamber and the sketch map.

Likewise, when separating the signals of n sources, it is necessary to modulate the sources by $n/2$ sets of double-frequency orthogonal square-wave signals, and at least $2\hat{[}(n/2)+1]$ subintervals are required. It is noteworthy that $n$ is supposed to be even here, and the methodology is similar if n is odd.

In the $i$th subinterval, the detected signal $I_{n_i}$ can be expressed as

$$I_{n_i} = \sum_{j=1}^{n} \omega_{ij} I_{LDj}, \tag{14}$$

where $\omega_{ij} = \begin{cases} 1, & LDj \text{ is on during } \mathrm{n_i}, \\ 0, & LDj \text{ is off during } \mathrm{n_i}. \end{cases}$

For all subintervals, it can be abbreviated as

$$\mathbf{I}_n = \mathbf{W}\mathbf{I}_{\mathrm{LD}}, \tag{15}$$

where $\mathbf{I}_n$ as the measurement data obtained by the detector is a $2\hat{}[(n/2)+1] \times 1$ column vector, $\mathbf{W}$ is a $2\hat{}[(n/2)+1] \times n$ matrix determined by switching on or off the light source during each subinterval, and $\mathbf{I_{LD}}$ is an $\mathrm{n} \times 1$ unknown vector to be solved and can be further deduced as

$$\mathbf{I}_{\mathrm{LD}} = \mathbf{W}^{-1}\mathbf{I}_n. \tag{16}$$

Now, we have theoretically derived the ideal case of separating $n$ source. In the actual measurement, however, considering that the signal-to-noise ratio of photon counting is related to the number of detected photons, the measurement integration time should be carefully selected to make the demodulation result more reliable. In addition, the phase-locked photon-counting strategy is based on the premise that the sources have excellent stability and reasonable gating time to ensure that the average of photons in different counting periods is approximately equal and the correct number of photons can be demodulated.

## 2.3. Series Parallel Measurement Mode

**Figure 3** illustrates the picture of the optical fiber distribution around a cylindrical imaging chamber and the sketch map. As shown in **Figure 3B**, taking the center of the cylindrical bottom as the origin of the coordinate system x, y, and z, 32 coaxial source–detector fibers are placed along the perpendicular $Z$-axis at the heights of $Z = 8$ mm, $Z = 24$ mm, $Z = 40$ mm, and $Z = 56$ mm and arranged at equal spacing on every layer to form a 4 (layers) × 8 (columns) distribution model. For illustration purposes, **Figure 3B** also displays the source and detector positions for the first measurement, where the D1-located column represents the detection positions and other five columns (S1–S5) except for the detection positions and their nearest neighbor points on both sides demonstrate the source positions, meaning 20 modulated sources simultaneously illuminate and four detectors in parallel probe at a time measurement. Similarly, when the positions of illuminating sources are changed, the corresponding detection positions are changed automatically via an optical switch, resulting in a total of 32D × 20S data acquired during a complete measurement for each wavelength. The acquisition time for collecting one complete frame of the projection data (32D × 20S) is approximately 2 s.

## 3. INSTRUMENT PERFORMANCE ASSESSMENT

To evaluate the performance of the system in terms of stability, the cross talk among channels, the ability to reject ambient light, and dynamic range, a series of phantom experiments were conducted. In all the experiments, the sources were modulated by doubled-frequency orthogonal square waves having the frequency range $2^2 \sim 2^{11}$Hz, and a cylindrical polyformaldehyde phantom with both a height and diameter of 80 mm was used to mimic breast tissue. Based on time-resolved measurement, the reduced scattering coefficient of the solid phantom was determined to be $0.8\ \mathrm{mm}^{-1}$ at 685 nm, 785, and 830 nm, since it was barely changed at the three wavelengths, and the absorption coefficients of the background were 0.0041, 0.0034, and $0.0031\ \mathrm{mm}^{-1}$ at 685, 785, and 830 nm, respectively.

### 3.1. Coefficient of Variation

It is an essential requirement for all the light sources to secure a stable operation with the constant current module. To characterize the stability, a metric, referred to as coefficient of variation (CV), is calculated using the following equation:

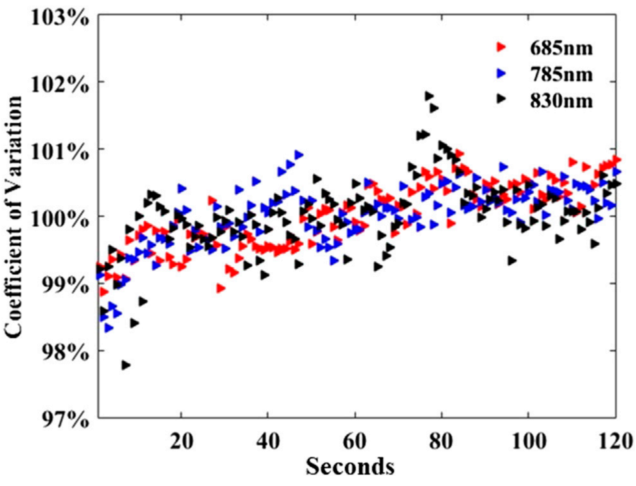

**FIGURE 4 |** Coefficient of variation of the one source at wavelengths of 685 nm, 785 nm, and 830 nm.

$$CV = N/\overline{N} \times 100\%, \tag{17}$$

where $N$ is the number of detected photons in a certain time interval, $\overline{N}$ represents the average value detected in a series of time intervals, and CV closer to 100% indicates better stability. In this experiment, we evaluate the CVs of the total 96 light sources after 120 consecutive measurements, with an integration time of 1 s. **Figure 4** representatively demonstrates the CVs of one of the sources at three wavelengths. It is shown that a very limited number of CVs fluctuate beyond 1% during 120 s, indicating excellent stability of the system.

## 3.2. Channel-to-Channel Cross Talk Ratio

Theoretically, the doubled-frequency orthogonal square wave modulation and demodulation strategy can separate multiple mixed source signals well; however, cross talk among different channels is inevitable due to source light fluctuation, counting noise, system noise, etc. In order to ensure the accuracy of the measurement results, cross talk ratio (CR) is defined to evaluate the cross talk among channels as follows

**TABLE 1 |** Counted photon number of ambient light under two counting modes.

| Counting mode | 1 | 2 | 3 | 4 |
|---|---|---|---|---|
| Single photon counting mode | 2,476 | 57,637 | 647,567 | 1,065,427 |
| Double-frequency counting mode | 18 | 35 | 40 | 76 |

$$CR = I_{\text{other}} \Big/ I_{\text{fn}} \times 100\%, \tag{18}$$

where $I_{\text{fn}}$ is the number of photons demodulated by the frequency $f_n$ when the other 19 light sources are off, which is the real counting result. Conversely, $I_{\text{other}}$ is the number of photons demodulated by other 19 frequencies, when the source with the frequency $f_n$ is off, which is considered to be the photon noise. In the ideal state, the value of the CR should be 0, and the larger CR is, the more serious the cross talk among different channels becomes.

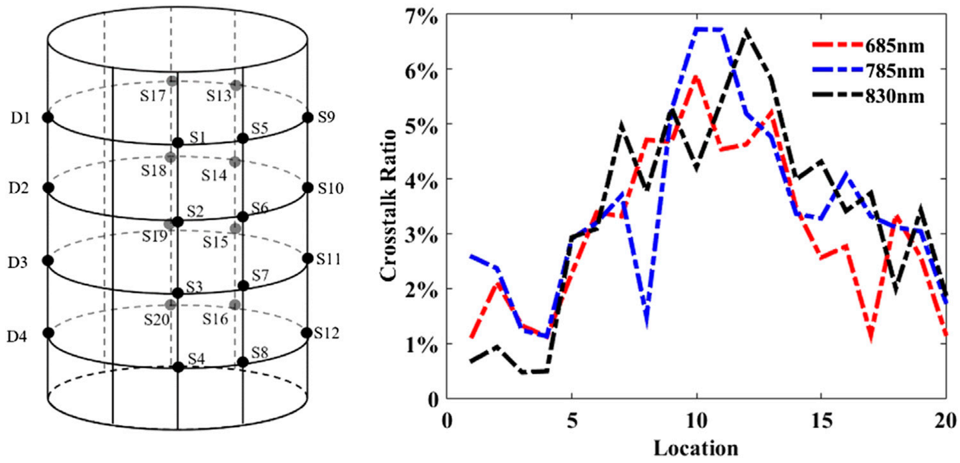

**FIGURE 5 |** Crosstalk assessments: source-detector array configuration **(left)** and the channel-to-channel crosstalk-ratio of 20 source locations at the wavelengths of 685 nm, 785 nm, and 830 nm **(right)**.

In this experiment, the average values of the detected photon number were calculated after ten times repeated measurements in order to minimize the error. The cross talk ratio plotted in **Figure 5** as a function of 20 source locations demonstrates that the CRs of the three wavelengths are similar and most CRs are low (less than 5%), except for the positions of No. 9, No. 10, No. 11, and No. 12, which is because they are farthest to the sources, resulting in lower detection SNR.

## 3.3. Anti-Interference Ability

In a conventional single photon counting mode, rejecting ambient light is essential to prevent undesired noise interference and to protect the PMT. However, in the phase-locked mode, the ambient light considered as a stationary signal

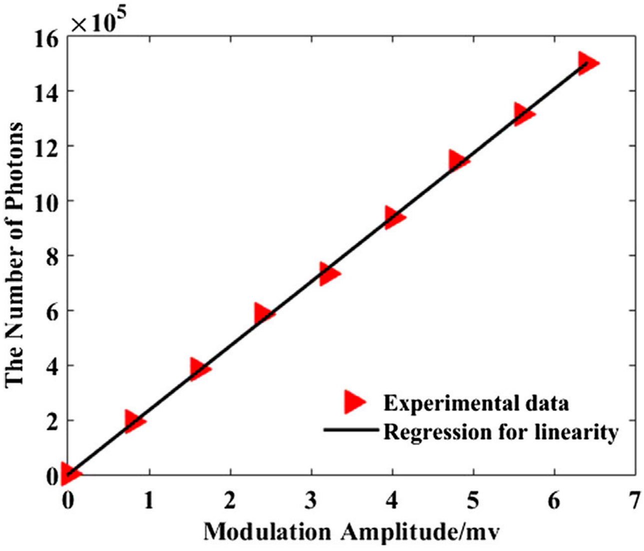

**FIGURE 6** | Measured dynamic range of the DOT system.

can be filtered out during the demodulation process. In order to evaluate the system's ability to reject ambient light, a continuous counting experiment was performed with the sources turned off and the ambient light intensity increased gradually. The experimental results listed in **Table 1** show that the photon number obtained using the conventional single photon counting mode increased from 2,476 to 1,065,427 with the increase of ambient light intensity; however, the photon number acquired using double-frequency counting mode increased from 18 to 76, meaning that the system has a significantly high ability to reject ambient light.

## 3.4. Dynamic Range

Dynamic range is an important evaluation criterion, since the detected photon number may vary by orders of magnitude in different measurement positions in large dimensions of biological tissues such as breast issues. The lower and upper bounds of dynamic range are, respectively, determined by noise equivalent power (the minimum optical power required for an output signal-to-noise ratio of 1) and the maximum detected value acquired in the linear range of the detector. First, we tested the behavior of dark counting in conventional and phase-locked photon-counting modes by placing the system in the dark room. Within the integration time of 1 s, the dark counting in the phase-locked photon-counting mode measurement was two orders of magnitude lower than the conventional method. Then, the light source was turned on and the intensity was gradually increased by enhancing the modulation amplitude with a fixed step, and the number of detected photons was recorded. Since this experiment is a methodological verification, only the light source with the wavelength of 685 nm was selected. **Figure 6** shows the photon number increased linearly until the maximum value of $1.5\times10^6$ with the increment of the source intensity, whereby the dynamic range can be calculated to be 109 dB. It is worth noting that the maximum number of photons is related to the maximum intensity of the source. Theoretically, the maximum linear photon count range of the PMT used in the system is $5 \times 10^6$, and thereby, the dynamic range is up to 120 dB.

## 4. PHANTOM VERIFICATION

To investigate the performance of the three-wavelength dynamic DOT system, a series of phantom experiments were conducted. In all the experiments, a cylinder hole (target henceforth) in the phantom was injected with a solution that has varying optical absorption coefficients by mixing different concentrations of Intralipid and India ink to mimic the tumor [22–24].

## 4.1. Static Phantom Experiment

As shown in **Figure 7A**, to evaluate the imaging sensitivity of the system, a target was drilled at 17 mm off-center of the phantom, with a diameter of 20 mm and a depth of 80 mm. Herein, four target-to-background absorption contrasts of 4, 2, 1.5, and 1.2 were prepared. After two sets of measurement, data were obtained by difference measurements (measure the change in the optical properties of the object based on measurements before and after the change); the images can be reconstructed by the Newton–Raphson-based nonlinear algorithm with the algebraic reconstruction technique embedded for the linear inversion [25].

**Figure 7B** shows the cross-sectional images with four different absorption contrasts at three wavelengths at Z = 24 mm. We can see that the position and size of the targets were reconstructed accurately for each wavelength, even with the absorption contrast as low as 1.2. The horizontal profiles passing through the target centers, that is, the X-profiles, of the images are also presented in **Figure 7C**. We can see that it quantitatively reflects the variation trend of the reconstructed absorption contrast, which is in accordance with the truth, suggesting the capability of the system to recognize targets with different absorption coefficients. Additionally, we can observe that the reconstructed image quality at 685 nm wavelength is superior to that at 785 and 830 nm, which ascribes to the higher response of the PMT to shorter wavelengths leading to larger photon-counting rate and corresponding higher signal-to-noise ratio.

## 4.2. Dynamic Phantom Experiment

To assess the system's capability to track the change in absorption property, a dynamic phantom experiment was designed to stimulate the process of breath hold which is commonly used in clinical diagnoses [18]. As illustrated in **Figure 8A**, the phantom used in this experiment is the same as mentioned above. The absorption coefficient of solution A composed of Intralip and India ink was set to $0.0034\ \mathrm{mm}^{-1}$ as the same as the background, while the absorption coefficient of solution B ($0.0068\ \mathrm{mm}^{-1}$) is twice of that of A. Switch 1 and switch 2 are used to select solutions A and B that enter the target, respectively. To simulate the change process of absorption

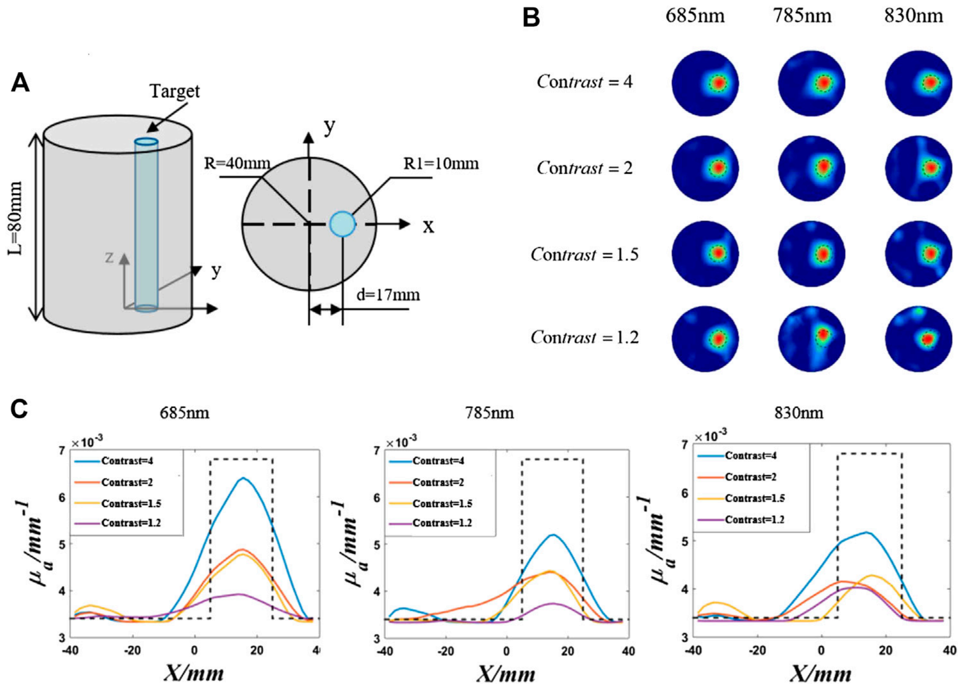

**FIGURE 7 |** Static phantom experiments: **(A)** sketch of the phantom, **(B)** cross-sectional reconstructed images with four different target-to-background absorption contrasts at three wavelengths at Z = 24 mm, and **(C)** profiles of the target-to-background absorption contrast along the *X*-axis.

property in the target region, two peristaltic pump-controlled silicone catheters (BT100–02, China) were utilized to add and remove the solutions to the target at the same speed, in order to maintain a constant target volume. To obtain consistent mixing of the solution during a limited time, the inlet catheter was placed near the top, while the outlet catheter was placed near the bottom. The entire experimental process lasted for 100 s and can be divided into four stages as summarized in **Table 2**, including a 5 -s baseline followed by a 45 -s breath hold, 45 -s recovery, and 5 -s baseline in the last stage.

The images were reconstructed with the temporal resolution of 2 s per frame; thus, a total of 50 frames of images were obtained. For simplicity, 10 frames in chronological order are representatively displayed in **Figure 8B**, where the reconstructed $\mu_a$ in the target region showed a trend of first decrease and then increase. **Figure 8C** shows the plots of the normalized theoretical values and the average values of reconstructed $\mu_a$ in the target region vs. measurement time. We can see that the reconstructed curve (solid line) has a similar variation tendency to the theoretical curve (dashed line), suggesting the tracking ability of the system. We can also observe that there are some differences between the reconstructed and theoretical values, which is mainly because that the exchange of the solution in the target needed some time, the absorption coefficients in the dynamic phantom experiments could not increase or decrease so fast as the theoretical calculating values.

## 5. DISCUSSION AND CONCLUSIONS

We have built a high-density continuous-wave dynamic diffusion optical tomography system. The system consists of 96 sources at three wavelengths (685, 785, and 830 nm) and can achieve simultaneous multipoint illumination and multichannel parallel measurement based on the phase-locked photon-counting detection of the square-wave modulation mode. To verify the performance of the system, we conducted a series of phantom experiments to assess the primary criteria including stability, channel cross talk, the ability to reject ambient light, and dynamic range. The experimental results demonstrated the CVs of the sources fluctuate within 1%, the channel-to-channel cross talk ratio is below 5%, the dynamic range is up to 120 dB, and the tolerance to ambient interference is strong, suggesting the proposed system demonstrates good performance. On these bases, static phantom imaging experiments showed that the system can distinguish the target-to-background absorption contrast as low as 1.2 and accurately reconstruct the position, size, and shape of the target. A self-designed dynamic experiment was conducted to mimic the process of breath hold by changing the absorption coefficient of the target region, which demonstrated that the changes in the trend of the absorption coefficient of the target region were tracked accurately. These preliminary findings indicate the future potential of the dynamic DOT system in breast tumor screening, which may provide help for clinical diagnosis and treatment of breast tumors.

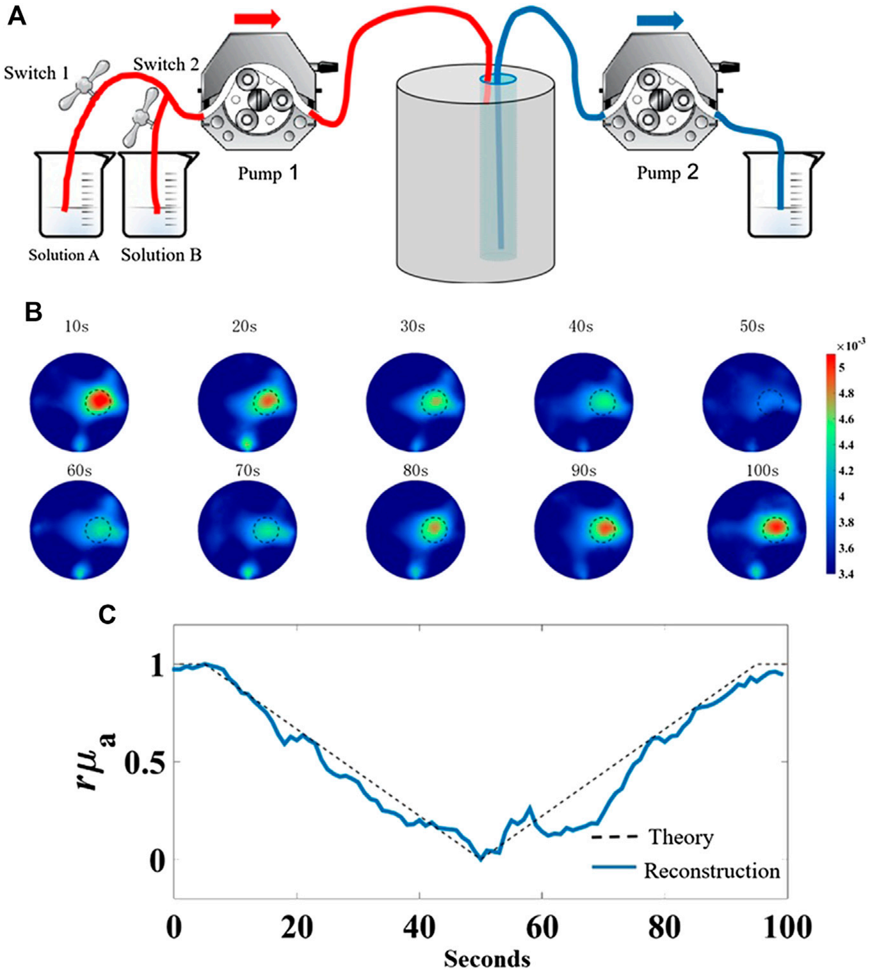

**FIGURE 8 |** Dynamic phantom experiment to mimic the process of breath hold. **(A)** Schematic of dynamic phantom, **(B)** representative 10 reconstructed absorption coefficient images in chronological order, **(C)** plots of the normalized theoretical values and average values of reconstructed absorption coefficient in the target region vs. measurement time.

**TABLE 2 |** Dynamic phantom experiment to mimic the process of breath hold.

| Time/s | Operation | Changes in $\mu_a$ |
|---|---|---|
| 0–5 | Switches 1 and 2 are both off and peristaltic pumps 1 and 2 neither work | $\mu_a$ = 0.0068 mm$^{-1}$ unchanging |
| 5–50 | Switch 1 is on, switch 2 is off, and peristaltic pumps 1 and 2 work | Decreasing (slightly higher or equal to the background solution) |
| 50–95 | Switch 1 is off, switch 2 is on, and peristaltic pumps 1 and 2 work | Increasing (slightly lower or equal to the target solution) |
| 95–100 | Switches 1 and 2 are both off and peristaltic pumps 1 and 2 neither work | $\mu_a$ = 0.0068 mm$^{-1}$ unchanging |

## DATA AVAILABILITY STATEMENT

The raw data supporting the conclusions of this article will be made available by the authors, without undue reservation.

## AUTHOR CONTRIBUTIONS

LZ supervised the project and wrote the manuscript. BC, XH, and ZS designed the experimental setup, collected experimental data, and participated in the manuscript writing. JL and ZZ offered manuscript revision. FG guided the experimental design. All authors contributed to the article and approved the submitted version.

## FUNDING

This work was financially supported by the National Natural Science Foundation of China (81671728, 81871393, 81771880, and 81971656) and Tianjin Municipal Government of China (18JCYBJC29400, 19JCQNJC12800, and 19JCYBJC28600).

## REFERENCES

1. Boas DA, Brooks DH, Miller EL, DiMarzio CA, Kilmer M, Gaudette RJ, et al. Imaging the body with diffuse optical tomography. *IEEE Signal Process Mag* (2001) 18:57–75. doi:10.1109/79.962278
2. Leff DR, Warren OJ, Enfield LC, Gibson A, Athanasiou T, Patten DK, et al. Diffuse optical imaging of the healthy and diseased breast: a systematic review. *Breast Canc Res Treat* (2008) 108:9–22 doi:10.1007/s10549-007-9582-z
3. Jiang HB, Paulsen KD, Osterberg UL, Pogue BW, Patterson MS Simultaneous reconstruction of optical absorption and scattering maps in turbid media from near-infrared frequency-domain data. *Opt Lett* (1995) 20:2128–30. doi:10.1364/OL.20.002128
4. Taroni P, Torricelli A, Lorenzo S, Pifferi A, Arpaia F, Danesini G, et al. Time-resolved optical mammography between 637 and 985 nm: clinical study on the detection and identification of breast lesions. *Phys Med Biol* (2005) 50(11): 2469–88. doi:10.1088/0031-9155/50/11/003
5. Rinneberg RH, Grosenick D, Moesta KT, Wabnitz H, Mucke J, Wübbeler G, et al. Detection and characterization of breast tumours by time-domain scanning optical mammography. *Opto-Electron Rev* (2008) 16:147–62. doi:10.2478/s11772-008-0004-5
6. Liang XP, Zhang QZ, Li CQ, Grobmyer SR, Fajardo LL, Jiang HB. Phase-contrast diffuse optical tomography pilot results in the breast. *Acad Radiol* (2008) 15:859–66. doi:10.1016/j.acra.2008.01.028
7. Ven S, Elias SG, Wiethoff AJ, Voort M, Nielsen T, Brendel B, et al. Diffuse optical tomography of the breast: preliminary findings of a new prototype and comparison with magnetic resonance imaging. *Eur Radiol* (2009) 19:1108–13. doi:10.1007/s00330-008-1268-3
8. Colier W, Sluijs M, Menssen J, Oeseburg B. A new and highly sensitive optical brain imager with 50 hz sampling rate. *Neuroimage* (2000) 11:S542. doi:10.1016/S1053-8119(00)91473-3
9. Chen NG, Guo P, Yan S, Piao D, Zhu Q. Simultaneous near-infrared diffusive light and ultrasound imaging. *Appl Optic* (2001) 40:6367–80. doi:10.1364/AO.40.006367
10. You SS, Jiang YX, Zhu QL, Liu JB, Zhang J, Dai Q, et al. US-guided diffused optical tomography: a promising functional imaging technique in breast lesions. *Eur Radiol* (2010) 20:309–17. doi:10.1007/s00330-009-1551-y
11. Fang QQ, Carp SA, Selb J, Boverman G, Zhang Q, Kopans DB, et al. Combined optical imaging and mammography of the healthy breast: optical contrast derived from breast structure and compression. *IEEE Trans Med Imag* (2009) 28:30–42. doi:10.1109/TMI.2008.925082
12. Brooksby B, Jiang SD, Dehghani H, Pogue BW, Paulsen KD, Kogel C, et al. Magnetic resonance-guided near-infrared tomography of the breast. *Rev Sci Instrum* (2004) 75:5262–70. doi:10.1063/1.1819634
13. Ntziachristos V, Ma XH, Chance B. Time-correlated single photon counting imager for simultaneous magnetic resonance and near infrared mammography. *Rev Sci Instrum* (1998) 69:4221–33. doi:10.1063/1.1149235
14. Jain RK. Normalizing tumor vasculature with anti-angiogenic therapy: a new paradigm for combination therapy. *Nat Med* (2001) 7:987–9. doi:10.1038/nm0901-987
15. Maki A, Yamashita Y, Watanabe E, Koizumi H. Visualizing human motor activity by using non-invasive optical topography. *Front Med Biol Eng* (1996) 7:285–97.
16. Jiang SD, Pogue BW, Laughney AM, Kogel CA, Paulsen KD. Measurement of pressure-displacement kinetics of hemoglobin in normal breast tissue with near-infrared spectral imaging. *Appl Optic* (2009) 48:130–6. doi:10.1364/AO.48.00D130
17. Carp SA, Selb J, Fang Q, Moore R, Kopans DB, Rafferty E, et al. Dynamic functional and mechanical response of breast tissue to compression. *Optic Express* (2008) 16:16064–78. doi:10.1364/OE.16.016064
18. Schmitz CH, Klemer DP, Hardin R, Katz MS, Pei YL, Graber HL, et al. Design and implementation of dynamic near-infrared optical tomographic imaging instrumentation for simultaneous dual breast measurements. *Appl Optic* (2005) 44:2140–53. doi:10.1364/AO.44.002140
19. Flexman ML, Khalil MA, Abdi RA, Kim HK, Fong CJ, Desperito E, et al. Digital optical tomography system for dynamic breast imaging. *J Biomed Optic* (2011) 16:076014. doi:10.1117/1.3599955
20. Intes X, Ripoll J, Chen Y, Nioka S, Yodh AG, Chance B. *In vivo* continuous-wave optical breast imaging enhanced with indocyanine green. *Med Phys* (2003) 30:1039–47. doi:10.1118/1.1573791
21. Scholkmann F, Kleiser S, Metz AJ, Zimmermann R, Pavia JM, Wolf U, et al. A review on continuous wave functional near-infrared spectroscopy and imaging instrumentation and methodology. *Neuroimage* (2014) 85:6–27. doi:10.1016/j.neuroimage.2013.05.004
22. Ninni PD, Martelli F, Zaccanti G. The use of India ink in tissue-simulating phantoms. *Optic Express* (2010) 18:26854–65. doi:10.1364/OE.18.026854
23. Pogue BW Patterson MS. Review of tissue simulating phantoms for optical spectroscopy, imaging and dosimetry. *J Biomed Optic* (2006) 5:2037–53. doi:10.1117/1.2335429
24. Spinelli L, Botwicz M, Zolek N, Kacprzak M, Milej D, Sawosz P, et al. Determination of reference values for optical properties of liquid phantoms based on intralipid and India ink. *Biomed Optic Express* (2014) 5:2037–53. doi:10.1364/BOE.5.002037
25. Arridge SR. Optical tomography in medical imaging. *Inverse Probl* (1999) 15: R41–93. doi:10.1088/0266-5611/15/2/022

**Conflict of Interest:** The authors declare that the research was conducted in the absence of any commercial or financial relationships that could be construed as a potential conflict of interest.

frontiers in Physics

ORIGINAL RESEARCH
published: 16 December 2020
doi: 10.3389/fphy.2020.601180

# Bone Chemical Composition Analysis Using Photoacoustic Technique

*Ting Feng*[1,2]*, Yejing Xie*[1]*, Weiya Xie*[2]*, Dean Ta*[3] *and Qian Cheng*[2,4]***

*[1]School of Electronic and Optical Engineering, Nanjing University of Science and Technology, Nanjing, China, [2]Institute of Acoustics, School of Physics Science and Engineering, Tongji University, Shanghai, China, [3]Department of Electronic Engineering, Fudan University, Shanghai, China, [4]Key Laboratory of Spine and Spinal Cord Injury Repair and Regeneration of Ministry of Education, Orthopaedic Department of Tongji Hospital, Tongji University School of Medicine, Shanghai, China*

Photoacoustic (PA) signal analysis based on ultrasonic wave detection can provide both high-sensitivity optical contrast information and micro-architectural information which is highly related with the chemical composition of tissue. In this study, the feasibility assessment of bone composition assessment was investigated using the multi-wavelength PA analysis (MWPA) method which could reflect the molecular information. By illuminating a bone specimen using a laser light with wavelength over an optical spectrum ranging from 680 to 950 nm, the optical absorption spectrum of the bone was acquired. Then, with the optical absorption spectra of all optical absorption chemical components in the known bone, a spectral unmixing procedure was performed to quantitatively assess the relative content of each chemical component. The experimental results from rabbit bones show that MWPA method can be used to assess chemical components related to bone metabolism. Our study confirmed that PA technique can be used as a novel bone diagnostic technique by providing new information about the quantity of bone and identifying biomarkers of bone that can improve the current diagnostic imaging techniques.

**Keywords: photoacoustic, bone assessment, chemical composition, multi-wavelength photoacoustic analysis, osteoporosis**

***Edited by:***
*Jun Xia,*
*University at Buffalo, United States*

***Reviewed by:***
*Silvia Capuani,*
*National Research Council (CNR), Italy*
*Shu-Chi A. Yeh,*
*Massachusetts General Hospital, United States*

****Correspondence:***
*Qian Cheng*
*q.cheng@tongji.edu.cn*

***Specialty section:***
*This article was submitted to Medical Physics and Imaging, a section of the journal Frontiers in Physics*

***Received:*** *01 September 2020*
***Accepted:*** *18 November 2020*
***Published:*** *16 December 2020*

***Citation:***
*Feng T, Xie Y, Xie W, Ta D and Cheng Q (2020) Bone Chemical Composition Analysis Using Photoacoustic Technique. Front. Phys. 8:601180. doi: 10.3389/fphy.2020.601180*

## INTRODUCTION

Osteoporosis, a serious public health threat with significant physical, psychological and economic impacts, is expected to increase in association with worldwide aging of the population. In osteoporosis, the bone mineral density (BMD) decreases, bone microarchitecture (BMA) deteriorates, and the amount and type of proteins in bone alter [1]. Currently, most clinically used non-invasive assessment methods are based on the use of X-ray or ultrasound [2, 3]. These methods, in spite of the applicability to measure bone mineral density (BMD) as well as some mechanical properties, have limited sensitivity to monitor the chemical or molecular changes in the bone. In addition, X-ray based techniques use ionizing radiation, which is not ideal for pediatric, or long-term repetitive monitoring. Quantitative ultrasound (QUS) technology as a practical, low-cost alternative has already led to clinical instrumentation [4, 5]. The QUS bone assessment method is primarily based on the measurement of sound velocity (SOS) and broadband ultrasound attenuation (BUA) through a given tissue. However, the specificity of QUS is limited when pathogenic bone diseases are determined by microstructure and chemical changes [6–8]. Bone quantity and quality are dependent on not only the mass and structure of non-organic mineral matrix but also the organic matrix which is associated with the bone blood flow and cellular metabolism. Recently, it has been

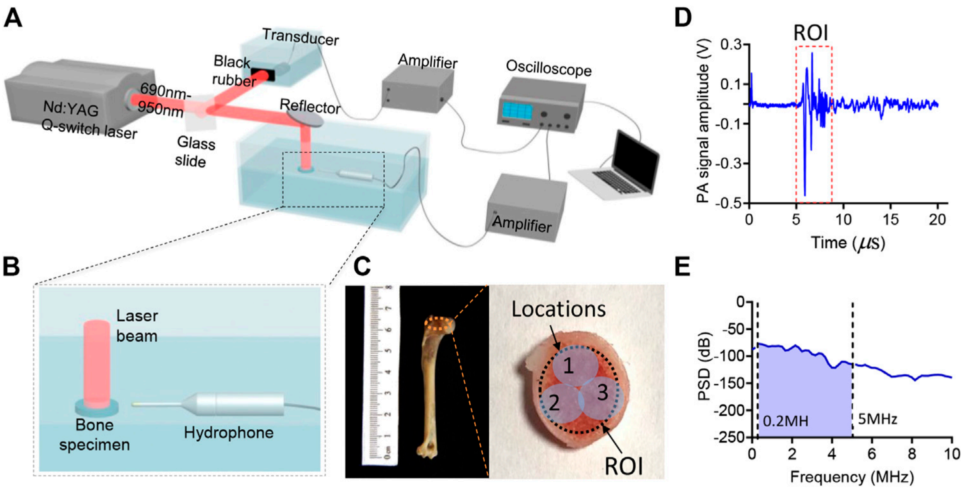

**FIGURE 1 | (A,B)** The schematic diagram of the experiment setup. **(C)** The photograph of the bone sample. **(D)** An example of the PA signal generated by the bone specimen. **(E)** An example of the power spectrum density (PSD) of the PA signal generated by the bone.

reported that magnetic resonance imaging (MRI) can distinguish changes in bone marrow lipid content and bone microarchitecture between normal bone and osteopenia bone [9–11]. Due to the high cost and complexity, MRI examinations are impossible to replace standard DEXA (Dual-Energy X-ray Absorptiometry) measurements with more advanced MRI analysis. In prior studies, optical spectroscopic techniques have been used to evaluate how the alterations of bone composition contribute to bone quality changes related to aging, disease, or injury [12–18]. However, traditional optical techniques suffer from limited spatial resolution and the overwhelming optical scattering in biological tissues, thus reducing the efficacy of skeletal imaging *in vivo*.

The emerging biomedical photoacoustic (PA) techniques have a unique ability to probe the highly sensitive optical absorption contrast in deep biological tissues [19–23]. The PA signal generated by the bone contains both the microstructural information and molecular information, which are both highly correlated with bone health. Lashkari et al. evaluated the cortical and trabecular bone structure and density variations by using a dual backscattered ultrasound and PA radar system [24, 25]. Furthermore, our group has studied the feasibility of accessing BMD and BMA of the trabecular bone in rat models through using thermal photoacoustic (TPA) and photoacoustic spectral analysis (PASA). Recently, Idan Steinberg et al. used the dual-modality multispectral photoacoustic system to quantify the blood/fat ratio present in the marrow, which has been correlated with molecular changes in the long bone.

In this study, the feasibility of the multi-wavelength PA analysis (MWPA) technique in quantifying the molecular information of trabecular bone based on rabbit models with different BMDs were studied. The experimental measurements on the rabbit models of control and osteoporosis groups were performed. The PA spectroscopic curves of the bone from different groups were obtained and decomposed. Then, the MWPA parameter "relative composition ratio" of different chemical components including hydroxyapatite, lipid, hemoglobin, oxy-hemoglobin, and whole blood were quantified and compared with the gold-standard X-ray images and the relative optical absorption spectrum obtained by the commercial spectrometer system.

# MATERIALS AND METHODS

## Experiment Setup

The bone composition of the two groups was measured by using MWPA at the range of 690–950 nm at 10 nm intervals. The experimental setup for studying the chemical components in bone is shown in **Figure 1A**. The light beam generated by an Nd: YAG laser pumped OPO (Vibrant B, Opotek) was divided into two parts. 10% of the laser energy was projected to a black rubber by a beam splitter and recorded by the ultrasound transducer (V310-SU, Olympus) for the calibration of subsequent signal magnitude. The remaining 90% illuminated the bone from one side on the surface of the bone. The diameter of the beam was 4 mm and the light fluency was controlled at 15–20 $mJ/cm^2$. Light passed through the bone and then excited PA signal. The PA signal was received by a needle hydrophone (HNC-1500, Onda Co., Sunnyvale, CA, United States) with a broad bandwidth from 0 to 10 MHz. A pre-amplifier was connected after the hydrophone to improve the signal-to-noise ratio (SNR), and then it was digitized and recorded by a digital oscilloscope (HDO6000, oscilloscope, Teledyne Lecroy, United States). To enhance the signal-to-noise ratio (SNR), the PA signal was averaged over 50 laser pulses. Furthermore, the gold-standard DEXA images was conducted by the commercial DEXA imaging system (InAlyzer) and the relative optical absorption spectrum obtained by the commercial spectrometer system were conducted for each bone samples.

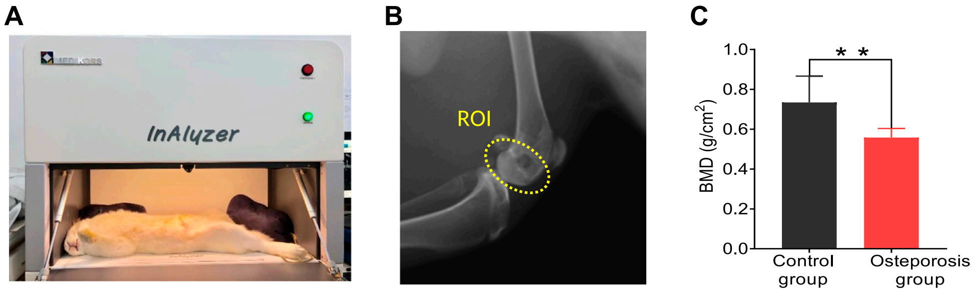

**FIGURE 2 |** DEXA images results. **(A)** Commercial DEXA imaging system. **(B)** DEXA images showing the regions of interests (ROI). **(C)** DEXA imaging at the ROI demonstrates significantly reduced BMD in the osteoporosis group vs. control group. ** stands for $p < 0.01$ in unpaired *t*-test comparing the results from the two bone groups (N = 8 for osteoporosis group, N = 8 for control group).

## Animal Models

In this study, the animal bone models we used in the MWPA measurements were distal end of forelimb, as shown in **Figure 1C**. 8 five-month-old, skeletally mature, female New Zealand white rabbits were divided randomly into two groups: osteoporosis group and control group. Bilateral ovariectomy was used in the osteoporosis group to simulate the symptoms of osteoporosis in elderly women, and sham surgery was used in the control group to avoid other factors affecting the experimental results. Twenty weeks after surgery, rabbits were euthanized, and the distal end of forelimb were dissected and subject to PA assessment.

## Signal Processing

First, the PA signal received by the Onda hydrophone was calibrated with the PA signal amplitude generated by the black rubber. The signal was related to the laser power of each wavelength. Secondly, the PA signal was transmitted to the frequency domain via fast Fourier transform, and the intensity of the PA frequency power at 0.2–5 MHz was summarized as the PA absorption value of each wavelength without being affected by low frequency (<0.2 MHz) noise or high frequency (>5 MHz) noise. The PA signal of each wavelength of light was then quantified and a PA absorption curve was obtained, which represented the spectral PA absorption of each bone. Thirdly, each bone sample was tested from three different directions in order to reduce measurement errors. The PA spectrum curves were obtained in at three different locations as shown in **Figure 1C** and were averaged for further analysis. Finally, spectral unmixing based on the least-square regression method was conducted, the PA absorption spectrum of each group of bones was decomposed to obtain the proportion of corresponding chemical components.

# RESULTS

## DEXA Imaging

The DEXA imaging results from osteoporosis group and control group are shown in **Figure 2**. DEXA images showing the regions of interests (ROI) is marked by the yellow circle as shown in **Figure 2B**. Correlations between the BMD results from DEXA were studied by using unpaired two-tailed independent samples *t*-tests (with Welch's correction in cases of unequal variances), which lead to $p < 0.01$, as shown in **Figure 2C**. This study based on commercial DEXA technologies confirmed the pathologic conditions of the osteoporosis group as well as the difference between the two groups of rabbit models.

## Optical Absorption Measurements

The results of optical absorption measurements are shown in **Figure 3**. **Figures 3AB** shows the commercial spectrometer system and the working principle. The mean and standard deviations of the relative optical absorption spectrum of the bone samples from the osteoporosis group and control group are compared in **Figure 3C**. By comparing with the control group, the bone sample from osteoporosis group has higher optical absorption at the range of 800–950 nm and lower optical absorption at the range of 690–800 nm.

## Multi-Wavelength Photoacoustic Measurements

In the spectral range of 690–950 nm, the main optical absorption components in the bone are oxygenated hemoglobin, deoxygenated hemoglobin, mineral (mostly hydroxyapatite), lipid. **Figure 4** shows the MWPA results of the osteoporosis group and control group. The two solid lines in **Figure 4A** show the averaged PA spectra measured from the two groups of bone samples, while the standard deviation is shown by the shaded area next to each curve. It is obviously that the absorption reached its peaks at 700, 760, and 930 nm. The difference is that the absorption of the osteoporosis group near 700–760 nm is stronger than that of the control group, while the absorption of the control group near 930 nm is stronger than that of the osteoporosis group. As expected, the corresponding content of the components in the osteoporosis group and the control group is consistent with the optical absorption results obtained by the commercial spectrometer system shown in **Figure 3C**. The optical absorption spectra of the main chemical components in the bone are shown in **Figure 4B**. By comparing the wavelength positions of the PA signal peaks and the component absorption peaks, it can be found that the strong absorption peak at 700 nm is mainly caused by the absorption of

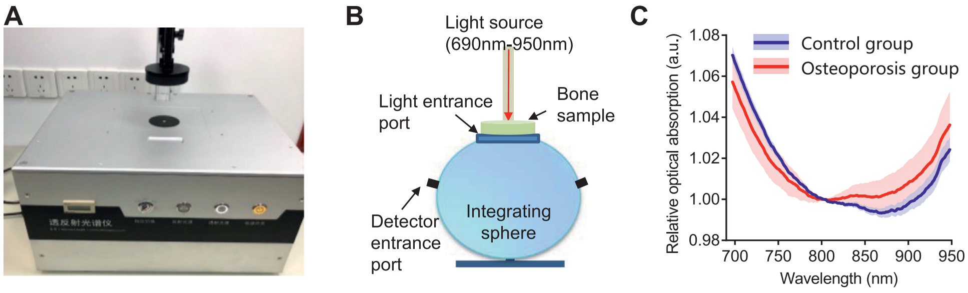

**FIGURE 3 |** The optical absorption system and results. **(A)** The commercial transmission and reflection spectrometer system used in this study. **(B)** The schematic diagram of the integrating sphere used in the commercial spectrometer system. **(C)**The relative optical absorption spectrum of the bone from the control group and osteoporosis group measured by the transmission and reflection spectrometer, each normalized at 800 nm.

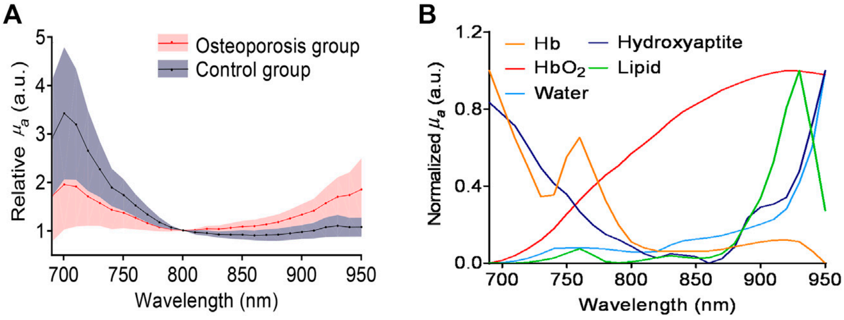

**FIGURE 4 | (A)** The averaged PA spectra measured from the osteoporosis group and control group. **(B)** Optical absorption spectra of major chemical components in the bone, including deoxygenated hemoglobin (Hb), lipids, hydroxyapatite, and oxygenated hemoglobin (HbO$_2$).

deoxygenated hemoglobin and hydroxyapatite. The absorption peak at 930 nm is mainly contributed by the lipid. Therefore, it can be preliminarily estimated that the lipid content of the osteoporosis group is higher than that of the control group, which is consistent with the past study [1, 9]. Besides, the deoxygenated hemoglobin content and the hydroxyapatite content are lower than that of the control group in the animal bone models we used.

For the PA absorption spectrum for each bone sample, it is given as [26]

$$[\mu_a(\lambda)]_{bone} = \sum_{i=1}^{n} [\mu_a(\lambda)]_i \cdot c_i \tag{1}$$

Where $\mu_a(\lambda)$ is the PA absorption spectrum as shown in **Figure 4A**, $n$ is the number of chromophore (absorber) types and $c_i$ and $\mu_a(\lambda)$ are the concentration and absorption coefficient of $i$ th chromophore type, respectively. The goal of quantitative WMPA unmixing is to estimate the relative concentration of a particular chemical component from the measurements given the known absorption spectrum $(\mu_a)_i$ of different chemical component. Thus, with the optical absorption spectra $[\mu_a(\lambda)]_i$ of the major chemical components in the bone known [27, 28], the relative content of each chemical component $c_i$ to the PA absorption spectrum can be derived by performing a spectral unmixing. The spectral unmixing based on the least-square regression method was adopted to obtain the quantitative changes in the contents of the chemical components [29]. **Figure 5A** shows the PA spectrum and the fitted spectrum of the osteoporosis group and the control group, respectively. The $R^2$ of the osteoporosis group and control was as high as 0.9095 and 0.9154, respectively. After the spectral unmixing, the relative contents of the five chemical components in the bone, including deoxygenated hemoglobin, lipid, hydroxyapatite, and oxygenated hemoglobin, were derived. The results of the two groups of bone samples are shown in **Figure 5B**. To evaluate whether each of the differences in chemical properties between the two bone groups has statistical significance, an unpaired two-tailed independent samples $t$-test (with Welch's correction in cases of unequal variances) was conducted. Compared to the control group, the chemical changes in the osteoporosis group showing statistical significance include the increased lipid content, the decreased deoxy-hemoglobin content which are correlation with the osteoporosis diseases. Compared to the control group, the bones in the osteoporosis group also show decreased hydroxyapatite content, whole blood content, which, however, is not statistically significant. These noticed chemical changes of lipid, hydroxyapatite and whole blood in osteoporosis bones are matched well with the findings reported in previous publications [10, 30–34]. However, for the *ex vivo* bone, the deoxygenated

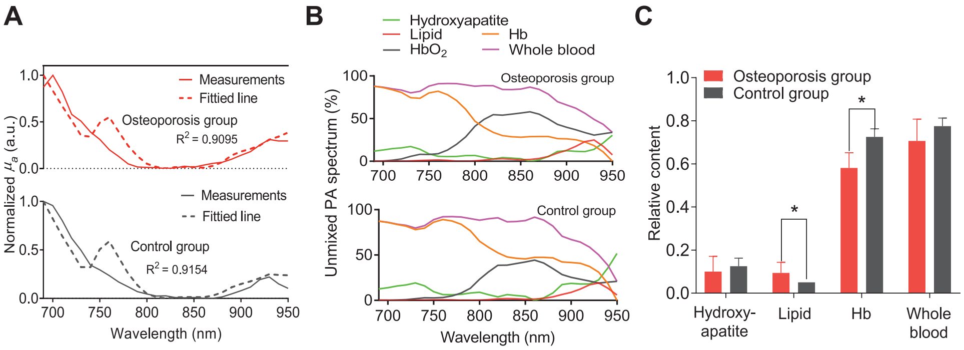

**FIGURE 5 | (A)** The averaged PA spectrum in comparison with the fitted spectrum by using the least-square method. **(B)** The unmixed spectrum of the MWPA curves for the sample from osteoporosis group and control group, respectively. **(C)**The relative contents of the hydroxyapatite, lipids, deoxygenated hemoglobin (Hb), and whole blood (Hb+$HbO_2$). * stands for $p < 0.05$.

hemoglobin and oxygenated hemoglobin are different from the *in vivo* bone sample, especially for the oxygenated hemoglobin. For example, the past study demonstrated the deoxygenation of blood in the *ex vivo* specimens and revealed that deoxygenation of blood occurs almost immediately after sacrificing the animals [35]. Therefore, in this *ex vivo* study, we did not compare the content of oxygenated hemoglobin for osteoporosis bone samples and control samples. Besides, since the deoxygenation of blood occurs in the bone samples, the blood was mostly composited by deoxygenated hemoglobin for the *ex vivo* bone samples in this study. It means that the total content of deoxygenated hemoglobin is highly related with the amount of the whole blood in the bone. Due to the fact that the amount of blood in the normal bone sample is higher than that in the osteoporosis bone sample [12], therefore, the deoxygenated hemoglobin in the control group is higher by comparing with the osteoporosis group in this *ex vivo* study.

## CONCLUSION AND DISCUSSION

The results of this study indicate the feasibility of MWPA method in assessing bone chemical composition. In addition to measuring the mineral content in bones, it can also measure the content of chemical components such as lipid, oxygenated hemoglobin and deoxygenated hemoglobin. The content and changes of these ingredients are inextricably related to bone health, and has the potential to used as a new way for bone health assessment.

This study currently has some limitations. First, the number of bone samples is not large enough. There are only four rabbit samples in each group, and only eight sets of data can be obtained, so data analysis is not universal. In the future, additional data should be collected and analyzed on a large group of samples. Second, the chemical composition has not been verified using the bone histomorphometry. In the future work, we plan to further indicate the differences in lipid and Hb content of those two groups though other pathways. For example, the MRI imaging can be used to get the lipid fraction as the gold-standard for lipid content [10, 36, 37]. The reticular fiber staining for quantification of blood vessels can be used as the gold-standard to reveal the differences in blood content of those two groups. Third, the influence of different types of fatty acids as well as the content of collagen which are also related with bone health are not considered in this study. In the future, with the wider range of the laser wavelength and higher resolution of scanning, it has the potential to distinguish the changes in different types of fatty acids and contents of collagen in the bone tissue. Forth, this study is mainly focusing on the isolated bones. In the future, this technology has the potential to be applied for clinical study *in vivo*. For *in vivo* study, the bone assessment technique based on the PA detecting method described in our manuscript may be not available and should be optimized with better design. For example, the transmission PA mode for multi-wavelength PA measurement of bone *in vivo* in our study published recently [38]. In addition, the effects of light attenuation and ultrasound attenuation need to be considered. Besides, not only the bone but also the overlying soft tissue absorb the light and leads to an increase of light attenuation. Therefore, it is necessary to consider the effect of light attenuation in the bone tissue as well as the overlying soft tissue. At the same time, it has a high attenuation of PA signal for the *in vivo* PA measurements, especially for the high frequency components. Thus, the optimized center frequency of the transducer at a relative lower frequency should be used.

Despite these limitations, this study has successfully demonstrated the feasibility of the emerging PA technology in assessing the chemical information in bones. Compared with DEXA, MRI, QUS and light based techniques, MWPA has the potential to provides more comprehensive bone assessment results, including not only the chemical compositions of bone but also the micro-structure which is highly correlated with bone health as reported in our previous paper [39]. For the gold standard DEXA imaging, since the X-rays are attenuated by both bone and bone marrow fat, therefore, the BMD results quantified by DEXA is altered by the changes in the lipid content of bones. For MRI, in particular MRI spectroscopy, it allows the quantification of bone marrow fats, however, it cannot provide the information of BMD [1]. In addition, the QUS cannot be used for assessing the components of bone composition. Besides, compared with the light based techniques, the PA sensing is based on the detection of light-induced ultrasonic signals which are much less scattered in biological tissues, it can present more spatial information in deep tissues than pure optical techniques. Furthermore, the PA bone assessment method proposed in this article has many advantages such as target-specific, non-ionizing, low-cost, and patient friendly. With all these unique advantages, this technology is expected to be improved and developed into a more accurate bone evaluation method in the future.

## DATA AVAILABILITY STATEMENT

The original contributions presented in the study are included in the article/Supplementary Material, further inquiries can be directed to the corresponding author.

## ETHICS STATEMENT

The animal study was reviewed and approved by Animal Ethics Committee of Tongji University, Shanghai.

## AUTHOR CONTRIBUTIONS

TF, YX, and WX conceived the study. TF and YX performed data acquisition. TF and YX analyzed all the PA data. TF and YX developed the data processing algorithms, TF, YX, WX, DT, and QC drafted the manuscript.

## FUNDING

This work was supported by the National Key Research and Development Project (nos. 2017YFC0111400 and 2016YFA0100800), National Natural Science Foundation of China (nos. 11704188 and 11827808, 12034015, 11674249, 81702962), the Natural Science Foundation of Jiangsu, China (no. BK 20170826), and the Postdoctoral Science Foundation of China under grant no. 2019M651564.

## REFERENCES

1. Di Pietro G, Capuani S, Manenti G, Vinicola V, Fusco A, Baldi J, et al. Bone marrow lipid profiles from peripheral skeleton as potential biomarkers for osteoporosis: a 1H-MR spectroscopy study. *Acad Radiol* (2016) 23(3):273–83. doi:10.1016/j.acra.2015.11.009
2. Kanis JA. Diagnosis and clinical aspects of osteoporosis. In: *Pocket reference to osteoporosis*. Dordrecht, Netherlands: Springer (2019). p 11–20.
3. Marcocci C, Saponaro F. *Osteoporosis diagnosis, multidisciplinary approach to osteoporosis*. Dordrecht, Netherlands: Springer (2018). p 45–57.
4. Raum K, Leguerney I, Chandelier F, Bossy E, Talmant M, Saïed A, et al. Bone microstructure and elastic tissue properties are reflected in QUS axial transmission measurements. *Ultrasound Med Biol* (2005) 31(9): 1225–35.doi:10.1016/j.ultrasmedbio.2005.05.002
5. Laugier P. Quantitative ultrasound instrumentation for bone in vivo characterization. In: P. Laugier G. Haïat, editors *Bone quantitative ultrasound*. Dordrecht, Netherlands: Springer (2011). p 47–71.
6. Töyräs J, Nieminen M, Kröger H, Jurvelin J. Bone mineral density, ultrasound velocity, and broadband attenuation predict mechanical properties of trabecular bone differently. *Bone* (2002) 31(4):503–7. doi:10.1016/s8756-3282(02)00843-8
7. Liu C, Ta D, Fujita F, Hachiken T, Matsukawa M, Mizuno K, et al. The relationship between ultrasonic backscatter and trabecular anisotropic microstructure in cancellous bone. *J Appl Phys* (2014) 115(6):064906. doi:10.1063/1.4865173
8. Njeh C, Boivin C, Langton C. The role of ultrasound in the assessment of osteoporosis: a review. *Osteoporos Int* (1997) 7(1):7–22. doi:10.1007/BF01623454
9. Griffith JF, Yeung DK, Antonio GE, Lee FK, Hong AW, Wong SY, et al. Vertebral bone mineral density, marrow perfusion, and fat content in healthy men and men with osteoporosis: dynamic contrast-enhanced MR imaging and MR spectroscopy. *Radiology* (2005) 236(3):945–51. doi:10.1148/radiol.2363041425
10. Griffith JF, Yeung DK, Antonio GE, Wong SY, Kwok TC, Woo J, et al. Vertebral marrow fat content and diffusion and perfusion indexes in women with varying bone density: MR evaluation. *Radiology* (2006) 241(3):831–8. doi:10.1148/radiol.2413051858
11. Patsch JM, Burghardt AJ, Kazakia G, Majumdar S. Noninvasive imaging of bone microarchitecture. *Ann N Y Acad Sci* (2011) 1240:77–87. doi:10.1111/j.1749-6632.2011.06282.x
12. Pifferi A, Torricelli A, Taroni P, Bassi AL, Chikoidze E, Giambattistelli E, et al. Optical biopsy of bone tissue: a step toward the diagnosis of bone pathologies. *J Biomed Optic* (2004) 9(3):474–80. doi:10.1117/1.1691029
13. Schulmerich MV, Dooley K, Morris MD, Vanasse TM, Goldstein SA. Transcutaneous fiber optic Raman spectroscopy of bone using annular illumination and a circular array of collection fibers. *J Biomed Optic* (2006) 11(6):060502. doi:10.1117/1.2400233
14. Morris MD, Mandair GS. Raman assessment of bone quality. *Clin Orthop Relat Res* (2011) 469(8):2160–9. doi:10.1007/s11999-010-1692-y
15. Draper ER, Morris MD, Camacho NP, Matousek P, Towrie M, Parker AW, et al. Novel assessment of bone using time-resolved transcutaneous Raman spectroscopy. *J Bone Miner Res* (2005) 20(11):1968–72. doi:10.1359/JBMR.050710
16. Ailavajhala R, Oswald J, Rajapakse CS, Pleshko N. Environmentally-controlled near infrared spectroscopic imaging of bone water. *Sci Rep* (2019) 9(1):10199. doi:10.1038/s41598-019-45897-3
17. Paschalis E, Gamsjaeger S, Klaushofer K. Vibrational spectroscopic techniques to assess bone quality. *Osteoporos Int* (2017) 28(8):2275–91. doi:10.1007/s00198-017-4019-y
18. Mandair GS, Steenhuis P, Ignelzi MA, Morris MD. Bone quality assessment of osteogenic cell cultures by Raman microscopy. *J Raman Spectrosc* (2018) 50(3): 360–70. doi:10.1002/jrs.5521
19. Wang X, Pang Y, Ku G, Xie X, Stoica G, Wang LV. Noninvasive laser-induced photoacoustic tomography for structural and functional *in vivo* imaging of the brain. *Nat Biotechnol* (2003) 21(7):803–6. doi:10.1038/nbt839
20. Wang LV, Hu S. Photoacoustic tomography: in vivo imaging from organelles to organs. *Science* (2012) 335(6075):1458–62. doi:10.1126/science.1216210
21. Steinberg I, Huland DM, Vermesh O, Frostig HE, Tummers WS, et al.. Photoacoustic clinical imaging. *Photoacoustics* (2019) 14:77–98. doi:10.1016/j.pacs.2019.05.001
22. Zhang W, Oraiqat I, Lei H, Carson PL, EI Naqa I, Wang X. Dual-modality X-ray-induced radiation acoustic and ultrasound imaging for real-time monitoring of radiotherapy. *BME Front* (2020) 2020:9853609. doi:10.34133/2020/9853609
23. Zhu Y, Lu X, Dong X, Yuan J, Fabiilli ML, Wang X. LED-based photoacoustic imaging for monitoring angiogenesis in fibrin scaffolds. *Tissue Eng C Methods* (2019) 25(9):523–31. doi:10.1089/ten.TEC.2019.0151
24. Lashkari B, Yang L, Mandelis A. The application of backscattered ultrasound and photoacoustic signals for assessment of bone collagen and mineral contents. *Quant Imaging Med Surg* (2015) 5(1):46–56. doi:10.3978/j.issn.2223-4292.2014.11.11
25. Yang L, Lashkari B, Mandelis A, Tan JW. Bone composition diagnostics: photoacoustics versus ultrasound. *Int J Thermophys* (2015) 36(5–6):862–7. doi:10.1007/s10765-014-1701-6
26. Kim MW, Jeng GS, O'Donnell M, Pelivanov I. Correction of wavelength-dependent laser fluence in swept-beam spectroscopic photoacoustic imaging with a hand-held probe. *Photoacoustics* (2020) 19:100192. doi:10.1016/j.pacs.2020.100192
27. Jacques SL. Optical properties of biological tissues: a review. *Phys Med Biol* (2013) 58(11):R37. doi:10.1088/0031-9155/58/11/R37

28. Feng T, Kozloff KM, Tian C, Perosky JE, Hsiao Y-S, Du S, et al. Bone assessment via thermal photo-acoustic measurements. *Opt Lett* (2015) 40(8):1721–4. doi:10.1364/OL.40.001721
29. Udelhoven T, Emmerling C, Jarmer T. Quantitative analysis of soil chemical properties with diffuse reflectance spectrometry and partial least-square regression: a feasibility study. *Plant Soil* (2003) 251(2):319–29. doi:10.1023/A:1023008322682
30. Patsch JM, Li X, Baum T, Yap SP, Karampinos DC, Schwartz AV, et al.. Bone marrow fat composition as a novel imaging biomarker in postmenopausal women with prevalent fragility fractures. *J Bone Miner Res* (2013) 28(8): 1721–8. doi:10.1002/jbmr.1950
31. Oei L, Koromani F, Rivadeneira F, Zillikens MC, Oei EH. Quantitative imaging methods in osteoporosis. *Quant Imaging Med Surg* (2016) 6(6):680–98. doi:10.21037/qims.2016.12.13
32. Rubin MR, Patsch JM. Assessment of bone turnover and bone quality in type 2 diabetic bone disease: current concepts and future directions. *Bone Res* (2016) 4:16001. doi:10.1038/boneres.2016.1
33. Shen W, Scherzer R, Gantz M, Chen J, Punyanitya M, Lewis CE, et al. Relationship between MRI-measured bone marrow adipose tissue and hip and spine bone mineral density in African-American and Caucasian participants: the CARDIA study. *J Clin Endocrinol Metab* (2012) 97(4): 1337–46. doi:10.1210/jc.2011-2605
34. Bredella MA, Daley SM, Kalra MK, Brown JK, Miller KK, Torriani M. Marrow adipose tissue quantification of the lumbar spine by using dual-energy CT and single-Voxel (1)H MR spectroscopy: a feasibility study. *Radiology* (2015) 277(1):230–5. doi:10.1148/radiol.2015142876
35. Salomatina E, Yaroslavsky A. Evaluation of the *in vivo* and *ex vivo* optical properties in a mouse ear model. *Phys Med Biol* (2008) 53(11):2797–807. doi:10.1088/0031-9155/53/11/003
36. Patsch JM, Li X, Baum T, Yap SP, Karampinos DC, Schwartz AV, et al. Bone marrow fat composition as a novel imaging biomarker in postmenopausal women with prevalent fragility fractures. *J Bone Miner Res* (2013) 28(8):1721–8. doi:10.1002/jbmr.1950
37. Baofeng L, Zhi Y, Bei C, Guolin M, Qingshui Y, Jian L. Characterization of a rabbit osteoporosis model induced by ovariectomy and glucocorticoid. *Acta Orthop* (2010) 81(3):396–401. doi:10.3109/17453674.2010.483986
38. Feng T, Zhu Y, Wang X. Functional photoacoustic and ultrasonic assessment of osteoporosis–a clinical feasibility study. *BME Front* (2020) 2020:1081540. doi:10.34133/2020/1081540
39. Feng T, Perosky JE, Kozloff KM, Xu G, Cheng Q, Du S, et al. Characterization of bone microstructure using photoacoustic spectrum analysis. *Opt Express* (2015) 23(19):25217–24. doi:10.1364/OE.23.025217

**Conflict of Interest:** The authors declare that the research was conducted in the absence of any commercial or financial relationships that could be construed as a potential conflict of interest.

frontiers
in Physics

REVIEW
published: 18 January 2021
doi: 10.3389/fphy.2020.616618

# Dual-Modal Photoacoustic Imaging and Optical Coherence Tomography [Review]

*Zohreh Hosseinaee, James A. Tummon Simmons and Parsin Haji Reza**

*PhotoMedicine Labs, Department of System Design Engineering, University of Waterloo, Waterloo, Canada*

Optical imaging technologies have enabled outstanding analysis of biomedical tissues through providing detailed functional and morphological contrast. Leveraging the valuable information provided by these modalities can help us build an understanding of tissues' characteristics. Among various optical imaging technologies, photoacoustic imaging (PAI) and optical coherence tomography (OCT) naturally complement each other in terms of contrast mechanism, penetration depth, and spatial resolution. The rich and unique molecular-specified absorption contrast offered by PAI would be well complemented by detailed scattering information of OCT. Together these two powerful imaging modalities can extract important characteristic of tissue such as depth-dependent scattering profile, volumetric structural information, chromophore concentration, flow velocity, polarization properties, and temperature distribution map. As a result, multimodal PAI-OCT imaging could impact a broad range of clinical and preclinical imaging applications including but not limited to oncology, neurology, dermatology, and ophthalmology. This review provides an overview of the technical specs of existing dual-modal PAI-OCT imaging systems, their applications, limitations, and future directions.

**Keywords: photoacoustic imaging, optical coherence tomogaphy, dual-modal bioimaging, photoacoustic tomography, photoacoustic microscopy**

OPEN ACCESS

***Edited by:***
*Jun Xia,*
*University at Buffalo, United States*

***Reviewed by:***
*Changhui Li,*
*Peking University, China*
*Ye Zhan,*
*University at Buffalo, United States*

****Correspondence:***
*Parsin Haji Reza*
*phajireza@uwaterloo.ca*

***Specialty section:***
*This article was submitted to Medical Physics and Imaging, a section of the journal Frontiers in Physics*

***Received:*** *12 October 2020*
***Accepted:*** *04 December 2020*
***Published:*** *18 January 2021*

***Citation:***
*Hosseinaee Z, Tummon Simmons JA and Reza PH (2021) Dual-Modal Photoacoustic Imaging and Optical Coherence Tomography [Review]. Front. Phys. 8:616618. doi: 10.3389/fphy.2020.616618*

## INTRODUCTION

The field of medical imaging has continued to grow quickly since the turn of the century, with many new modalities becoming a critical step in a variety of different disease care pathways. Novel imaging technologies continue to be developed, opening new routes to valuable functional and morphological information. Each imaging modality has its own specific strength and intrinsic limitations, such as spatial resolution, penetration depth, contrast mechanism, and sensitivity leading to precise and reliable images correlated with true anatomy. To compensate the weak aspects of different modalities, multimodal imaging concepts have been considered in recent years [1–3]. Multimodal imaging can play an important role in the clinical care of various diseases by improving the clinician's ability to perform monitoring, surveillance, staging, diagnosis, planning and therapy guidance, screening therapy efficacy, and evaluating recurrence [2]. Multimodal imaging systems have been widely used in medical research and clinical practice, such as cardiovascular diseases [4, 5], neuropsychiatric diseases [6], Alzheimer [7], and tumor resection surgeries [8].

Photoacoustic imaging (PAI) is one recent example of the successful rise of a novel optical imaging modality. PAI uses the absorption characteristics of specific endogenous or exogenous biomarkers to generate targeted image contrast with a wide scalable range of spatial resolution and penetration depths [9, 10]. The rich absorption information that PAI provides would be well complemented by an imaging modality which offers detailed scattering information. Optical coherence tomography (OCT) is a well-established imaging technology which can provide excellent depth-resolved morphological information. OCT is currently used in a broad range of clinical applications and is a standard of care in the field of ophthalmology for the diagnosis of various critical eye diseases [11–13]. OCT is considered as an ideal companion for PAI by providing complementary imaging contrast, strongly motivating the development of multimodal PAI and OCT systems. While OCT can image microanatomy of biological tissues, PAI devices could provide detailed molecular and metabolic information of the sample [14–16]. This multimodal system could provide access to valuable information about biological tissues and has the potential to impact a broad range of clinical and preclinical imaging applications including but not limited to oncology, neurology, dermatology, and ophthalmology. In this review, we first introduce the basic mechanisms of PAI and OCT and discuss their current applications. Then, we compare PAI and OCT, contrasting the strengths and limitations of each modality while highlighting the potential applications of a multimodal system. Finally, we review the development of existing dual-modal systems, emphasizing their strengths along with the challenges they need to overcome to move to the clinic.

## PHOTOACOUSTIC IMAGING: PRINCIPLES AND APPLICATIONS

Photoacoustic imaging is among the most rapidly growing technologies in biomedical imaging [17, 18]. The modality is based on the photoacoustic effect, which was discovered by Bell in 1880 [19]. In general, once the tissue is irradiated by short laser pulses, endogenous or exogenous chromophores inside the tissue absorb the photon's energy. This absorbed energy then induces a transient local temperature rise, which in turn generates pressure waves through thermoelastic expansion. These pressure waves, which propagate in tissue as ultrasound signals, can be captured by acoustic detectors to form images of the chromophore's distribution inside the sample [20]. Depending on the spatial scales of optical absorbers, the frequency content of generated ultrasound signals might extend to several tens or even hundreds of megahertz. The bandwidth of this signal and corresponding spatial resolution is not limited by the PA generation process. Instead, the frequency-dependent acoustic attenuation happening in soft tissue limits the maximum frequency content of PA wave and therefore defines the achievable spatial resolution. As a result, the spatial resolution in PAI scales with depth. In addition, ultrasound detector's properties such as bandwidth, center frequency, element size, and detection aperture can limit the spatial resolutions of PAI devices [21].

Based on the way images are formed, PAI can be split into two main categories: photoacoustic tomography (PAT), which uses reconstruction-based image formation, and photoacoustic microscopy (PAM) which uses focused-based image formation [22]. In photoacoustic tomography, usually a widefield unfocused excitation beam is used together with an array of ultrasonic detectors which measure the generated ultrasound waves in multiple positions simultaneously [23–25]. It can provide large field of view (FOV) images and has been used in applications such as whole-body imaging of small animals [26] and breast cancer studies [27]. In contrast to PAT, PAM is based on raster-scanning of optical and acoustic foci and forms images directly from recorded depth-resolved signals [28]. Generally, PAM is the preferred configuration for use in applications which require high resolution over deep penetration depth, for example, in single-cell imaging [29]. PAM can be further divided into acoustic-resolution PAM (AR-PAM), where the acoustic focusing is tighter than optical focusing [30], and optical-resolution PAM (OR-PAM), where the optical focusing dominates the resolution [31]. **Figure 1** demonstrates the imaging setup for different possible configurations of photoacoustic imaging systems. Photoacoustic endoscopy (PAE) can be considered as a subcategory of both PAM and PAT (depending on the implementation), which is applied for imaging internal tissue/organs and usually provides micron-scale spatial resolution and millimeter-scale imaging depth [32].

Photoacoustic imaging devices offer two distinct advantages which primarily stem from the combination of optical excitation and acoustic detection. First, they provide the unique imaging contrast of optical absorption. As a result, PAI enables high-sensitivity detection of endogenous chromophores which are weakly fluorescent and difficult or impractical to be labeled with exogenous fluorophores, including but not limited to hemoglobin, melanin, collagen, cytochrome, and lipid [33]. This complements established imaging technologies including fluorescence imaging, which is currently one of the leading technologies for *in vivo* optical molecular imaging [34]. Second, PAI enables a wide scalable range of spatial resolution and penetration depths across macroscopic (i.e., 100-400 μm resolution at the depth of several centimeters) [18], mesoscopic (i.e., tens of micrometer resolution at the depth of 1–10 mm) [35], and microscopic (i.e., micrometer resolution at the depth of submillimeter) [36]. Additionally, the modality has practical functional and molecular imaging capabilities making it a powerful tool for biomedical investigations [21]. One of these well-known capabilities is photoacoustic spectroscopy which is based on the ability to selectively image specific chromophores by tuning the excitation wavelength [37]. Here, by acquiring images at multiple wavelengths and undertaking spectroscopic analysis, the concentration of specific chromophores can be quantified. For example, in the visible and NIR wavelength, the absorption spectrum of blood is highly dependent on its oxygen saturation ($SO_2$) and consequently the significant spectral difference between oxyhemoglobin ($HbO_2$) and deoxyhemoglobin (HHb). Using this spectral difference, it is possible to quantify the concentration of $HbO_2$ and HHb and estimate $SO_2$ which is an important physiological parameter related to several pathophysiological processes and inflammatory conditions. Other functional extensions of PAI such as Doppler flowmetry [38, 39] and photoacoustic thermometry [40, 41] have enabled measurement of blood flow velocity and acquiring maps of temperature distributions in tissue, respectively.

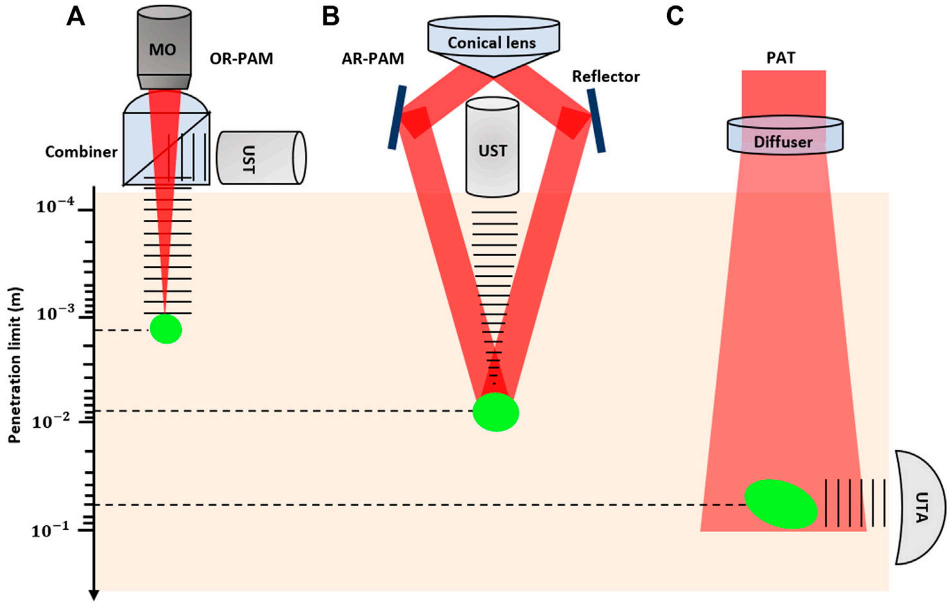

**FIGURE 1 |** Signal generation and detection in different implementations of PAI and penetration limits in scattering tissue. **(A)** Reflection-mode OR-PAM system with an optical–acoustic combiner that transmits light but reflects sound; **(B)** AR-PAM system where the laser light is poorly focused; **(C)** PAT system with ultrasonic transducer array (UTA). The laser beam is expanded and homogenized by a diffuser to provide widefield illumination.

These unique and important imaging advantages offered by PAI make it the preferred modality for a broad range of functional and molecular imaging applications. It has been used in numerous preclinical and clinical applications including but not limited to blood oxygen saturation imaging [42, 43], brain vasculature and functional imaging [44, 45], gene expression [46], vulnerable atherosclerotic plaques diagnosis [47], skin melanomas [48], histology-like tissue imaging [49, 50], longitudinal tumor angiogenesis studies [51], imaging and detection of protein interactions [52], ophthalmic imaging [53], and tissue engineering scaffolds [54].

## OPTICAL COHERENCE TOMOGRAPHY: PRINCIPLES AND APPLICATIONS

Optical coherence tomography (OCT) is an optical imaging technique with high-resolution structural content. Unlike photoacoustic imaging, OCT obtains its imaging contrast from optical scattering of internal tissue microstructures and can be considered as an optical analogy to ultrasound pulse echo imaging [55]. The modality is based on the principles of low-coherence interferometry, where a low-coherence light beam is directed on to the targeted tissue. The backscattered light is combined with a reference beam, which was split off from the original light beam. The resulting interference patterns are used to reconstruct cross-sectional images, which represent the reflectivity profile of the tissue along the beam path [56, 57].

The first generation of OCT known as time domain OCT (TD-OCT) was developed in the 1990s [55]. The technology required acquisition of a depth scan for every location and subsequently suffered from slow imaging speed and poor image quality that limited adoption of the technology. The introduction of Fourier domain OCT (FD-OCT) overcame these limitations by providing a more efficient implementation of low-coherence interferometry principles [58]. Unlike TD-OCT, FD-OCT uses spectral information to generate a depth profile without the need for mechanical scanning of the optical path length [59]. It offers >100x improvement of the image acquisition rate and >20 dB signal-to-noise ratio (SNR) compared to TD-OCT systems.

Depending on whether spectral information in FD-OCT is separated at the system's input (tunable laser) or system's detection end (spectrometer), FD-OCT systems can be classified into two major groups: spectral-domain OCT (SD-OCT) in which a broad bandwidth light source is used as the interferometer input and a spectrometer with a linear array camera at the interferometer output, or swept-source OCT (SS-OCT), which uses a tunable laser as the interferometer input and a single photodiode at the interferometer output [60]. **Figure 2** depicts schematic of different OCT modalities.

OCT technology has enabled noncontact, high speed, cross-sectional imaging over a large field of view with submicron resolution in biological tissues. It is currently the preferred technology in ophthalmology for corneal imaging, as well as retinal structural and vascular imaging [61–63]. Various functional extensions of OCT have been developed including: Doppler OCT [64], OCT angiography (OCTA) [65], polarization sensitive OCT (PS-OCT) [66], OCT elastography [67], and

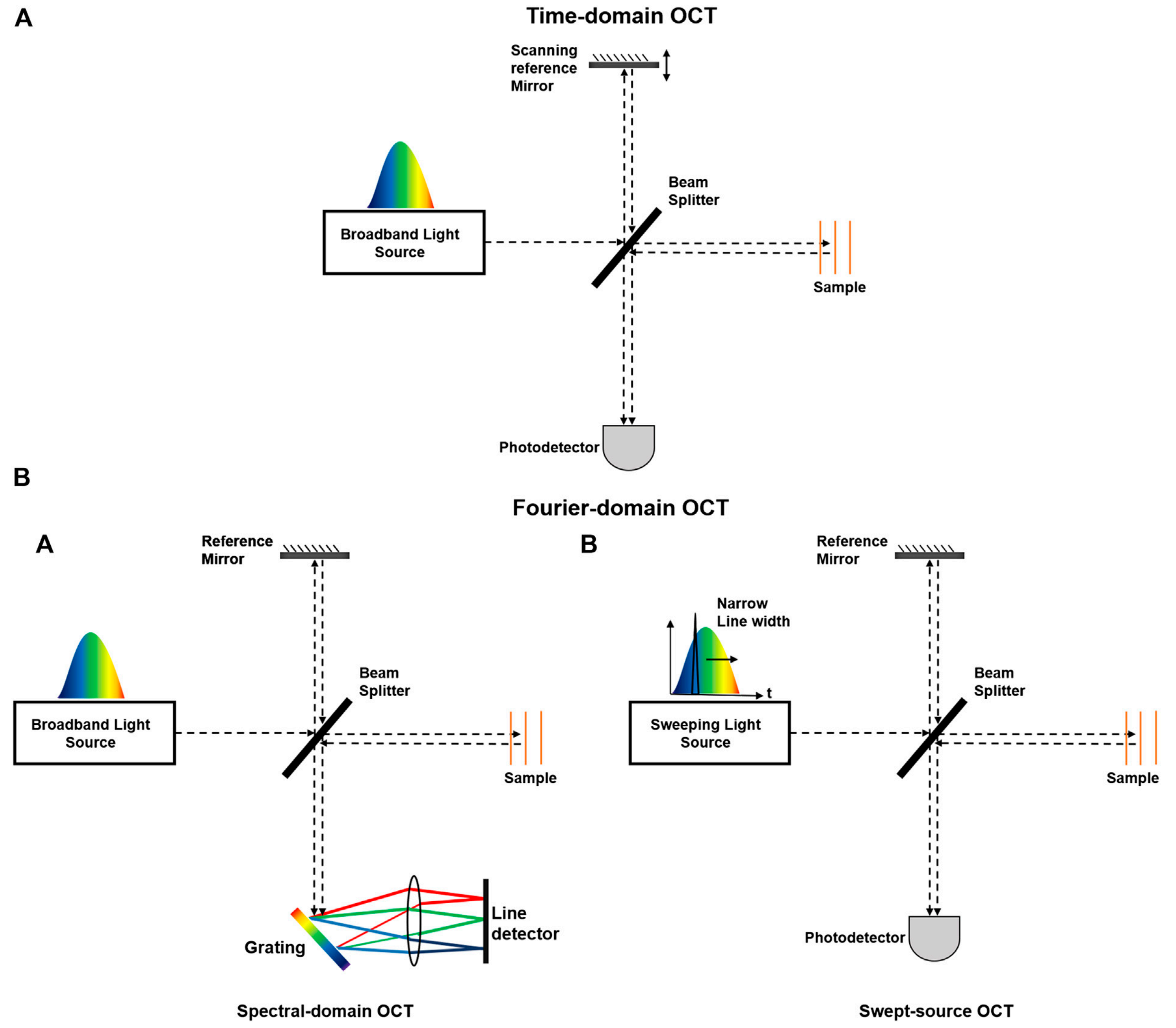

**FIGURE 2 |** Schematic of different OCT modalities. OCT systems can be classified into **(A)** time domain (TD) and **(B)** Fourier domain (FD) systems. FD-OCT systems can be further divided into **(A)** spectrometer-based and **(B)** swept source-based systems.

spectroscopic OCT [68]. Besides ophthalmic applications, OCT has been applied in other clinical applications such as brain imaging [69, 70], tissue engineering [71], cardiology and cardiovascular imaging [72], skin imaging [73], neuroimaging [74], gynecology [75], oncology [76], and dental imaging [77].

Due to highly scattering nature of biological tissues and the contrast mechanism of OCT, the penetration depth of OCT devices is limited to be within a few millimeters [13]. In addition, OCT relies on variation in scattering information to derive useful imaging contrast about the sample, making it unable to effectively image interconnected soft tissues with similar scattering properties. To provide additional contrast information, efforts have been made to integrate OCT with other optical imaging modalities such as multiphoton microscopy [78] and confocal microscopy [79]. While these technologies provide new contrast information, they both rely on fluorescence as their contrast mechanism. In addition, they cannot enhance the depth information that OCT devices currently obtain.

## DUAL-MODAL PHOTOACOUSTIC IMAGING AND OPTICAL COHERENCE TOMOGRAPHY

The performance characteristics of PAI and OCT imaging systems make them a suitable companion for a multimodal imaging system. A brief comparison of important features of both PAI and OCT modalities is given in **Table 1**. The spatial resolution of both modalities is highly dependent on their implementation and can range from submicron resolution for OCT [80, 81] and OR-PAM [36] to a few hundreds of micron in

**TABLE 1 |** Comparison of photoacoustic imaging and optical coherence tomography.

| Imaging parameter | Photoacoustic imaging | Optical coherence tomography |
|---|---|---|
| Axial resolution | Determined by the detected photoacoustic bandwidth, usually several tens of microns | Determined by the central wavelength and coherence length of the light source, generally within a few microns |
| Lateral resolution | Depending on the implementation can range from ~0.3 to 400 μm | Determined by the central wavelength of the light source and imaging optics, usually within tens of microns |
| Imaging depth | Depending on the implementation range from ~1.5 to ~ 7 cm | Restricted by the optical transport mean free path ~2 mm |
| Imaging speed | Defined by the laser pulse repetition rate, mechanical scanning speed, or the multiplexed data acquisition time | Usually defined by the sweep rate of laser or speed of spectrometer's camera |
| Contrast mechanism | Absorption | Scattering |

PAT systems [82]. While available imaging depth of OCT is restricted by the optical transport mean free path to ~2 mm, AR-PAM and PAT systems can achieve imaging depth of a few millimeters [35] to a few centimeters [27], respectively. In terms of speed, both modalities offer a wide range of imaging speed with submilliseconds to a hundred of seconds range [83, 84], which should be chosen based on intended applications.

The complementary information of PAI and OCT makes them the favored modality for a wide range of imaging applications. For example, in blood flow imaging, OCT angiography and Doppler OCT could obtain high-resolution images based on the backscattering properties of moving red blood cells, while PAI would remain sensitive to all blood cells, regardless of their flowing state. Therefore, the integrated system provides a powerful tool for blood flow imaging in vascular diseases such as stroke, hemorrhage, vascular occlusions, or certain pathologies with flow stasis such as tumors [85, 86].

For spectroscopic analysis and blood oxygen saturation measurements, despite recent advances in the spectroscopic OCT [87–89], the technology is not background free and suffers from sensitivity to speckle noise and polarization changes. In addition, the scattering loses alter the spectral signal components and makes it difficult to quantify blood oxygen. On the other hand, spectroscopic PAI methods are well-established for quantifying blood oxygen saturation. This information would be well complemented with Doppler OCT flow measurements and help to quantify metabolic rate of oxygen consumption. This will open up a broad range of applications for pathophysiological conditions such as angiogenesis, tissue inflammatory, and healing responses. For example, in ophthalmology measuring, metabolic rate of oxygen is a sensitive biomarker for early-stage diagnosis and an indicator for progression of several retinal diseases including glaucoma, diabetic retinopathy, and age-related macular degeneration [90–93]. Alternatively, in oncology and metastasis detection, the spectroscopic and metabolic information available through the dual-modal PAI-OCT system could reveal changes in endogenous chromophore concentrations and be employed for differentiating normal and pathological tissues [94]. It may facilitate longitudinal assessment of tumor growth and evaluate treatment success of novel therapeutic agents [95, 96]. In brain imaging applications, this metabolic information can be used to extract brain oxygenation and metabolism of oxygen and glucose [97] and resting-state connectivity [98] and to study how the brain responds to various physiological and pathological conditions [99]. Furthermore, the fine vascular structure and subcellular features available through high spatial resolution of OCT and OR-PAM could facilitate diagnosis of brain disorders such as stroke, epilepsy, and edema [100–102].

The combination of PAI and OCT is a powerful tool in dermatology by providing detailed morphology and complete description map of skin perfusion. It enables studying the texture of skin and determines the margin of morphological changes caused by skin disorders [103]. The technique may overcome the limitations of histology-based margin assessment methodologies and facilitate tumor resections in surgical rooms [104, 105]. Subsequently, it can be used to improve the rate of complete excision and to reduce the average number of stages during Mohs micrographic surgery [106, 107]. The dual-modal imaging platform can be applied for studying a wide range of skin conditions such as melanoma tumors, vascular lesions, soft tissue damages such as wounds and burns, inflammatory conditions, and other superficial tissue abnormalities characterized by morphology and function of supplying vasculature [108].

The dual-modal PAI-OCT system could have a significant impact for endoscopic applications as well. Currently, most of endoscopic imaging devices rely on widefield white-light optical methods, which are limited by what the human eye can see and therefore suffer from lack of sensitivity to subsurface and physiological changes. The combination of deep tissue penetration and high resolution along with functional and molecular information makes PAI-OCT the favorable endoscope to observe inside the body and visualize physiological processes and microscopic features of tissues [109, 110]. The targeted molecular imaging may allow for the detection of small and invisible lesions in epithelial surfaces that line the internal organs such as gastrointestinal, pulmonary, and ductal. This information can be used to facilitate detecting cancer at early stages [111]. Another important application for endoscopic PAI-OCT would be intravascular atherosclerotic imaging, where the PAI subsystem could penetrate deep and provide molecular information about the plaque composition and OCT maintains high-resolution, depth-resolved scattering contrast for lipid rich plaques [112].

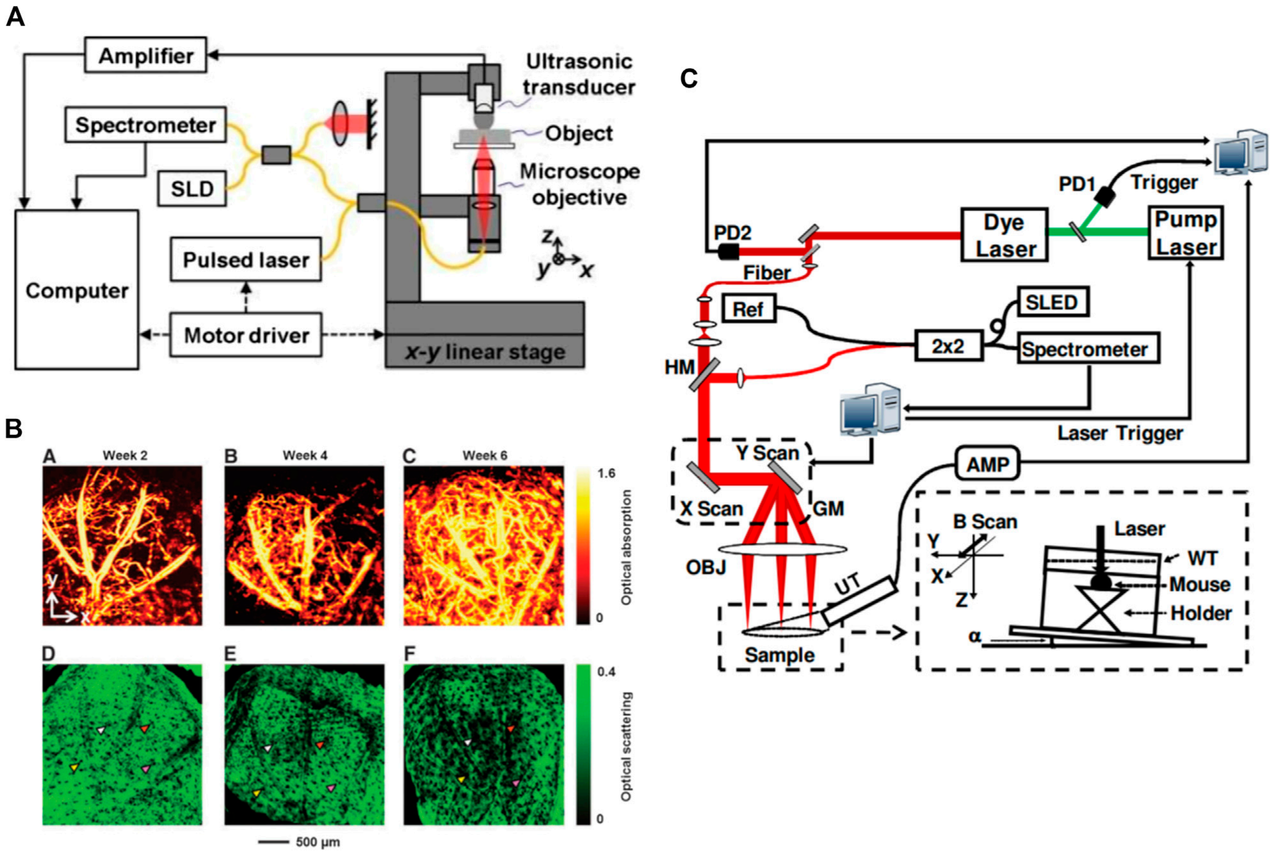

**FIGURE 3 | (A)** Schematic of the combined PAM-OCT. SLD: superluminescent diode. Solid lines represent single-mode optical fibers. Reprinted with permission from [113]; **(B)** PAM and OCT images showing the vasculature and tissue structure for an inverse scaffold with a pore size of 200 μm; **(A–C)** PAM images showing the development of blood vessels at 2, 4, and 6 weeks after implantation, respectively; **(D–F)** the corresponding OCT images showing the tissue structure. Reprinted with permission from [114]; **(C)** schematics of the combined PAM and OCT. PD: photodiode; HM: hot mirror; GM: 2D galvanometer; OBJ: objective lens; AMP: amplifier; UT: ultrasonic transducer; WT: water tank; SLED: superluminescent emitting diode; Ref: OCT reference arm. Reprinted with permission from [116].

It is clear that there are a diverse set of biomedical applications for a functional multimodal PAI-OCT system. The potential impact of such a broadly applicable technology has motivated the further investigation of possible multimodal system configurations. Here, depending on the photoacoustic imaging system, the multimodal PAI-OCT imaging systems are divided into three main categories of PAM-OCT, PAT-OCT, and PAE-OCT. The developed configurations for each category are reviewed, and their advantages and technical challenges are discussed.

## Photoacoustic Microscopy Combined With Optical Coherence Tomography

One of the earliest works on the feasibility of multimodal PAM-OCT was demonstrated by Li et al. in 2009 [113]. Their proposed system operated in transmission mode and was only capable of imaging thin samples (**Figure 3A**). The reported penetration depth was ~1.5 and 1.8 mm for the PAM and OCT subsystems, respectively. Due to the mechanically translating objective, the system had slow acquisition time which highly limited its *in vivo* applications. Despite this limitation, the system was later used to look at the neovascularization of the mouse ear [114] (**Figure 3B**). Later Jiao et al. [115] developed a reflection-mode PAM-OCT system and imaged microvasculature of the mouse ear. The temporal resolution of their dual-modal system was limited by the pulse repetition rate of the PAM excitation source (~1 KHz). Liu et al. [116] developed a dual-modal system where a tunable dye laser was used as excitation source (**Figure 3C**). It leveraged the spectroscopic measurement capabilities of the PAM subsystem to evaluate total hemoglobin concentration as well as the metabolic rate of oxygen consumption in the mouse ear. Dual-modal PAM-OCT systems were further applied on various samples such as animal model of epilepsy progress [117], bovine cartilage osteoarthritis tissue [118], and imaging/needle guiding for injection and drug delivery in mouse thigh [104, 119].

Qin et al. [120] were among the first to develop the portable dual-modal PAM-OCT system. Their system was used for monitoring the recovery of an ulcer wound in the human lip. They carried out quantitative analysis by measuring total hemoglobin concentration as well as the size of the ulcer. *In vivo* images recorded from healing process of human lip ulcer are

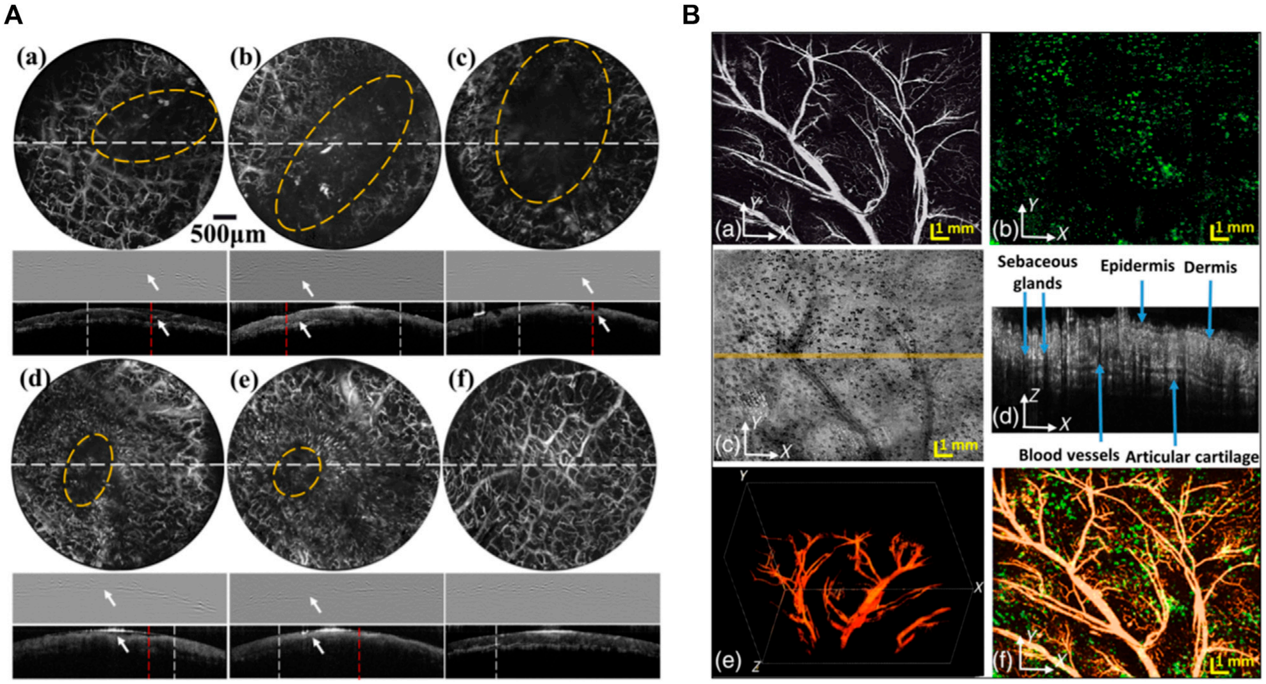

**FIGURE 4 | (A)** PAM and OCT results of the microvascular distribution and microstructures of the lower lip during the healing process of an ulcer wound. Row 1 in PAM images of the lip from day 1 to day 6. Row 2 PAM B-scans of the lip along the dashed white lines in Row1. Row3 OCT B-scans of the lip along the dashed white lines in Row1. The wounds are indicated by the yellow circles in PAM images and the white arrows in PAM B-scans. Scale bars: 500 μm. Reprinted with permission from [120]; **(B)** simultaneously acquired PAM, confocal microscopy (CFM), and OCT images of a mouse ear with dynamic focusing. **(A)** PAM image; **(B)** CFM image; **(C)** OCT images; **(D)** OCT B-scan at the location marked in panel; **(C)** by a solid line; **(E)** PAM 3-D image reconstruction; and **(F)** fused PAM projection and CFM images; bar: 1 mm. Reprinted with permission from [122].

shown in **Figure 4A**. The system offered lateral resolutions of ~8 μm for both modalities, and axial resolutions of 116.5 μm for PAM and 6.1 μm for OCT. However, since the system suffered from bulky size, in 2018 the same author demonstrated a handheld version of the system implemented with an MEMS-based optical scanner that offered more flexibility for oral tissue imaging [121]. The lateral resolutions of the system were improved to 3.7 μm for PAM and 5.6 μm for OCT, sufficient for visualizing morphological features and capillary loops in human oral tissue. Dadkhah et al. [122] took an additional step forward and developed a multimodal imaging system by integrating photoacoustic microscopy, OCT, and confocal fluorescence microscopy in one platform. The combination of optical and mechanical scanning together with dynamic focusing improved the sharpness and field of view of the images. The system achieved uniform resolution in a field-of-view of 12 mm × 12 mm with an imaging time of ~5 min for simultaneous *in vivo* imaging of the mouse ear (**Figure 4B**). The imaging speed of their system was limited by the pulse-repetition-rate of the PAM excitation laser.

In early 2020, Liu et al. [123] developed a dual-modal system in the NIR range for real-time, *in vivo* visualization of the tumor microenvironment changes during chemotherapy. The PAM subsystem utilized an optical parametric oscillation laser which had a wavelength range of 680–1,064 nm. The OCT subsystem was based on a commercial system with a center wavelength of ~1,300 nm, providing 12 μm axial resolution. This study worked to characterize tumor angiogenesis by monitoring changes in the vascular network's density, quantitative total hemoglobin concentration, and oxygen saturation of cancerous tissue. They suggested the dual-modal imaging-guided dose control system as a more efficient technology compared to the presently utilized tumor treatment options.

The majority of PAM-OCT configurations discussed earlier utilized ultrasound transducers for detecting acoustic waves. Despite offering high sensitivity, these transducers pose challenges when integrating PAM and OCT subsystems [124]. In transmission mode, the sample needs to be placed in a water tank or be in contact with ultrasound gel as a coupling medium [125–127], which limits the application of the technique to thin specimens. In reflection mode, because the opaque transducer obstructs the optical beam path, it needs to be positioned obliquely with respect to the optical axis which causes sensitivity loss [115, 128, 129]. In 2019, Hindl et al. [130] developed a reflection-mode OCT-PAM system using an all-optical akinetic Fabry–Perot etalon sensor. The miniature sensor included a rigid, fiber-based Fabry–Perot etalon with a transparent central opening and enabled linear signal detection over a broad bandwidth [131]. A schematic of the system is presented in **Figure 5A**. The OCT subsystem used a broadband laser centered at 840 nm, with a 5 μm axial resolution, and the PAM subsystem used a 532 nm pulsed laser operating at a pulse

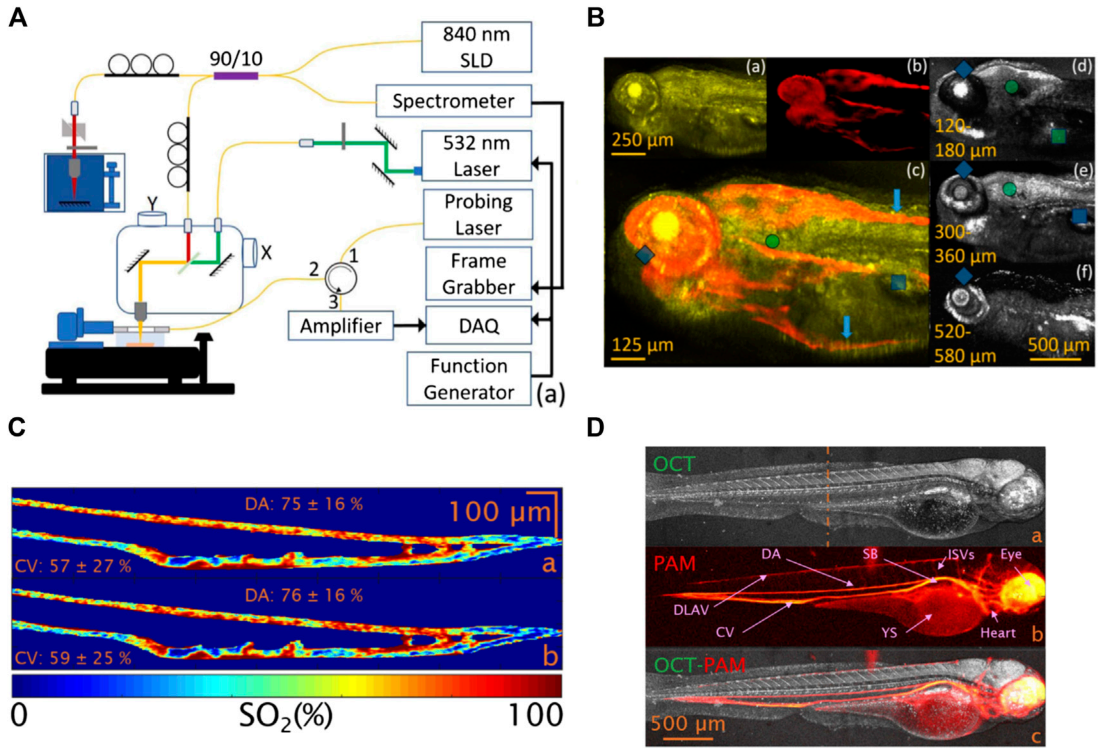

**FIGURE 5 | (A)** Schematic of the reflection-mode PAM-OCT system [130]; **(B)** images of a zebrafish larva. **(a)** OCT image; **(b)** PAM image; **(c)** color blended PAM-OCT image using **(a)** and **(b)**. **(d–f)** Images of OCT integrating 60 μm depth range. Reprinted with permission from [130]. **(C)** Oxygenation map of a zebrafish larval tail. The image is acquired after spectral unmixing using the absorption coefficients of human **(a)** and zebrafish blood **(b)**, respectively [132]. **(D)** OCT-PAM image of a zebrafish larva. **(a)** OCT average intensity projection, **(b)** PAM maximum amplitude projection, and **(c)** multimodal OCT-PAM. Reprinted with permission from [132].

repetition rate of 50 kHz. This system acquired OCT and PAM images sequentially. *In vivo* images of zebrafish larva's tissue and vascular morphologies are presented (**Figure 5B**). The system had limited imaging speed due to the use of stepper motors for scanning and the need for signal averaging to provide increased SNR. In addition, the OCT light source combined three superluminescent diodes which were not polarization aligned and resulted in various imaging artifacts and a degraded axial resolution. They recently reported a dual-modal system using a Ti:Sapphire broadband light source and fast laser scanning [132]. The axial resolution was 2.4 μm enabling visualization of retinal layers in the zebrafish model. Functional extensions of the PAM-OCT system including Doppler OCT and spectroscopic PAM were applied to monitor arterial pulsation and to measure absolute blood flow and oxygen saturation. The *in vivo* oxygenation measurement was acquired using a dye laser with a 10 KHz repetition rate at 578, 570, and 562 nm wavelengths. Representative images recorded using the system are presented in **Figure 5C&D**.

In the system configurations discussed earlier, both PAM and OCT subsystems used their own specific light source. Normally, PAM excitation is based on a narrowband pulsed laser, while OCT requires broadband, continuous light (e.g., superluminescent diode), or virtually continuous light (e.g., Ti: Sapphire laser). The other important difference in their light source is that OCT systems usually use near infrared (NIR) light for deeper penetration, but PAM mainly uses visible light to target the absorption peak of hemoglobin and melanin [133]. However, this apparent difference in wavelength, does not impede applying visible light for OCT or NIR light for PAM. Recent experiments have demonstrated applications of visible OCT for high-resolution imaging and measuring metabolic rate of oxygen for clinical studies [134, 135], while NIR light has been used for imaging lipid and collagen tissues in PAM [136–138]. Several studies explored the feasibility of using a single light source for PAM excitation and OCT imaging, which would reduce the complexity and costs of the system; in addition, it will generate synchronized and coregistered PAM and OCT images. Zhang et al. [14] demonstrated the first single pulsed light source for PAM-OCT in 2012 and termed the technique optical coherence photoacoustic microscopy (OC-PAM). Experimental setup of the proposed system is demonstrated in **Figure 6A**. The system was in transmission mode with a custom-designed broadband dye laser centered at 580 nm with 20 nm bandwidth, and a 5 KHz pulse repetition rate. The system was tested on the *in vivo* mouse ear, and promising results were demonstrated; however, the low repetition rate of the light source limited the imaging speed, and the noisy spectrum of the laser degraded the quality of OCT images. Due to their broad spectral bandwidth, supercontinuum (SC) sources were employed in OC-

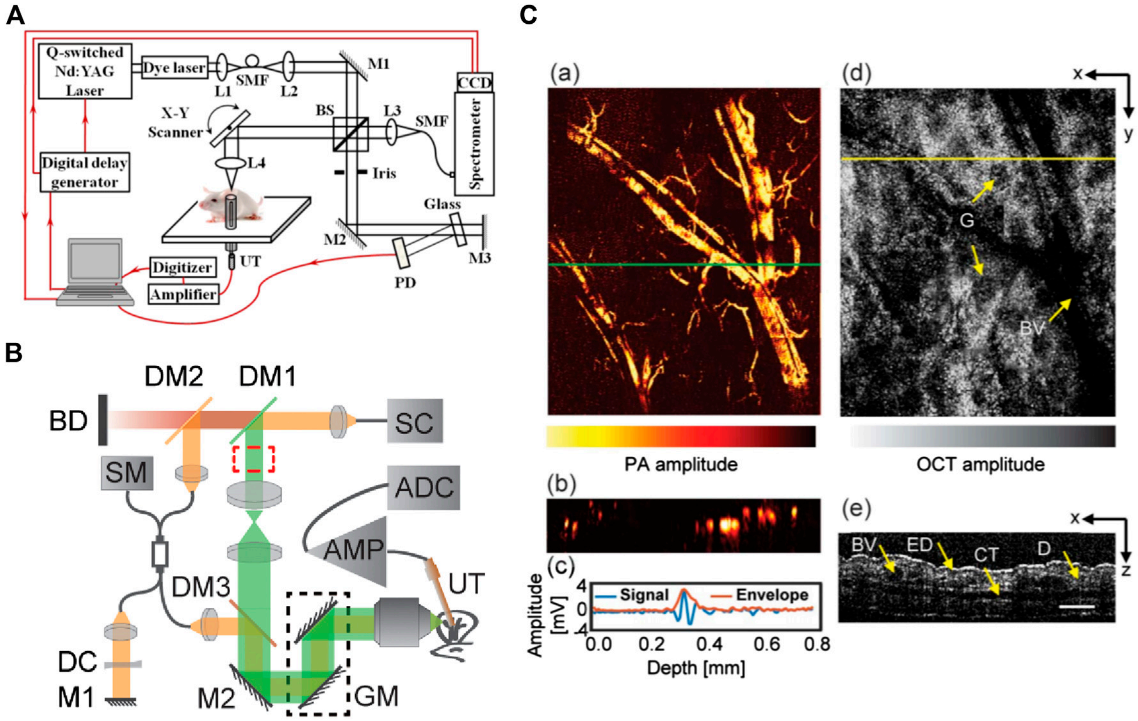

**FIGURE 6 | (A)** Schematic of the experimental system of a free-space OC-PAM. BS, beam splitter; SMF, single-mode fiber; PD, photodiode; UT, ultrasonic transducer; L, lens, M, mirror. Reprinted with permission from [14]. **(B)** Schematic of PAM-OCT system setup. SC, supercontinuum; DM, dichroic mirrors; GM, galvanometer; UT, ultrasound transducer; AMP, amplifier; ADC, digitizer; SM, spectrometer; DC, dispersion compensating slab; M, mirrors; BD, beam dump. Reprinted with permission from [129]. **(C)** Results of *in vivo* mouse ear imaging. **(a)** En-face PAM image; **(b)** PAM B-scan taken from location indicated by the green line in **(a)**. **(c)** Typical PA A-line and its signal envelope obtained by a Hilbert transform. **(d)** En-face OCT image. G, gland; BV, blood vessel. **(e)** OCT B-scan taken from location indicated by yellow line in **(d)**. ED, epidermis; CT, cartilage; D, dermis. Scale bar, 150 μm. Reprinted with permission from [129].

PAM systems as well [125, 139]. In 2016, Shu et al. [129] reported a dual-modality OC-PAM system using a homebuilt fiber-based SC source (**Figure 6B**). The beam coming from the light source was split into a shorter wavelength band (500–800 nm) for PAM and a longer wavelength band (800–900 nm) for OCT. The system was tested for *in vivo* imaging of the mouse ear, and multispectral PAM was performed on the *ex vivo* porcine retinal sample (**Figure 6C**).

## Photoacoustic Microscopy Combined With Optical Coherence Tomography for Ophthalmic Applications

One of the few and important applications that developed dual-modal PAM-OCT systems have explored so far is ophthalmic imaging. Due to the prevalence of OCT imaging for clinical ophthalmology, dual-modal PAM-OCT is a natural extension for imaging the eye. In ophthalmic application, access to the absorption information could provide information about the functional and molecular properties of the tissue, such as evaluating the retinal pigment epithelium in diseases such as age-related macular degeneration or measuring metabolic rate of oxygen in retinal and choroidal circulations in diabetic retinopathy. In 2010, Jiao et al. [140] reported one of the first multimodal PAM-OCT ophthalmoscopes which used an unfocused transducer directly placed on the sclera. The OCT subsystem was based on an SD-OCT design consisting of a superluminescent diode centered at 870 nm. Experimental results were demonstrated for *in vivo* imaging of retinal vessels and the retinal pigment epithelium layer in rat eyes, with a laser pulse energy well within the ANSI safety limits. Song et al. [141] further extended this system to include additional modalities such as scanning laser ophthalmoscopy and fluorescein angiography and imaged rat retina. They also measured the metabolic rate of oxygen in rat retina [90]. **Figure 7** illustrates the developed functional imaging system and the combined PAM and OCT scanning pattern on the retina. In 2015, Liu et al. [142] developed an OC-PAM system by using a single pulsed broadband light source with a central wavelength of 800 nm. Since the absorption coefficient of hemoglobin is relatively weak at this wavelength, the PAM signals were mainly providing melanin-specific information of the retina. The imaging speed of the system was limited by the 10 KHz pulse repetition rate of the light source, which is not as high as conventional ophthalmic OCT systems. To avoid possible motion artifacts and image blurring/disruption, high imaging speed is required. Robinson et al. [143] reported that the eye has a fixation time of ~500 ms. Increasing the repetition rate can improve the imaging speed; however, it will also increase the average power of the light source which is

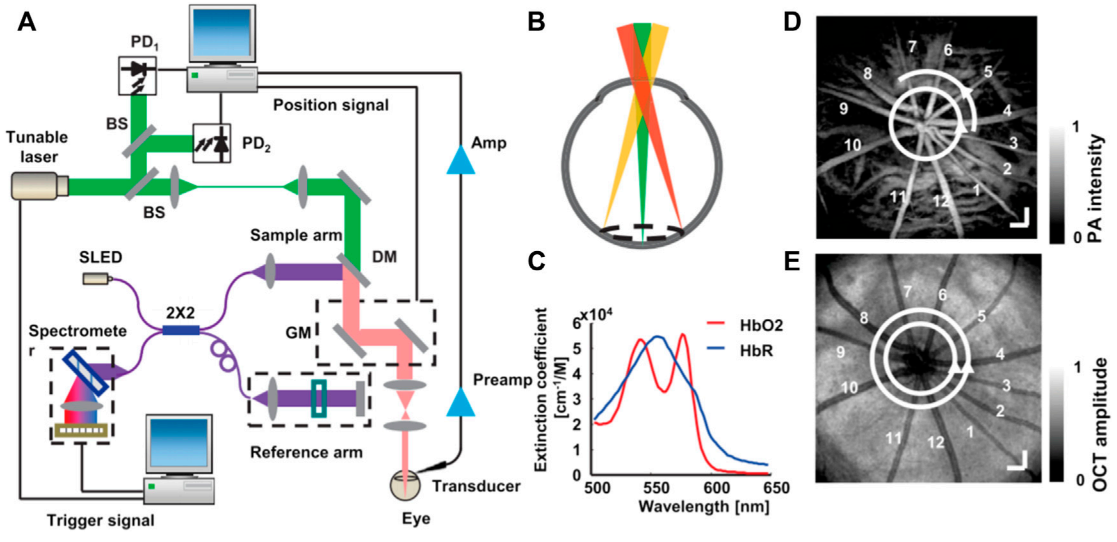

**FIGURE 7 |** Illustration of integrated PAM and SD-OCT to measure retinal metabolic rate of oxygen. **(A)** Schematic of the experimental setup; **(B)** circular scanning pattern on the retina; **(C)** molar extinction coefficient spectrum of oxy- and deoxyhemoglobin; **(D)** a maximum-amplitude-projection PAM fundus image showing major retinal vessels. Bar: 200 mm; **(E)** an OCT fundus image of the same rat showed in the panel **(D)**. Bar: 200 mm. Reprinted with permission from [90].

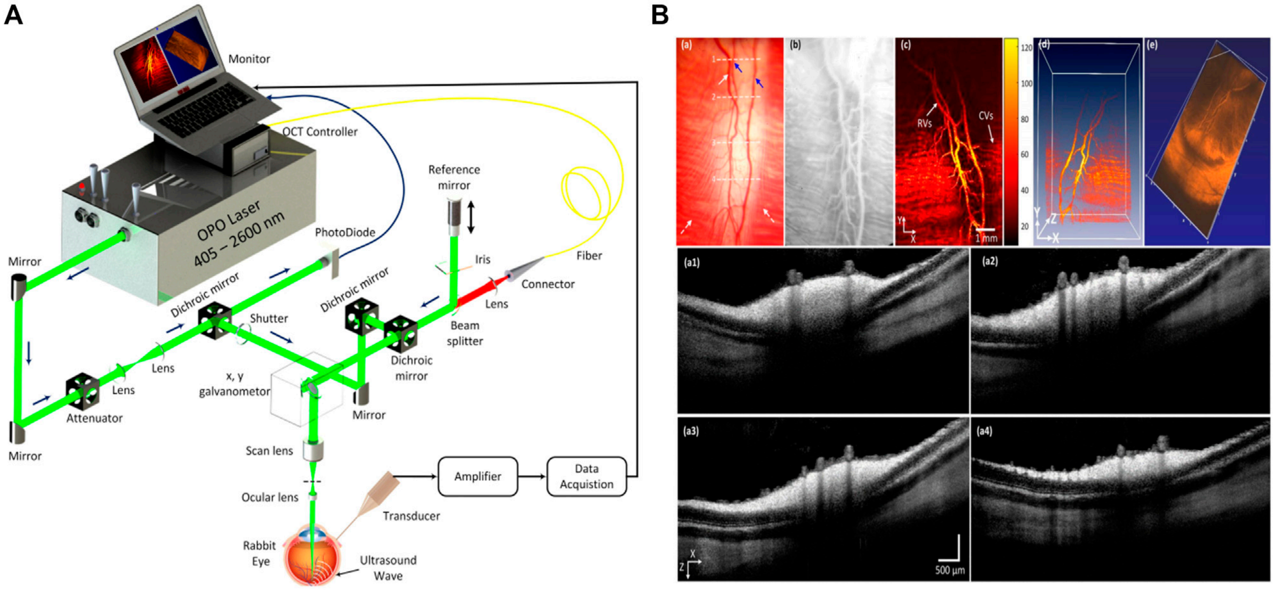

**FIGURE 8 |** **(A)** Schematic diagram of the integrated PAM and OCT systems for multimodal retinal imaging. Reprinted with permission from [147]; **(B)** images of retinal blood vessels in rabbits: **(a)** color fundus photography of retina. **(b)** Fluorescein angiography image showing retinal and choroidal capillaries. **(c)** Corresponding maximum amplitude projection PAM images of retina; **(d,e)** volumetric PAM and OCT image, respectively. **(a1–a4)** Cross-sectional OCT images acquired along the scanning lines from **(a)**. Reprinted with permission from [148].

constrained by existing laser safety limits. This may cause issues in practical applications where there are pulses overlapping in the retina. This highlights the trade-off between pulse repetition rate and pulse energy. Developing a highly sensitive PA detection method is the key for reducing the pulse energy and thus making it safe for clinical eye imaging.

Mice and rat eye models have been extensively used in preclinical ophthalmic imaging experiments. The eyeballs of these animals are smaller (axial length of mouse eyeballs ~3 mm, rats ~6 mm) compared to humans (~25 mm). Therefore, using animals with larger eyeballs, such as rabbits and monkeys, could help benefit ophthalmic studies. Tian et al.

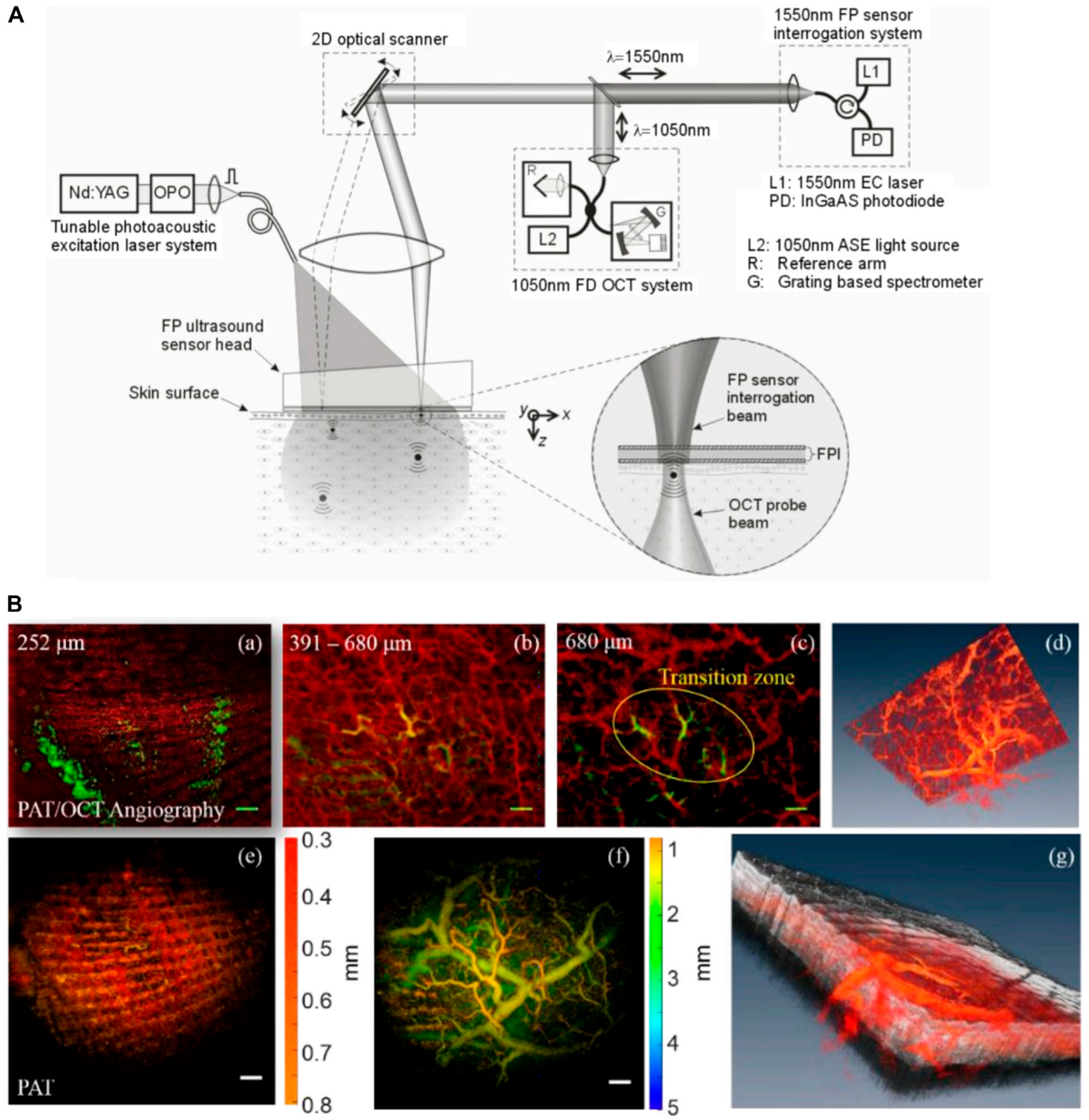

**FIGURE 9 | (A)** Dual-modal PAT-OCT scanner. Reprinted with permission from [151]. **(B) (a–c)** overlaid PAT-OCTA images with PAT in the green channel and OCTA in the red channel. **(d)** Blood vessel network given in volumetric display by fused OCTA and PAT data. **(e)** PAT image. **(f)** PAT image in deeper region. **(g)** A snapshot of the 3D volume with OCT in gray, OCTA, and PAT in red color map. Scale bar = 1 mm. Reprinted with permission from [153].

[144] were among the first groups to demonstrate the application of the PAM-OCT system for chorioretinal imaging of rabbits in 2017. They were able to visualize depth-resolved retinal and choroidal vessels using laser exposure well below the ANSI safety limit. A multimodal imaging system combining PAM, OCT, and florescence microscopy was demonstrated by Zhang et al. [145, 146], and it was applied to evaluate angiogenesis in both albino and pigmented live rabbit eyes. The authors claimed that in pigmented rabbits, melanin from the retinal pigment epithelium overlies the choroid and thus possibly blocks the diffuse choroidal hyperfluorescence and improve the image quality of all the three modalities. Nguyen et al. [95] employed gold nanoparticles as a contrast agent for both OCT and PAM imaging. They imaged *in vivo* rabbit retina, and the exogenous

contrast agent improved the efficiency for visualizing capillaries, and retinal and choroidal vessels. The speed of the system was defined by 1 KHz pulse repetition rate of the excitation laser. The system was later used to evaluate optical properties of retinal vein occlusion and retinal neovascularization in living rabbits [147]. Spectroscopic PAM was performed at wavelengths ranging from 510 to 600 nm to further evaluate dynamic changes in the retinal morphology [148]. The schematic of the developed system and recorded images using the multimodal system are presented in **Figure 8A B**, respectively.

In general, PAM devices have relatively low axial resolution compared to OCT systems, and there is a large resolution gap between two modalities. Unlike, OCT, whose axial resolution is defined by the spectral bandwidth of the light source in PAM axial resolution, depends on the detector's bandwidth and ultrasound attenuation [33]. The typical axial resolution of OCT systems is less than 10 μm, which corresponds to ~100 MHz ultrasound signal frequency. These high-frequency signals can hardly survive in some cases where the distance from the source to the detector is long such as retina imaging. Therefore, for ophthalmic PAM-OCT, it is importance to enhance PA detection mechanism to reduce the gap in axial resolution.

## Photoacoustic Tomography Combined With Optical Coherence Tomography

Due to the high penetration depth benefits, dual-modal PAT-OCT systems are mainly used for applications where depth information is required [108, 149]. For example, in dermatology, while OCT techniques visualize superficial small capillary loops with vessel diameters from 10 to 200 μm to a depth of 1 mm, PAT enables visualization of vasculatures with diameters from 100 μm down to a depth of several centimeters. Therefore, the combination of these modalities could provide a complete perfusion map of the skin [150]. In addition, acquiring PAT and OCT images from overlapping or identical regions has the advantage that highly absorbing structures, which appear as shadow in OCT images (e.g., blood vessels), can be observed in PAT images [16].

In 2011, Zhang et al. [151] developed a PAT-OCT system and demonstrated *in vivo* volumetric images of vasculature and surrounding tissue in mouse and human skin. The schematic of their system is presented in **Figure 9A**. The system employed an integrated all-optical detection scheme for both modalities in reflection-mode maintaining a field of view of ~13 mm × 13 mm. The photoacoustic waves were detected using a Fabry–Perot sensor place on the surface of the skin. The planar-view PAT system based on the Fabry–Perot interferometer is of particular interest in most dual-modal PAT-OCT applications because of the simplicity of sample positioning and optical detection mechanism [149, 152]. The study reported tissue information of vascular structure to a depth of ~5 mm. Similar systems were further developed, and *in vivo* clinical experiments were performed on healthy and pathological skin [103, 153–156] (**Figure 9B**). Initial clinical studies demonstrate that the dual-modal PAT-OCT systems hold a great potential for applications in dermatology [157]. Recently, Liu et al. [108] published a comprehensive overview of the dual-modality PAT-OCT system in the field of dermatology and the challenges and prospects of these two imaging modalities for dermatology were discussed thoroughly.

## Photoacoustic Endoscopy Combined With Optical Coherence Tomography

Toward realizing dual-modality PAE-OCT, in 2011 Yang et al. [158] made the initial step by integrating ultrasound tomography with photoacoustic and OCT imaging in a single intraoperative probe. The performance of the system was demonstrated on *ex vivo* porcine and human ovaries. The OCT subsystem used a swept-source laser centered at ~1,300 nm with 110 nm spectral bandwidth and a 20 KHz scan rate, and the PAE subsystem had a tunable Ti: Sapphire laser with a spectral range of 700–950 nm and a 15 Hz repetition rate. The ultrasound transducer operated as both PAI detection and ultrasound transmission and detection. **Figure 10A** depicts the combined three-modality endoscopic probe. The overall diameter of the endoscope was 5 mm and included a ball-lensed OCT sample arm probe, and a multimode fiber to deliver light for photoacoustic imaging. Later, in 2013, Xi et al. [159] reported an endoscopic delivery probe with a diameter of 2.3 mm. The system had a low-frequency unfocused 10 MHz transducer for photoacoustic signal detection and a time-domain OCT system at 1 kHz. The performance of their system could be improved in several ways such as increasing the central frequency of photoacoustic transducer, employing a higher-resolution DAQ card, and replacing the time-domain OCT device with a frequency-domain OCT device to enhance the sensitivity. Inspired by one of the initial efforts in the field (Yang et al. [158] study), Dai et al. [160] developed a multimodal miniature probe through which OR-PAM, OCT, and pulsed-echo ultrasound images were acquired coaxially and were displayed simultaneously. **Figure 10B** depicts the schematic of the integrated miniature probe. The 2 mm diameter probe had a 40 MHz unfocused ultrasound transducer for both OR-PAM detection and ultrasound transmission and receiving, and *in vivo* images of the rat ear were recorded (**Figure 10C**). The results show cross-sectional images acquired by OR-PAM, OCT, ultrasound, and combined images, corresponding to the three dashed lines in the respective maximum-amplitude-projection image. Despite offering high imaging resolution, the system suffered from lack of rotational scanning and its imaging speed was limited by the slow repetition rate (20 Hz) of the pulsed laser. Mathews et al. [161] developed a dual-modal intravascular imaging probe using a commercial OCT catheter and a fiber optic ultrasound sensor based on Fabry–Perot cavity. Their experimental setup and the enlarged view of the distal end of the probe is presented in **Figure 10D**. They demonstrated circumferential PAE-OCT imaging and multispectral PAI on a synthetic phantom. One limitation of their probe configuration was that the stationary fiber optic ultrasound receiver resulted in shielding of the photoacoustic waves by the OCT catheter for certain excitation angles. As a result, the detected photoacoustic signal amplitude varied relatively with respect to the receiving

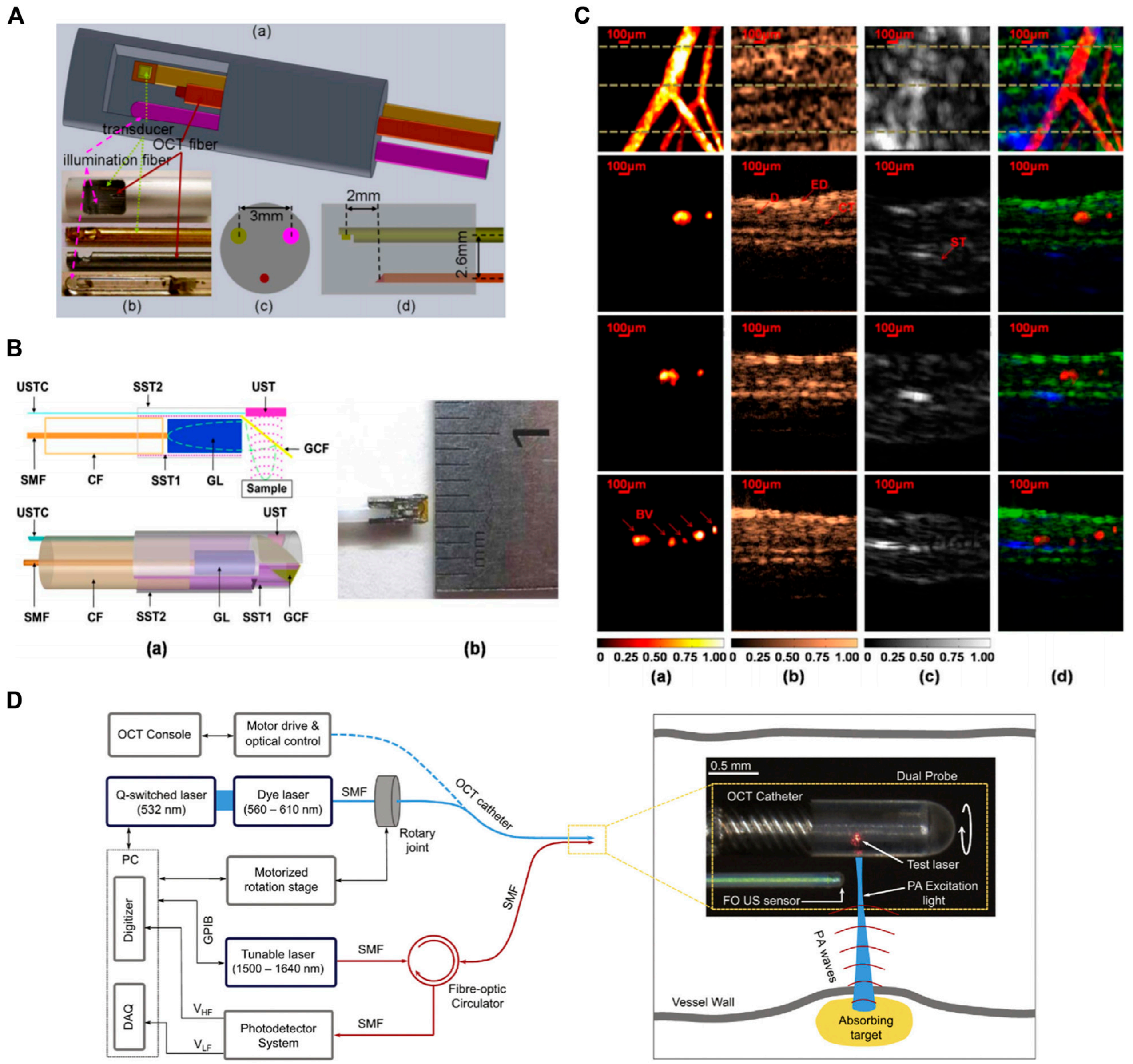

**FIGURE 10 | (A)** Integrated OCT-US-PAI three-modality endoscopic probe. Reprinted with permission from [158]. **(B)** Schematic and photograph of miniature integrated probe. Reprinted with permission from [160]. **(C)** *In vivo* images of a rat ear. Maximum amplitude projection images (top row) and cross-sectional images (2nd, 3rd, and bottom rows) corresponding to the dotted lines in first row images. **(a)** OR-PAM, **(b)** OCT, **(c)** US, and **(d)** fused images. Reprinted with permission from [160]. **(D)** Schematic of the dual-modality PA-OCT system. An enlarged image of the distal end of the probe. Reprinted with permission from [161].

angle in the rotation plane. In general, future direction for multimodal PAE-OCT studies can be focused on improving scanning speed, miniaturizing the probe size, and enhancing detection mechanism.

## DISCUSSION

The combination of PAI and OCT has drawn a large amount of research interest throughout the past decade. This multimodal technology has the potential to provide chromophore selective image contrast in concert with depth-resolved scattering contrast. Despite offering several advantages, there are still a couple of key challenges to overcome.

One of the major limitations of current systems is the significant imaging speed mismatch between OCT and PAI subsystems. Imaging speed is a critical parameter when it comes to real-time functional studies. Additionally, faster imaging speeds will help systems mitigate image artifacts due to involuntary motion. Thanks to technological developments, current OCT systems are able to reach video rate over a large scanning area [162–164]. The same is not true for PAI systems, and as a result, the imaging speed of the dual-modal system is defined by the pulse repetition rate of the PA excitation light source or mechanical scanning speed of the PAI probe head. Widespread implementation of PAI-OCT systems will depend on the development and integration of suitable light sources with high repetition rate, stable short pulse illumination, and high output energy at multiple wavelengths. This development would enable PAI-OCT systems to capture real-time large field-of-view images.

The other major constraint in most PAI systems is that most ultrasound detectors are opaque. Therefore, the physical size of the sensor obstructs the optical path required for OCT acquisition. To overcome this limitation, in some studies the active size of the transducer was reduced, or the transducer was positioned obliquely [131]. However, since the sensitivity of the photoacoustic imaging scales with the active element size of the detector, these methods effect the sensitivity of the photoacoustic images and will degrade image quality [165]. Several studies have investigated optimizing light delivery to improve PA image contrast and signal-to-noise ratio [166–168]. Monte Carlo simulations suggest that the optimal PA illumination depends on the optical properties of the sample [169]. Improvements in light delivery have also be investigated through using optically transparent spacer between the transducer and sample to directly deliver light to the surface underneath the transducer [170–172]. In addition, custom transducers and new materials have been explored to develop different illumination geometries and improve the quality of the PA image [173, 174]. However, these methods require significant modification of the system and cannot be readily integrated into standard clinical scanners [175].

Another important constraint of ultrasound transducers used in most PAI systems rises from their need for physical contact with the sample through a coupling medium. This contact-based detection minimizes the acoustic reflection losses at poorly matched interfaces such as tissue and air. However, it is not suitable for several clinical and preclinical applications such as wound assessment, brain imaging, or ophthalmic imaging [176]. Various approaches have been suggested to overcome this limitation among which optical detection approaches hold the promise to provide high sensitivity over a wide frequency range [177–180]. Optical detection methods also offer the opportunity of developing miniaturized and optically transparent ultrasound detectors [181]. The pure optical PAI-OCT system is more attractive nowadays and offers a better choice for the multimodal imaging. Different studies have been conducted on the performance of pure optical photoacoustic imaging integrated with optical coherence tomography [182, 183]. In [119], authors proposed a resolution-matched reflection-mode PAM-OCT system for *in vivo* imaging applications. The PAM subsystem is based on a polarization-dependent reflection ultrasonic detection (PRUD), which still requires water as a coupling medium and complicated optical alignment. The akinetic sensor employed in [130] is another example of the pure optical PA detection sensor, which also suffers from the need for acoustic gel as a coupling medium. All-optical PA detection methods have been investigated for noncontact, dual-modal PAI-OCT system as well. These methods include homodyne interferometer [85], heterodyne interferometer [184], and two-wave mixing interferometer [185]. These methods are mainly based on detection of surface vibrations induce by photoacoustic pressure waves. While they bring noncontact PA imaging into the field, detecting surface vibrations using an interferometer requires high phase stability. Thus, to maintain these interferometric PA detection systems at their highest sensitivity, complicated phase stabilization techniques are required. In addition, the success of the methods relies on surface topography and has difficulty while applied to uneven surfaces or *in vivo* applications where motion is undeniable. Recent advances in noninterferometric photoacoustic remote sensing (PARS) have proved the potential of technique for various imaging applications [186–190]. Martell et al. [191] have reported all-optical, noncontact, dual-modal PARS-OCT and discussed the potential of the system for different *in vivo* applications.

As a hybrid imaging modality, PAI-OCT imaging combines naturally complimentary advantages of photoacoustic imaging and optical coherence tomography. Despite the aforementioned technical challenges, the possible impact of a PAI-OCT to many biomedical applications explored in this paper warrants significant further investigation. With the continued advancements of new detection methods, along with new light sources, multimodal PAI-OCT imaging has a promising future in biomedical imaging as a powerful tool for diagnostics.

## AUTHOR CONTRIBUTIONS

ZH compiled the article and prepared figures, JS edited parts of the article, and PR was the principle investigator, set the article scope, and proofread the article.

## FUNDING

New Frontiers in Research Fund–Exploration (NFRFE-2019-01012); Natural Sciences and Engineering Research Council of Canada (DGECR-2019-00143, RGPIN2019-06134); Canada Foundation for Innovation (JELF #38000); Mitacs (IT13594); Center for Bioengineering and Biotechnology (CBB Seed fund); University of Waterloo; illumiSonics (SRA #083181).

## ACKNOWLEDGMENTS

The authors acknowledge funding from the University of Waterloo, NSERC Discovery grant, MITACS accelerator program, Canada Foundation for Innovation (CFI-JEFL), Center for Bioengineering and Biotechnology seed funding, New Frontiers in Research Fund–exploration, and research partnership support from illumiSonics Inc.

# REFERENCES

1. Tempany CM, Jayender N, Kapur A, Bueno R, Golby T, Agar J, et al. Multimodal imaging for improved diagnosis and treatment of cancers. *Cancer* (2015) 121(6):817–27. doi:10.1002/cncr.29012
2. JoleszJayender M, Shu J. Multimodal molecular imaging: current status and future directions. *Contrast Media Mol Imag*. (2018) 2018, 1382183. doi:10.1155/2018/1382183
3. Rodríguez-Palomares JF, García Fernández MA, Barba Cosials J. Integrating multimodal imaging in clinical practice: the importance of a multidisciplinary approach. *Rev Esp Cardiol*. (2016) 69(5):477–9. doi:10.1016/j.rec.2016.01.019
4. Pan H, Myerson J, Yang X, Lanza G, Wickline SA. Atherosclerosis endothelial activation quantification *in vivo* with fluorine magnetic resonance imaging and spectroscopy. *J Cardiovasc Magn Reson* (2014) 16(1):O91. doi:10.1186/1532-429X-16-S1-O91
5. Bruckman MA, Jiang K, Simpson MJ, Randolph LN, LuytL G, Steinmetz NF. Dual-modal magnetic resonance and fluorescence imaging of atherosclerotic plaques *in vivo* using VCAM-1 targeted tobacco mosaic virus. *Nano Lett*. (2014) 14(3):1551–8. doi:10.1021/nl404816m
6. O'HalloranJiang R, Kopell BH, Sprooten E, Goodman WK, Frangou S. Multimodal neuroimaging-informed clinical applications in neuropsychiatric disorders. *Front Psychiatr*. (2016) 7:63. doi:10.3389/fpsyt.2016.00063
7. Teipel S, Drzezga A, Grothe MJ, Barthel H, Chételat G, Schuff N, et al. Multimodal imaging in Alzheimer's disease: validity and usefulness for early detection. *Lancet Neurol* (2015) 14(10):1037–53. doi:10.1016/S1474-4422(15)00093-9
8. FellgiebelDrzezga MF, Zerda A, Jokerst JV, Zavaleta CL, Kempen PJ, Mittra E, Pitter K, et al. A brain tumor molecular imaging strategy using a new triple-modality MRI-photoacoustic-Raman nanoparticle. *Nat Med* (2012) 18(5):829–34. doi:10.1038/nm.2721
9. Gambhirde la Zerda J, Wang LV. Photoacoustic microscopy. *Laser Photon Rev*. (2013) 7(5):758–78. doi:10.1002/lpor.201200060
10. Wang LV, Hu S. Photoacoustic tomography: in vivo imaging from organelles to organs. *Science*. (2012) 335(6075):1458–62. doi:10.1126/science.1216210
11. Tan ACS, Tan GS, Denniston AK, Keane PA, Ang M, Milea D, et al. An overview of the clinical applications of optical coherence tomography angiography. *Eye* (2018)32(2). doi:10.1038/eye.2017.181
12. Kashani AH, Chen CL, Gahmc JK, Zheng F, Richtera GM, Rosenfeld PJ, et al. Optical coherence tomography angiography: a comprehensive review of current methods and clinical applications. *Prog Retin Eye Res* (2017) 60:66–100. doi:10.1016/j.preteyeres.2017.07.002
13. WangChen AM, Nguyen FT, Oldenburg AL, Marks DL, Boppart SA. Optical coherence tomography: a review of clinical development from bench to bedside. *J Biomed Optic*. (2007) 12(5):051403. doi:10.1117/1.2793736
14. Boppart X, Zhang HF, Jiao S. Optical coherence photoacoustic microscopy: accomplishing optical coherence tomography and photoacoustic microscopy with a single light source. *J Biomed Optic*. (2012) 17(3):030502. doi:10.1117/1.JBO.17.3.030502
15. Brunker J, Yao J, Laufer J, Bohndiek SE. Photoacoustic imaging using genetically encoded reporters: a review (2017). Available at: https://www-spiedigitallibrary-org.proxy.lib.uwaterloo.ca/journals/journal-of-biomedical-optics/volume-22/issue-07/070901/Photoacoustic-imaging-using-genetically-encoded-reporters-a-review/10.1117/1.JBO.22.7.070901.full (Accessed June 17, 2020).
16. Drexler W, Fujimoto JG. *Optical coherence tomography: technology and applications*. AG Switzerland: Springer Science & Business Media (2008). 1346 p.
17. Wang LV. Multiscale photoacoustic microscopy and computed tomography. *Nat Photon*. (2009) 3(9):503–9. doi:10.1038/nphoton.2009.157
18. Wang LV, Hu S. Photoacoustic tomography: in vivo imaging from organelles to organs. *Science*. (2012) 335(6075):1458–62. doi:10.1126/science.1216210
19. Bell AG. On the production and reproduction of sound by light. *In Proc Am Assoc Adv Sci*. (1881) 29:115–36. doi:10.2475/ajs.s3-20.118.305
20. Wang LV, Wu H-I. *Biomedical optics: principles and imaging*. Hoboken, NJ: John Wiley & Sons, Inc. (2009). p 376.
21. Beard P. Biomedical photoacoustic imaging. *Interface Focus*. (2011) 1(4):602–31. doi:10.1098/rsfs.2011.0028
22. Chan J, Zheng Z, Bell K, Le M, Reza PH, Yeow JT. Photoacoustic imaging with capacitive micromachined ultrasound transducers: principles and developments. *Sensors*. (2019) 19(16):3617. 10.3390/s19163617
23. Bowen T. Radiation-Induced thermoacoustic soft tissue imaging. In: 1981 ultrasonics symposium; 1981 October 14–16; Chicago, IL. IEEE (1981). p. 817–22.
24. Kolkman RGM, Hondebrink E, Steenbergen W, de Mul FFM. *In vivo* photoacoustic imaging of blood vessels using an extreme-narrow aperture sensor. *IEEE J Sel Top Quant Electron*. (2003) 9(2):343–6. doi:10.1109/JSTQE.2003.813302
25. Hajireza P, Sorge J, Brett M, Zemp R. *In vivo* optical resolution photoacoustic microscopy using glancing angle-deposited nanostructured Fabry-Perot etalons. *Opt Lett*. (2015) 40(7):1350–3.doi:10.1364/OL.40.001350
26. Xia J, Chatni MR, Maslov K, Guo Z, Wang K, Anastasio M, et al. Whole-body ring-shaped confocal photoacoustic computed tomography of small animals *in vivo*. *J Biomed Optic*. (2012) 17(5):050506. doi:10.1117/1.JBO.17.5.050506
27. WangChatni L, Hu P, Shi J, Appleton CM, Maslov K, Li L, et al. Single-breath-hold photoacoustic computed tomography of the breast. *Nat Commun*. (2018) 9(1):2352. doi:10.1038/s41467-018-04576-z
28. WangHu CL, Luke GP, Emelianov SY. Photoacoustic imaging for medical diagnostics. *Acoust Today*. (2012) 8(4):15. doi:10.1121/1.4788648
29. Stein EW, Maslov K, Wang LV. Noninvasive, *in vivo* imaging of blood-oxygenation dynamics within the mouse brain using photoacoustic microscopy. *J Biomed Optic*. (020502200) 14(2):020502. doi:10.1117/1.3095799
30. Yao J, Wang LV. Photoacoustic microscopy. *Laser Photon Rev*. (2013) 7(5):758–78. doi:10.1002/lpor.201200060
31. Hu S, Wang LV. Photoacoustic imaging and characterization of the microvasculature. *J Biomed Optic*. (2010) 15(1):011101. doi:10.1117/1.3281673
32. Guo H, Li Y, Qi W, Xi L. Photoacoustic endoscopy: a progress review. *J Biophot*. n/a:e202000217. doi:10.1002/jbio.202000217
33. Yao J, Wang LV. Sensitivity of photoacoustic microscopy. *Photoacoustics*. (2014) 2(2):87–101. doi:10.1016/j.pacs.2014.04.002
34. Hu S. Emerging concepts in functional and molecular photoacoustic imaging. *Curr Opin Chem Biol*. (2016) 33:25–31. doi:10.1016/j.cbpa.2016.04.003
35. Moothanchery M, Pramanik M. Performance characterization of a switchable acoustic resolution and optical resolution photoacoustic microscopy system. *Sensors*. (2017) 17(2):357. doi:10.3390/s17020357
36. Zhang C, Maslov K, Wang LV. Subwavelength-resolution label-free photoacoustic microscopy of optical absorption *in vivo*. *Opt Lett*. (2010) 35(19):3195. doi:10.1364/OL.35.003195
37. Li M, Tang Y, Yao J. Photoacoustic tomography of blood oxygenation: a mini review. *Photoacoustics*. (2018) 10:65–73. doi:10.1016/j.pacs.2018.05.001
38. Yao J, Maslov KI, Shi Y, Taber LA, Wang LV. *In vivo* photoacoustic imaging of transverse blood flow by using Doppler broadening of bandwidth. *Opt Lett*. (2010) 35(9):1419–21. doi:10.1364/OL.35.001419
39. Yao J, Wang LV. Transverse flow imaging based on photoacoustic Doppler bandwidth broadening. *J Biomed Optic*. (2010) 15(2):021304. doi:10.1117/1.3339953
40. Yao J, Ke H, Tai S, Zhou Y, Wang LV. Absolute photoacoustic thermometry in deep tissue. *Opt Lett*. (2013) 38(24):5228–31. doi:10.1364/ol.38.005228
41. Gao L, Wang L, Li C, Liu Y, Ke H, Zhang C, et al. Single-cell photoacoustic thermometry. *J Biomed Optic*. (2013) 18(2):26003. doi:10.1117/1.JBO.18.2.026003
42. WangWang P, Forbrich A, Zemp R. *In-Vivo* functional optical-resolution photoacoustic microscopy with stimulated Raman scattering fiber-laser source. *Biomed Optic Express*. (2014) 5(2):539. doi:10.1364/BOE.5.000539
43. Yao J, Wang L, Yang TT, Maslov KI, Wong JM, Li L, et al. High-speed label-free functional photoacoustic microscopy of mouse brain in action. *Nat Methods*. (2015) 12(5):407–10. doi:10.1038/nmeth.3336
44. Chen Z, Rank E, Meiburger KM, Sinz C, Hodul A, Zhang E, et al. Non-invasive multimodal optical coherence and photoacoustic tomography for human skin imaging. *Sci Rep*. (2017) 7(1):17975. doi:10.1038/s41598-017-18331-9
45. Laufer J, Zhang E, Raivich G, Beard P. Three-dimensional noninvasive imaging of the vasculature in the mouse brain using a high resolution photoacoustic scanner. *Appl Optic*. (2009) 48(10):D299–306. doi:10.1364/ao.48.00d299

46. Paproski RJ, Heinmiller A, Wachowicz K, Zemp RJ. Multi-wavelength photoacoustic imaging of inducible tyrosinase reporter gene expression in xenograft tumors. *Sci Rep*. (2014) 4:5329. doi:10.1038/srep05329
47. Sethuraman S, Amirian JH, Litovsky SH, Smalling RW, Emelianov SY. *Ex vivo* characterization of atherosclerosis using intravascular photoacoustic imaging. *Optic Express*. (2007) 15(25):16657. doi:10.1364/OE.15.016657
48. Oh JT, Li ML, Zhang HF, Maslov K, Stoica G, Wang LV. Three-dimensional imaging of skin melanoma *in vivo* by dual-wavelength photoacoustic microscopy. *J Biomed Optic*. (2006) 11(3):34032. doi:10.1117/1.2210907
49. Wang SM, Ibey BL, Roth CC, Tsyboulski DA, Beier HT, Glickman RD, et al. All-optical optoacoustic microscopy based on probe beam deflection technique. *Photoacoustics*. (2016) 4(3):91–101. doi:10.1016/j.pacs.2016.02.001
50. Wong TTW, Zhang R, Hai P, Zhang C, Pleitez MA, Aft RL, et al. Fast label-free multilayered histology-like imaging of human breast cancer by photoacoustic microscopy. *Sci Adv*. (2017) 3(5):e1602168. doi:10.1126/sciadv.1602168
51. WangZhang R, Chen J, Wang H, Yan M, Zheng W, Song L. Longitudinal label-free optical-resolution photoacoustic microscopy of tumor angiogenesis *in vivo*. *Quant Imag Med Surg*. (2015) 5(1):23–9. doi:10.3978/j.issn.2223-4292.2014.11.08
52. Li L, Shemetov AA, Baloban M, Hu P, Zhu L, Shcherbakova DM, et al. Small near-infrared photochromic protein for photoacoustic multi-contrast imaging and detection of protein interactions *in vivo*. *Nat Commun*. (2018) 9(1):2734. doi:10.1038/s41467-018-05231-3
53. Nguyen VP, Paulus YM. Photoacoustic ophthalmoscopy: principle, application, and future directions. *J Imag*. (2018) 4(12):149. doi:10.3390/jimaging4120149
54. Nam SY, Ricles LM, Suggs LJ, Emelianov SY. *In vivo* ultrasound and photoacoustic monitoring of mesenchymal stem cells labeled with gold nanotracers. *PloS One*. (2012) 7(5):e37267. doi:10.1371/journal.pone.0037267
55. Huang D, Swanson W, Lin WG, Schuman JS, Stinson CP, Chang EA, et al. Optical coherence tomography. *Science*. (1991) 254(5035):1178–81. doi:10.1126/science.1957169
56. Puliafito CA, Yehoshua Z, Gregori G, Puliafito CA, Rosenfeld PJ. Chapter 3–optical coherence tomography. In: SJ Ryan, SR Sadda, DR Hinton, AP Schachat, SR Sadda, CP Wilkinson, et al. editors. *In retina*. 5th ed. London, United Kingdom: W.B. Saunders (2013). p. 82–110.
57. de Boer JF, Leitgeb R, Wojtkowski M. Twenty-five years of optical coherence tomography: the paradigm shift in sensitivity and speed provided by Fourier domain OCT [Invited]. *Biomed Optic Express*. (2017) 8(7):3248. doi:10.1364/BOE.8.003248
58. Fercher AF, Leitgeb R, Hitzenberger CK, Sattmann H, Wojtkowski M. “Complex spectral interferometry OCT,” in medical applications of lasers in dermatology, cardiology, ophthalmology, and dentistry II. *Feb*. (1999) 3564:173–8. doi:10.1117/12.339152
59. Aumann S, Donner S, Fischer J, Müller F. Optical coherence tomography (OCT): principle and technical realization. In: JF Bille., editor *High resolution imaging in microscopy and ophthalmology: new frontiers in biomedical optics*. Cham, Switzerland: Springer International Publishing (2019). p. 59–85.
60. Yaqoob Z, Wu J, Yang C. Spectral domain optical coherence tomography: a better OCT imaging strategy. *Biotechniques*. (2005) 39(6 Suppl. l):S6–13. doi:10.2144/000112090
61. Hahn P, Migacz J, O’Connell R, Maldonado RS, Izatt JA, Toth CA. The use of optical coherence tomography in intraoperative ophthalmic imaging. *Ophthalmic Surg Laser Imag*. (2011) 42 Suppl(4):S85–94. doi:10.3928/15428877-20110627-08
62. Pircher M, Zawadzki RJ. Review of adaptive optics OCT (AO-OCT): principles and applications for retinal imaging [Invited]. *Biomed Optic Express*. (2017) 8(5):2536–62. doi:10.1364/BOE.8.002536
63. Ramos JL, Li Y, Huang D. Clinical and research applications of anterior segment optical coherence tomography–a review. *Clin Exp Ophthalmol*. (2009) 37(1):81–9. doi:10.1111/j.1442-9071.2008.01823.x
64. Leitgeb RA, Werkmeister RM, Blatter C, Schmetterer L. Doppler optical coherence tomography. *Prog Retin Eye Res*. (2014) 41:26–43. doi:10.1016/j.preteyeres.2014.03.004
65. Chen CL, Wang RK. Optical coherence tomography based angiography [Invited]. *Biomed Optic Express*. (2017) 8(2):1056–82. doi:10.1364/BOE.8.001056
66. De Boer JF, Hitzenberger CK, Yasuno Y. Polarization sensitive optical coherence tomography–a review [Invited]. *Biomed Optic Express*. (2017) 8(3):1838–73. doi:10.1364/BOE.8.001838
67. Liang X, Boppart SA, Boppart SA. Biomechanical properties of *in vivo* human skin from dynamic optical coherence elastography. *IEEE Trans Biomed Eng*. (2010) 57(04):953–9. doi:10.1109/TBME.2009.2033464
68. Shu X, Liu W, Duan L, Zhang HF. Visible spectroscopic doppler analysis for visible-light optical coherence tomography. *J Biomed Optic*. (2017) 22(12):1. doi:10.1117/1.JBO.22.12.121702
69. Zhang PJ, Bouwens A, Szlag D, Lasser T, Extermann J. Brain imaging with extended-focus optical coherence tomography at different scales and spectral ranges (Conference Presentation). In: Optical coherence tomography and coherence domain optical methods in biomedicine, XXIII; 2019 March 4; San Jose, CA: SPIE BiOS (2019). p. 108671U.
70. Magnain C. Human brain imaging by optical coherence tomography. In: *Handbook of Neurophotonics*., 399. Boca Raton, FL: CRC Press (2020). 448 p.
71. Ling Y, Li C, Purslow C, Yang Y, Huang Z. Evaluation of human corneal ulcer healing process using optical coherence tomography: an *in vitro* study. In: Optical elastography and tissue biomechanics VI; 2019 Feburary 21; San Jose, CA: SPIE BiOS (2019). p. 108801H.
72. Hendon CP, Lye TH, Yao X, Gan Y, Marboe CC. Optical coherence tomography imaging of cardiac substrates. *Quant Imag Med Surg*. (2019) 9(5):882. doi:10.21037/qims.2019.05.09
73. Rajabi-Estarabadi A, Bittar LG, Zheng I, Nascimento V, Camacho C, Feun JM, et al. Optical coherence tomography imaging of melanoma skin cancer. *Laser Med Sci*. (2019) 34(2):411–20. doi:10.1007/s10103-018-2696-1
74. NouriBittar A, Huang D. Optical coherence tomography angiography in neurology and neuro-ophthalmology. In: *OCT and imaging in central nervous system diseases*. AG Switzerland: Springer (2020). p. 523–44.
75. Malone J, Hohert G, Hoang L, Miller DM, McAlpine J, MacAulay C, et al. Endoscopic optical coherence tomography (OCT) and autofluorescence imaging (AFI) of *ex vivo* fallopian tubes. *Multimodal Biomed Imag XV*. (2020) 11232:1123202. 10.1117/12.2544475
76. Freund JE, Buijs M, Bruin DM, Savci-Heijink CD, Rosette JJMCH, Leeuwen TGV, et al. Optical coherence tomography in urologic oncology: a comprehensive review. *SN Comprehen Clin Med*. (2019) 1(2):67–84.
77. Fried D. Optical coherence tomography for imaging dental caries. In *Detection and assessment of dental caries*. Cham, Switzerland: Springer (2019). p. 199–208.
78. Beaurepaire E, Moreaux L, Amblard F, Mertz J. Combined scanning optical coherence and two-photon-excited fluorescence microscopy. *Opt Lett*. (1999) 24(14):969–71. doi:10.1364/OL.24.000969
79. Dunkers J, Cicerone M, Washburn N. Collinear optical coherence and confocal fluorescence microscopies for tissue engineering. *Optic Express*. (2003) 11(23):3074–9. doi:10.1364/OE.11.003074
80. Harper DJ, Augustin M, Lichtenegger A, Eugui P, Glösmann M, Hitzenberger CK, et al. White light optical coherence tomography for sub-micron resolution and spectroscopic imaging in the mouse retina. *Invest Ophthalmol Vis Sci*. (2018) 59(9):5826. 10.1364/BOE.9.002115
81. Marchand PJ, Szlag D, Bouwens A, Lasser T. *In vivo* high-resolution cortical imaging with extended-focus optical coherence microscopy in the visible-NIR wavelength range. *J Biomed Optic*. (2018) 23(3):1–7. doi:10.1117/1.JBO.23.3.036012
82. Wang LV, Hu S. Photoacoustic tomography: *in vivo* imaging from organelles to organs. *Science*. (2012) 335(6075):1458–62. doi:10.1126/science.1216210
83. Wang LV, Yao J. A practical guide to photoacoustic tomography in the life sciences. *Nat Methods*. (2016) 13(8):627–38. doi:10.1038/nmeth.3925
84. Marsh-Armstrong B, Migacz J, Jonnal R, Werner JS. Automated quantification of choriocapillaris anatomical features in ultrahigh-speed optical coherence tomography angiograms. *Biomed Optic Express*. (2019) 10(10):5337–50. doi:10.1364/BOE.10.005337
85. Ma Z, Luo S, Yu M, Liu J, Zhao Y, Yu Y, et al. Assessment of microvasculature flow state with a high speed all-optic dual-modal system of optical coherence tomography and photoacoustic imaging. *Biomed Optic Express*. (2018) 9(12):6103–15. doi:10.1364/BOE.9.006103
86. WangLuo EZ, Povazay B, Laufer J, Alex A, Hofer B, Pedley B, et al. Multimodal photoacoustic and optical coherence tomography scanner using an all optical

detection scheme for 3D morphological skin imaging. *Biomed Optic Express*. (2011) 2(8):2202–15. doi:10.1364/BOE.2.002202

87. DrexlerPovazay BJ, Lanning RM, Tyrrell JA, Padera TP, Bartlett LA, Stylianopoulos T, et al. Three-dimensional microscopy of the tumor microenvironment *in vivo* using optical frequency domain imaging. *Nat Med*. (2009) 15(10):1219–23. doi:10.1038/nm.1971
88. BoumaLanning HS, Yoo H. Spectroscopic optical coherence tomography: a review of concepts and biomedical applications. *Appl Spectrosc Rev*. (2018) 53(2–4):91–111. doi:10.1080/05704928.2017.1324876
89. Morgner U, Drexler W, Kärtner FX, Pitris XD, Ippen C, Fujimoto EP. Spectroscopic optical coherence tomography. *Opt Lett*. (2000) 25(2):111–3. doi:10.1364/OL.25.000111
90. FujimotoDrexler W, Wei Q, Liu W, Liu T, Yi J, Sheibani N, et al. A combined method to quantify the retinal metabolic rate of oxygen using photoacoustic ophthalmoscopy and optical coherence tomography. *Sci Rep*. (2015) 4(1):6525. doi:10.1038/srep06525
91. Zhang ND, Linsenmeier RA. Retinal oxygen: fundamental and clinical aspects. *Arch Ophthalmol*. (2003) 121(4):547–57. doi:10.1001/archopht.121.4.547
92. Hammes H-P. Pericytes and the pathogenesis of diabetic retinopathy. *Horm Metab Res*. (2005) 37 Suppl 1(1):39–43. doi:10.1055/s-2005-861361
93. Mozaffarieh M, Grieshaber MC, Flammer J. Oxygen and blood flow: players in the pathogenesis of glaucoma. *Mol Vis*. (2008) 14:224–33.
94. Wilson KE, Bachawal SV, Tian L, Willmann JK. Multiparametric spectroscopic photoacoustic imaging of breast cancer development in a transgenic mouse model. *Theranostics*. (2014) 4(11):1062–71. doi:10.7150/thno.9922
95. Nguyen VP, Li Y, Qian W, Liu B, Tian C, Zhang W, et al. Contrast agent enhanced multimodal photoacoustic microscopy and optical coherence tomography for imaging of rabbit choroidal and retinal vessels *in vivo*. *Sci Rep*. (2019) 9(1):5945. doi:10.1038/s41598-019-42324-5
96. Nguyen VP, Li Y, Aaberg M, Zhang W, Wang X, Paulus YM. In Vivo 3D imaging of retinal neovascularization using multimodal photoacoustic microscopy and optical coherence tomography imaging–PubMed (2018). Available at: https://pubmed-ncbi-nlm-nih-gov.proxy.lib.uwaterloo.ca/31681820/ (Accessed June 17, 2020).
97. PaulusLi J, Xia J, Maslov KI, Nasiriavanaki M, Tsytsare V, Demchenko AV, et al. Noninvasive photoacoustic computed tomography of mouse brain metabolism *in vivo*. *Neuroimage*. (2013) 64:257–66. doi:10.1016/j.neuroimage.2012.08.054
98. WangXia M, Xia J, Wan H, Bauer AQ, Culver JP, Wang LV. High-resolution photoacoustic tomography of resting-state functional connectivity in the mouse brain. *Proc Natl Acad Sci USA*. (2014) 111(1):21–6. doi:10.1073/pnas.1311868111
99. Jo J, Yang X. Functional photoacoustic imaging to observe regional brain activation induced by cocaine hydrochloride. *J Biomed Optic*. (2011) 16(9):090506. doi:10.1117/1.3626576
100. Marchand PJ, Bouwens A, Szlag D, Nguyen D, Descloux A, Sison M, et al. Visible spectrum extended-focus optical coherence microscopy for label-free sub-cellular tomography. *Biomed Optic Express*. (2017) 8(7):3343. doi:10.1364/BOE.8.003343
101. LasserBouwens PJ, Szlag D, Bouwens A, Lasser T. *In vivo* high-resolution cortical imaging with extended-focus optical coherence microscopy in the visible-NIR wavelength range. *JBO*. (2018) 23(3):036012. doi:10.1117/1.JBO.23.3.036012
102. Hu S, Maslov K, Tsytsarev V, Wang LV. Functional transcranial brain imaging by optical-resolution photoacoustic microscopy. *J Biomed Optic*. (2009) 14(4):040503. doi:10.1117/1.3194136
103. Zabihian B, Weingast J, Liu M, Zhang E, Beard P, Pehamberger H, et al. *In vivo* dual-modality photoacoustic and optical coherence tomography imaging of human dermatological pathologies. *Biomed Optic Express*. (2015) 6(9):3163. doi:10.1364/BOE.6.003163
104. HermannWeingast D, Lee C, Kim S, Zhou Q, Kim J, Kim C. *In Vivo* near infrared virtual intraoperative surgical photoacoustic optical coherence tomography. *Sci Rep*. (2016) 6(1):35176. doi:10.1038/srep35176
105. Cash KJ, Li C, Xia J, Wang LV, Clark HA. Optical drug monitoring: photoacoustic imaging of nanosensors to monitor therapeutic lithium *in Vivo*. *ACS Nano*. (2015) 9(2):1692–8. doi:10.1021/nn5064858
106. Pomerantz R, Zell D, McKenzie G, Siegel DM. Optical coherence tomography used as a modality to delineate basal cell carcinoma prior to Mohs micrographic surgery. *Case Rep Dermatol*. (2011) 3(3):212–8. doi:10.1159/000333000
107. Dahlstrand U, Sheikh R, Merdasa A, Chakari R, Persson B, Cinthio M, et al. Photoacoustic imaging for three-dimensional visualization and delineation of basal cell carcinoma in patients. *Photoacoustics*. (2020) 18:100187. doi:10.1016/j.pacs.2020.100187
108. MalmsjöSheikh M, Drexler W. Optical coherence tomography angiography and photoacoustic imaging in dermatology. *Photochem Photobiol Sci*. (2019) 18(5):945–62. doi:10.1039/C8PP00471D
109. Yoon TJ, Cho YS. Recent advances in photoacoustic endoscopy. *World J Gastrointest Endosc*. (2013) 5(11):534–9. doi:10.4253/wjge.v5.i11.534
110. Gora MJ, Suter MJ, Tearney GJ, Li X. Endoscopic optical coherence tomography: technologies and clinical applications [Invited]. *Biomed Optic Express*. (2017) 8(5):2405–44. doi:10.1364/BOE.8.002405
111. Zackrisson S, van de Ven SMWY, Gambhir SS. Light in and sound out: emerging translational strategies for photoacoustic imaging. *Canc Res*. (2014) 74(4):979–1004. doi:10.1158/0008-5472.CAN-13-2387
112. Wu M, Fw van der Steen A, Regar E, van Soest G. Emerging technology update intravascular photoacoustic imaging of vulnerable atherosclerotic plaque. *Intervent Cardiol*. (2016) 11(2):120–3. doi:10.15420/icr.2016:13:3
113. Li L, Maslov K, Ku G, Wang LV. Three-dimensional combined photoacoustic and optical coherence microscopy for *in vivo* microcirculation studies. *Optic Express*. (2009) 17(19):16450–5. doi:10.1364/OE.17.016450
114. Cai X, Zhang Y, Li L, Choi S-W, MacEwan SW, Yao MR, et al. Investigation of neovascularization in three-dimensional porous scaffolds *in vivo* by a combination of multiscale photoacoustic microscopy and optical coherence tomography. *Tissue Eng C Methods*. (2013) 19(3):196–204. doi:10.1089/ten.TEC.2012.0326
115. WangZhang S, Xie Z, Zhang HF, Puliafito CA. Simultaneous multimodal imaging with integrated photoacoustic microscopy and optical coherence tomography. *Opt Lett*. (2009) 34(19):2961–3. doi:10.1364/OL.34.002961
116. Liu T, Wei Q, Wang J, Jiao S, Zhang HF. Combined photoacoustic microscopy and optical coherence tomography can measure metabolic rate of oxygen. *Biomed Optic Express*. (2011) 2(5):1359–65. doi:10.1364/BOE.2.001359
117. Tsytsarev V, Rao B, Maslov KI, Li L, Wang LV. Photoacoustic and optical coherence tomography of epilepsy with high temporal and spatial resolution and dual optical contrasts. *J Neurosci Methods*. (2013) 216(2):142–5. doi:10.1016/j.jneumeth.2013.04.001
118. Liu M. A study of spectral domain optical coherence tomography and photoacoustic microscopy for biometric and biomedical applications. [Master's thesis]. Newark (United States): University of Delaware (2011).
119. Zhu X, Huang Z, Li Z, Li W, Liu X, Chen Z, et al. Resolution-matched reflection mode photoacoustic microscopy and optical coherence tomography dual modality system. *Photoacoustics*. (2020) 19:100188. doi:10.1016/j.pacs.2020.100188
120. Qin W, Qi W, Jin T, Guo H, Xi L. *In vivo* oral imaging with integrated portable photoacoustic microscopy and optical coherence tomography. *Appl Phys Lett*. (2017) 111(26):263704. doi:10.1063/1.5006234
121. Qin W, Chen Q, Xi L. A handheld microscope integrating photoacoustic microscopy and optical coherence tomography. *Biomed Optic Express*. (2018) 9(5):2205. doi:10.1364/BOE.9.002205
122. Dadkhah A, Jiao S. Optical coherence tomography-guided dynamic focusing for combined optical and mechanical scanning multimodal photoacoustic microscopy. *J Biomed Optic*. (2019) 24(12):1. doi:10.1117/1.JBO.24.12.121906.2019
123. Liu Y, Xu M, Dai Y, Zhao Q, Zhu L, Guan X, et al. NIR-II dual-modal optical coherence tomography and photoacoustic imaging-guided dose-control cancer chemotherapy. *ACS Appl Polym Mater*. (2020) 2(5):1964–73. doi:10.1021/acsapm.0c00155
124. Dong B, Sun C, Zhang HF. Optical detection of ultrasound in photoacoustic imaging. *IEEE Trans Biomed Eng*. (2017) 64(1):4–15. doi:10.1109/TBME.2016.2605451
125. Lee C, Han S, Kim S, Jeon M, Jeon MY, Kim C, et al. Combined photoacoustic and optical coherence tomography using a single near-infrared

supercontinuum laser source. *Appl Optic*. (2013) 52(9):1824–8. doi:10.1364/AO.52.001824

126. Hermann B, Li N, Schmitner B, Meyer D, Weninger WJ, Drexler W, et al. Hybrid ultrahigh resolution optical coherence/ photoacoustic microscopy. *Photon Plus Ultrasound*. (2015) 9323:93232N. doi:10.1117/12.2079232
127. Li L, Dai C, Li Q, Zhao Q, Jiang X, Chai X, et al. Fast subcellular optical coherence photoacoustic microscopy for pigment cell imaging. *Opt Lett*. (2015) 40(19):4448–51. doi:10.1364/OL.40.004448
128. ZhouDai S, Chen Z, Zhao Y, Yang S, Xing D. Simultaneous imaging of atherosclerotic plaque composition and structure with dual-mode photoacoustic and optical coherence tomography. *Optic Express*. (2017) 25(2):530–9. doi:10.1364/OE.25.000530
129. Shu X, Bondu M, Dong B, Podoleanu A, Leick L, Zhang HF. Single all-fiber-based nanosecond-pulsed supercontinuum source for multispectral photoacoustic microscopy and optical coherence tomography. *Opt Lett*. (2016) 41(12):2743. doi:10.1364/OL.41.002743
130. Haindl R, Preisser S, Andreana M, Rohringer W, Sturtzel C, Distel M, et al. Dual modality reflection mode optical coherence and photoacoustic microscopy using an akinetic sensor. *Opt Lett*. (2017) 42(21):4319–22. doi:10.1364/OL.42.004319
131. LiuPreisser S, Rohringer W, Liu M, Kollmann C, Zotter S, Fischer B, et al. All-optical highly sensitive akinetic sensor for ultrasound detection and photoacoustic imaging. *Biomed Optic Express*. (2016) 7(10):4171–86. doi:10.1364/BOE.7.004171
132. DrexlerRohringer R, Deloria AJ, Sturtzel C, Sattmann H, Rohringer W, Fischer B, et al. Functional optical coherence tomography and photoacoustic microscopy imaging for zebrafish larvae. *Biomed Optic Express*. (2020) 11(4):2137–51. doi:10.1364/BOE.390410
133. Liu LV. Multiscale photoacoustic microscopy and computed tomography. *Nat Photon*. (2009) 3(9):503. doi:10.1038/nphoton.2009.157
134. Chen S, Shu X, Nesper PL, Liu W, Fawzi AA, Zhang HF. Retinal oximetry in humans using visible-light optical coherence tomography [Invited]. *Biomed Optic Express*. (2017) 8(3):1415. doi:10.1364/BOE.8.001415
135. Pi S, Camino A, Wei X, Simonett J, Cepurna W, Huang D, et al. Rodent retinal circulation organization and oxygen metabolism revealed by visible-light optical coherence tomography. *Biomed Optic Express*. (2018) 9(11):5851. doi:10.1364/BOE.9.005851
136. JiaCamino J, Li R, Phillips EH, Goergen CJ, Sturek M, Cheng JX. Bond-selective photoacoustic imaging by converting molecular vibration into acoustic waves. *Photoacoustics*. (2016) 4(1):11–21. doi:10.1016/j.pacs.2016.01.002
137. Lee HD, Shin JG, Hyun H, Yu BA, Eom TJ. Label-free photoacoustic microscopy for *in-vivo* tendon imaging using a fiber-based pulse laser. *Sci Rep*. (2018) 8(1):4805. doi:10.1038/s41598-018-23113-y
138. Upputuri PK, Pramanik M. Photoacoustic imaging in the second near-infrared window: a review–PubMed (2019). Available at: https://pubmed-ncbi-nlm-nih-gov.proxy.lib.uwaterloo.ca/30968648/ (Accessed Jun. 18, 2020).
139. Bondu M, Marques MJ, Moselund PM, Lall G, Bradu A, Podoleanu A. Multispectral photoacoustic microscopy and optical coherence tomography using a single supercontinuum source. *Photoacoustics*. (2018) 9:21–30. doi:10.1016/j.pacs.2017.11.002
140. Jiao S, Jiang M, Hu J, Fawzi A, Zhou Q, Shung KK, et al. Photoacoustic ophthalmoscopy for *in vivo* retinal imaging. *Optic Express*. (2010) 18(4): 3967–72. doi:10.1364/OE.18.003967
141. ZhangJiang W, Wei Q, Liu T, Kuai D, Burke JM, Jiao S, et al. Integrating photoacoustic ophthalmoscopy with scanning laser ophthalmoscopy, optical coherence tomography, and fluorescein angiography for a multimodal retinal imaging platform. *J Biomed Optic*. (2012) 17(6):061206. doi:10.1117/1.JBO.17.6.061206
142. ZhangWei X, Liu T, Wen R, Li Y, Puliafito CA, Zhang HF, et al. Optical coherence photoacoustic microscopy for *in vivo* multimodal retinal imaging. *Opt Lett*. (2015) 40(7):1370. doi:10.1364/OL.40.001370
143. JiaoLiu DA. The mechanics of human saccadic eye movement. *J Physiol*. (1964) 174(2):245–64. doi:10.1113/jphysiol.1964.sp007485
144. Tian C, Zhang W, Mordovanakis A, Wang X, Paulus YM. Noninvasive chorioretinal imaging in living rabbits using integrated photoacoustic microscopy and optical coherence tomography. *Optic Express*. (15942017) 25(14):15947. doi:10.1364/OE.25.015947
145. Zhang W, Li Y, Nguyen VP, Huang Z, Liu Z, Wang X, et al. High-resolution, *in vivo* multimodal photoacoustic microscopy, optical coherence tomography, and fluorescence microscopy imaging of rabbit retinal neovascularization. *Light Sci Appl*. (2018) 7(1):103. doi:10.1038/s41377-018-0093-y
146. PaulusLi W, Li Y, Yu Y, Derouin K, Qin VP, Nguyen X, et al. Simultaneous photoacoustic microscopy, spectral-domain optical coherence tomography, and fluorescein microscopy multi-modality retinal imaging. *Photoacoustics*. (2020) 20:100194. doi:10.1016/j.pacs.2020.100194
147. PaulusLi VP, Li Y, Zhang W, Wang X, Paulus YM. Multi-wavelength, en-face photoacoustic microscopy and optical coherence tomography imaging for early and selective detection of laser induced retinal vein occlusion. *Biomed Optic Express*. (2018) 9(12):5915. doi:10.1364/BOE.9.005915
148. Nguyen VP, Li Y, Zhang W, Wang X, Paulus YM. High-resolution multimodal photoacoustic microscopy and optical coherence tomography image-guided laser induced branch retinal vein occlusion in living rabbits. *Sci Rep*. (2019) 9(1):10560. doi:10.1038/s41598-019-47062-2
149. Liu M, Maurer B, Hermann A, Zabihian MG, Sandrian B, Unterhuber B, et al. Dual modality optical coherence and whole-body photoacoustic tomography imaging of chick embryos in multiple development stages. *Biomed Optic Express*. (2014) 5(9):3150. doi:10.1364/BOE.5.003150
150. DrexlerMaurer RA, Baumann B. Multimodal optical medical imaging concepts based on optical coherence tomography. *Front Physiol*. (2018) 6: 114. doi:10.3389/fphy.2018.00114
151. Zhang EZ, Maurer B, Hermann J, Zabihian A, Sandrian B, Unterhuber B, et al. Multimodal photoacoustic and optical coherence tomography scanner using an all optical detection scheme for 3D morphological skin imaging. *Biomed Optic Express*. (2011) 2(8):2202–15. doi:10.1364/BOE.2.002202
152. DrexlerPovazay J, Wang LV. Small-animal whole-body photoacoustic tomography: a review. *IEEE Trans Biomed Eng*. (2014) 61(5):1380–9. doi:10.1109/TBME.2013.2283507
153. Liu M, Chen Z, Zabihian B, Sinz C, Zhang E, Beard PC, et al. Combined multi-modal photoacoustic tomography, optical coherence tomography (OCT) and OCT angiography system with an articulated probe for *in vivo* human skin structure and vasculature imaging. *Biomed Optic Express*. (2016) 7(9):3390. doi:10.1364/BOE.7.003390
154. Zabihian B, Chen Z, Rank E, Sinz C, Bonesi M, Sattmann H, et al. Comprehensive vascular imaging using optical coherence tomography-based angiography and photoacoustic tomography. *J Biomed Optic*. (2016) 21(9):96011. doi:10.1117/1.JBO.21.9.096011
155. LiuChen W, Chen Z, Yang S, Xing D. Optical biopsy approach to basal cell carcinoma and melanoma based on all-optically integrated photoacoustic and optical coherence tomography. *Opt Lett*. (2017) 42(11):2145. doi:10.1364/OL.42.002145
156. Kratkiewicz K, Manwar R, Rajabi-Estarabadi A, Fakhoury J, Meiliute J, Daveluy S, et al. Photoacoustic/ultrasound/optical coherence tomography evaluation of melanoma lesion and healthy skin in a swine model. *Sensors*. (2019) 19(12):2815. doi:10.3390/s19122815
157. Chen Z, Rank E, Meiburger KM, Sinz C. Non-invasive multimodal optical coherence and photoacoustic tomography for human skin imaging (2017). Scientific Reports. Available from: https://www-nature-com.proxy.lib.uwaterloo.ca/articles/s41598-017-18331-9 (Accessed October 03, 2020).
158. Yang Y, Li X, Wang T, Kumavor PD, Aguirre A, Shung KK, et al. Integrated optical coherence tomography, ultrasound and photoacoustic imaging for ovarian tissue characterization. *Biomed Optic Express*. (2011) 2(9):2551–61. doi:10.1364/BOE.2.002551
159. ZhuLi L, Duan C, Xie H, Jiang H. Miniature probe combining optical-resolution photoacoustic microscopy and optical coherence tomography for *in vivo* microcirculation study. *Appl Optic*. (2013) 52(9):1928–31. doi:10.1364/AO.52.001928
160. Dai X, Xi L, Duan C, Yang H, Xie H, Jiang H. Miniature probe integrating optical-resolution photoacoustic microscopy, optical coherence tomography, and ultrasound imaging: proof-of-concept. *Opt Lett*. (2015) 40(12):2921. doi:10.1364/OL.40.002921

161. Mathews SJ, Little C, Loderc CD, Rakhitc RD, Xia W, Zhang EZ, et al. All-optical dual photoacoustic and optical coherence tomography intravascular probe. *Photoacoustics*. (2018) 11:65–70. doi:10.1016/j.pacs.2018.07.002
162. DesjardinsLittle L, Chen LK, Hosseinaee Z, Bizheva K. “*In-vivo*, non-contact, cellular resolution imaging of the human cornea with line-field SD-OCT at 2.5 kHz frame rate (conference presentation),” in optical coherence tomography and coherence domain optical methods in biomedicine XXIV. *Mar*. (2020) 11228:112280J. doi:10.1117/12.2547884
163. Kawana K, Yasuno Y, Yatagai T, Oshika T. High-speed, swept-source optical coherence tomography: a 3-dimensional view of anterior chamber angle recession. *Acta Ophthalmol Scand*. (2007) 85(6):684–5. doi:10.1111/j.1600-0420.2006.00836.x
164. Auksorius E, Borycki D, Stremplewski P, Liżewski K, Niedźwiedziuk P, Tomczewski BL, et al. *In vivo* imaging of the human cornea with high-speed and high-resolution Fourier-domain full-field optical coherence tomography. *Biomed Optic Express*. (2020) 11(5):2849–65. doi:10.1364/BOE.393801
165. WojtkowskiBorycki W, Liu M, Kumar A, Kamali T, Unterhuber A, Leitgeb RA. Optical coherence tomography today: speed, contrast, and multimodality. *J Biomed Optic*. (2014) 19(7):071412. doi:10.1117/1.JBO.19.7.071412
166. Held G, Preisser S, Akarçay HG, Peeters S, Frenz M, Jaeger M. Effect of irradiation distance on image contrast in epi-optoacoustic imaging of human volunteers. *Biomed Optic Express*. (2014) 5(11):3765–80. doi:10.1364/BOE.5.003765
167. Haisch C, Eilert-Zell K, Vogel MM, Menzenbach P, Niessner R. Combined optoacoustic/ultrasound system for tomographic absorption measurements: possibilities and limitations. *Anal Bioanal Chem*. (2010) 397(4):1503–10. doi:10.1007/s00216-010-3685-9
168. Sangha GS, Hale NJ, Goergen CJ. Adjustable photoacoustic tomography probe improves light delivery and image quality. *Photoacoustics*. (2018) 12:6–13. doi:10.1016/j.pacs.2018.08.002
169. Sowers T, Yoon H, Emelianov S. Investigation of light delivery geometries for photoacoustic applications using Monte Carlo simulations with multiple wavelengths, tissue types, and species characteristics (2020). Available at: https://www-spiedigitallibrary-org.proxy.lib.uwaterloo.ca/journals/journal-of-biomedical-optics/volume-25/issue-01/016005/Investigation-of-light-delivery-geometries-for-photoacoustic-applications-using-Monte/10.1117/1.JBO.25.1.016005.full?SSO=1 (Accessed November 23, 2020).
170. Daoudi K, Berg PJ, Rabot O, Kohl A, Tisserand S, Brands P, et al. Handheld probe integrating laser diode and ultrasound transducer array for ultrasound/photoacoustic dual modality imaging. *Optic Express*. (2014) 22(21):26365–74. doi:10.1364/OE.22.026365
171. Steenbergenvan den Berg L, Yang M, Jiang Y, Li C. Optical fluence compensation for handheld photoacoustic probe: an *in vivo* human study case. *J Innov Opt Health Sci*. (2017) 10(04):1740002. doi:10.1142/S1793545817400028
172. Zhou Y, Liang J, Wang LV. Cuffing-based photoacoustic flowmetry in humans in the optical diffusive regime. *J Biophot*. (2016) 9(3):208–12. doi:10.1002/jbio.201500181
173. Zhang X, Wu X, Adelegan OJ, Yamaner FY, Oralkan Ö. Backward-mode photoacoustic imaging using illumination through a CMUT with improved transparency. *IEEE Trans Ultrason Ferroelectrics Freq Contr*. (2018) 65(1):85–94. doi:10.1109/TUFFC.2017.2774283
174. Laufer J, Zhang E, Raivich G, Beard P. Three-dimensional noninvasive imaging of the vasculature in the mouse brain using a high resolution photoacoustic scanner. *Appl Optic*. (2009) 48(10):D299–306. doi:10.1364/AO.48.00D299
175. Uliana JH, Sampaio DRT, Fernandes GSP, Brassesco MS, Nogueira-Barbosa MHN, Carneiro AAO, et al. Multiangle long-Axis lateral illumination photoacoustic imaging using linear array transducer. *Sensors*. (2020) 20(14):4052. doi:10.3390/s20144052
176. Jeon S, Song HB, Kim J, Lee BJ, Managuli R, Kim JH, et al. *In vivo* photoacoustic imaging of anterior ocular vasculature: a random sample consensus approach. *Sci Rep*. (2017) 7(1):4318. doi:10.1038/s41598-017-04334-z
177. KimSong S, Rim S, Kim Y, Lee BH. Noncontact photoacoustic imaging based on optical quadrature detection with a multiport interferometer. *Opt Lett*. (2019) 44(10):2590–3. doi:10.1364/OL.44.002590
178. Wang Y, Li C, Wang RK. Noncontact photoacoustic imaging achieved by using a low-coherence interferometer as the acoustic detector. *Opt Lett*. (2011) 36(20):3975–7. doi:10.1364/OL.36.003975
179. Wang Y, Hu Y, Peng B, Zhou H, Zhao Y, Ma Z. Complete-noncontact photoacoustic microscopy by detection of initial pressures using a 3×3 coupler-based fiber-optic interferometer. *Biomed Optic Express*. (2020) 11(1):505–16. doi:10.1364/BOE.381129
180. Hosseinaee Z, Le M, Bell K, reza PH. Towards non-contact photoacoustic imaging [Review]. *Photoacoustics*., 20 (2020) 100207. doi:10.1016/j.pacs.2020.100207
181. Dong B, Sun C, Zhang HF. Optical detection of ultrasound in photoacoustic imaging. *IEEE Trans Biomed Eng*. (2017) 64(1):4–15.doi:10.1109/TBME.2016.2605451
182. Eom J, Shin JG, Park S, Rim S, Lee BH. An all-fiber-optic combined system of noncontact photoacoustic tomography and optical coherence tomography. *Sensors*. (2016) 16(5):734. doi:10.3390/s16050734
183. Berer T, Leiss-Holzinger E, Hochreiner A, Bauer-Marschallinger J, Buchsbaum A. Multimodal noncontact photoacoustic and optical coherence tomography imaging using wavelength-division multiplexing. *J Biomed Optic*. (2015) 20(4):46013. doi:10.1117/1.JBO.20.4.046013
184. Eom J, Shin JG, Park S, Rim S, Lee BH. An all-fiber-optic combined system of noncontact photoacoustic tomography and optical coherence tomography. *Sensors*. (2016) 16(5):734. doi:10.3390/s16050734
185. Berer T, Leiss-Holzinger E, Hochreiner A, Bauer-Marschallinger J, Buchsbaum A. Multimodal noncontact photoacoustic and optical coherence tomography imaging using wavelength-division multiplexing. *J Biomed Optic*. (2015) 20(4):46013. doi:10.1117/1.JBO.20.4.046013
186. Hajireza P, Shi W, Bell K, Paproski RJ, Zemp RJ. Non-interferometric photoacoustic remote sensing microscopy. *Light Sci Appl*. (2017) 6(6):e16278. doi:10.1038/lsa.2016.278
187. Abbasi S, Bell K, Haji Reza P. Rapid high-resolution mosaic acquisition for photoacoustic remote sensing. *Sensors*. (2020) 20(4):1027. doi:10.3390/s20041027
188. Reza PH, Bell K, Shi W, Shapiro J, Zemp RJ. Deep non-contact photoacoustic initial pressure imaging. *Optica*. (2018) 5(7):814–20. doi:1364/OPTICA.5.000814
189. Abbasi S, Le K, Sonier G, Dinakaran D, Bigras B, Bell M, et al. All-optical reflection-mode microscopic histology of unstained human tissues. *Sci Rep*. (2019) 9(1):13392–11. doi:10.1038/s41598-019-49849-9
190. Hosseinaee Z, Khalili L, Simmons JAT, Bell K, Reza PH. Label-free, non-contact, in-vivo ophthalmic imaging using photoacoustic remote sensing microscopy. *Opt Lett* (2020) 45:6254–57.
191. Martell MT, Haven NJM, Zemp RJ. Multimodal imaging with spectral-domain optical coherence tomography and photoacoustic remote sensing microscopy. *Opt Lett*. (2020) 45(17):4859–62. doi:10.1364/OL.398940

**Conflict of Interest:** Author PHR has financial interests in illumiSonics Inc. IllumiSonics partially supported this work.

The remaining authors declare that the research was conducted in the absence of any commercial or financial relationships that could be construed as a potential conflict of interest.

frontiers
in Physics

ORIGINAL RESEARCH
published: 19 January 2021
doi: 10.3389/fphy.2020.613342

# *In Vivo* Pulse Wave Measurement Through a Multimode Fiber Diffuse Speckle Analysis System

**Zhongshuai Teng[1], Feng Gao[1,2], Hua Xia[1], Wenliang Chen[1] and Chenxi Li[1,2]***

*[1]School of Precision Instruments and Opto-electronics Engineering, Tianjin University, Tianjin, China, [2]Tianjin Key Laboratory of Biomedical Detecting Techniques and Instruments, Tianjin, China*

Continuous monitoring of *in vivo* pulsatile blood flow and pulse wave velocity (PWV) is important for clinical applications. These parameters are correlated with physiological parameters, such as blood pressure and elasticity of blood vessels. A multimode fiber diffuse speckle contrast analysis (MMF-DSCA) system was developed for fast measurement of *in vivo* pulsatile blood flow and pulse wave velocity. With MMF and CCD sensor, the diffuse speckle could be captured and processed with higher temporal resolution of 3 ms. We also induced for the first time an MMF-DSCA for evaluation of PWV, which allows estimation of the blood pressure continuously. To validate its performance, both phantom and *in vivo* experiments were conducted. The results demonstrate that MMF-DSCA could achieve fast pulsatile blood flow measurement with detailed information of the pulse wave profile and velocity. Taking the advantages of being simple and cost-effective, the flexible system can be easily adapted for continuous monitoring of vital biosigns, such as heart rate, pulse wave, and blood pressure.

**Keywords: pulse wave velocity, blood flow, multimode optical fibers, blood pressure, diffuse speckle**

OPEN ACCESS

***Edited by:***
*Chao Tian,*
*University of Science and Technology of China, China*

***Reviewed by:***
*Peng Li,*
*Zhejiang University, China*
*Cheng Wang,*
*University of Shanghai for Science and Technology, China*

****Correspondence:***
*Chenxi Li*
*lichenxi@tju.edu.cn*

***Specialty section:***
*This article was submitted to Medical Physics and Imaging, a section of the journal Frontiers in Physics*

***Received:*** *02 October 2020*
***Accepted:*** *09 December 2020*
***Published:*** *19 January 2021*

***Citation:***
*Teng Z, Gao F, Xia H, Chen W and Li C (2021) In Vivo Pulse Wave Measurement Through a Multimode Fiber Diffuse Speckle Analysis System. Front. Phys. 8:613342. doi: 10.3389/fphy.2020.613342*

## INTRODUCTION

Cardiopulmonary parameters, such as pulse wave velocity (PWV) and heart rate, are crucial for clinical diagnosing and daily healthcare monitoring [1]. PWV is the speed of the pulse wave generated by the heart and transfers along the arterials. It is considerably high (5–15 m/s) and carries information of cardiovascular function and vessel viability [2]. The monitoring and analysis of PWV provide a good vital biomarker to assess the status of cardiovascular system and microcirculation [3–6]. In clinic applications, PWV in the aorta has been estimated by measuring the delay in the foot of the wave between ascending aorta and femoral artery. But the intelligent instruments and skillful operators are needed to obtain reliable results. On the other hand, assessment of PWV is also important for daily healthcare monitoring, especially for infants and elderly [7].

Taking the advantages of noninvasive and real-time measurement, optical approach is an attractive way to measure *in vivo* blood perfusion, heart rate, and pulse wave. Most of the optical modalities require a coherent light source and follow the working principle of dynamic light scattering [8]. Laser speckle contrast imaging (LSCI) is a powerful tool for wide-field blood flow imaging of superficial tissue [9–11]. But the penetration depth limits its applications in deep tissue blood flow and PWV measurement. Considering the highly scattering properties of biological tissue, diffuse optical methods have been developed for blood flow index (BFI) measurement and obtaining the fast pulsatile blood flow in deep tissue. Among these methods, diffuse correlation spectroscopy (DCS) system [12–14] adopts high-sensitivity single-photon counting and correlator, which increases the hardware cost significantly with multiple channels. However, the fiber-based diffuse speckle contrast analysis (DSCA) system [15, 16] can be extended into multiple channels without significant additional cost and is still able to obtain deep tissue blood perfusion information at satisfied accuracy. Similar to LSCI, DSCA could perform with spatial processing algorithm, which will provide better temporal resolution.

Taking the advantages of flexibility and robustness, fiber-based diffuse optical methods are very popular in clinical applications of deep tissue blood flow measurement. Many systems use multimode (MM) source fiber [7, 17] to obtain the contrast information from the diffuse laser speckles and extract blood flow information. Therefore, it is also possible to use MM detection fiber combined with area array camera for diffuse pattern detection [18]. That makes the measurement rate of deep tissue blood flow the same as the frames per second (fps) of camera. Although sensing of pulsatile blood flow and heart rate has been previously demonstrated, other parameters such as PWV have not been further investigated. The previous works also indicated that PWV is highly related to the blood pressure (BP) and age [19]. Studying the properties and velocity of pulse wave of macro- and microcirculations may lead to an early diagnosis of many disorders [20].

In this paper, we presented a method for fast pulsatile blood flow and pulse wave velocity measurement in deep tissue. With the MM fiber delivering speckles pattern into the CCD sensor, the diffuse speckle contrast could be calculated spatially at each frame. The MMF-DSCA system achieves 300 Hz simultaneous measurement of pulsatile blood flow, which is further used to determine the pulse shapes and temporal delays propagation through the arterial tree. Both phantom validation and *in vivo* blood flow measurement are demonstrated. Thus, the linear regression model gives a good approximation between the BP and PWV. It is demonstrated that MMF-DSCA is one of the fastest noninvasive methods for deep tissue blood flow and pulse wave measurement. Taking the advantages of being simple and cost-effective, MMF-DSCA system can be easily adapted for clinical applications, such as continuous monitoring of heart rate, pulse wave, and blood pressure.

## MATERIALS AND METHODS

### Theoretical Background

From theoretical analysis, DCS and LSCI probe different aspects of the field autocorrelation curve, which shows how fast the optical signal loses its self-similarity [21]. The decay rate of this curve is a good indicator of flow speed. From DCS measurements, it is necessary to extract the speed by calculating the electric field temporal autocorrelation function $G_1(r,\tau)$ [22], as follows:

$$G_1(r,\tau) = \frac{3\mu'_s}{4\pi}\left(\frac{e^{-k(\tau)r_1}}{r_1} - \frac{e^{-k(\tau)r_2}}{r_2}\right) \tag{1}$$

$$k(\tau) = \sqrt{3\mu_a\mu'_s + \alpha\mu'_s k_0^2\langle\Delta r^2(\tau)\rangle} \tag{2}$$

$$r_1 = \sqrt{\rho^2 + \left(\frac{1}{\mu'_s}\right)^2} \tag{3}$$

$$r_2 = \sqrt{\rho^2 + \left(\frac{1}{\mu'_s} + \frac{4}{3\mu'_s}\frac{1+R_{eff}}{1-R_{eff}}\right)^2} \tag{4}$$

where $\rho$ is the distance between the source fiber and the detector fiber, $\mu_a$ is the absorption coefficient of the tissue, and $\mu'_s$ is the reduced scattering coefficient of the tissue. $R_{eff} = -1.440n^{-2} + 0.710n^{-1} + 0.668 + 0.00636n$ represents the effective reflection coefficient of the medium and the $n$ is refractive index of tissue relative to air, $k_0 = 2\pi/\lambda$ is the wavenumber of light in the medium, $\lambda$ is wavelength of the incident light, $\alpha$ is the fraction of dynamic photon scattering events in the medium, and $\langle\Delta r^2(\tau)\rangle$ is the mean square displacement of the moving scatterers in a delay time of $\tau$. Brown model approximation is used in analysis and research; it defines $\langle\Delta r^2(\tau)\rangle = 6D_B\tau$, where $D_B$ is the effective diffuse coefficient [23].

When a coherent light illuminates the blood perfused tissue, the speckle pattern is decorrelated. The level of blurring is quantified by the speckle contrast value, which could be calculated by the following equation [24]:

$$K^2(T) = \frac{2\beta}{T}\int_0^T (1-\tau/T)g_1^2(\tau)d\tau \tag{5}$$

where $T$ refers to the exposure time, $\beta$ is the coherence factor determined by the ratio of detector pixel size to speckle size, and $g_1(\tau) = G_1(r,\tau)/G_1(r,0)$ is the normalized electric field temporal autocorrelation function. In practice, $K = \sigma/I$, where $\sigma$ and $I$ are the standard deviation and the mean value of speckle pattern, respectively.

Previous work established the fact that both speckle contrast and intensity autocorrelation carried information about the blood flow. Under certain conditions, the recovery of blood flow using both speckle contrast and field/intensity autocorrelation is equivalent. The contrast has the maximal sensitivity if the exposure time is of the order of the correlation time. And there is a linear correlation [25] between $1/K^2$ and BFI.

When the MMF is used, photons from the source fiber experience multiple scattering. The diffuser photons that reach the detector fiber will carry the information of blood flow in deep tissue. Because the speckle pattern output by an MMF is not ideal, it is necessary to correct the raw speckle pattern. In each measurement, we average 3,000 images and normalize them to the maximum intensity as the background intensity $I_M$ (x,y). The raw speckle pattern $I_o$ (x,y) will be divided by $I_M$ (x,y) to obtain the corrected result I (x,y), which is used for spatial speckle contrast calculation [18].

### Pulse Wave Analysis

With MMF-DSCA system, BFI can be calculated spatially from each frame captured by the CCD camera. That makes the sampling rate much faster than DCS systems. The pulsatile changes of BFI are related to the pulse wave, which is an

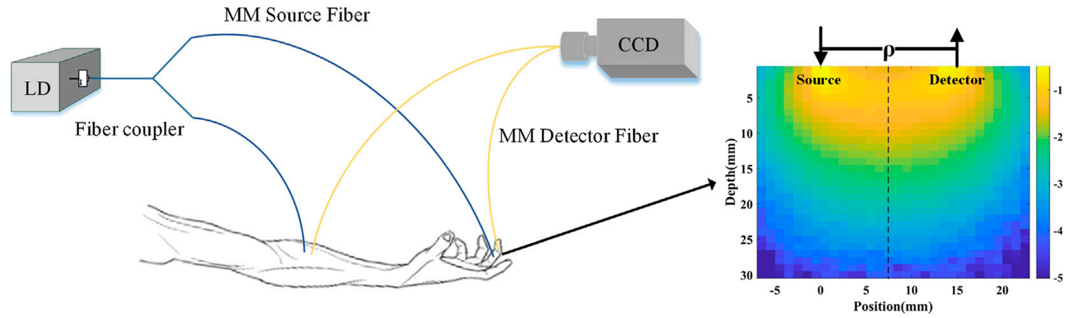

**FIGURE 1 |** Structure diagram of the MMF-DSCA system.

indicator of cardiovascular status. The frequency spectrum of pulse wave provides additional information about the speed transverse to the beam axis, and this initial result merits a more detailed investigation. In this study, the frequency characteristic was analyzed and extracted by the Fourier transform, as

$$P(f) = \frac{1}{N}\left|\sum_{n=0}^{N-1} x_n e^{-2\pi jnf}\right|^2 \tag{6}$$

where f represents the frequency of signal, N is the length of signal, and $x_n$ is the signal amplitude.

The diastolic time is an important parameter that is highly related to the systolic blood pressure (SBP) and diastolic blood pressure (DBP). To determine the diastolic time, the first-order derivative algorithm was applied to the time-domain pulse waveform to obtain the characteristic points within one cycle. Then, linear regression analysis was performed between the diastolic time and BP.

As the pulse wave propagates through the arterial tree from the heart to the periphery, pulse wave velocity could be estimated by recording the pressure wave transition time (PTT) between two selected areas in the arterial tree. In this study, we choose the forearm and fingertip as the measuring locations. Considering time-varying BFI signal obtained at adjacent locations in forearm (*F1*) and fingertip (*F2*), when the pulse wave travels from *F1* to *F2*, the BFI feature keeps constant in the stream, resulting in the time series of $F1_B(t)$ and $F2_B(t)$ appearing in nearly identical shapes with a time lag of $\tau$. Then, the cross-correlation function is used to determine the time delay between two time-varying dynamic speckle signals, as follows:

$$r_{xy}(k) = \frac{\sum_{t=1-k}^{N-k}\left(F1_B(t) - \overline{F1_B(t)}\right)\left(F2_B(t+k) - \overline{F2_B(t)}\right)}{\sqrt{\sum_{t=1-k}^{N-k}\left(F1_B(t) - \overline{F1_B(t)}\right)^2 \sum_{t=1-k}^{N-k}\left(F2_B(t) - \overline{F2_B(t)}\right)^2}} \tag{7}$$

$$\mathrm{PTT} = \max_k\left[r_{xy}(k)\right] \tag{8}$$

where $r_{xy}$ represents the correlation coefficient, k is the time difference of two signals, N is the maximum time difference, and the $\overline{F1_B(t)}$, $\overline{F2_B(t)}$ are mean value of amplitudes of two signals, respectively. The average PWV can be evaluated with the following equation [26]:

$$\mathrm{PWV} = \mathrm{L}/\mathrm{PTT} \tag{9}$$

where *L* is the arterial length between two selected areas.

## Experimental Setup

The setup of MMF-DSCA system is shown in **Figure 1**. A long coherence length (>10 m) laser diode (785 nm, 15 mW, LP785-SAV50, Thorlabs, United States) was used to illuminate the sample. In order to achieve synchronization, a 50:50 1 × 2 fiber coupler was used to split the light into two identical MMFs (d = 200 μm, NA = 0.22). For *in vivo* measurement, the first fiber was attached to the subject's forearm, near the brachial artery, while the second fiber was attached to the subject's fingertip. Two multimode fibers were used as detector fibers with the other ends touching onto the CCD directly. The distance of source-detector fiber can be adjusted in the range of 5–20 mm. To avoid the need to synchronize two cameras, the diffuse speckle pattern of both fibers was collected by a single CCD camera (Basler aca1920–155um, Germany). The magnification was adjusted to make sure the speckle patterns from the two fibers are projected without overlapping and meet the requirement of diffuse speckle sampling.

For speckle analysis, both the spatial resolution and exposure time are important for the sensitivity and dynamic range of flow measurement. In the MMF-DSCA system, the multimode fibers with core diameter of 200 um were used to collect the diffuse speckle of *in vivo* tissue, resulting in the spatial resolution of 0.2 mm. The size of a single speckle is about 11 μm, which is twice the size of a single pixel size of 5.6 μm. That satisfies the Nyquist sampling criterion and maximizes the contrast of the imaged speckle pattern. However, each MMF speckle pattern contains more than 1,000 speckles, which provides a sufficient statistical sample to analyze the spatial speckle contrast. The exposure time is also important for the sensitivity and SNR of blood flow measurement. Dunn's results suggested that any exposure time greater than 2 ms will provide optimal sensitivity to blood flow changes [27]. However, the exposure time should also meet the requirement of monitoring the pulsatile blood flow. Considering

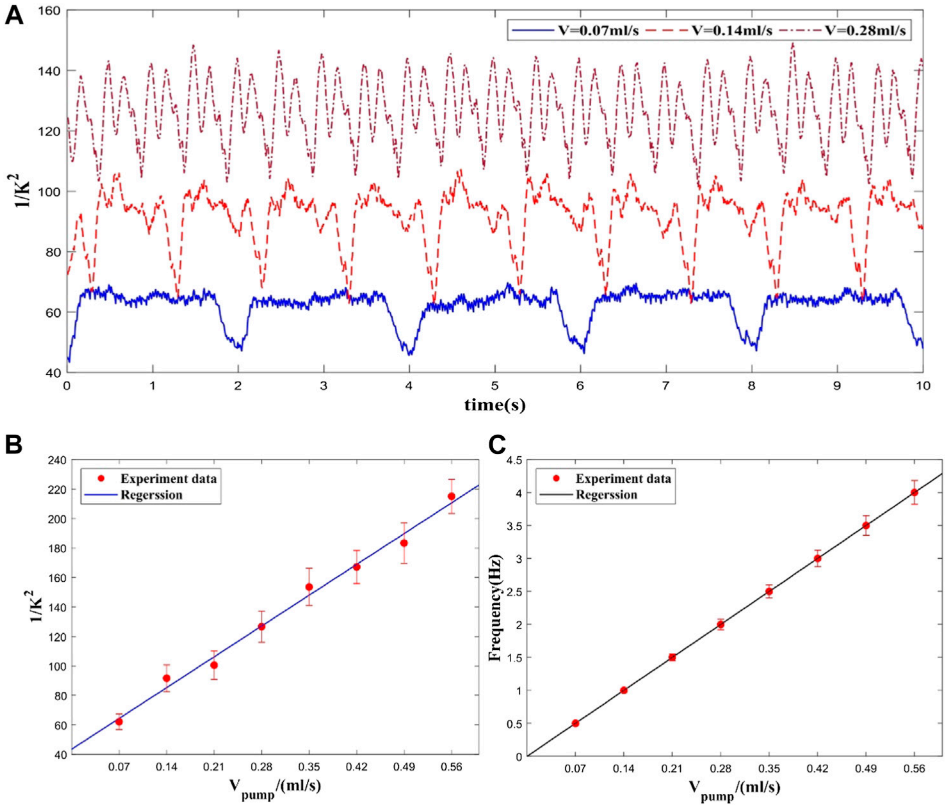

**FIGURE 2 |** Experimental results at different flow rates. **(A)** Flow rate waveform at different pumping rates (only three velocities), **(B)** Averaged flow measurement at each flow rate. **(C)** Frequencies of flow rate waveforms at each flow rate.

temporal resolution for pulse wave monitoring, we set the exposure time to be 3 ms.

In this paper, the diffuse speckle contrast was calculated spatially from each frame, resulting in that the temporal resolution for blood flow measurement is approximately 3.3 ms. The corresponding cross-correlation is calculated with **Eq. 7**, which has the same temporal resolution of 3.3 ms. According to the distance between two locations and the speed of PWV, the time delay of pulse waves is generally over 30 ms. It is demonstrated that the MMF-DSCA system has a sufficiently high temporal resolution for PWV measurement.

Most of the arteries are in the subcutaneous layer with depth varying from 2 to 10 mm below the surface. According to the theory of diffuse optics, the effective detection depth is around a half of source-detector separation. Since source-detector separation is 15 mm with *in vivo* measurement, the diffuse speckle signal is mainly from the depth range around 7.5 mm. The penetration depth is also demonstrated with Monte Carlo simulations and phantom experiments. The cloud map of the light intensity with Monte Carlo simulation is shown in **Figure 1**. The simulation results indicated that the penetration depth of diffuse light collected by the detection fibers is in the range of 5–12 mm. Based on the distribution of photon number and penetration depth, the average penetration depth is further calculated to be 7 mm, which agrees with the theory of diffuse optics. The depth of MMF-DSCA measurement is also validated by the phantom experiments.

## Phantom Experiments

To verify the performance of the system in deep tissue flow measurement, a phantom experiment was designed with a hollow plastic tube that was embedded inside a solid scattering phantom body ($\mu_a = 0.01\ \text{mm}^{-1}$, $\mu_s = 0.4\ \text{mm}^{-1}$). The tube was buried 5 mm underneath the phantom surface. Liquid with the similar scattering coefficient as blood was pumped through the tube by a peristaltic pump. Since the liquid was pumped by pinching the rubber tube through the rotating rollers of the peristaltic pump, a higher flow rate could be achieved by increasing the pinching frequency. During the experiment, the pumping rate was set from 0 to 0.56 ml/s with step size of 0.07 ml/s.

## *In Vivo* Measurements

For *in vivo* measurements, the subjects were requested to sit on a chair and keep still during the experiments. The experiments were carried out on 10 healthy volunteers (including seven males and three females) aged 24–26. To evaluate the relationship between PWV and BP, the experiments were performed on five individuals during the recovery period after the stair climbing exercise, and the interval of each measurement was

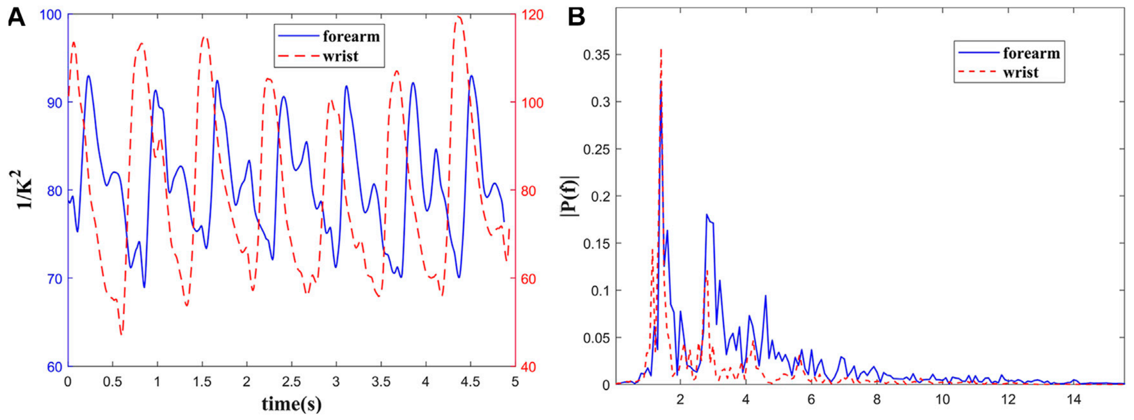

**FIGURE 3 |** Blood flow measurement of a healthy subject's **(A)** forearm and wrist; **(B)** the power spectrum of pulse wave.

10 min (5 times in total). The blood pressure was also measured by a commercial BP monitor.

# RESULTS AND DISCUSSION

## Phantom Result

As shown in **Figure 2**, the phantom results demonstrate the good correlation between the flow rate and $1/K^2$. Since the system provided a sampling rate at 300 Hz, the flow waveforms at each pumping period could be resolved clearly, as shown in **Figure 2A**. A good linear relationship between the pumping rate and the averaged BFI can be observed in **Figure 2B**. Because the MMF-DSCA system provides high temporal resolution, the periodical changes of the flow inside the phantom could be resolved clearly. Therefore, the roller pinching frequency can be calculated from the peak-to-peak time interval of the flow waveform. **Figure 2C** demonstrates a very good linear relationship between the flow rate and the measured pinching frequency.

## *In Vivo* Result

### Pulse Wave Measurement

The *in vivo* BFI measured with MMF-DSCA system are shown in **Figure 3A**. The temporal blood flow profile is in good agreement with previous research [28]. The pulse waveform in the forearm has more features within each cycle. Compared with the standard pulse waveform, the two obvious peaks are related to the main wave and the repulse wave. However, the pulse waveform from the wrist has sharper peaks and smoother repulse wave.

To quantify this difference, the time-domain pulse wave signals were Fourier transformed as shown in **Figure 3B**. The power spectra of the pulse waves demonstrate that the energy in higher frequency of pulse wave on forearm is greater than wrist, which is consistent with temporal profile. Meanwhile, the energy of both pulse waves is concentrated in the range of 0.5–10 Hz. The peaks in 1.4, 2.8, and 4.2 Hz are related to the heartbeat rate and its higher harmonic frequencies. It can be concluded that the frequency spectrum distribution of pulse waves in different parts of the human body is relatively consistent.

Compared with forearm, the radial artery at the wrist is shallower and far from heart. That makes its ascending branch steeper. As shown in **Figure 3**, the position and amplitude of the repulse wave descend, and the sharp corners of the waveform are smoother. The time-domain and frequency-domain characteristics of the pulse waves measured with our system also agree with the pulse theory [29].

### Correlation Between Blood Pressure and Pulse Wave

In order to analyze the features of the pulse wave in more detail, the individual waveforms of one heart beat were averaged during a period of five adjacent pulse cycles. After baseline correction and noise reduction, the division of temporal pulse wave characteristics is shown as **Figure 4A**. With systolic peak, dicrotic notch, and diastolic runoff, the well-known characteristics for arterial pulsation behavior could be observed clearly. The waveform of the directed movement shows three peaks located at 0.93 ms, 1.08 ms, and 1.15 ms and relative heights of 87.25, 83.30, and 84.31, respectively. Among them, the first peak (P1) represents maximum vascular pressure and there is a shoulder compared to a second peak (P2) and is followed by a shallower third peak (P3). The diastolic time could be calculated with first-order differential algorithm and selected to validate the correlation between the temporal characteristic and BP.

The linear relationship between the diastolic time and BP (SBP and DBP) is shown in **Figure 4B**. Because the diastolic period occupies most of the time in a cardiac cycle, the amount of blood transported by the large artery to the periphery may decrease with the reduction of diastolic time. As a result, the vascular part is filled with blood and induces a much higher pressure. These results were measured during the resting period on seven volunteers. Diastolic times (t) and BP measured with different volunteers all passed the $t$ test with significant $p < 0.05$. The result demonstrates that the diastolic time could be preliminarily used for BP prediction.

To test the reliability and consistency of this approach, the *in vivo* experiments were conducted with seven healthy subjects. Every subject was tested more than 10 times. The statistical parameters, such as the average value and standard deviation,

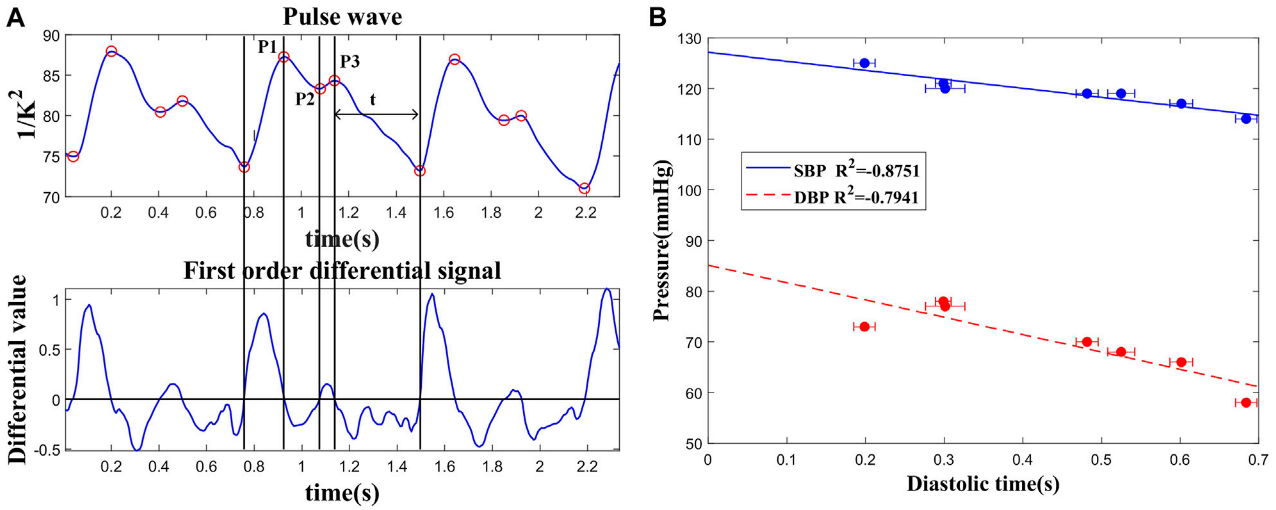

**FIGURE 4 | (A)** Recognition of characteristic points of pulse wave and division of time periods. **(B)** Correlation of the diastolic time and blood pressure.

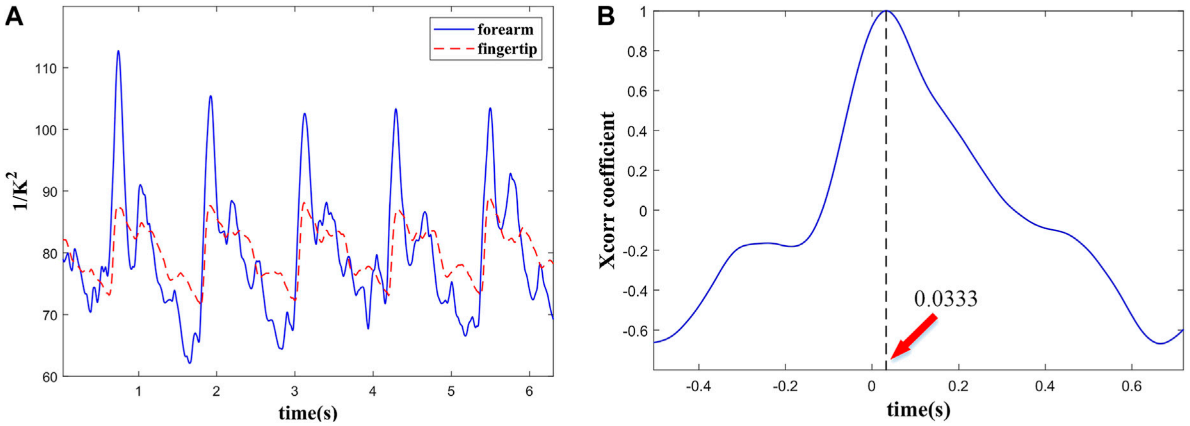

**FIGURE 5 | (A)** Simultaneous recording of pulse wave from the forearm and the fingertip and **(B)** PTT between them.

were calculated with each subject's results. As shown in **Figure 4**, the diastolic time varied in the range of 5% with stable PWV measurement.

## Correlation Between Blood Pressure and Pulse Wave Velocity

To obtain the PWV, the pulse waves of forearm and fingertip were measured simultaneously. As shown in **Figure 5**, in addition to the different pulse shape, the pulse wave of fingertip is slightly delayed to forearm. The time delay between two locations is caused by the pressure wave propagation along the artery tree. At the cardiac frequency, the mean delay time is about 33.34 ms. Accordingly, the length of the arterial tree pass between the measured spots was about 34.50 cm. Based on **Eq. 9**, the PWV is about 10.36 m/s. Given the PWV determined in the human vascular system, as well as the theory of pulse propagation, our results seem realistic.

To determine the relationship between BP and PWV, the experiments were performed on five subjects. During exercise, the cardiac output and blood velocities are both increasing. That may cause additional flow resistance and consequent raise of blood pressure. The experimental results were approximated and validated by linear regression and presented in **Figure 6**. The coefficient of determination values between the SBP and PWV is in the range of 0.88–0.95. Thus, the linear regression model gives a good approximation between BP and PWV. However, SBP is highly related to the blood vessel elasticity, because it is caused by the heart's active and instantaneous pumping of blood. A rise in SBP causes temporary stiffening of the vessels, which results in a higher PWV. Meanwhile, DBP, which is related to the diastolic time and vascular recovery period, is not sensitive to changes in blood vessel elasticity. As a result, linear approximation of the relation between DBP and PWV shows lower level of correlation.

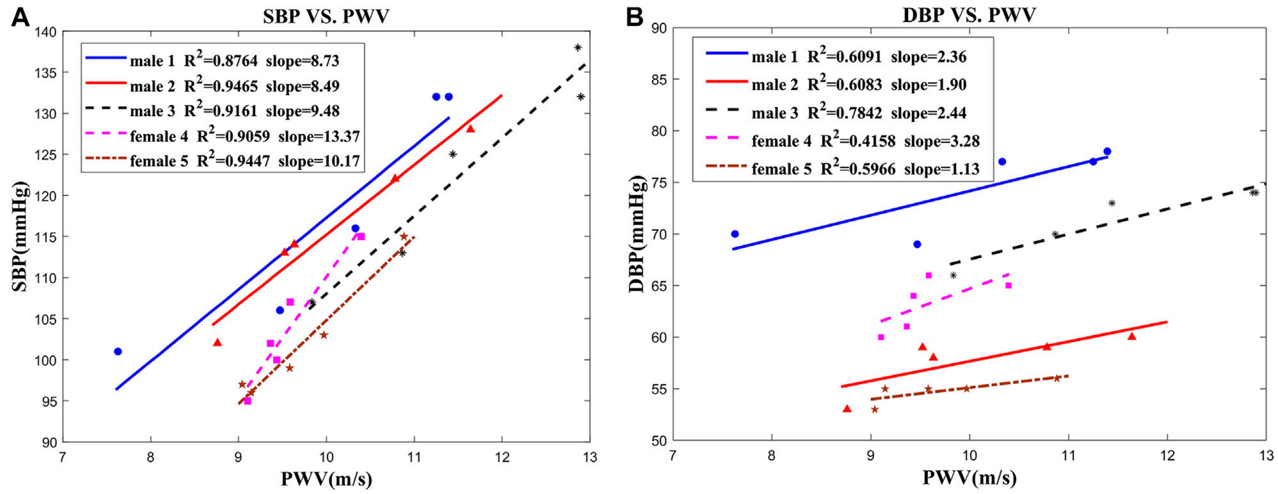

**FIGURE 6 |** Correlation between blood pressure and PWV in five subjects: **(A)** SBP vs. PWV; **(B)** DBP vs. PWV.

These results demonstrated that MMF-DSCA system achieved fast pulsatile blood flow measurement and extraction of the PWV and BP. However, this system and method also have some disadvantages. The fiber probe needs to be fixed on the location, and the measurement may be influenced by the motion artifacts. In clinical applications, the artifacts can be eliminated with improvements of fiber probe design and signal process. The fiber probe should be carefully designed and combined with special cuffs to fix the probe more stably on the arm and fingertip. Because the motion artifacts are generally embodied as DC or low-frequency signals, high-pass filtering can be used to eliminate the artifacts. Therefore, modern signal process methods, such as wavelet and empirical transverse decomposition filtering method, should also be used for further processing. Furthermore, with multiwavelength light sources, this system could be extended to measure oxygen saturation.

## CONCLUSION

We present an MMF-DSCA system for measuring instantaneous blood flow and pulse wave velocity in deep tissue. With a CCD sensor, the diffuse speckle could be captured and processed at each frame. This approach enabled the observation of PWV in deep tissue with a temporal resolution of 3 ms. Optical synchronization of the speckle patterns measured in different body parts was achieved by using 2 MM fibers and a single CCD camera. The simultaneous measurement of pulsatile blood flow in different parts could be further analyzed to obtain the pulse wave characteristics. In this work, we also induced for the first time MMF-DSCA system for evaluation of PWV, which allows estimation of the systolic blood pressure. Taking advantages of being simple and cost-effective, the flexible system will be further developed for continuous monitoring of vital biosigns, such as heart rate and blood pressure, as part of individual healthcare.

## DATA AVAILABILITY STATEMENT

The original contributions presented in the study are included in the article/Supplementary Material, further inquiries can be directed to the corresponding author.

## ETHICS STATEMENT

Ethical review and approval was not required for the study on human participants in accordance with the local legislation and institutional requirements. The patients/participants provided their written informed consent to participate in this study.

## AUTHOR CONTRIBUTIONS

CL was responsible for conceptualization, project administration, and funding acquisition. ZT was responsible for methodology, software, validation, formal analysis, investigation, data curation, and writing—original draft preparation. WC was responsible for resources and visualization. HX was responsible for writing—review and editing. FG was responsible for supervision. All authors have read and agreed to the published version of the manuscript.

## ACKNOWLEDGMENTS

The authors thank every volunteer who offered help with the experiments. The authors acknowledge the financial support provided by the National Natural Science Foundation of China (81871396, 81971657, 81871393, and 81671727) and Tianjin Natural Science Foundation (19JCYBJC29100 and 19JCTPJC42200).

## REFERENCES

1. Hoilett SO, Twibell AM, Rohit S, Linnes CJ. Kick ll: a smartwatch for monitoring respiration and heart rate using photoplethysmography. In: 2018 40th Annual international conference of the IEEE engineering in medicine and biology society; 2018 July 18–21; Honolulu, HI. Hawaii: IEEE (2018). p. 3821–3824. doi:10.1109/EMBC.2018.8513356
2. Townsend RR, Wimmer NJ, Chirinos JA, Parsa A, Weir M, Perumal K, et al. Aortic PWV in chronic kidney disease: a CRIC ancillary study. *Am J Hypertens* (2010) 23(3):282–9. doi:10.1038/ajh.2009.240
3. JoffeLash A, Morrell CH, Fegatelli DA, Fiorillo E, Delitala A, Orru' M, et al. Arterial stiffness and multiple organ damage: a longitudinal study in population. *Aging Clin Exp Res* (2020) 32(5):781–8. doi:10.1007/s40520-019-01260-0
4. CuccaMarongiu XN, Gao HQ, Li BY, Cheng M, Ma YB, Zhang ZM, et al. Pulse wave velocity as a marker of arteriosclerosis and its comorbidities in Chinese patients. *Hypertens Res* (2007) 30(3):237–42. doi:10.1291/hypres.30.237
5. WangGao AY, Mohamed MS, Ibrahim S, Hun TM, Musa KI, Yusof Z. Pulse wave velocity as a marker of severity of coronary artery disease. *J Clin Hypertens* (2010) 11(1):17–21. doi:10.1111/j.1751-7176.2008.00061.x
6. Kim HL, Kim SH. Pulse wave velocity in atherosclerosis. *Front Cardiovasc Med* (2019) 6:41. doi:10.3389/fcvm.2019.00041
7. Bennett A, Beiderman Y, Agdarov S, Beiderman Y, Hendel R, Straussman B, et al. Monitoring of vital bio-signs by analysis of speckle patterns in a fabric-integrated multimode optical fiber sensor. *Optic Express* (2020) 28(14): 20830–44. doi:10.1364/OE.384423
8. Zalevsky B, Jing D, Loo PC, Kijoon L. Optical methods for blood perfusion measurement--theoretical comparison among four different modalities. *J Optic Soc Am A* (2015) 32(5):860–6. doi:10.1364/JOSAA.32.000860
9. Boas DA, Dunn AK. Laser speckle contrast imaging in biomedical optics. *J Biomed Optic* (2010) 15(1):011109. doi:10.1117/1.3285504
10. Ring LL, Strandby RB, Henriksen A, Ambrus R, Sørensen H, Gøtze JP, et al. Laser speckle contrast imaging for quantitative assessment of facial flushing during mesenteric traction syndrome in upper gastrointestinal surgery. *J Clin Monit Comput* (2019) 33(5):903–10. doi:10.1007/s10877-018-0226-0
11. AchiamSvendsen JH, Nerup N, Strandby RB, Svendsen MBS, Ambrus R, Svendsen LB, et al. Laser speckle contrast imaging and quantitative fluorescence angiography for perfusion assessment. *Langenbeck's Arch Surg* (2019) 404(4):1–11. doi:10.1007/s00423-019-01789-8
12. Buckley EM, Parthasarathy AB, Grant PE, Yodh AG, Franceschini MA. Diffuse correlation spectroscopy for measurement of cerebral blood flow: future prospects. *Neurophotonics* (2014) 1(1):011009. doi:10.1117/1.NPh.1.1.011009
13. Verdecchia K, Diop M, Lawrence KS. Investigation of the best model to characterize diffuse correlation spectroscopy measurements acquired directly on the brain. *Biomed Appl Light Scatter* (2015) Ix:9333. doi:10.1117/12.2079499
14. Kyle V, Mamadou D, Albert L, Morrison LB, Ting-Yim L, Keith SL. Assessment of a multi-layered diffuse correlation spectroscopy method for monitoring cerebral blood flow in adults. *Biomed Optic Express* (2016) 7(9): 3659–74. doi:10.1364/BOE.7.003659
15. Bi R, Dong J, Lee K. Deep tissue flowmetry based on diffuse speckle contrast analysis. *Opt Lett* (2013) 38(9):1401–3. doi:10.1364/OL.38.001401
16. Huang C, Seong M, Morgan JP, Mazdeyasna S, Kim JG, Hastings JT, et al. Low-cost compact diffuse speckle contrast flowmeter using small laser diode and bare charge-coupled-device. *J Biomed Optic* (2016) 21(8):80501. doi:10.1117/1.JBO.21.8.080501
17. Yu T, Beiderman Y, Agdarov S, Beiderman Y, Zalevsky Z. Fiber sensor for non-contact estimation of vital bio-signs. *Optic Commun* (2017) 391:63–7. doi:10.1016/j.optcom.2017.01.013
18. Bi R, Du Y, Singh G, Ho CJ, Zhang S, Attia ABE, et al. Fast pulsatile blood flow measurement in deep tissue through a multimode detection fiber. *J Biomed Optic* (2020) 25(5):1–10. doi:10.1117/1.JBO.25.5.055003
19. OlivoLi EJ, Park CG, Park JS, Suh SY, Choi CU, Kim JW, et al. Relationship between blood pressure parameters and pulse wave velocity in normotensive and hypertensive subjects: invasive study. *J Hum Hypertens* (2007) 21(2): 141–8. doi:10.1038/sj.jhh.1002120
20. OhKim L, Song Z, Wenming Y, Zibin Y. A research on characteristic information of pulse wave. *J Beijing Polytech Univ* (1996) 22(1):71–9.
21. Durduran T, Choe R, Baker BW, Yodh GA. Diffuse optics for tissue monitoring and tomography. Reports on progress in physics. *Phys Soc* (2010) 73(7):76701–43. doi:10.1088/0034-4885/73/7/076701
22. Xie JB, He XD, Zhang LM, Li J, Qin ZP, Gao F. Diffuse correlation spectroscopy towards dynamic topography of blood flow index in deep tissues: a multi-channel system and experiment validation. *Infrared Phys Technol* (2020) 107:103298. doi:10.1016/j.infrared.2020.103298
23. Boas DA, Yodh AG. Spatially varying dynamical properties of turbid media probed with diffusing temporal light correlation. *J Opt Soc Am A* (1997) 14(1): 192–215. doi:10.1364/JOSAA.14.000192
24. Bandyopadhyay R, Gittings AS, Suh SS, Dixon PK, Durian DJ. Speckle-visibility spectroscopy: a tool to study time-varying dynamics. *Rev Sci Instrum* (2005) 76(9):093110. doi:10.1063/1.2037987
25. Kim S, Kim M, Kim JG. Development of simple diffuse optical metabolic spectroscopy for tissue metabolism measurement. *Biomed Optic Express* (2019) 10(6):2956–66. doi:10.1364/BOE.10.002956
26. Ding X, Yan BP, Zhang YT, Liu J, Zhao N, Tsang HK. Pulse transit time based continuous cuffless blood pressure estimation: a new extension and A comprehensive evaluation. *Sci Rep* (2017) 7(1):11554. doi:10.1038/s41598-017-11507-3
27. Yuan S, Devor A, Boas DA, Dunn AK. Determination of optimal exposure time for imaging of blood flow changes with laser speckle contrast imaging. *Appl Optic* (2005) 44(10):1823–30. doi:10.1364/ao.44.001823
28. Michael G, Rice TB, Bruce Y, White SM, Tromberg BJ. Wearable speckle plethysmography (SPG) for characterizing microvascular flow and resistance. *Biomed Optic Express* (2018) 9(8):3937–52. doi:10.1364/BOE.9.003937
29. Jin W, Sang S, Xin C. Study on pressure pulsation and flow pulsation in pulse diagnosis. *Clin J Chin Med* (2014) 6(06):33–4 [in Chinese, with English summary]. doi:10.3969/j.issn.1674-7860.

**Conflict of Interest:** The authors declare that the research was conducted in the absence of any commercial or financial relationships that could be construed as a potential conflict of interest.

frontiers in Physics

BRIEF RESEARCH REPORT
published: 16 February 2021
doi: 10.3389/fphy.2021.637101

# Molecular Response of Skin to Micromachining by Femtosecond Laser

**Yutong Wang**[1†], **Shaoyang Wang**[2†], **Yujie Zhu**[1*], **Hui Xu**[1*] **and Hao He**[2]

[1]Department of Dermatology and Department of Laser and Aesthetic Medicine, Shanghai Ninth People's Hospital, School of Medicine, Shanghai Jiao Tong University, Shanghai, China, [2]School of Biomedical Engineering, Shanghai Jiao Tong University, Shanghai, China

Pulsed lasers at the near infrared (NIR) range have been widely used in dermatology. Ultrashort pulsed picosecond lasers are found with the specific ability of very effective activation of skin repair and remodeling along with significant photodamage. Femtosecond lasers, with a shorter pulse width, may be a promising alternative to current NIR lasers in clinic. In this study, we performed optical micromachining by a femtosecond laser at 1,030 nm to skin of live mice in two modes of scanning of focused laser and direct irradiation by unfocused laser. The acute and one-day delayed immune molecular responses of the skin to the micromachining are studied by immunofluorescence microscopy of the skin sections. Our data shows the focused laser can activate remodeling of skin without any significant immune responses. In contrast, the direct irradiation by the unfocused laser activate significant immune responses in the deep dermis with high regulation of interleukin. Those results suggest focused femtosecond laser is of good promising potential in activation of skin remodeling and repairing with little immune or physical damage.

**Keywords: femtosecond laser, micromachining, skin, immune response, clinic application**

***Edited by:***
*Chao Tian,*
*University of Science and Technology of China, China*

***Reviewed by:***
*Zhichao Fan,*
*UCONN Health, United States*
*Hong Leng,*
*Soochow University, China*
*Cheng Lei,*
*Wuhan University, China*

***Correspondence:***
*Yujie Zhu*
*zyjfd@163.com*
*Hui Xu*
*2201691904@qq.com*

*†These authors have contributed equally to this work*

***Specialty section:***
*This article was submitted to Medical Physics and Imaging, a section of the journal Frontiers in Physics*

***Received:*** *02 December 2020*
***Accepted:*** *11 January 2021*
***Published:*** *16 February 2021*

***Citation:***
*Wang Y, Wang S, Zhu Y, Xu H and He H (2021) Molecular Response of Skin to Micromachining by Femtosecond Laser. Front. Phys. 9:637101. doi: 10.3389/fphy.2021.637101*

## INTRODUCTION

Lasers have been widely used in clinical dermatology for diagnostics and therapy. In the treatment of immune and pigmented diseases of skin, micro-plastic surgery, and photo-rejuvenation, different types of lasers are selected for different therapy purposes [1–8]. The continuous-wave lasers at different wavelengths (usually at the visible range) that can be directly absorbed by the pigments and biomolecules in skin can disrupt the abnormal pigments and activate immune processes for inflammation treatment. The pulsed lasers, especially the Q-switched nanosecond lasers at the near infrared (NIR) range, can generate significant thermal effect in dermis for wound healing, regenerative medicine and photo-rejuvenation. Recently, ultrashort picosecond pulsed lasers are found with significant improvement on tattoo removal treatment of discrete pigmented lesions, rejuvenation, melasma treatment and scar revision in clinic [9–17].

Generally, the pulse width of practical picosecond lasers varies from 300 to 900 ps in clinical dermatology. Compared with the traditional nanosecond pulsed and continuous-wave lasers, the short pulse width of picosecond laser brings a series of advantages [18–20]. Specifically, the thermal deposition decreased significantly. . Briefly, focused picosecond laser pulses contribute high peak power density (over $10^{13}$ W/cm$^2$) within the focus of laser beam to produce optical breakdown via multiphoton absorption. This process generates microscopic cavitation bubbles in tissue. The bubbles expand, further generate strong mechanical shockwaves, and finally result in tissue

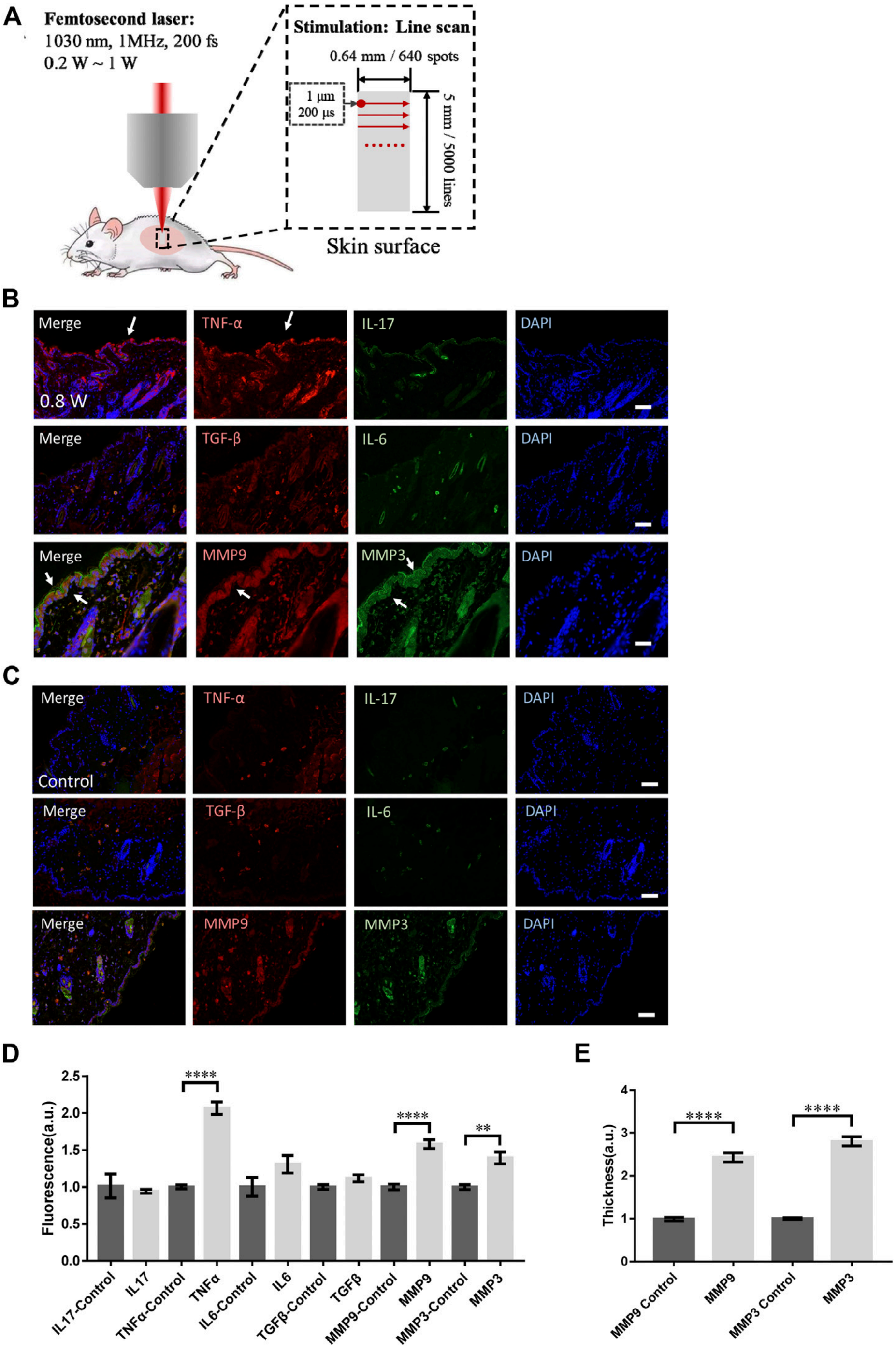

**FIGURE 1 |** Skin responses to micromachining by femtosecond laser. **(A)** The scheme of micromachining by femtosecond laser on skin of mouse. The scanning of femtosecond laser was controlled by a pair of galvo-mirror. The molecular responses to femtosecond laser micromachining of the skin tissue at 0.8 W **(B)** and control **(C)**. Arrows: the immunofluorescence of the molecules. Bar: 100 µm. **(D)** Statistic results of the fluorescence intensity in the experimental and control groups (n = 24 samples from six independent trails). **(E)** The skin thickness with positive MMP3 and MMP9 signals (n = 24 samples from six independent trails). *$p < 0.05$. **$p < 0.01$. ***$p < 0.001$. ****$p < 0.0001$, by *students' t-test*.

disruption. Notably, residual thermal damage around the micro damage areas is involved in this process. The intense photomechanical effect provides efficient removal of target pigment molecules and promotes skin rejuvenation by direct damage to collagen [9, 21]. Nevertheless, the laser pulses at 100 ps level still lead large thermal diffusion to induce off-target area mechanical damage and non-negligible thermal damage and subsequent edema, inflammation, and other complex immune processes. Currently, the clinical picosecond laser therapy has been found with postoperative complications including

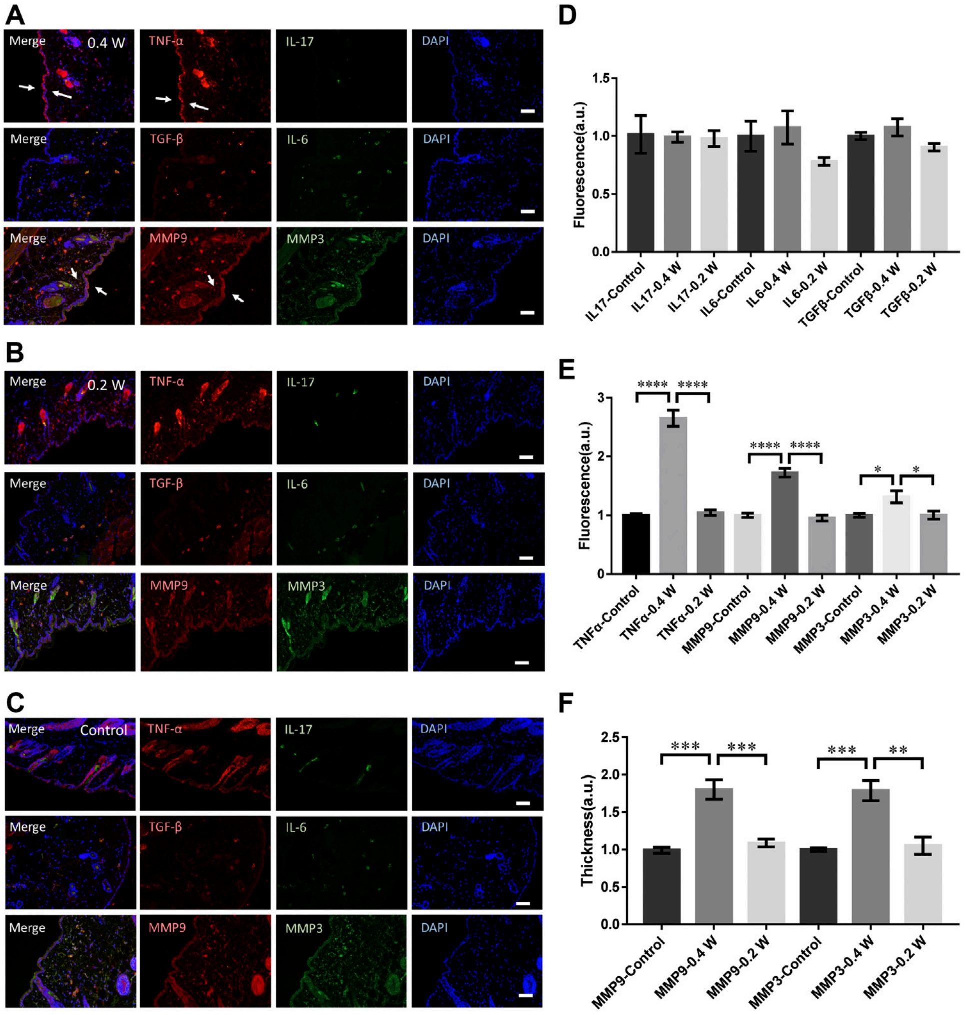

**FIGURE 2 |** Molecular responses of skin to femtosecond-laser micromachining at 0.4 W **(A)** and 0.2 W **(B)** respectively. **(C)** negative control. **(D)** Statistic results of the fluorescence intensity of IL-17, IL-6, and TGF-β in the experimental and control groups (n = 24 samples from six independent trails). Statistic results of the fluorescence intensity **(E)** and skin thickness **(F)** of TNF-α, MMP3, and MMP9 in the experimental and control groups respectively (n = 24 samples from six independent trails). Bar: 100 μm. **p* < 0.05. ***p* < 0.01. ****p* < 0.001. *****p* < 0.0001, by *students' t-test*.

erythema, post-inflammatory, hyperpigmentation and blister [9, 22, 23]. Therefore, it is promising to explore lasers with even shorter pulse width in skin micromachining.

In last decades, femtosecond laser has been applied in clinical diagnosis and treatment as a new generation laser technology. Compared to picosecond lasers, femtosecond lasers have much shorter pulse duration (tens to hundreds femtosecond) and thus totally different mechanism of acting with tissue [24, 25]. Optical ablation by femtosecond laser is easily restricted in the focused area with little thermal effect, also enabling the refractive surgery by femtosecond laser [23]. However, femtosecond laser is rarely applied in dermatology. In this study, we visualize the key immune molecular dynamics of skin to micromachining by femtosecond laser. Our data present the activation of skin immune processes and tissue remodeling, and further the molecular mechanism of skin after the laser micromachining.

# MATERIALS AND METHODS

## Femtosecond-Laser Micromachining

A femtosecond laser at 1,030 nm (pulse width: 200 fs, repetition rate: 1 MHz) was coupled into a microscope system to perform micromachining on live mice (**Figure 1A**). The laser beam was expanded to match the back aperture of the objective (×20, N.A. = 0.65) and then focused by it onto the mouse skin at around 50–100 μm deep. The laser focus was around 1 μm in diameter. The micromachining was accomplished by the scanning of the galvo-mirror that could be predefined by any region on the skin of mice. In this study, a rectangular area of 5 mm × 0.64 mm at the mouse back was scanned line by line by the laser. Each line was 0.64 mm, defined by 640 points. Each point was exposed to the laser for 200 μs. The area was finally scanned by 5,000 lines as a trial. The laser power was used at 0.2 W–1 W at the skin surface.

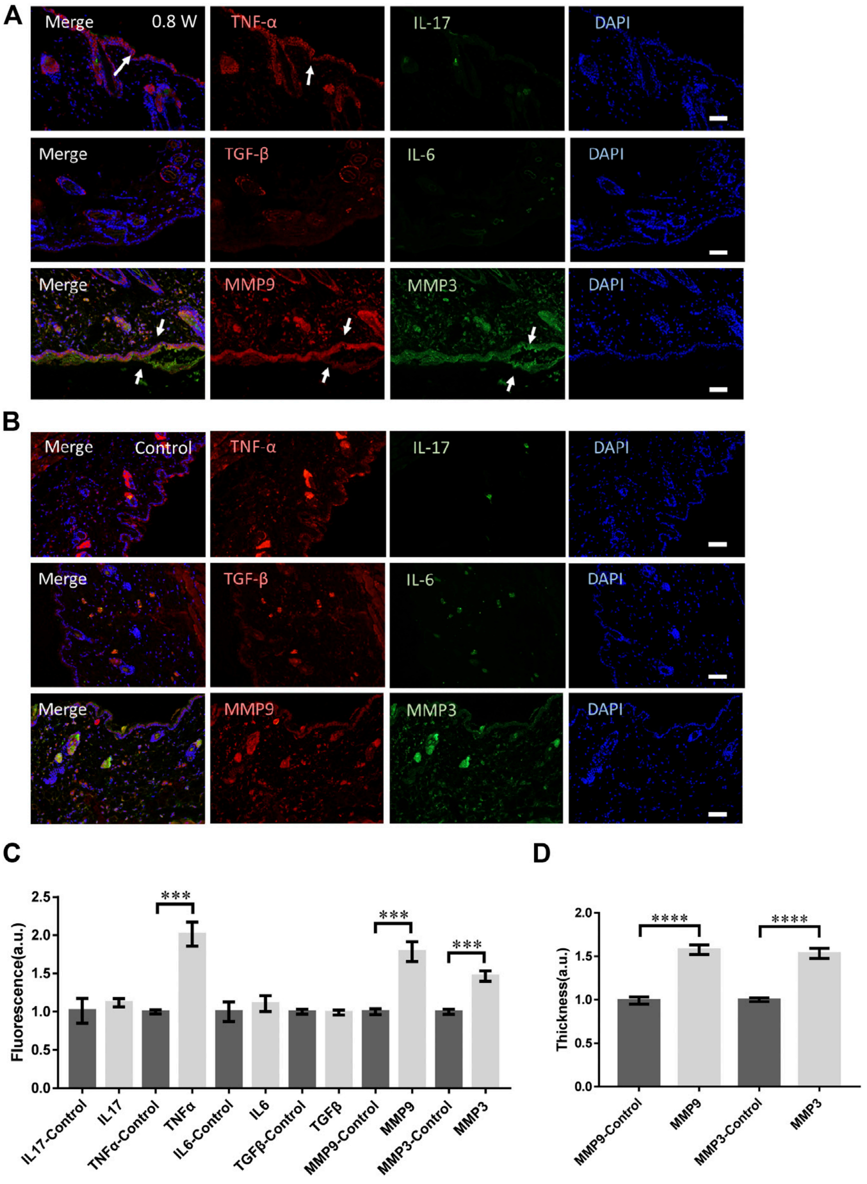

**FIGURE 3 |** The molecular responses to the laser micromachining after one-day recovery. The immunofluorescence of the skin treated at 0.8 W after one-day recovery **(A)** and the control **(B)** respectively. **(C)** The statistics of the fluorescence intensity of each molecule with immune-staining. **(D)** The skin thickness with MMP3 and MMP9 positive. n = 12 samples from four independent trails. Bar: 100 μm. *$p < 0.05$. **$p < 0.01$. ***$p < 0.001$. ****$p < 0.0001$, by *students' t-test*.

After experiments, the mice were sacrificed and the skin tissue were dissected for analysis.

## Animal Preparation and Histological Section of Skin

For *in vivo* experiments, 6- to 9-weeks-old Kunming mice were anesthetized with 4% chloral hydrate. Before experiments, the hair was removed by hair removal cream (Veet Hair Removal Cream, Reckitt Benckiser Ltd.). After the surgical level of anesthesia was reached, the skin was treated by the femtosecond laser. After that, the skin tissues were removed and fixed in 4% paraformaldehyde. All experimental procedures regarding the care and use of SD rat pups were reviewed and approved by the Animal Ethics Committee of Shanghai ninth People's Hospital and the School of Biomedical Engineering, Shanghai Jiao Tong University. All efforts were made to minimize possible pain and discomfort of the animals during the experimental procedures.

## Immunofluorescence Labeling and Microscopy

Paraffin-embedded skin biopsies were cut into 5 μm sections and placed on glass slides. Slides were placed in a 60°C oven overnight,

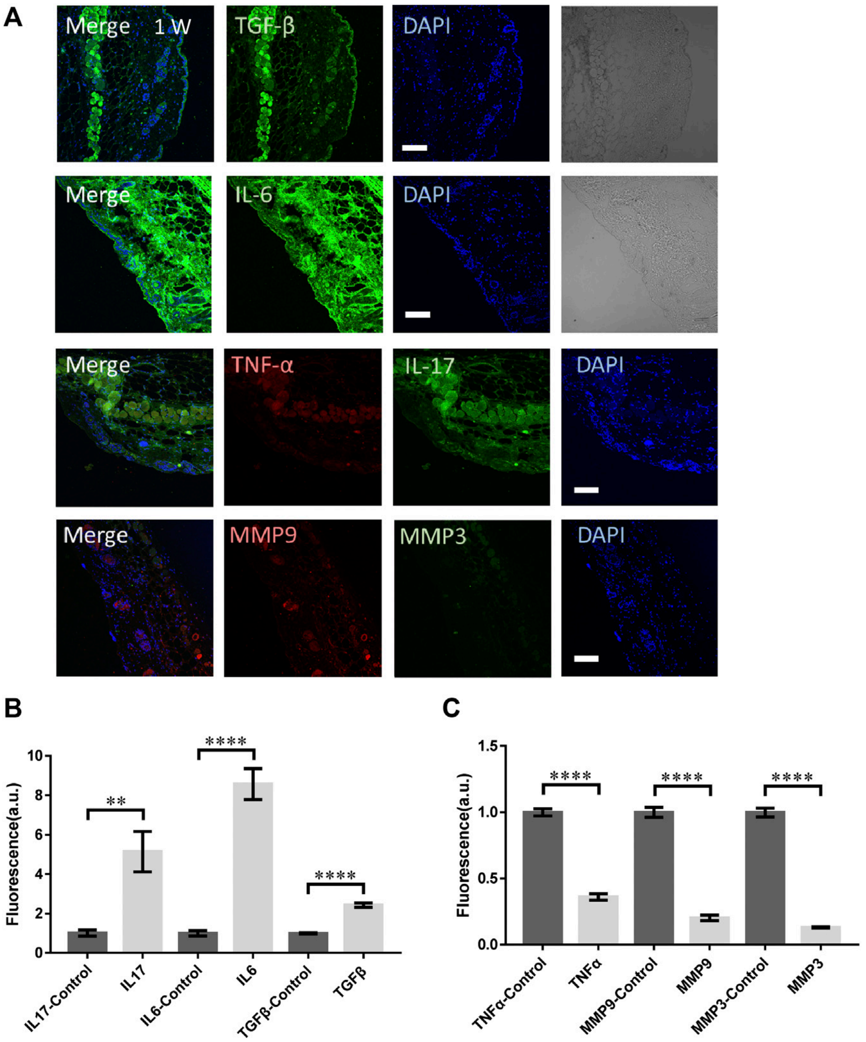

**FIGURE 4 |** The molecular responses of skin to the unfocused laser irradiation at 1 W. **(A)** The immunofluorescence images and **(B,C)** the statistical analysis of the laser-treated samples and control respectively. *n* = 6 samples from three independent trails. Bar: 100 μm. $^*p < 0.05$. $^{**}p < 0.01$. $^{***}p < 0.001$. $^{****}p < 0.0001$, by students' t-test.

deparaffinized with xylene, then rehydrated with serial ethanol dilutions. The tissue section was placed in a repair box filled with EDTA antigen retrieval buffer (PH 8.0) in a microwave oven for antigen retrieval and were blocked using 10% rabbit serum. Sections were incubated with primary antibodies overnight at 4°C. Sections were double-stained for immunofluorescence of TNF-α (rabbit polyclonal anti-TNF-α, 1:200, Affinity Biosciences, AF7014) and IL-17 (mouse monoclonal anti-IL-17, 1:200, Santa Cruz, sc-374218), MMP3 (mouse monoclonal anti-MMP3,1:200, Proteintech, 66338-1-lg) and MMP9 (rabbit polyclonal anti-MMP9, 1:200, Proteintech, 10375-2-AP), and IL-6 (rat monoclonal anti-IL6R, 1:100, Abcam, ab83053) and TGF-β (rabbit polyclonal anti- TGF-β, 1:200, Proteintech, 21898-1-AP). Then the sections were washed with PBS for 5 min and incubated with diluted secondary antibody for 1.5 h at room temperature. Goat anti-Rat IgG secondary antibody conjugated with FITC (1:200, Servicebio), Goat anti-Mouse IgG secondary antibody conjugated with Alexa Fluor ® 488 (1:400, Servicebio) and Goat anti-rabbit IgG secondary antibody conjugated with Cy3 (1:300, Servicebio) were used for microscopy. Sections were simultaneously counterstained with DAPI before fluorescent microscopy.

Images were acquired by a confocal microscopy system (Olympus FV3000). The power of three excitation lasers at 405 nm, 473 nm, and 543 nm was set at the level of 0.1 mW, which could excite fluorophores effectively with moderate photobleaching. The image size was set as 512 × 512 pixels and time interval for each pixel was 2 μs.

## RESULTS

### Acute Molecular Responses to Femtosecond Laser Micromachining

We investigated the responses of immune molecules in skin tissue to femtosecond laser micromachining at different powers. To eliminate the thermal accumulation between laser pulses, the pulse repetition

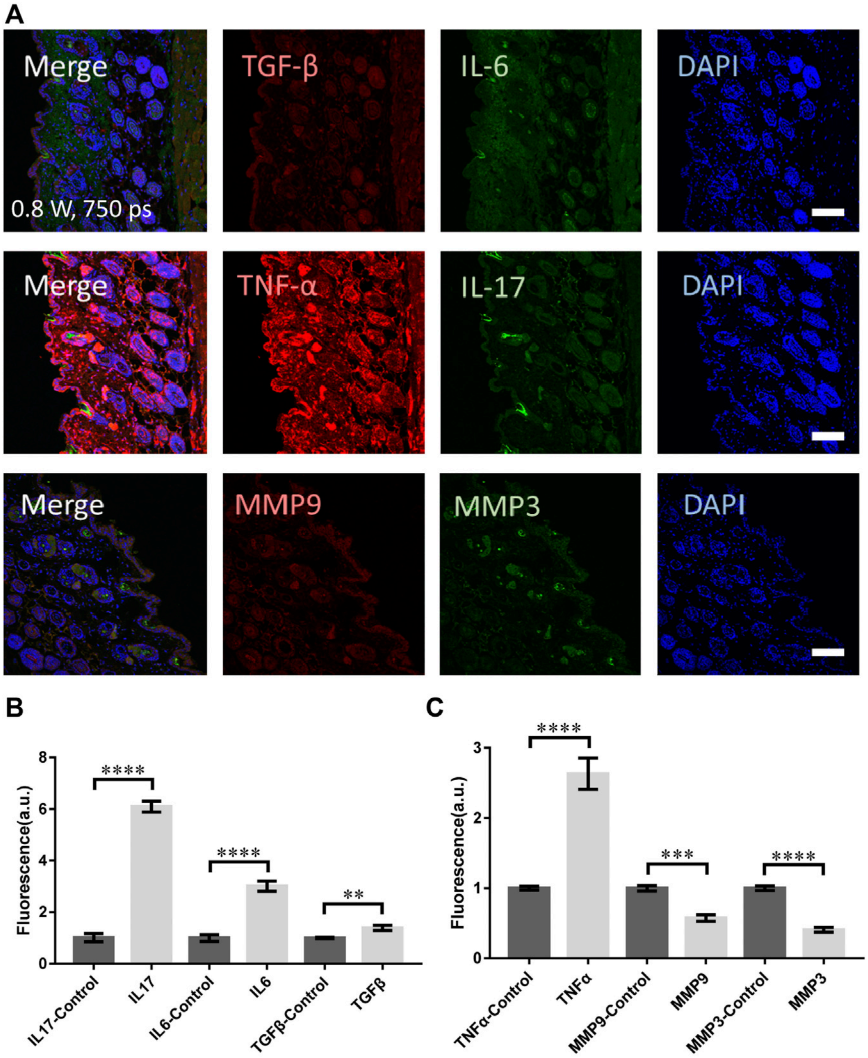

**FIGURE 5 |** The molecular responses of skin to the clinical picosecond laser at 755 nm, irradiation at 0.8 W for 6 s. **(A)** The immunofluorescence images and **(B,C)** the statistical analysis of the samples with and without laser treatment respectively. n = 6 samples from three independent trails. Bar: 100 μm. $^*p < 0.05$. $^{**}p < 0.01$. $^{***}p < 0.001$. $^{****}p < 0.0001$, by students' t-test.

rate was set at only 1 MHz. During the micromachining, the transient thermal effect of each femtosecond pulse can decay before the subsequent following pulse. In this regard, the average total thermal effect of the laser was little. At first, the skin tissue scanned by the focused femtosecond laser at 0.8 W line by line was dissected. The immunofluorescence microscopy of IL-17, TNF-α, IL-6, and TGF-β in the histosections of the tissue were performed respectively. Immediately it could be found TNF-α was significantly assembled in the epidermis (**Figure 1B**) compared with the control (**Figure 1C**). The immune molecules might come from the keratinocytes in epidermis that suffered the laser stimulation. No signals from IL-17, IL-6, or TGF-β that are usually involved in T cells could be found, indicating the acute response of the skin activated by the focused laser was only unspecific innate immune responses at epidermis (**Figure 1D**).

Specifically, we examined the matrix metalloproteinase 3 (MMP3) and 9 (MMP9) that are involved in tissue remodeling, wound healing, and breakdown of extracellular matrix proteins including collagen and elastin. As shown in **Figures 1B,D**, the MMP3 and MMP9 were both significantly upregulated in both epidermis and dermis, indicating the remodeling initiation of the laser-treated skin. The thickness of the skin with those molecular distribution was quantified in **Figure 1E**. Notably, MMP3 could be found highly in epidermis. In those processes, no physical or physiological damage could be found in the histosections. Still, the focused femtosecond laser could activate the collagen or elastin repair. This result suggests the upregulation of MMP family does not require physical injury by optical micromachining to collagen or elastin. The low level of TGF-β under this condition was consistent with this suspicion.

We then measured the molecular responses to the laser stimulation at different powers. As shown in **Figures 2A,B**, the TNF-α in epidermis increased moderately at 0.4 W but no signals could be found at 0.2 W. Compared with the control

(**Figure 1C**), no significant differences could be found in IL-6, IL-17, or TGF-β (**Figure 2D**). The TNF-α level treated at 0.4 W was still significantly higher (**Figure 2E**). Consistently, the upregulation of MMP3 and MMP9 was also significantly higher at 0.4 W but no signals at 0.2 W (**Figure 2E**). The thickness of the skin stained with MMP9 and MMP3 signals was also consistent with the result of immunofluorescence (**Figure 2F**). Therefore, the immune process initiation requires a laser power threshold. At lower laser powers, cells deep in dermis could not be activated for MMP3 and MMP9 expression.

## Long-Term Molecular Dynamics to Femtosecond Laser Micromachining

We investigated the long-term molecular responses of skin, in which the mice recovered 1 day after the laser micromachining at 0.8 W. The skin was then dissected for immunofluorescence microscopy, as shown in **Figure 3A**. The TNF-α level decreased significantly compared with the acute responses, indicating an anti-inflammatory and repair process of skin tissue. But it was still significantly higher than it of control (**Figures 3B,C**). No signals from IL-17, IL-6, or TGF-β were found either (**Figures 3A,C**). Therefore, the tissue damage was strictly confined in the laser scanning volume and only innate immune responses were activated. The expression level of MMP3 and MMP9 were still significantly high (**Figure 3C**). The thickness of the skin with positive MMP3 and MMP9 was consistently higher (**Figure 3D**). During the repair, the irradiated epidermis initiated cornification to detach from the skin, together with MMP3. Hence, taken the acute MMP expression together, MMP3 might be involved in the remodeling of both dermis, epidermis, and specifically, keratoderma. In general, the focused femtosecond laser could effectively activate the remodeling of collagen/elastin without complex immune responses of skin.

## Molecular Responses to Defocused Laser Irradiation

As a comparison, the mice were irradiated by the femtosecond laser at 1 W directly without any focusing for 15 s. The laser spot was around 2 mm in diameter. In this case, the laser could propagate into skin in a deeper distance while the photon density was lower ($10^6$ fold lower). As shown in **Figure 4A**, no obvious physical damage could be found in those skin tissues. The immunofluorescence of TGF-β, IL-17, and IL-6 were all significantly higher (**Figure 4B**). The TGF-β generally distributed in the epidermis, suggesting the physical damage to skin. IL-6 was upregulated through the whole skin tissue and the muscle, fat under it. But the signals from TNF-α, MMP3, and MMP9 all decreased significantly (**Figure 4C**), indicating the tissue remodeling might not be initiated. The collagen and elastin repair was not activated either.

To compare with the clinic treatment, a widely-used picosecond laser in clinic (PicoSure, Cynosure) at 755 nm was used to treat skin of mouse. The laser spot was 2.5 mm in diameter and pulse width 750 ps. The micromachining was performed at 0.8 W (4.07 J/cm$^2$) for 6 s. As presented in **Figures 5A,B**, the signals from TNF-α, TGF-β, IL-17, and IL-6 were all significantly higher. Unfortunately, the MMP3 and MMP9 did not show any increase (**Figure 5C**). Hence the skin suffered mostly damage with little remodeling or repairing.

## CONCLUSION

In this study, we for the first time report the molecular responses of skin tissue from live mice to the femtosecond laser micromachining. According to our data, the focused femtosecond laser can activate the remodeling of skin tissue effectively by the immediately upregulation of MMP3 and MMP9. The low level of IL-6, IL-17, and TGF-β in the skin tissue after laser micromachining suggest no significant immune response or the involvement of T cells participate in this process. The upregulation of TNF-α indicates only innate immune response is activated accompanying with the repair of collagen/elastin initiate in the dermis. In contrast, the unfocused femtosecond laser can activate significant immune responses in deep dermis, indicated by the high-level IL-6, IL-17, and TGF-β. But no collagen repair or skin remodeling could be found in this case. The clinical picosecond laser showed similar results but less damage effect. Those results suggest the focused femtosecond-laser stimulation can activate repair and remodeling of skin tissue without any damage (including physical damage and immune damage) or inflammation. Therefore, focused femtosecond laser micromachining is of promising potential in skin repair and photorejuvenation.

## DATA AVAILABILITY STATEMENT

The original contributions presented in the study are included in the article/Supplementary Material, further inquiries can be directed to the corresponding authors

## ETHICS STATEMENT

The animal study was reviewed and approved by the Animal Ethics Committee of School of Biomedical Engineering and Shanghai Ninth People's Hospital, Shanghai Jiao Tong University.

## AUTHOR CONTRIBUTIONS

HX, YZ, and HH conceived the study. YW and SW performed the experiments. HH contributed to data analysis and manuscript preparation.

## FUNDING

The work was supported by Science and Technology Commission Shanghai Municipality 18QA1402300, and National Natural Science Foundation of China (81661168014 and 62022056).

## REFERENCES

1. Yun SH, Kwok SJJ. Light in diagnosis, therapy and surgery. *Nat Biomed Eng* (2017) 1:1–16. doi:10.1038/s41551-016-0008
2. Alexiades-Armenakas MR, Dover JS, Arndt KA. The spectrum of laser skin resurfacing: nonablative, fractional, and ablative laser resurfacing. *J Am Acad Dermatol* (2008) 58:719–40. doi:10.1016/j.jaad.2008.01.003
3. Novoselova EG, Glushkova OV, Cherenkov DA, Chudnovsky VM, Fesenko EE. Effects of low-power laser radiation on mice immunity. *Photodermatol Photoimmunol Photomed* (2006) 22:33–8. doi:10.1111/j.1600-0781.2006.00191.x
4. Shah S, Alster TS. Laser treatment of dark skin: an updated review. *Am J Clin Dermatol* (2010) 11:389–97. doi:10.2165/11538940-000000000-00000
5. Hsu VM, Aldahan AS, Mlacker S, Shah VV, Nouri K. The picosecond laser for tattoo removal. *Laser Med Sci* (2016) 31:1733–7. doi:10.1007/s10103-016-1924-9
6. Kung K, Shek SY, Yeung CK, Chan HH. Evaluation of the safety and efficacy of the dual wavelength picosecond laser for the treatment of benign pigmented lesions in Asians. *Laser Surg Med* (2019) 51:14–22. doi:10.1002/lsm.23028
7. Habbema L, Verhagen R, Van Hal R, Liu Y, Varghese B. Minimally invasive non-thermal laser technology using laser-induced optical breakdown for skin rejuvenation. *J Biophot* (2012) 5:194–9. doi:10.1002/jbio.201100083
8. DiBernardo BE, Pozner JN. Intense pulsed light therapy for skin rejuvenation. *Clin Plast Surg* (2016) 43:535–40. doi:10.1016/j.cps.2016.03.008
9. Wu DC, Goldman MP, Wat H, Chan HHL. A systematic review of picosecond laser in dermatology: evidence and recommendations. *Laser Surg Med* (2020) [Epub ahead of print]. doi:10.1002/lsm.23244
10. Alegre-Sanchez A, Jiménez-Gómez N, Moreno-Arrones ÓM, Fonda-Pascual P, Pérez-García B, Jaén-Olasolo P, et al. Treatment of flat and elevated pigmented disorders with a 755-nm alexandrite picosecond laser: clinical and histological evaluation. *Laser Med Sci* (2018) 33:1827–31. doi:10.1007/s10103-018-2459-z
11. Chalermchai T, Rummaneethorn P. Effects of a fractional picosecond 1,064 nm laser for the treatment of dermal and mixed type melasma. *J Cosmet Laser Ther* (2018) 20:134–9. doi:10.1080/14764172.2017.1376098
12. Khetarpal S, Desai S, Kruter L, Prather H, Petrell K, Depina J, et al. Picosecond laser with specialized optic for facial rejuvenation using a compressed treatment interval. *Laser Surg Med* (2016) 48:723–6. doi:10.1002/lsm.22551
13. Weiss RA, McDaniel DH, Weiss MA, Mahoney AM, Beasley KL, Halvorson CR. Safety and efficacy of a novel diffractive lens array using a picosecond 755 nm alexandrite laser for treatment of wrinkles. *Laser Surg Med* (2017) 49:40–4. doi:10.1002/lsm.22577
14. Choi YJ, Nam JH, Kim JY, Min JH, Park KY, Ko EJ, et al. Efficacy and safety of a novel picosecond laser using combination of 1 064 and 595 nm on patients with melasma: a prospective, randomized, multicenter, split-face, 2% hydroquinone cream-controlled clinical trial. *Laser Surg Med* (2017) 49:899–907. doi:10.1002/lsm.22735
15. Chayavichitsilp P, Limtong P, Triyangkulsri K, Pratumchart N. Comparison of fractional neodymium-doped yttrium aluminum garnet (Nd:YAG) 1064-nm picosecond laser and fractional 1550-nm erbium fiber laser in facial acne scar treatment. *Laser Med Sci* (2020) 35:695–700. doi:10.1007/s10103-019-02891-5
16. Brauer JA, Reddy KK, Anolik R, Weiss ET, Karen JK, Hale EK, et al. Successful and rapid treatment of blue and green tattoo pigment with a novel picosecond laser. *Arch Dermatol* (2012) 148:820–3. doi:10.1001/archdermatol.2012.901
17. Tanghetti EA. The histology of skin treated with a picosecond alexandrite laser and a fractional lens array. *Laser Surg Med* (2016) 48:646–52. doi:10.1002/lsm.22540
18. Balu M, Lentsch G, Korta DZ, König K, Kelly KM, Tromberg BJ, et al. *In vivo* multiphoton-microscopy of picosecond-laser-induced optical breakdown in human skin. *Laser Surg Med* (2017) 49:555–62. doi:10.1002/lsm.22655
19. Chung HJ, Lee HC, Park J, Childs J, Hong J, Kim H, et al. Pattern analysis of 532- and 1064-nm microlens array-type, picosecond-domain laser-induced tissue reactions in *ex vivo* human skin. *Laser Med Sci* (2019) 34:1207–15. doi:10.1007/s10103-018-02711-2
20. Habbema L, Verhagen R, Van Hal R, Liu Y, Varghese B. Efficacy of minimally invasive nonthermal laser-induced optical breakdown technology for skin rejuvenation. *Laser Med Sci* (2013) 28:935–40. doi:10.1007/s10103-012-1179-z
21. Sakio R, Ohshiro T, Sasaki K, Ohshiro T. Usefulness of picosecond pulse alexandrite laser treatment for nevus of Ota. *Laser Ther* (2018) 27:251–5. doi:10.5978/islsm.27_18-OR-22
22. Bernstein EF, Schomacker KT, Basilavecchio LD, Plugis JM, Bhawalkar JD. Treatment of acne scarring with a novel fractionated, dual-wavelength, picosecond-domain laser incorporating a novel holographic beam-splitter. *Laser Surg Med* (2017) 49:796–802. doi:10.1002/lsm.22734
23. Vogel A, Noack J, Hüttman G, Paltauf G. Mechanisms of femtosecond laser nanosurgery of cells and tissues. *Appl Phys B* (2005) 81(8):1015–47. doi:10.1007/s00340-005-2036-6
24. Chung SH, Mazur E. Surgical applications of femtosecond lasers. *J Biophotonics* (2009) 2:557–72. doi:10.1002/jbio.200910053
25. Kymionis GD, Kankariya VP, Plaka AD, Reinstein DZ. Femtosecond laser technology in corneal refractive surgery: a review. *J Refract Surg* (2012) 28:912–20. doi:10.3928/1081597X-20121116-01

**Conflict of Interest:** The authors declare that the research was conducted in the absence of any commercial or financial relationships that could be construed as a potential conflict of interest.

frontiers
in Physics

MINI REVIEW
published: 24 March 2021
doi: 10.3389/fphy.2021.636985

# Therapeutic Ultrasound-Enhanced Immune Checkpoint Inhibitor Therapy

*Jinyun Yuan*[1], *Dezhuang Ye*[1], *Si Chen*[1] *and Hong Chen*[1,2]*

[1]*Department of Biomedical Engineering, Washington University in St. Louis, Saint Louis, MO, United States,* [2]*Department of Radiation Oncology, Washington University School of Medicine, Saint Louis, MO, United States*

Immune checkpoint inhibitors (ICIs) are designed to reinvigorate antitumor immune responses by interrupting inhibitory signaling pathways and promote the immune-mediated elimination of malignant cells. Although ICI therapy has transformed the landscape of cancer treatment, only a subset of patients achieve a complete response. Focused ultrasound (FUS) is a noninvasive, nonionizing, deep penetrating focal therapy that has great potential to improve the efficacy of ICIs in solid tumors. Five FUS modalities have been incorporated with ICIs to explore their antitumor effects in preclinical studies, namely, high-intensity focused ultrasound (HIFU) thermal ablation, HIFU hyperthermia, HIFU mechanical ablation, ultrasound-targeted microbubble destruction (UTMD), and sonodynamic therapy (SDT). The enhancement of the antitumor immune responses by these FUS modalities demonstrates the great promise of FUS as a transformative cancer treatment modality to improve ICI therapy. Here, this review summarizes these emerging applications of FUS modalities in combination with ICIs. It discusses each FUS modality, the experimental protocol for each combination strategy, the induced immune effects, and therapeutic outcomes.

**Keywords: focused ultrasound, immune checkpoint inhibitor, antitumor immune response, combination therapy, high-intensity focused ultrasound, low-intensity focused ultrasound**

***Edited by:***
*Chao Tian,*
*University of Science and Technology of China, China*

***Reviewed by:***
*Clifford Cho,*
*University of Michigan, United States*
*Emma Jane Harris,*
*Institute of Cancer Research (ICR), United Kingdom*

***Correspondence:**
*Hong Chen*
*hongchen@wustl.edu*

***Specialty section:***
*This article was submitted to Medical Physics and Imaging, a section of the journal Frontiers in Physics*

***Received:*** *02 December 2020*
***Accepted:*** *09 February 2021*
***Published:*** *24 March 2021*

***Citation:***
*Yuan J, Ye D, Chen S and Chen H (2021) Therapeutic Ultrasound-Enhanced Immune Checkpoint Inhibitor Therapy.*
*Front. Phys. 9:636985.*
*doi: 10.3389/fphy.2021.636985*

## INTRODUCTION

Immune checkpoint inhibitor (ICI) therapy has revolutionized the paradigm of cancer immunotherapy. Under normal physiological conditions, immune checkpoints are crucial to maintaining immune tolerance. However, in the tumor environment, tumor cells hijack these inhibitory mechanisms to avoid antitumor immune responses. ICIs are monoclonal antibodies that disrupt the engagement of immune checkpoints, which enables tumor-reactive T cells to overcome inhibitory mechanisms and mount effective antitumor immune responses [1]. The United States Food and Drug Administration (FDA) has approved ICIs that target cytotoxic T lymphocyte-associated protein-4 (CTLA-4), programmed cell death-1 (PD-1), and programmed cell death-ligand 1 (PD-L1) for the treatment of a wide variety of cancers [2]. Despite the clinical success of ICIs, advancing clinical applications of ICIs face challenges related to both efficacy and safety. Most cancer patients are unable to derive durable remission, while >50% of cancer patients develop immune adverse events after they receive ICIs [3]. The combination of multiple ICIs with other cancer therapies has improved cancer treatment by enhancing direct tumor killing and indirect antitumor immunity [4].

The past two decades have witnessed exciting breakthroughs in the clinical translations of focused ultrasound (FUS) modalities for cancer treatment [5]. FUS concentrates extracorporeally generated ultrasound energy through the body to a tight focus with an exceptional spatial resolution (on the millimeter scale) and deep penetration depth. The focal point can be mechanically and electronically steered in three-dimensional space to form a sonication volume that conforms to the shape of the target. FUS therapy is often performed under the guidance of magnetic resonance imaging or ultrasound imaging [6]. As a promising therapeutic technology, FUS has the unique combined advantages of being noninvasive, nonionizing, nonpharmaceutical, spatially targeted, and deeply penetrating the body. Since 2017, five FUS modalities, including high-intensity focused ultrasound (HIFU) thermal ablation [7–11], HIFU hyperthermia [12], HIFU mechanical ablation [13–17], ultrasound-targeted microbubble destruction (UTMD) [18–20], and sonodynamic therapy (SDT) [21, 22], have been investigated in combination with ICIs for treating solid tumors in mouse models. The enhancement of antitumor immune responses by these FUS modalities demonstrated the great promise of FUS as a transformative cancer treatment modality to improve ICI therapy.

In this review, we provide a brief introduction of ICI therapy basics and discuss the challenges facing ICI therapy. We then introduce each FUS-enhanced ICI therapy and summarize the therapeutic outcomes achieved by the combination therapy. Finally, we discuss the limitations of existing studies and provide future perspectives.

## Immune Checkpoint Inhibitor Therapy Basics and Challenges

ICIs bind to immune checkpoints, including CTLA-4, PD-1, and PD-L1, and "release the brakes" on T cells, resulting in anticancer immune responses. CTLA-4 inhibits T-cell activation by attenuating T-cell receptor signaling through competing with the costimulatory molecule CD28 for binding to B7 ligands on antigen-presenting cells (APCs) [23]. PD-1 regulates T-cell activation through interaction with its ligand PD-L1. The engagement of PD-1 and PD-L1 results in a negative costimulatory signal and leads to T-cell apoptosis, anergy, and exhaustion [24]. Efficient ICI therapy requires reactivation and clonal expansion of antigen-experienced T cells present in the tumor microenvironment (TME) [25]. Initially, naive tumor-specific CD8 T cells are primed by antigen presentation by APCs (often referred to as immune priming) and activated in the presence of costimulatory pathways and cytokines. Tumor-specific CD8 T cells subsequently differentiate into effector T cells, undergo clonal expansion, traffic to the TME, and ultimately kill tumor cells. A subset of effector T cells can differentiate into memory T cells under the guidance of CD4 T cells and dendritic cells (DCs) to develop long-term immunologic memory against the tumor.

The introduction of ICI therapy in the clinic has been considered to be a paramount achievement in cancer treatment in the last decade [26]. Since 2011, the FDA has approved ICIs targeting PD-1 (pembrolizumab, nivolumab, and cemiplimab), PD-L1 (atezolizumab, durvalumab, and avelumab), and CTLA-4 (ipilimumab). They have produced remarkable results regarding tumor control in many malignancies, such as melanoma, metastatic non-small-cell lung cancer (NSCLC), head and neck squamous cancers, urothelial carcinoma, gastric adenocarcinoma, mismatch-repair-deficient solid tumors, and classic Hodgkin lymphoma. Many clinical studies with ICIs are currently underway to test their efficacy in various other diseases.

Despite the clinical success of ICIs, ICI therapy faces challenges related to both efficacy and safety. With regard to ICI efficacy, the majority of patients do not benefit from the treatment, and some responders relapse after a period of response. Ongoing studies indicate that both tumor cell-intrinsic and tumor cell-extrinsic factors contribute to the resistance mechanisms [27]. Tumor cell-intrinsic factors include lack of tumor-associated antigens (TAAs), ineffective antigen presentation, activation of oncogenic pathways, and insufficient interferon-$\gamma$ (IFN-$\gamma$) signaling. Tumor cell-extrinsic factors are within the TME and include exhausted CD8 T cells, regulatory T cells (Tregs), myeloid-derived suppressor cells (MDSCs), and other immunosuppressive cells and factors. With regard to safety, a significant number of patients on ICIs develop immune-related adverse events affecting almost every organ. Immune-related adverse events occur when ICIs result in an immune-based attack on normal tissue. These events, such as dermatitis, thyroiditis, pneumonitis, colitis, hepatitis, and nephritis, are unpredictable, heterogeneous, and in some instances life-threatening. Management of these adverse events remains a challenge [28]. These challenges call for concepts to maximize the clinical benefits of ICIs in combination with other therapies. An abundance of clinical trials are currently underway in evaluating the combination of ICIs with other immunotherapies, chemotherapy, radiotherapy, or targeted therapies. Strategies that can improve antigen presentation and immune recognition, reinforce the activity and infiltration of CD8 T cells, and reduce immunosuppression can potentially be combined with ICIs to improve the efficacy of ICI therapy [27]. Meanwhile, novel drug delivery strategies that enable the targeted delivery of ICIs within the TME have the potential to reduce the toxicities associated with ICIs [29, 30].

FUS is a promising platform technology to be combined with ICIs to improve its efficacy and safety. Various FUS therapeutic modalities have been developed, and some of them have been used in the clinic for the treatment of various diseases (**Table 1**). Among them, HIFU thermal ablation has been approved by the FDA for the treatment of prostate cancer, uterine fibroids, bone metastasis, and essential tremor and has been used worldwide for the treatment of various diseases. Although other FUS modalities, including HIFU hyperthermia, HIFU mechanical ablation, UTMD, and SDT, have not been approved for clinical use, clinical studies are currently ongoing, with multiple studies already reported. Advances in the clinical applications of these FUS techniques have encouraged new studies to combine FUS with ICIs, as summarized in **Table 2**. The effectiveness of FUS-enhanced ICI therapy is often demonstrated by increased tumor infiltrated CD8 T cells, decreased tumor volume, and prolonged survival. The systemic immune response of ICI therapy can also be demonstrated by the presence of the abscopal effect, which occurs when the treatment not only shrinks the targeted tumor but also leads to shrinkage of untreated tumors elsewhere in the

**TABLE 1 |** Overview of different FUS modalities.

| Modalities | Commonly used FUS parameters | Physical mechanism | Clinical applications |
|---|---|---|---|
| HIFU thermal ablation | Continuous (duty cycle = 100%) HIFU with spatial peak temporal average intensity ($I_{SPTA}$) >1000 W/cm$^2$ and relative high pressure (a few MPa) to rapidly heat tumor to >60°C within a few seconds | Coagulative thermal necrosis due to tissue absorption of ultrasound energy | The only modality currently approved for use in the clinic worldwide for the treatment of a variety of solid malignant tumors (e.g., tumors in the pancreas, liver, kidney, bone, prostate, and breast), benign tumors (e.g., uterine fibroids and fibroadenomata), and non-tumor diseases (e.g., essential tremor and Parkinson's disease) [32] |
| HIFU hyperthemia | HIFU with a high duty cycle (up to 70%) and relative high pressure (a few MPa) to heat up tissue to 40–45°C for up to 60 min [35] | Thermally controlled drug release and increasing blood flow and oxygen | Mutiple reported clinical studies of HIFU hyperthermia to enhance the delivery of thermosensitive liposomal doxorubicine in patients with liver tumors [35] |
| HIFU mechanical ablation | HIFU with $I_{SPTA}$ >100 W/cm$^2$ and a low duty cycle (1–2%) and extremely high pressure (>10 MPa) to induce mechanical tissue damage while minimizing heating [49] | High-amplitude HIFU pusles are used to induce bubble cavitation to fractionate tissue by mechanical effects | No reported clinical results, but clinical trials ongoing for the treatment of primary and metastatic liver tumors (ClinicalTrials.gov Identifier: NCT04572633) |
| UTMD | LIFU with $I_{SPTA}$ <10 W/cm$^2$ and a low duty cycle (e.g., 10%) and relative low pressure (<1 MPa) to induce mechanical effects [42] | Targeted and controlled release of therapeutics, sonoporation for drug/gene delivery, and mechanical disruption of the blood vessels and tumor tissue [50] | One reported clinical study of drug delivery using UTMD in pancreatic patients [51]. Multiple reported clinical studies on opening the blood-brain barrier for brain drug delivery in patients with glioblastoma [52, 53], Alzheimer's disease [54], and amyotrophic lateral sclerosis [55] |
| SDT | LIFU with $I_{SPTA}$ <10 W/cm$^2$ and a duty cycle of 10–100% to activate sonosensitizers [56] | Sensitizer-dependent sonochemical or sonophotochemical reactions in an acoustic field that lead to cytotoxicity [48] | Several reported clinical studies investigated a combination of light and ultrasound to stimulate a sensitizer in patients with a variety of cancer [57] |

*HIFU (high-intesity focused ultrasound), LIFU (low-intensity focused ultrasound), UTMD (ultrasound-targeted microbubble destruction, SDT (sonodynamic therapy).*

body. In the following, each FUS-enhanced ICI therapy is introduced.

## High-Intensity Focused Ultrasound Thermal Ablation-Enhanced Immune Checkpoint Inhibitor Therapy

HIFU thermal ablation induces thermal coagulation by rapidly (in a few seconds) heating tissue at the focus to >60°C, often with high-intensity continuous ultrasound waves. Only tissue within the focal region is selectively ablated, while tissue in the ultrasound beam path is spared from ablation [31]. Compared with other local ablative therapies, such as ablative radiotherapy, radiofrequency ablation, and cryotherapy, HIFU thermal ablation is the only noninvasive and nonionizing ablation technique, allowing the procedure to be performed and repeated without the need for surgical implantation of applicators and concerns about radiation-induced toxicities. HIFU thermal ablation causes very few side effects to normal surrounding tissues, and patient comfort and safety are maximized [32]. HIFU thermal ablation has been widely applied for the treatment of a variety of solid tumors, as well as many other benign diseases in the clinic [32]. HIFU thermal ablation has been reported to increase the release of damage-associated molecular patterns (DAMPs) and TAAs, promote DC maturation, increase tumor-infiltrating lymphocytes, and change circulating immunosuppressive cytokine levels [33], suggesting the potential to improve ICI efficacy for tumors that do not respond well to ICIs.

The first study on therapeutic ultrasound-enhanced ICI therapy was reported in 2017 by Silvestrini et al. [7]. They explored whether HIFU thermal ablation could be effectively incorporated with ICIs to boost antitumor immune responses in murine breast cancer models. Breast cancer is often resistant to most chemotherapies and molecular targeted therapies, including ICI therapies [7]. Half of the reported FUS-enhanced ICI studies summarized in **Table 2** used murine breast cancer models. In Silvestrini's study, systemic anti-PD-1 antibody (αPD-1) and local adjuvant, CpG, were administered prior to HIFU thermal ablation for immunotherapy priming. Only with initial immunotherapy priming, coincident HIFU thermal ablation and immunotherapy suppressed tumor growth in both treated and contralateral nontreated tumors and increased the survival rate [7]. The potential mechanisms for the enhanced antitumor response from this multistep protocol were proposed as follows [8]: immunotherapy priming expanded the number of tumor-infiltrating CD8$^+$ T cells and macrophages. The subsequent HIFU thermal ablation released tumor antigens, inflammatory chemokines and cytokines, increased interferon stimulating genes, and altered the local macrophage phenotype. These effects led to cross-presentation and cross-priming mediated by macrophages and DCs, resulting in an effective abscopal response.

The combination of HIFU thermal ablation with ICIs has also been explored to treat colorectal tumors since some of them are not suitable for ICIs [34]. Without immunotherapy priming, the combination of HIFU thermal ablation with ICIs and local adjuvants was able to produce therapeutic benefits in colorectal tumor-bearing mice [9]. HIFU thermal ablation was followed by direct injection of nanoadjuvants into the ablated site and intravenous injection of anti-CTLA-4 antibody (αCTLA-4).

**TABLE 2 |** Summary of therapeutic ultrasound-enhanced ICI therapies.

| FUS modality | References | Cell/mouse (tumor model) | FUS parameters | Combined FUS and ICI protocol | Key results from combination therapy |
|---|---|---|---|---|---|
| HIFU thermal ablation | Silvestrini et al. [7] | NDL/FVB/n (orthotopic breast cancer) | 3 MHz, 3.1 MPa, T > 65°C, target: circular pattern within 1–2 mm of the tumor edge | Adjuvant CpG (i.t.) injected to single tumor on days 21, 24, 28, 31, 38, 45; αPD-1 (i.p.) injected on days 21, 28, and 35; HIFU thermal ablation applied to tumor on days 31, 38, 45 | Distant tumor leukocytes ↑ and CD8$^+$ ↑; spleen IFN-$\gamma^+$CD8$^+$ ↑; treated and distant tumor volume ↓; survival ↑ |
| | Chavez et al. [8] | NDL/FVB/n (orthotopic breast cancer)<br>PyMT/PyVT (spontaneous breast cancer) | 3 MHz, T > 60°C, target: 2–3 mm within tumor | Adjuvant CpG (i.t.) injected to single tumor on days 21, 24, 28, 31; αPD-1 (i.p.) injected on days 21, 28, 35, HIFU thermal ablation applied to tumor on day 31 | Treated tumor interferon-stimulated gene expression ↑; treated tumor CD169$^+$DCs ↑ and CD169$^+$MPs ↑; distant tumor DCs ↑; spleen CD169$^+$MPs ↑ |
| | Han et al. [9] | CT26/BALB/c (subcutaneous colorectal cancer) | 4 MHz, 43 W, FUS on = 1 s, FUS off = 5 s for a single point, repeat 20 rounds to completely eliminate tumor | For metastatic tumor: HIFU thermal ablation performed to remove tumor on day 7; adjuvants directly injected into ablated site afterward; αCTLA-4 (i.v.) injected on days 8, 10, 12, 14<br>For recurrent tumor: HIFU thermal ablation performed to remove tumor on day 7, adjuvants directly injected into ablated site afterward; tumor rechallenged on day 47; αCTLA-4 (i.v.) injected on days 48, 50, 52, 54 | Distant tumor CD8$^+$/Tregs ↑ and MDSCs ↓; spleen effector memory T cell (CD3$^+$CD44$^{Hi}$CD62$^{Lo}$) ↑; serum IFN-$\gamma$ ↑ and TNF-α ↑; distant tumor volume ↓; survival ↑; tumor rechallenge suppressed |
| | Sheybani et al. [10] | 4T1/BALB/c (subcutaneous breast cancer) | 3 MHz, 15 W, FUS on = 10 s for each sonication, target: ~10–20% of total tumor volume | Every 3 days for a total of five doses of αPD-1 (i.p.) injected prior to or with HIFU thermal ablation with gemcitabine | Tumor volume ↓ |
| | Fite et al. [11] | NDL/FVB/n (orthotopic breast cancer) | 3 MHz, 3.1 MPa, T > 65°C, circular pattern within 1–2 mm of the tumor edge | Adjuvant CpG (i.t.) injected to single tumor on days 21, 24, 28, 30; αPD-1 (i.p.) injected on days 21, 28, 34, HIFU thermal ablation applied to tumor on day 30 | Treated tumor IL-6 and IL-β mRNA ↑; treated tumor MDSCs ↑; distant tumor MDSCs ↑ |
| HIFU hyperthermia | Kheirolomoom et al. [12] | NDL/FVB/n (orthotopic breast cancer)<br>PyMT/PyVT (spontaneous breast cancer) | 1.5 MHz, PNP 2.5 MPa, PRF 100 Hz, pulse length 0–7 ms, heating at 42°C for 5 min before and 20 min post liposome injection | Copper-doxorubicin-loaded temperature-sensitive liposomes (i.v.) injected on day 31, HIFU hyperthermia applied to tumor afterward; adjuvant CpG (i.t.) injected to single tumor on days 21, 24, 28, 35, 49; αPD-1 (i.p.) injected on days 21, 28, 35 | Treated and distant tumor CD8$^+$ ↑; treated and distant tumor volume ↓; survival ↑ |

(Continued on following page)

**TABLE 2 |** (*Continued*) Summary of therapeutic ultrasound-enhanced ICI therapies.

| FUS modality | References | Cell/mouse (tumor model) | FUS parameters | Combined FUS and ICI protocol | Key results from combination therapy |
|---|---|---|---|---|---|
| HIFU mechanical ablation | Wang et al. [13] | GL261/C57BL/6 (subcutaneous glioblastoma) | 1.1 MHz, duty cycle 2%, treatment duration 2 min | Perfluorocarbon-filled microshells directly injected to large tumors (400–700 mm$^3$), HIFU mechanical ablation applied to tumor afterward; αPD-1 (i.p.) injected on days 0, 2, 4, 6, 8, 10$^a$ | Tumor CD45$^+$ ↑, CD3$^+$ ↑, CD8$^+$ ↑, and IFN-γ ↑; tumor size ↓; survival ↑; tumor rechallenge rejected |
| | Eranki et al. [14] | Neuro2a/C57BL/6 (subcutaneous neuroblastoma) | 1.5 MHz, PNP 14 MPa, PRF 1 Hz, pulse duration 13.33 ms, 5 s/location, 3 locations, cover 2% tumor volume | Histotripsy applied to tumor on day 8; αCTLA-4 (i.p.) + αPD-L1 (i.p.) injected on days 9, 12, 15 | Tumor CD4$^+$ ↑, CD8α$^+$ ↑ and CD8α$^+$CD11c$^+$ ↑; spleen and TDLN CD8α$^+$CD11c$^+$ ↑; spleen CD11b$^{low}$ ↑; spleen effector memory T cells (CD4$^+$ or CD8$^+$CD44$^+$hiCD62L$^+$low) ↑; serum IFN-γ↑, IL-6↑ and IL-10↓; complete abscopal response; survival ↑; transferred T cells suppressed tumor in recipients |
| | Nam et al. [15] | 4TI/BALB/c (subcutaneous breast caner); CT26/BALB/c (subcutaneous colorectal cancer) | 1.5 MHz, electrical power 525 W, PRF 1 Hz, duty cycle 1%, pulse length 10 ms, 50 pulses | Histotripsy applied to tumor on days 6, 7, 8; αPD-1 (i.p.) injected on day 9, 11, 13 | Tumor CD8$^+$ ↑, CD8$^+$CD107α$^+$ ↑, CD8$^+$PD-1$^+$ ↑ and MDSCs ↓; tumor volume ↓; tumor weight ↓ |
| | Qu et al. [16] | B16GP33/C57BL/6 (subcutaneous melanoma)<br>Hepa1-6/C57BL/6 (subcutaneous hepatoma) | 1 MHz, PNP 30 MPa, PRF 100 Hz, 50 pulses, pulse duration 1–2 μs; total treatment duration 4–15 min depending on tumor volume | For B16GP33 tumor, histotripsy applied to tumor on day 7; αCTLA-4 (i.p.) injected at days 6, 9, 12<br>For Hepa1-6 tumor, histotripsy applied to tumor on day 10; αCTLA-4 (i.p.) injected on days 3, 6, 9, 12 | Tumor CD8$^+$ ↑; tumor volume ↓ |
| | Singh et al. [17] | B16F10/C57/BL-6 (subcutaneous melanoma) | 1.5 MHz, acoustic power 450 W, PRF 1 Hz, duty cycle 1%, cover 40–50% of the tumor | Histotripsy applied to tumor (330–400 mm$^3$); single dose of αCD40 (i.t.) injected afterward (within 2 h); 3 dose of αCTLA-4 (i.p.) + αPD-L1 (i.p.) injected at 3 days interval | Tumor growth ↓; survival ↑ |
| UTMD | Li et al. [18] | LLC/C57BL/6 (subcutaneous and orthotopic lung cancer) | 1 MHz, 2.0 W/cm$^2$, duty cycle 50%, treatment duration 5 min | Docetaxel and αPD-L1-coloaded microbubbles (i.v.) followed by LIFU applied to tumor on days 8, 11, 14, 17, 20 for subcutaneous tumor and on days 6, 9, 12, 15, 18 for orthotopic tumor | Tumor TUNEL ↑, Ki67$^+$ ↓, CD4$^+$ ↑, CD8$^+$ ↑; tumor growth ↓; body weight loss ↓; survival ↑ |
| | Bulner et al. [19] | CT26/BALB/c (subcutaneous colorectal cancer) | 1 MHz, PNP 1.65 MPa, pulse length 0.1 ms, duty cycle 10%, wait 20 s after every 50 pulses, total treatment duration 2 min | LIFU+microbubbles two repeats with 10 min interval on day 10–12; αPD-1 (i.p.) injected on days 0, 3, 6 after LIFU+microbubbles for acute study and 0, 3, 5, 9, 12 for longitudinal study | Tumor necrosis↑ and growth↓; survival ↑; one survived mouse suppressed tumor rechallenge |
| | Ilovitsh et al. [20] | NDL/FVB/n (orthotopic breast cancer) | 250 kHz, PNP 500 kPa, PRF 30 Hz, burst length 4 ms, total treatment duration 3 min | αCD326-loaded microbubbles and pIFN-β (i.t.) injected followed by LIFU applied to tumor on day 14; αPD-L1 (i.p.) injected on days 11, 16 | Tumor CD8$^+$ ↑ and F4/80 MPs ↑; treated and distant tumor growth ↓; survival ↑ |

(Continued on following page)

**TABLE 2 |** (*Continued*) Summary of therapeutic ultrasound-enhanced ICI therapies.

| FUS modality | References | Cell/mouse (tumor model) | FUS parameters | Combined FUS and ICI protocol | Key results from combination therapy |
|---|---|---|---|---|---|
| SDT | Yue et al. [21] | 4T1/BALB/c (breast cancer, orthotopic and intravenous injection); CT26/BALB/c (subcutaneous colorectal cancer) | 1 MHz, 1.5 W/cm$^2$, 50% duty cycle, treatment duration 5 min | Sonosensitizers and adjuvant loaded liposomes (i.v.) injected on days 7, 8, 10, 11; LIFU applied to tumor 12 and 24 h post injection; αPD-L1 (i.v.) injected on days 8, 11, 13, 15 | Tumor leucocytes ↑, CD8$^+$ ↑ and CD8$^+$/Tregs ↑; serum IFN-γ ↑ and TNF-α ↑; tumor volume ↓; survival ↑ |
| | Um et al. [22] | CT26/BALB/c (colorectal cancer, subcutaneous and intravenous injeciton) | Acoustic power 10 W, duty cycle 20%, PRF 1 Hz, treatment duration 10 min | Sonosensitizers and gas loaded PEGylated carboxymethyl dextran (i.v.) injected and 6 hrs later LIFU applied on tumor on days 8, 11, 14; αPD-L1 (i.p.) injected on days 9, 12, 15 | Tumor CD8$^+$ ↑; tumor volume ↓; tumor weight ↓ |

[a] *Days referred to treatment start date, all the other days referred to tumor implantation date.*

*T (temperature), PNP (peak negative pressure), PRF (pulse repetition frequency), i. p. (intraperitoneally), i. v. (intravenously), i. t. (intratumorally), FUS (focused ultrasound), HIFU (high-intensity focused ultrasound), LIFU (low-intensity focused ultrasound), UTMD (ultrasound-targeted microbubble destruction), SDT (sonodynamic therapy), Tregs (regulatory T cells), MPs (macrophages), MDSCs (myeloid-derived suppressor cells), TDLN (tumor-draining lymph nodes), IFN-γ (interferon-gamma), TNF-α (tumor necrosis factor-alpha), IL-6 (interleukin 6), IL-1β (interleukin 1 beta), IL-10 (interleukin 10), TUNEL (terminal deoxynucleotidyl transferase dUTP nick end labeling), CpG (cytosine-phosphodiester-guanine oligodeoxynucleotide).*

The nanoadjuvants were formed by loading poly (lactic-co-glycolic) acid nanoparticles with either a TLR7 agonist (imiquimod, R837) or TLR4 agonist (monophosphoryl lipid A, MPLA). This combination strategy increased the intratumoral CD8 T cell/Treg ratio, reduced MDSCs within tumors, achieved complete distant tumor eradication, prolonged mouse survival, and prevented tumor recurrence, indicating the generation of sustained immune memory against colorectal tumors. In contrast, none of the mice given HIFU thermal ablation plus either nanoadjuvants or αCLTA-4 survived [9], which suggests that additional agents (e.g., adjuvants, chemotherapeutics) may be required for the success of HIFU thermal ablation and ICI combination treatment. Another study reported that initiating αPD-1 treatment prior to versus shortly after HIFU thermal ablation with chemotherapy did not bear a marked difference in primary tumor growth in a murine breast cancer model [10].

These studies suggest that the optimal protocol for HIFU thermal ablation-enhanced ICI therapy may depend on the tumor model, the type of adjuvants used, with or without immunotherapy priming, and the HIFU ablation protocol. HIFU thermal ablation as a combination therapy with ICIs has the potential limitation that excessive heat generation by HIFU thermal ablation may induce protein denaturation and inactivate antigen presentation [13]. Meanwhile, HIFU thermal ablation was also reported to increase tumor infiltrated MDSCs and Tregs at both directly treated and distant tumors, leading to inhibition of antitumor immunotherapy [11]. These negative effects highlight the complexity of combining HIFU thermal ablation with ICI therapy.

## High-Intensity Focused Ultrasound Hyperthermia-Enhanced Immune Checkpoint Inhibitor Therapy

HIFU hyperthermia raises tissue temperature within the focal region to 40–45°C for up to 60 min. It is different from thermal ablation in that hyperthermia is not intended to produce substantial cell death directly. Instead, HIFU hyperthermia is often combined with chemotherapy and radiation therapy or used for local drug release in combination with temperature-sensitive nanoparticles [35]. HIFU hyperthermia can directly promote antigen cross-presentation and tumor-reactive T cell formation and expansion [36].

Kheirolomoom et al. investigated the combination of HIFU hyperthermia with chemotherapy, CpG, and αPD-1 [12]. HIFU hyperthermia was utilized to control the release of temperature-sensitive liposomes loaded with a chemotherapy drug, doxorubicin (Dox). The liposome carrier was designed to minimize the severe cardiac toxicity of Dox and enhance its delivery efficiency to tumors. Dox released at HIFU hyperthermia-treated tumors enhanced the presentation of tumor-specific antigens at distant tumor sites. Similar to HIFU thermal ablation [7], only with immunotherapy priming by CpG and αPD-1, the combined HIFU hyperthermia, Dox-loaded liposomes, and αPD-1 treatment increased tumor infiltrated CD8 T cells and achieved complete tumor destruction in both treated and distant tumors as well as prolonged tumor-free survival. However, repeated Dox delivery by HIFU hyperthermia either with or without immunotherapy priming reduced the complete response rate, which was considered to be caused by rapid tumor cell death resulting from repeated Dox release that weakened the impact of local antigen and cytokine release. These findings highlighted the importance of the dosing of HIFU hyperthermia-mediated chemotherapy and the timing of immunotherapy to augment ICI efficacy for cancer treatment.

These reported studies [7, 9, 10, 12] suggest that neither HIFU thermal ablation nor HIFU hyperthermia alone is sufficient to enhance ICI efficacy in murine tumor models. Both FUS modalities were found to enhance the release of TAAs and recruitment of CD8 T cells, but in the absence of additional stimuli (e.g., adjuvants, chemotherapeutics), the recruited CD8 T cells might not have sufficient antigen cross-presentation and cross-priming mediated by DCs and macrophages [8, 11]. Future studies are needed to investigate the optimal combination therapy by HIFU thermal ablation or hyperthermia with ICIs and adjuvants/chemotherapeutics to achieve systemic, long-term effects for cancer treatment.

## High-Intensity Focused Ultrasound Mechanical Ablation-Enhanced Immune Checkpoint Inhibitor Therapy

HIFU mechanical ablation utilizes short pulse lengths (microsecond to millisecond) and low duty cycles to produce mechanical ablation of tissues while limiting tissue temperature increase. The primary physical mechanism of HIFU mechanical ablation is cavitation, which is defined as the formation, oscillation, and collapse of bubbles in the acoustic field. Cavitation can induce tissue damage by various mechanisms, including microjecting, streaming, and shear stresses [37]. The formation of cavitation in tissue by HIFU can be facilitated by the injection of exogenously made cavitation nuclei, for example, microbubbles or phase-changing materials (e.g., perfluorocarbon). Without the injection of cavitation nuclei, cavitation can be initiated using ultrasound pulses with high tensile pressure, which stretches the tissue and generates cavitation bubbles *in situ*. When extremely high tensile pressures are generated, HIFU can lead to complete liquefaction of the tumor tissue into submicron fragments, which is named histotripsy [38]. Several reports have shown that HIFU mechanical ablation can cause immunogenic cell death and release tumor debris *in situ*, promote antigen presentation, and enhance the inflammatory response [33].

The clinical applications of ICIs in brain tumors (e.g., glioblastoma and neuroblastoma) have been challenging, potentially because these tumors harbor a “cold” immune microenvironment that lacks requisite T cells and sufficient TAAs and contains high densities of immunosuppressive cell populations [39, 40]. One recent study demonstrated that HIFU mechanical ablation combined with silica microshells mechanically disrupted glioblastoma tumors and augmented the efficacy of αPD-1 [13]. The combination of HIFU mechanical ablation with microshells and αPD-1 increased tumor-infiltrating CD8 and IFN-$\gamma^{+}$CD8 T cells, prolonged tumor-free survival and protected against tumor rechallenge, suggesting the formation of long-term immune memory against glioblastoma. In a murine neuroblastoma model, Eranki et al. demonstrated that histotripsy potentially transformed immunologically "cold" tumors into responsive "hot' tumors and provided an efficacious adjuvant to ICI therapy [14]. Histotripsy followed by systemic injection of αCTLA-4 and αPD-1 induced significant increases in intratumoral CD4, CD8α, and CD8α$^{+}$ DCs in regional lymph nodes and circulating IFN-$\gamma$ and decreases in circulating IL-10. Notably, the combination therapy improved long-term survival, achieved complete bilateral tumor regression, and induced an effective long-term immune memory response to suppress subsequent tumor engraftment. Other recent studies found that histotripsy stimulated more potent intratumoral CD8 T cells and antigen presentation than HIFU thermal ablation in a murine breast cancer model [15] and melanoma model [16]. One recent study showed that combining histotripsy with intratumor anti-CD40 agonist antibody, αCTLA-4, and anti-PD-L1 antibody (αPD-L1) significantly improved the therapeutic efficacy against ICI refractory murine melanoma [17].

These findings [13–16] suggest that HIFU mechanical ablation alone, without the need for adjuvants, is sufficient to enhance ICI therapy for the treatment of cancers that are unresponsive to ICIs. One advantage of HIFU mechanical ablation over HIFU thermal ablation is that tumor fragmentation instead of tumor coagulation may protect TAAs and DAMPs from protein denaturation by excessive heat and stimulate more effective antitumor immune responses [15, 16, 33, 41].

## Ultrasound-Targeted Microbubble Destruction-Enhanced Immune Checkpoint Inhibitor Therapy

There is no consensus regarding the definition of low-intensity focused ultrasound (LIFU). It can be regarded as FUS with pulse intensity similar to that of diagnostic ultrasound. Microbubbles are made of a phospholipid, surfactant, albumin, or synthetic polymer shell filled with a high molecular weight gas with low water solubility. These microbubbles were initially introduced into the clinic as ultrasound contrast agents to enhance ultrasound signals from the blood circulation [42]. Over the past decades, they have been developed into theranostic agents. Their shells can be used for disease-specific targeting and loaded with drugs as carriers for controlled drug release at the LIFU-targeted region. Moreover, microbubble cavitation upon LIFU sonication can generate mechanical forces on surrounding tissue and induce vascular disruption [43].

PD1/PD-L1 ICIs have been used in the clinic for the treatment of NSCLC in combination with chemotherapeutic drugs. However, the combination of these drugs leads to aggravated cardiotoxicity, hematotoxicity, hepatotoxicity, and neurotoxicity [44]. Li et al. used microbubbles as carriers of immunotherapy and chemotherapy drugs to produce antitumor effects while reducing the toxicities of the drug combination [18]. Docetaxel was loaded inside the lipid shell of the microbubbles, and αPD-L1 was conjugated to the surface of the microbubbles. UTMD improved drug delivery to the tumor potentially through three combined effects: αPD-L1 on the surface of the microbubbles specifically targeted the tumor cells; ultrasound sonication ruptured the microbubbles and released the carried drug at the LIFU-targeted tumor site; microbubble cavitation increased tumor permeability and promoted drug penetration across the vessel and into the tumor tissue. As a result, this therapeutic strategy inhibited tumor growth and improved the survival of mice implanted with tumor cells in the lung. It is worth to point out that lung diseases are often considered difficult to treat with FUS because the lungs are air-filled cavities. However, clinical studies have combined ultrasound and microbubbles to enhance drug delivery to the lungs of patients with pneumonia, acute respiratory distress syndrome, and NSCLC [45, 46]. It was proposed that because the diseased areas of the lung are filled with fluid, ultrasound waves could penetrate through the diseased area and leave normal air-filled areas of lung unaffected.

Microbubbles were also used as "anti-vascular" agents to disrupt blood vessels and increase the antitumor effects of ICI therapy of colorectal cancer in a study by Bulner et al. [19]. They found that UTMD alone induced an instant shutdown of blood flow within tumor tissue and resulted in tumor necrosis in a mouse model of colorectal cancer. The combination of UTMD and αPD-1 treatment conferred better tumor growth constriction and a higher survival rate than USMB or αPD-1 alone and rejected subsequent tumor rechallenge. However, the results did not support that the combined UTMD and αPD-1 treatment shifted T-cell subpopulations to a more favorable antitumor state.

In a murine breast cancer model, UTMD produced triple antitumor effects simultaneously: carrying an anti-CD326 antibody to target tumor cells, nonviral gene transduction of IFN-β by sonoporation, and tumor debulking by mechanical forces [20]. Such proximity of microbubbles to tumor cells using targeted microbubbles was crucial for effective sonoporation to transfect tumor cells. IFN-β expression plus αPD-1 led to a decreased tumor cell population and increased tumor-infiltrating CD8 T cells. The complete combination treatment attained greater tumor growth reduction in treated and distant tumors and prolonged survival than any partial treatments in the murine breast cancer model.

## Sonodynamic Therapy-Enhanced Immune Checkpoint Inhibitor Therapy

SDT utilizes LIFU to activate sonosensitizers and induces cytotoxicity [47, 48]. Unlike chemotherapy drugs that have massive toxicity on healthy cells, SDT induces tumor cell disruption only at the LIFU-targeted site. Preclinical studies have found that tumor cell debris generated by SDT could provide TAAs for initiating antitumor immunological effects [47, 48]. One report employed SDT using liposomes loaded with sonosensitizers and adjuvants [21]. Strikingly, SDT combined with αPD-L1 eradicated the primary tumor, suppressed distant tumor growth, inhibited whole-body metastasis in murine breast cancer models and produced sufficient immune memory responses to reject subsequent tumor rechallenge in murine breast and colorectal cancer models. The SDT-elicited antitumor effects, immune adjuvant-containing sonosensitizers, and αPD-L1-mediated systemic antitumor immune response were attributed to the robust antitumor response.

Recently, Um et al. used nanobubbles loaded with a sonosensitizer (chlorin e6) for the treatment of pulmonary metastasis of colorectal cancer [22]. Upon sonication, these nanobubbles caused cell membrane disruption by cavitation, which triggers immunogenic cancer cell death and releases intact DAMPs for *in situ* cancer vaccination. The combination of αPD-L1 with nanobubbles loaded with the sonosensitizer effectively suppressed primary and metastatic tumors, which suggested that physically induced tumor cell death by the nanobubbles combined with SDT can augment the efficacy of ICIs. More work is needed to determine whether this strategy can improve long-term survival and generate long-lasting immune memory responses against tumor recurrence.

# DISCUSSION

Recent publications have presented exciting and promising results that FUS modalities can improve ICI therapy. Combination therapies were reported to suppress tumor growth, achieve tumor remission, improve long-term survival, and prevent tumor recurrence for cancer types that are not readily responsive to ICI treatments. The field of FUS-enhanced IC therapy is still in its infancy, with all existing studies focused on proofing the concept. Further development of the combination strategy requires a multidisciplinary approach with a proper choice of FUS parameters for particular tumors, a complete examination of the correlation between FUS parameters and antitumor immune effects, a thorough evaluation of the biological mechanisms for therapeutic outcome, and a good understanding of the clinical challenges in cancer immunotherapy.

Although each FUS modality has the capability to improve ICI immunotherapy, it is still unknown which regimen has the greatest potential to combine with ICIs. One major challenge is the inconsistent reporting of FUS parameters and antitumor immune effects, which prevents correlating FUS parameters with antitumor immune effects. It is important to standardize reporting on FUS procedures to include all key parameters, such as ultrasound frequency, intensity, pressure, duty cycle, pulse repetition frequency, sonication target locations, and sonication duration. It is also critical to establish standards in reporting antitumor immune effects to enable comparisons across different studies. Another challenge is that the choice of the optimal FUS modality to improve ICI immunotherapy may depend on tumor type.

The biological mechanisms of each FUS-enhanced ICI therapy remain to be revealed. The reported HIFU thermal ablation-enhanced therapy required adjuvants to provide sufficient antigen cross-presentation and cross-priming for CD8 T cells. In contrast, HIFU mechanical ablation alone was sufficient to effectively stimulate antitumor immune responses to enhance ICI therapy. There was only one report on HIFU hyperthermia-enhanced ICI therapy. UTMD has great potential to improve ICI therapy through targeted and controlled release of therapeutics, sonoporation, and mechanical disruption of the blood vessels and tumor tissue. SDT induces tumor cell disruption only at the FUS-targeted site, resulting in reduced toxicity. Further investigations are warrant to better understand the biological mechanisms of each combination therapy.

FUS-enhanced ICI therapies have already undergone early stage clinical evaluations. Currently, two clinical trials have begun to evaluate the combination of HIFU thermal ablation with pembrolizumab (αPD-1) for the treatment of various advanced solid tumors, such as melanoma, breast cancer, and Merkel cell carcinoma (ClinicalTrials.gov Identifier: NCT04116320 and NCT03237572). The primary outcome will assess a change in the CD8/CD4 T cell ratio in the ablation zone, and the secondary outcome will assess adverse events. Meanwhile, one clinical trial has started evaluating the use of UTMD to enhance the permeability of the blood-brain barrier without causing vascular damage to facilitate the delivery of nivolumab (αPD-1) to melanoma metastases in the brain and boost immunity in the brain (NCT04021420).

For the successful clinical translation of FUS-enhanced ICI therapy, we need strong collaboration between ultrasound engineers and immunologists. Ultrasound engineers can optimize FUS parameters to induce the optimal biological effects that effectively induce antitumor immune responses with minimized side effects. Immunologists can better characterize the resulting antitumor immune responses and therapeutic outcomes. Through appropriate tuning of FUS exposure conditions and comprehensive immunological characterization, the prospect of unmasking the utility of FUS with ICI therapy could be attainable.

## AUTHOR CONTRIBUTIONS

HC conceived the outline of the review article and edited the manuscript. JY collected the literature, wrote the initial manuscript, and revised the manuscript. DY and SC revised the manuscript. All authors proofread and approved the final manuscript.

## FUNDING

National Institutes of Health (NIH) Grants R01EB027223, R01EB030102, and R01MH116981. The Charlie Teo Foundation and Little Legs Foundation.

## REFERENCES

1. Pardoll DM. The blockade of immune checkpoints in cancer immunotherapy. *Nat Rev Cancer* (2012) 12:252–64. doi:10.1038/nrc3239
2. Topalian SL, Taube JM, Pardoll DM. Neoadjuvant checkpoint blockade for cancer immunotherapy. *Science* (2020) 367:eaax0182. doi:10.1126/science.aax0182
3. Sharma P, Allison JP. Dissecting the mechanisms of immune checkpoint therapy. *Nat Rev Immunol* (2020) 20:75–6. doi:10.1038/s41577-020-0275-8
4. Zappasodi R, Merghoub T, Wolchok JD. Emerging concepts for immune checkpoint blockade-based combination therapies. *Cancer Cell* (2018) 33: 581–98. doi:10.1016/j.ccell.2018.03.005
5. Tempany CM, McDannold NJ, Hynynen K, Jolesz FA. Focused ultrasound surgery in oncology: Overview and principles. *Radiolgy* (2011) 259:39–56. doi:10.1148/radiol.11100155
6. Jolesz FA. MRI-guided focused ultrasound surgery. *Annu Rev Med.*60 (2009). p. 417–30. doi:10.1146/annurev.med.60.041707.170303
7. Silvestrini MT, Ingham ES, Mahakian LM, Kheirolomoom A, Liu Y, Fite BZ, et al. Priming is key to effective incorporation of image-guided thermal ablation into immunotherapy protocols. *JCI insight* (2017) 2:e90521. doi:10.1172/jci.insight.90521
8. Chavez M, Silvestrini MT, Ingham ES, Fite BZ, Mahakian LM, Tam SM, et al. Distinct immune signatures in directly treated and distant tumors result from TLR adjuvants and focal ablation. *Theranostics* (2018) 8:3611–28. doi:10.7150/thno.25613
9. Han X, Wang R, Xu J, Chen Q, Liang C, Chen J, et al. *In situ* thermal ablation of tumors in combination with nano-adjuvant and immune checkpoint blockade to inhibit cancer metastasis and recurrence. *Biomaterials* (2019) 224:119490. doi:10.1016/j.biomaterials.2019.119490
10. Sheybani ND, Witter AR, Thim EA, Yagita H, Bullock TNJ, Price RJ. Combination of thermally ablative focused ultrasound with gemcitabine controls breast cancer via adaptive immunity. *J Immunother Cancer* (2020) 8:e001008. doi:10.1136/jitc-2020-001008
11. Fite BZ, Wang J, Kare AJ, Ilovitsh A, Chavez M, Ilovitsh T, et al. Immune modulation resulting from MR-guided high intensity focused ultrasound in a model of murine breast cancer. *Sci Rep* (2021) 11:927–15. doi:10.1038/s41598-020-80135-1
12. Kheirolomoom A, Silvestrini MT, Ingham ES, Mahakian LM, Tam SM, Tumbale SK, et al. Combining activatable nanodelivery with immunotherapy in a murine breast cancer model. *J Control Release* (2019) 303:42–54. doi:10.1016/j.jconrel.2019.04.008
13. Wang J, Huang CH, Echeagaray OH, Amirfakhri S, Blair SL, Trogler WC, et al. Microshell enhanced acoustic adjuvants for immunotherapy in glioblastoma. *Adv Therap* (2019) 2:1900066. doi:10.1002/adtp.201900066
14. Eranki A, Srinivasan P, Ries M, Kim A, Lazarski CA, Rossi CT, et al. High-intensity focused ultrasound (HIFU) triggers immune sensitization of refractory murine neuroblastoma to checkpoint inhibitor therapy. *Clin Cancer Res* (2020) 26:1152–61. doi:10.1158/1078-0432.CCR-19-1604
15. Nam GH, Pahk KJ, Jeon S, Park HJ, Kim GB, Oh SJ, et al. Investigation of the potential immunological effects of boiling histotripsy for cancer treatment. *Adv Therap* (2020) 3:1900214. doi:10.1002/adtp.201900214
16. Qu S, Worlikar T, Felsted AE, Ganguly A, Beems MV, Hubbard R, et al. Non-thermal histotripsy tumor ablation promotes abscopal immune responses that enhance cancer immunotherapy. *J Immunother Cancer* (2020) 8:e000200. doi:10.1136/jitc-2019-000200
17. Singh MP, Sethuraman SN, Miller C, Malayer J, Ranjan A. *Boiling histotripsy and in-situ CD40 stimulation improve the checkpoint blockade therapy of poorly immunogenic tumors* (2021). p. 11. doi:10.7150/thno.49517
18. Li T, Hu Z, Wang C, Yang J, Zeng C, Fan R, et al. PD-L1-targeted microbubbles loaded with docetaxel produce a synergistic effect for the treatment of lung cancer under ultrasound irradiation. *Biomater Sci* (2020) 8:1418–30. doi:10.1039/c9bm01575b
19. Bulner S, Prodeus A, Gariepy J, Hynynen K, Goertz DE. Enhancing checkpoint inhibitor therapy with ultrasound stimulated microbubbles. *Ultrasound Med Biol* (2019) 45:500–12. doi:10.1016/j.ultrasmedbio.2018.10.002
20. Ilovitsh T, Feng Y, Foiret J, Kheirolomoom A, Zhang H, Ingham ES, et al. Low-frequency ultrasound-mediated cytokine transfection enhances T cell recruitment at local and distant tumor sites. *Proc Natl Acad Sci USA* (2020) 117:12674–85. doi:10.1073/pnas.1914906117
21. Yue W, Chen L, Yu L, Zhou B, Yin H, Ren W, et al. Checkpoint blockade and nanosonosensitizer-augmented noninvasive sonodynamic therapy

combination reduces tumour growth and metastases in mice. *Nat Commun* (2019) 10:1–15. doi:10.1038/s41467-019-09760-3

22. Um W, Ko H, You DG, Lim S, Kwak G, Shim MK, et al. Necroptosis-inducible polymeric nanobubbles for enhanced cancer sonoimmunotherapy. *Adv Mater* (2020) 32:e1907953. doi:10.1002/adma.201907953
23. Rowshanravan B, Halliday N, Sansom DM. CTLA-4: a moving target in immunotherapy. *Blood* (2018) 131:58–67. doi:10.1182/blood-2017-06-741033
24. Qin W, Hu L, Zhang X, Jiang S, Li J, Zhang Z, et al. The diverse function of PD-1/PD-L pathway beyond cancer. *Front Immunol* (2019) 10:2298–16. doi:10.3389/fimmu.2019.02298
25. Shi H, Lan J, Yang J. *Mechanisms of resistance to checkpoint blockade therapy*. Singapore: Springer (2020) doi:10.1007/978-981-15-3266-5_5
26. Robert C. A decade of immune-checkpoint inhibitors in cancer therapy. *Nat Commun* (2020) 11:10–2. doi:10.1038/s41467-020-17670-y
27. Pitt JM, Vétizou M, Daillère R, Roberti MP, Yamazaki T, Routy B, et al. Resistance mechanisms to immune-checkpoint blockade in cancer: tumor-intrinsic and -extrinsic factors. *Immunity* (2016) 44:1255–69. doi:10.1016/j.immuni.2016.06.001
28. Pauken KE, Dougan M, Rose NR, Lichtman AH, Sharpe AH. Adverse events following cancer immunotherapy: obstacles and opportunities. *Trends Immunol* (2019) 40:511–23. doi:10.1016/j.it.2019.04.002
29. Riley RS, June CH, Langer R, Mitchell MJ. Delivery technologies for cancer immunotherapy. *Nat Rev Drug Discov* (2019) 18:175–96. doi:10.1038/s41573-018-0006-z
30. Ye D, Yuan J, Yue Y, Rubin JB, Chen H. Focused ultrasound-enhanced delivery of intranasally administered anti-programmed cell death-ligand 1 antibody to an intracranial murine glioma model. *Pharmaceutics* (2021). 13(2):1–12. doi:10.3390/pharmaceutics13020190
31. Kennedy JE. High-intensity focused ultrasound in the treatment of solid tumours. *Nat Rev Cancer* (2005) 5:321–7. doi:10.1182/blood-2004-10-413510.1038/nrc1591
32. Izadifar Z, Izadifar Z, Chapman D, Babyn P. An introduction to high intensity focused ultrasound: systematic review on principles, devices, and clinical applications. *Jcm* (2020) 9:460. doi:10.3390/jcm9020460
33. van den Bijgaart RJ, Eikelenboom DC, Hoogenboom M, Fütterer JJ, den Brok MH, Adema GJ. Thermal and mechanical high-intensity focused ultrasound: perspectives on tumor ablation, immune effects and combination strategies. *Cancer Immunol Immunother* (2017) 66:247–58. doi:10.1007/s00262-016-1891-9
34. Yaghoubi N, Soltani A, Ghazvini K, Hassanian SM, Hashemy SI. PD-1/PD-L1 blockade as a novel treatment for colorectal cancer. *Biomed Pharmacother* (2019) 110:312–8. doi:10.1016/j.biopha.2018.11.105
35. Zhu L, Altman MB, Laszlo A, Straube W, Zoberi I, Hallahan DE, et al. Ultrasound hyperthermia technology for radiosensitization. *Ultrasound Med Biol* (2019) 45:1025. doi:10.1016/j.ultrasmedbio.2018.12.007
36. Baronzio GF, Delia Seta R, D'Amico M, Baronzio A, Freitas I, Forzenigo G, et al. Effects of local and whole body hyperthermia on immunity. In: *Hyperth cancer treat A prim* (2006) p. 247–75. doi:10.1007/978-0-387-33441-7_20
37. Chen H, Kreider W, Brayman AA, Bailey MR, Matula TJ. Blood vessel deformations on microsecond time scales by ultrasonic cavitation. *Phys Rev Lett* (2011) 106:034301. doi:10.1103/PhysRevLett.106.034301
38. Khokhlova VA, Fowlkes JB, Roberts WW, Schade GR, Xu Z, Khokhlova TD, et al. Histotripsy methods in mechanical disintegration of tissue: towards clinical applications. *Int J Hyperthermia* (2015) 31:145–62. doi:10.3109/02656736.2015.1007538
39. Duan Q, Zhang H, Zheng J, Zhang L. Turning cold into hot: firing up the tumor microenvironment. *Trends Cancer* (2020) 6:605–18. doi:10.1016/j.trecan.2020.02.022
40. Wang SS, Bandopadhayay P, Jenkins MR. Towards immunotherapy for pediatric brain tumors. *Trends Immunol* (2019) 40:748–61. doi:10.1016/j.it.2019.05.009
41. Hoogenboom M, Eikelenboom D, den Brok MH, Heerschap A, Fütterer JJ, Adema GJ. Mechanical high-intensity focused ultrasound destruction of soft tissue: working mechanisms and physiologic effects. *Ultrasound Med Biol* (2015) 41:1500–17. doi:10.1016/j.ultrasmedbio.2015.02.006
42. Chen H, Hwang JH. Ultrasound-targeted microbubble destruction for chemotherapeutic drug delivery to solid tumors. *J Ther Ultrasound* (2013) 1:10. doi:10.1186/2050-5736-1-10
43. Ferrara K, Pollard R, Borden M. Ultrasound microbubble contrast agents: fundamentals and application to gene and drug delivery. *Annu Rev Biomed Eng* (2007) 9:415–47. doi:10.1146/annurev.bioeng.8.061505.095852
44. Kanda S, Goto K, Shiraishi H, Kubo E, Tanaka A, Utsumi H, et al. Safety and efficacy of nivolumab and standard chemotherapy drug combination in patients with advanced non-small-cell lung cancer: a four arms phase Ib study. *Ann Oncol* (2016) 27:2242–50. doi:10.1093/annonc/mdw416
45. Lu B, Sun L, Yan X, Ai Z, Xu J. Intratumoral chemotherapy with paclitaxel liposome combined with systemic chemotherapy: a new method of neoadjuvant chemotherapy for stage III unresectable non-small cell lung cancer. *Med Oncol* (2015) 32:345–8. doi:10.1007/s12032-014-0345-5
46. Sugiyama MG, Mintsopoulos V, Raheel H, Goldenberg NM, Batt JE, Brochard L, et al. Lung ultrasound and microbubbles enhance aminoglycoside efficacy and delivery to the lung in Escherichia coli-induced pneumonia and acute respiratory distress syndrome. *Am J Respir Crit Care Med* (2018) 198:404–8. doi:10.1164/rccm.201711-2259LE
47. Wan GY, Liu Y, Chen BW, Liu YY, Wang YS, Zhang N. Recent advances of sonodynamic therapy in cancer treatment. *Cancer Biol Med* (2016) 13:325–38. doi:10.20892/j.issn.2095-3941.2016.0068
48. McHale AP, Callan JF, Nomikou N, Fowley C, Callan B. Sonodynamic therapy: concept, mechanism and application to cancer treatment. *Adv Exp Med Biol* (2016) 880:429–50. doi:10.1007/978-3-319-22536-4_22
49. Parsons JE, Cain CA, Abrams GD, Fowlkes JB. Pulsed cavitational ultrasound therapy for controlled tissue homogenization. *Ultrasound Med Biol* (2006) 32: 115–29. doi:10.1016/j.ultrasmedbio.2005.09.005
50. Roovers S, Segers T, Lajoinie G, Deprez J, Versluis M, De Smedt SC, et al. The role of ultrasound-driven microbubble dynamics in drug delivery: from microbubble fundamentals to clinical translation. *Langmuir* (2019) 35: 10173–91. doi:10.1021/acs.langmuir.8b03779
51. Dimcevski G, Kotopoulis S, Bjånes T, Hoem D, Schjøtt J, Gjertsen BT, et al. A human clinical trial using ultrasound and microbubbles to enhance gemcitabine treatment of inoperable pancreatic cancer. *J Control Release* (2016) 243:172–81. doi:10.1016/j.jconrel.2016.10.007
52. Carpentier A, Canney M, Vignot A, Reina V, Beccaria K, Horodyckid C, et al. Clinical trial of blood-brain barrier disruption by pulsed ultrasound. *Sci Transl Med* (2016) 8:343re2. doi:10.1126/scitranslmed.aaf6086
53. Park SH, Kim MJ, Jung HH, Chang WS, Choi HS, Rachmilevitch I, et al. Safety and feasibility of multiple blood-brain barrier disruptions for the treatment of glioblastoma in patients undergoing standard adjuvant chemotherapy. *J Neurosurg* (2020) 1–9. doi:10.3171/2019.10.jns192206
54. Lipsman N, Meng Y, Bethune AJ, Huang Y, Lam B, Masellis M, et al. Blood-brain barrier opening in Alzheimer's disease using MR-guided focused ultrasound. *Nat Commun* (2018) 9:2336. doi:10.1038/s41467-018-04529-6
55. Abrahao A, Meng Y, Llinas M, Huang Y, Hamani C, Mainprize T, et al. First-in-human trial of blood-brain barrier opening in amyotrophic lateral sclerosis using MR-guided focused ultrasound. *Nat Commun* (2019) 10:4373. doi:10.1038/s41467-019-12426-9
56. Rosenthal I, Sostaric JZ, Riesz P. Sonodynamic therapy–a review of the synergistic effects of drugs and ultrasound. *Ultrason Sonochem* (2004) 11: 349–63. doi:10.1016/j.ultsonch.2004.03.004
57. Kenyon J, Fulle R, Lewis T. Activated cancer therapy using light and ultrasound - a case series of sonodynamic photodynamic therapy in 115 patients over a 4 Year period. *Cdth* (2009) 4:179–93. doi:10.2174/157488509789055036

**Conflict of Interest:** The authors declare that the research was conducted in the absence of any commercial or financial relationships that could be construed as a potential conflict of interest.

# Advantages of publishing in Frontiers

**OPEN ACCESS**
Articles are free to read
for greatest visibility
and readership

**FAST PUBLICATION**
Around 90 days
from submission
to decision

**HIGH QUALITY PEER-REVIEW**
Rigorous, collaborative,
and constructive
peer-review

**TRANSPARENT PEER-REVIEW**
Editors and reviewers
acknowledged by name
on published articles

**Frontiers**
Avenue du Tribunal-Fédéral 34
1005 Lausanne | Switzerland

**Visit us:** www.frontiersin.org
**Contact us:** frontiersin.org/about/contact

**REPRODUCIBILITY OF RESEARCH**
Support open data
and methods to enhance
research reproducibility

**DIGITAL PUBLISHING**
Articles designed
for optimal readership
across devices

**FOLLOW US**
@frontiersin

**IMPACT METRICS**
Advanced article metrics
track visibility across
digital media

**EXTENSIVE PROMOTION**
Marketing
and promotion
of impactful research

**LOOP RESEARCH NETWORK**
Our network
increases your
article's readership